ORE LIBERATION AND CHARACTERIZATION USING ELECTRIC PULSE DISAGGREGATION AND OTHER NOVEL TECHNIQUES

A THESIS SUBMITTED TO THE FACULTY OF THE UNIVERSITY OF MINNESOTA DULUTH BY

Matthew Matko

IN PARTIAL FULFILLMENT OF THE REQUIREMENTS FOR THE DEGREE OF MASTER OF SCIENCE

Adviser: Dr. Howard Mooers

March 2020

Acknowledgments

I would like to take some space to acknowledge all the individuals who have provided me with help and support throughout this journey. Firstly, I would like to thank Dr. Howard Mooers for taking over as my primary advisor after the departure of Dr. Christian Schardt,. While Dr. Schardt provided the original concept behind this project Dr. Mooers gave me the necessary focus and direction to complete it. Secondly, I would like to thank both Dr. Nigel Wattrus and Dr. Rodney Johnson who were both thesis committee members, answering any additional questions and concerns that I had. Dr. Wattrus was also of great assistance in guiding me towards a path to completion. I would also like to express my sincerest thanks to Dr. John Goodge and Dr. Latisha Brengman. Without their help and guidance, I might still be collecting data, trying to find my way blindly out of a dark cave.

In addition to those listed above, I would also like to thank several individuals that provided significant help with different aspects of my thesis. Dr. Brian Bagley the lab manager at the XRCT lab at the University of Minnesota – Twin Cities campus for providing the crucial help of scanning my samples and all the additional questions and help I needed in learning how to process XRCT data. Dr. Tsutomu Shimotori the lab manager at the RIL in Duluth for all his help with scanning my samples in the SEM using the MLA software package. Steven Hauck the then Director of Economic Geology at UMD's NRRI for donating samples of Duluth Complex material. Bob Mahin, Exploration Manager at Eagle Mine, for donating samples of ore from their Cu-Ni mine. The SELFRAG Company, which loaned us the use of one of their EPD machines. A final

thanks must go to Ross Solerno my graduate student peer that was an essential source of encouragement, always pushing me forward when I felt lost.

Dedication

I dedicate this body of work to my wife, Tara Marie Matko, and my son and daughter, Wakefield, and Larkin Matko. Without the deep well of support that you all provided me I would have never been able to complete this journey. I recognize that this has been a very hard and long journey for you guys too and I truly appreciate all the sacrifices you have made for me along the way. I love you guys so much.

I would also like to dedicate this to my parents William and Ann Matko and Michael and Brenda Daniels. I could have never done this without all the help and support that you provided us. Love you all.

A final dedication goes to my dear sister, Tara Elizabeth; I started this journey with you but am sadly finishing it without you. I will love and miss you forever.

Abstract

Preliminary tests were performed to determine the efficiency of electric pulse disaggregation (EPD) technology on ore mineral liberation, from the surrounding gangue material on a wide range of ore deposits types. In addition to processing using EPD technology, samples were scanned using X-ray computed tomography (XRCT). All the collected data were then used to characterize the ore particles in novel ways. The samples in this investigation came from the following deposit types; a liquid-magmatic deposit that represents Si-differentiation, liquid-magmatic deposits that represent immiscible sulfide melts, porphyry deposits, VHMS deposits, an MVT deposit, and an SSC deposit.

Ten samples from different ore deposits were processed in a SELFRAG EPD machine. The samples were then fractionated by sieving where a grain size of -250 μm to +150 μm was chosen for constructing grain mounts. The grain mounts were scanned in an SEM using mineral liberation software where the percentage of ore that had achieved liberation was used to evaluate the efficiency of the EPD process. Solid portions of all the samples that were not disaggregated were scanned in an XRCT. Data from these scans were then processed as raw numerical information or processed using 3D visualization software.

The results from EPD efficiency display a wide range of possibilities, anywhere from no liberation to values as high as 97%, with most samples displaying good liberation percentages in the high 60% if the null liberation values are ignored. Null liberation values were ignored because it was discovered, through analysis of ore grain size data exported from XRCT scans, that the in-situ ore grain size was greater than that

of the material selected for the grain mounts. This realization informed the decision to ignore these null values when calculating the average liberation of all samples.

By using data acquired from XRCT scans, three useful techniques were employed that have the potential to aid in future studies of ore bodies. 3D reconstructions of scanned cores allowed for the identification of micro-structures such as; planar mineralization pathways that were sub-100 μm thick, possible shear surfaces expressed as abrupt planar terminations of ore occurrences, and interruptions in stratigraphically controlled ore that may have been important fluid migration pathways for the movement of ore-bearing fluids. Shape analysis graphs were constructed comparing the long and short axis information exported from XRCT scans. The results of these graphs revealed that most samples contained roughly equal proportions of spherical and elongate ore grains, but a sample from a liquid-magmatic Si-differentiation deposit was much more spherical in its ore morphology while a sample from an SSC deposit was the most elongate in morphology. Finally, vector graphs were constructed that illustrate the long axis orientation of ore grains in-situ within scanned samples. A number of these samples display apparent preferred orientation directions. For samples that originated in deposits where fluid flow is a key factor in ore emplacement, these vector graphs have the potential to inform the investigator as to the direction of ore propagation. The results that were arrived at in this study, while promising, are preliminary and further work is required verify the utility of the techniques.

Table of Contents

List of Tables

List of Figures

1. Introduction

Electric pulse disaggregation (EPD) is a relatively new technology, and its utility within the realm of the geological sciences or more specifically within the realm of economic geology is under investigation. This technology was originally developed in the Soviet Union in the 1960's and was kept as a military secret until 1977 when a member of the original research team emigrated and published a paper on the technology (van der Wielen et al., 2014). The technology's potential usefulness stems from its ability to separate ore minerals/aggregates from rock-forming minerals in a manner that results in a coarser final product than traditional crushing and grinding methods. The method by which separation is achieved is by sending pulses of high voltage electricity through sample material that has been submerged in water. While water is normally a good electrical conductor, at voltages in excess of 100 kV the dielectric property of water is overcome. This causes water to act effectively as an insulator, which forces the electrical pulse generated to travel through the sample material. As ore minerals are typically more conductive that silicates, pulses of electricity will travel through the sample material by preferentially branching off and passing through ore minerals and liberating them from the gangue. The liberation is achieved by the electricity that is traveling through the sample material forming a plasma wave that collapses, creating tensile fracturing (van der Wielen et al., 2014; Sperner et al., 2015).

To test the effectiveness of EPD technology at separating ore minerals from silicates, ten samples were selected from a wide range of ore deposit styles. The deposit types represented liquid-magmatic (representing both Si-differentiation and immiscible S

melts), porphyry, volcanic-hosted massive sulfide (VHMS), Mississippi Valley-type (MVT), and sediment-hosted stratiform copper (SSC) deposits.

In order to quantify how well the ore minerals were separated from the gangue, grains mounts were constructed using the disaggregated material that resulted from EPD processing and scanned in a scanning electron microscope (SEM) using mineral liberation analysis (MLA) software. The MLA software classified what percentage of ore grains had over 95% of their perimeter free from any other mineral making them effectively liberated.

In addition to the previously described tests, all samples also were scanned using x-ray computed tomography (XRCT), which allowed for the inspection of ore grains in-situ; key properties of the ore that were of interest were shape, size, and orientation of the ore grains. This technique was performed so that in-situ ore data could be compared to data that resulted from material processed by the EPD technology.

2. Project Goals

There have been numerous studies that have investigated the use of electric pulse disaggregation (EPD) as a tool for liberating ore particles from the surrounding gangue (Andres and Bialecki, 1986; Andres, 1989, 1995 ,2010; Rudashevsky et al., 1995; Lastra et al., 2003; Wang et al., 2011, 2012) . However, none of these studies addressed the question of the efficiency of this process at mineral liberation with respect to different ore deposit types. As such, the primary goal of this investigation is to quantify mineral

liberation, with a specific focus on any differences in liberation efficiency that occur between different ore deposit types and mineralization styles. Liberation efficiency in this study is defined as the overall percentage of grains that are classified as liberated by mineral liberation analysis (MLA) software; where liberation is established as grains that have over 95% of their grain boundary free of any other mineral.

Two secondary goals evolved over the course of the investigation and will be addressed within this manuscript. First, how well does EPD technology preserve mineral grain morphology; and second, evaluate the potential of the various technologies and techniques used in this study to characterize ore mineralization within an ore deposit.

Previous studies indicate that EPD technology preserves a mineral's grain morphology whereas conventional ore processing/crushing creates fractures and usually destroys the original boundaries (Rudashevsky et al., 1995; Saini-Eidukat and Weiblen, 1996; Cabri et al., 2008) . Most of these studies utilized SEM secondary electron images to show the morphological characteristics that are distinct to each mineral in question, which provides evidence of the non-destructive capabilities of the EPD. Given that advanced imaging techniques in the form of x-ray computed tomography (XRCT) were utilized for this study, results will be evaluated to determine how XRCT data, representing in-situ material conditions, compared to material processed by EPD.

Since technologies such as EPD and XRCT are still relatively new and not widely used, their usefulness and applicability for both economic geology and mineral comminution was evaluated throughout this study.

3. Background

Since EPD technology is not widely used, it may be unfamiliar to many readers, so a brief overview of the technology has been provided in this chapter. As the material studied here comes from a variety of geological settings this chapter will mainly focus on briefly describing the different deposit types that are represented by the samples investigated. Current and accepted hypotheses for how these deposits form will be reviewed with the goal of providing additional insights.

3.1 Electric Pulse Disaggregation

The science behind the EPD technology was pioneered by Soviet scientists during the 1940's and didn't become well described until the 1960's by Western scientists (Saini-Eidukat and Weiblen, 1996). More recent, work has focused on this technology's potential use for things like ore comminution, pre-weakening ores, fossil liberation, and tracer mineral liberation such as zircon and apatite grains (Saini-Eidukat and Weiblen, 1996; Andres, 2010; Giese et al., 2010; Wang et al., 2011; Sperner et al., 2014) . This technology works by submerging a sample within a water-filled vessel between an electrode and anode and subjecting it to pulses of high voltage electricity. The electricity travels from the anode positioned above the sample to the cathode built into the base of the sample vessel (fig 3.1). At voltages above 100 kV the water in the sample vessel acts as an insulator forcing the electricity to travel through the rock instead (fig 4.4; Saini-Eidukat and Weiblen, 1996). As the electricity travels through the rock sample it creates a plasma wave. It is the propagation and radial expansion of this wave that creates the tensional forces that eventually lead to the disaggregation of the rock as these forces

travel along grain boundaries. A typical setup for the samples that were processed was described in chapter 4.1.4 (Sperner et al., 2014).

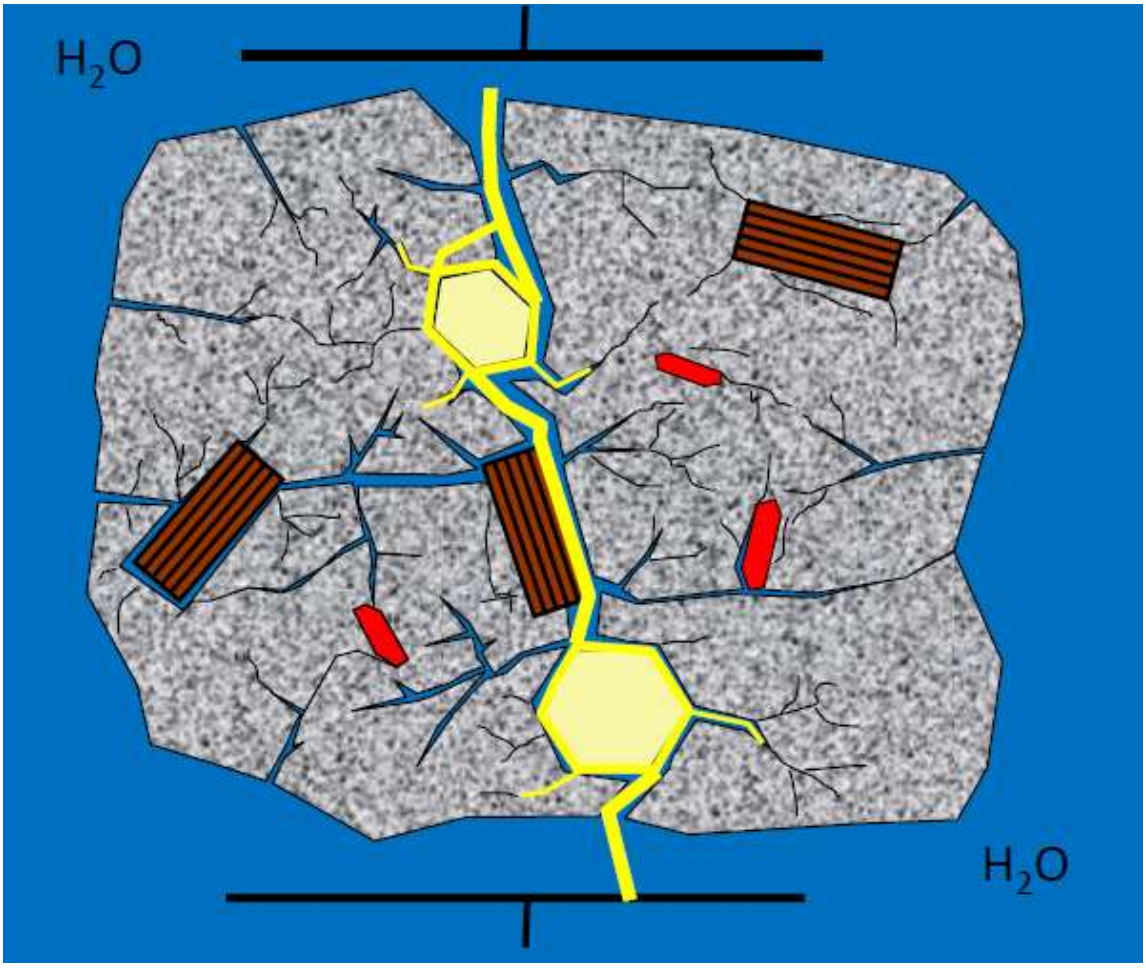

Figure 3.1 A schematic diagram illustrating an electric pulse moving through a rock sample during disaggregation (Weh, 2013).

3.2 Ore Deposit Models

Ore deposits are formed in a wide variety of geological settings. Concentration of ore minerals can occur within magmatic systems by differentiation of a silicate melt or by concentration of immiscible Sulfide minerals. Hydrothermal systems, generally associated with magmatic systems, result in a wide variety of ore deposits including porphyry ore deposits, skarns, epithermal hydrothermal vein deposits, volcanogenic

massive sulfides, sedimentary exhalative, and Mississippi Valley type deposits. Sedimentary systems also contain various ore deposit types, including sediment-hosted stratabound copper deposit.

Each of the aforementioned ore deposits types are associated with particular ore minerals, and each has a characteristic ore mineral grain size, concentration, and relationship to gangue. Appendix 4 contains an in-depth summary of the major ore deposit types.

4. Methods

4.1 Sampling

To apply the analytical techniques, described below in section 4.2, to a diverse representation of deposit types, sampling was accomplished primarily by selecting material from the University of Minnesota – Duluth's (UMD) economic geology collection. In addition, mineralized Duluth Complex material was acquired from Steven Hauck the former Director of Economic Geology at UMD's Natural Resources Research Institute (NRRI). Samples of Cu-Ni disseminated sulfide ore from the Eagle Mine/Michigan were obtained from Bob Mahin, Exploration Manager at Eagle Mine in Marquette, Michigan. A sample of mineralized MVT was donated by Latisha Brengman in the Department of Earth and Environmental Sciences at UMD.

4.1.1 Sample Preparation

After sample selection, detailed petrographic descriptions for each sample were prepared with specific focus on ore mineralogy, existing textures, and alteration mineral assemblages present. From the sample material, slabs and cores were extracted for a variety of invasive and non-invasive analyses.

4.1.2 Slabs and Cores

Slabs were cut from each sample for the purpose of mechanical disaggregation and subsequent sieve analysis. The resulting aggregate was then used to produce grain stacks and grain mounts for selected samples for further analysis. Slabs (8 x 4 cm) were prepared from each hand sample using a MK Diamond Blade Rock Saw.

Small, 25 mm cores from selected samples were also removed from the remaining portion of hand sample to be scanned using X-Ray Computed Tomography (XRCT) and/or produce thick sections for reflected light microscopy. A drill press equipped with a 25 mm diamond core bit was used to remove cores 40 to 70 mm long. Resulting cores were cut to appropriate 30 mm length for XRCT use and about 10 mm long for the creation of thick sections using the MK Diamond Bladed Rock Saw.

4.1.3 Thick Sections

Polished thick sections of selected samples were produced to aid in the identification and description of ore minerals and associated textures using reflected light microscopy. Reflected light microscopy allows of the identification of opaque minerals

that would otherwise be unidentifiable using standard transmitted light microscopy (Nesse, 2012)

Plastic cylinder molds were used to mount the discs in an epoxy resin. The inside of the mold was coated with Beuhler Release Agent to ensure easy removal of the section later on. Samples discs were placed in the molds and a mixture of Buehler Epoxicure resin and hardener were poured over the top to fill the mold. The ratio of resin to hardener used was 10 g of resin to 1.2 g of hardener. Molds were allowed to set for a minimum of 48 hours to ensure that the epoxy had completely hardened. Once the epoxy pucks had been removed from the plastic molds they were ground down using a series of increasingly finer grit silicon carbide discs (180-grit, 320-grit, 600-grit, and 1200-grit) and then polished using a series of increasingly finer aluminum oxide powders (9 μm, 3 μm, 1 μm, and 0.05 μm).

All grinding and polishing work was accomplished using an Allied M-Prep 5 Grinder/Polisher. Between each step of grinding, the samples were inspected using a binocular microscope. After grinding was complete, all the samples were cleaned in a Branson 1510 Ultrasonic Cleaner for 5 minutes before the final polishing process. Much like the grinding procedure, samples were visually inspected between each polishing step to verify that scratches left by the previous step were being reduced or removed completely.

4.1.4 Electric Pulse Disaggregation

Electric Pulse Disaggregation (EPD) was used to break down sample material cut from the original hand samples into their mineral aggregates used to produce grain

mounts and grain stacks. Details of this technology are provided below (4.2.2). Rock samples were placed into a water filled sample vessel of the SELFRAG High Voltage Pulse Power Fragmentation EPD device (fig. 4.1). Closing the doors of the machine creates a closed Faraday cage that protects the operator from the high voltages used.

Figure 4.1 SELFRAG High Voltage Power Fragmentation EPD device with the sample chamber doors closed and touch panel controls (a). Sample chamber doors open displaying the sample vessel resting on the green lifting platform (b). Close-up of the control panel displaying the 4 variables than can be adjusted before sample processing (c); see 4.2.2 for details.

Using a touchscreen electrode gap, pulses, frequency, and voltage can be controlled (fig. 4.1c). The gap is the distance between the upper and lower anode/cathode. The pulses setting is the number of pulses of a specified voltage administered to a sample. Frequency is the number of pulses that are discharged in a single second and can be set from 1 to 5 Hz. The voltage setting is how much energy will be discharged with each individual pulse and ranges from 100 to 200 kV.

A typical setup used was an initial gap of 40 mm, a voltage of 140 kV, and 20 pulses per run. An initial run was used to break the sample down into smaller fragments to allow for a smaller gap between the anode and cathode and a more effective utilization of subsequent electric pulses since a shorter distance between the anode and cathode allows a more efficiently electrical discharge. The machine was then routinely set to a gap of 20 mm at 180 kV delivering 200 pulses for a complete sample disaggregation.

Between the processing of each sample, a rigorous cleaning procedure was followed. The entire sample vessel was disassembled and thorough cleaned to avoid contamination and maximum sample retrieval. The vessel was then reassembled for the next sample to be processed. Disaggregated sample material was collected into plastic containers and dried in a sediment oven set at 60 °C for 2 hours.

4.1.5 Grain Mounts

Grain mounts were analyzed by Scanning Electron Microscopy (SEM) using Mineral Liberation Analysis (MLA). Mounts were made by selecting specific grain size fractions from EPD processing. Visual inspection of sieved aggregate indicated that the

150 to < 250 μm size fraction best represented gangue-ore mineral separation. This material was then separated and prepared for grain mounting.

Aggregate material needed to be affixed in epoxy to allow for grinding and polishing for SEM analysis. 1 g of aggregate sample with a 1.5" mold produces a suitable grain mount (Drexler, 2007). Additionally, when running MLA analysis, grain separation is vitally important because grain contact will cause the MLA software to identify them as a single object. To aid in the separation of grains spherical graphite particles (150 μm size) were added to the sample aggregate at a ratio of 2-parts graphite to 1-part sample. Powders were thoroughly mixed to maximize the distribution of graphite throughout the sample material. The graphite signal is filtered out by the MLA software during data processing and does not interfere with the analysis.

After the sample material and graphite were thoroughly mixed, it was placed in the mold and a mixture of Buehler Epoxicure resin and hardener were poured over the top to fill the mold. A very fine stirring tool was used to ensure that all the air was able to escape from the mold and that the epoxy had reached the bottom of the mold. Molds were allowed to set at least 48 hours to guarantee complete hardening. Once the epoxy pucks had been removed from the plastic molds, they were first ground down using a series of increasingly finer grit silicon carbide discs and then polished using a series of increasingly finer aluminum oxide powders.

As with thick sections, grinding and polishing were completed using the Allied M-Prep 5 Grinder/Polisher. Each grain mount was inspected using a binocular microscope after 2 minutes of grinding and polishing and if needed rechecked after 4

minutes. After grinding was complete all the samples were run in the Ultrasonic Cleaner for 5 minutes before the polishing.

For the polishing process, the M-Prep 5 had its speed reduced to 100 rpm to avoid grains being plucked out of the epoxy molds. Like the thick section procedure, the polishing cloth pads were used with the slurries of increasingly finer aluminum oxide polishing media. Between each polishing stage, samples were washed in the ultrasonic bath for 5 minutes and then visually inspection using the binocular microscope. All the polished grain mounts then have a 15 to 20 nm carbon coating applied using a Ladd Research Industries Batch Carbon Coater.

4.1.6 Grain Stacks

Grain stacks were produced to be scanned using the XRCT for the purpose of analyzing the grain morphology of material processed using EPD. A sieve analysis was performed from the material that was processed through the EPD. The series of sieves used are listed in Table 4.1.

Aperture Opening (μm)	Designation
2812	7
2057	10
1405	14
1204	18
710	25
600	30
250	60
150	100
75	200
45	325

Table 4.1: ASTM Sieve Designation and Corresponding Nominal Aperture Openings

Grain stacks were produced to allow inclusion of different, separated grain size fractions for each sample in one stack. To make the grain stacks 3M VHB double-sided tape was cut into 24 mm by 24 mm squares with one corner notched to track sample orientation. One side of the adhesive was exposed and sample material from one size fraction was carefully distributed onto one-half of one side of the exposed side of the tape with a different size fraction being applied to the other half. Another square portion of tape was cut, notched, and the bottom portion of the adhesive exposed. This piece was then laid on top of the previous, sample-coated, piece of tape. This created a sandwich-like structure with sample material trapped between two pieces of tape. The upper portion of adhesive was then exposed on the second piece of tape and once again two size fractions of a sample were applied onto a half of one side of the tape. This process was repeated until a stack of tape layers with sample material in between was created that was 30 mm tall. Grain stacks were created in this manner until all the selected size fractions of the samples were represented (35 samples total). For all samples four size fractions, 250 μm,

150 µm, 75 µm, and 45 µm, are represented, which resulted in the construction of 3 grain stacks (fig. 4.2).

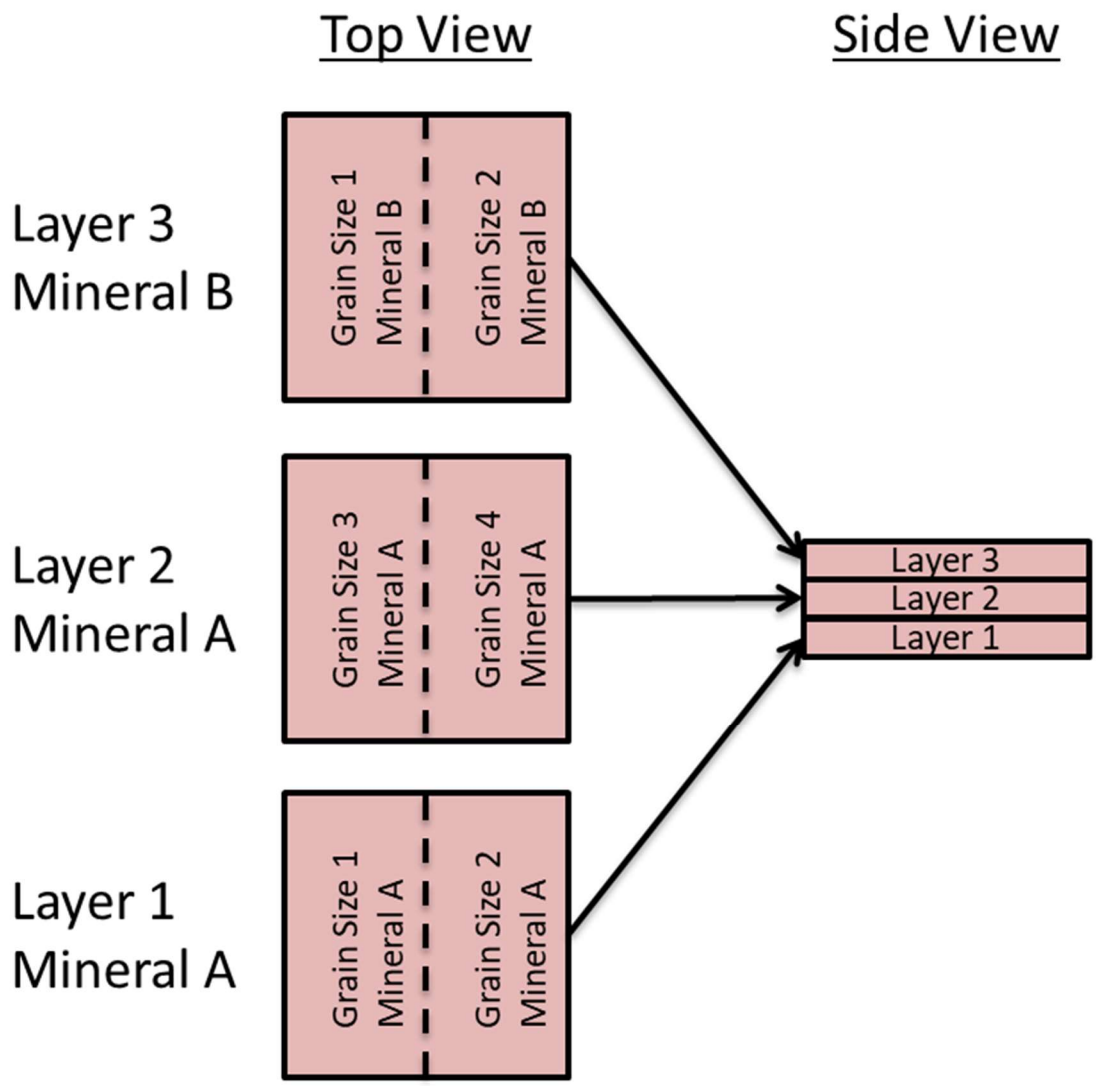

Figure 4.2 A schematic diagram illustrating how the grain stacks were constructed.

4.2 Analytical Methods

A variety of samples were selected for this study to represent a wide range of ore deposit types. Each sample was cut in half. One-half was disaggregated using EPD technology while the other half had a small 2.5 cm diameter core removed from it. The

core was scanned using XRCT so that in-situ properties could be examined. Samples that were disaggregated ranged from 60 to 300 g depending on the original size of the sample. Using the disaggregated material, a sieve analysis was performed for each sample and grain mounts were made using material from the 150 µm to 250 µm size fraction. These grain mounts were then used in an SEM and run through an MLA analysis. Small discs of material were removed from the cores scanned by XRCT so that thick sections could be produced for use in reflected light petrography

4.2.1 X-ray Computed Tomography (XRCT)

The basis of XRCT scanning originated in the medical field and functions in a similar way to CT or "CAT scan". In a medical CT scan a patient is slowly moved through the CT scanner while lying on a platform. While the patient moves through the circular opening of the machine an x-ray source is emitting an x-ray bean that is then received by a detector opposite the beam source. The source and detector are in fixed locations relative to each other but can freely rotate as a unit. As the scan is proceeding, the source/detector unit rotates around the circular opening as the patient moves through. The resulting data obtained are used to create a series of images, called slices, where each image represents what the patient's body would look like if sliced along the scan plane. All of the recorded slices are then recombined, called a stack, using 3D visualization software to create spatial reconstructions of specific internal organs or bones (fig. 4.3; Ketcham and Iturrino, 2005; Brenner and Hall, 2007). The main difference between a CT scan and an XRCT scan is that the x-ray source and detector are truly fixed in an XRCT (fig. 4.4).

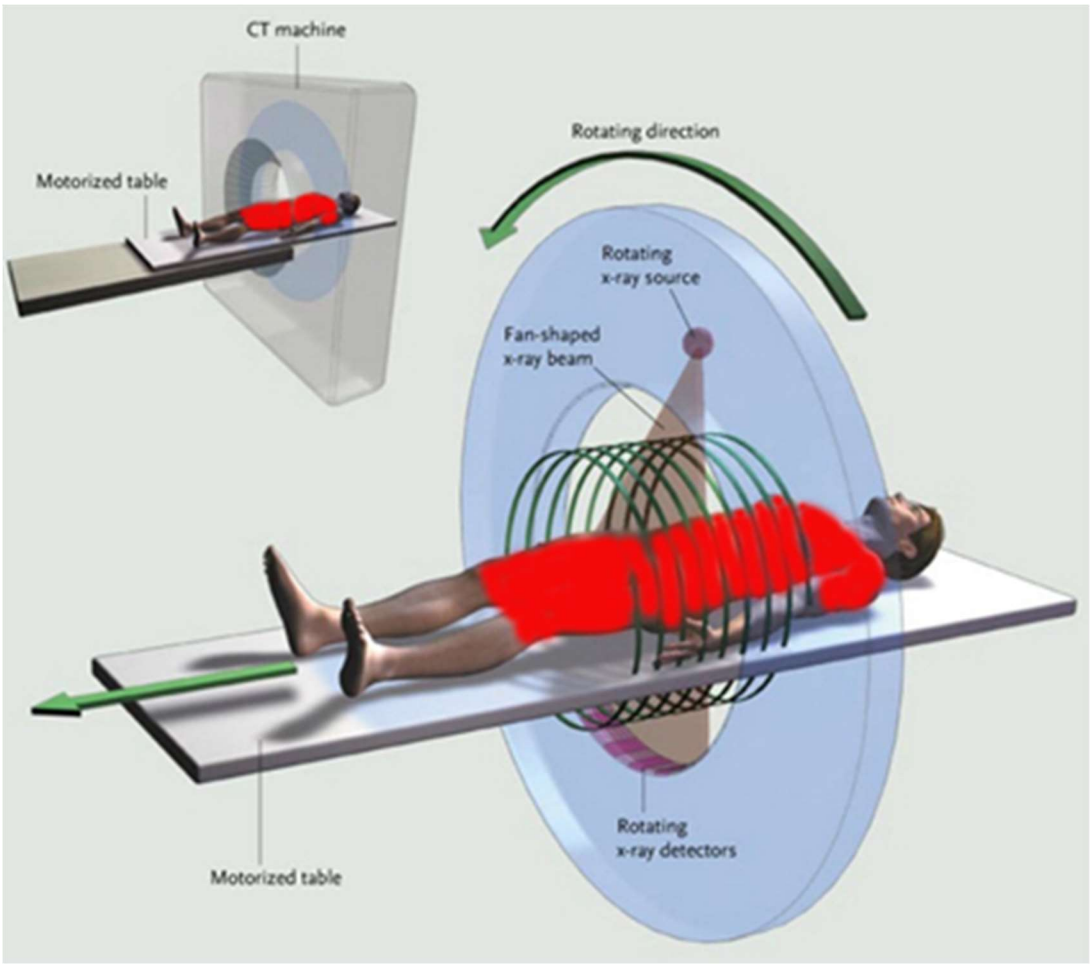

Figure 4.3 A schematic diagram illustrating the basic parts and functions of a medical CT scanner (Brenner and Hall, 2007)

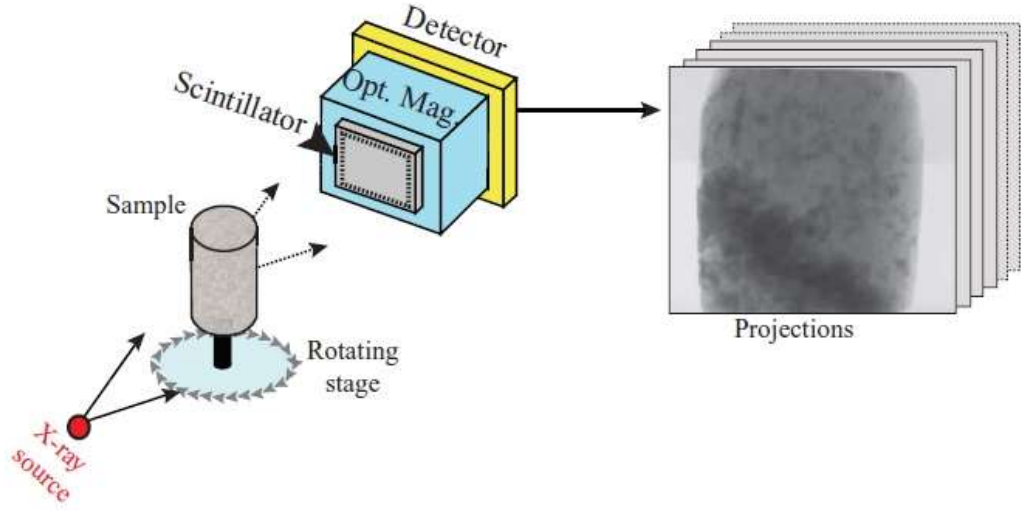

Figure 4.4 A schematic diagram illustrating the main components of an XRCT scanner (Godel, 2013).

Since the size of the objects scanned in an XRCT are significantly smaller than a human the object itself is rotated. Another key difference is the number of slices that are recorded. A CT typically consists of a few hundred slices being recorded while an XRCT scan, even though it is typically performed on much smaller objects, results in thousands of slices being recorded. This means that the overall resolution of an XRCT scan is much better than a medical CT scan (Brenner and Hall, 2007; Godel, 2013) .

All scans were performed at the X-ray Computed Tomography Lab at the University of Minnesota – Twin Cities. The lab houses a X5000 high resolution microCT system with a twin head 225 kV FeinFocus FXE-225.99 X-ray tube, which is capable of a <6 μm focal spot size, and a Dexela 2923 area detector with a resolution of 3889 x 3073 pixels. All the data processing was performed using Avizo a 3D data visualization and analysis software package. All samples were scanned using a voltage of 150 kV and an average scan time of about 1 hour. All samples scanned utilized a 1 mm Al filter except for the sample 1716 which utilized a 0.127 mm Cu filter. A total of 1080 projections were collected throughout 360 degrees of rotation. The calibration reports and technique sheets for each sample can be found in appendix 4; these documents show the x-ray settings for each scan along with the voxel size.

4.2.2 Electric Pulse Disaggregation (EPD)

Using XRCT provides a unique way to investigate in-situ material properties without any mechanical disaggregation. The EPD however, provides an avenue to investigate samples that have been disaggregated while at the same time not using the

traditional jaw crusher method. This method provided an opportunity to characterize ore minerals present within these samples as separate particles removed from any silicate material that surrounded them. To achieve this goal EPD technology was utilized to disaggregate the samples as it has been shown to liberate minerals from one another at coarser size fractions than mechanical grinding and ideally preserves mineral grain shape characteristics (Saini-Eidukat and Weiblen, 1996; Wang et al., 2012).

Tables 4.2 through 4.4 contain the EPD settings for samples processed using the EPD laboratory. Table 4.2 highlights samples that were run through all the techniques (EPD, XRCT, and MLA). The gap setting represents the distance between the anode and cathode that discharge the electric pulses. A smaller gap is preferred as this allows for more consistent discharges of energy. To achieve the smallest gap possible samples were initially set with a gap of roughly 40 mm and were then subjected to 20 lower voltage pulses (140 kV) to facilitate in the breakdown of the sample into smaller pieces. The samples then had their gap decreased (ideally to 20 mm but this was not always achieved) so that the main disaggregation could be performed using a higher number of pulses at 180 kV. The starting and ending weights record the loss of sample material either because of being trapped in the sample vessel (a sample vessel design limitation) or by being suspended in the water bath; the water bath was not retained for these samples.

Sample Name	Gap (mm)	Number of Pulses	Voltage (kV)	Starting Weight (g)	Ending Weight (g)	Total Energy Discharged (J)
EG-181	25	20	140			
	20	200	180	107.2	105.8	3.951×10^4
Eagle-1	35	20	140			
	35	40	160			
	25	200	180	204.5	202.1	7.013×10^4
DC	40	20	140			
	20	100	160			
	20	200	180	292.5	289.5	9.802×10^4
Bag-1	40	21	140			
	25	200	180	156.8	154.7	6.061×10^4
V-1	30	20	140			
	20	76	180	80.5	77.2	1.735×10^4
O-219	20	20	140			
	20	100	180	51.6	50.4	1.933×10^4
SLC-55	20	20	140			
	20	200	180	64.5	62.6	6.434×10^4
SLC-2476	30	20	140			
	20	200	180	84.3	83.3	6.969×10^4
MVT-1	20	20	140			
	20	116	180	62.5	61.3	2.683×10^4
1716	35	20	140			
	25	300	180	161.7	159.5	6.291×10^4

Table 4.2 EPD settings for samples processed using EPD along with starting and ending sample weights and total energy discharged by the machine. The gap is the distance between the anode and cathode which discharge the electric pulses. All samples had the additional setting of their frequency being set to 5 Hz, meaning there were 5 pulses discharged every second.

Tables 4.3 and 4.4 highlight two suites of samples that were processed using EPD only. Both suites are composed of samples that originated from the Duluth Complex Mesaba deposit. The first suite, DC-1 through DC-8 (Table 4.3) were all processed using a voltage of 120 kV. The second suite, DC-9 through DC-16 (Table 4.4) were all processed using a voltage of 180 kV. The purpose of these two sample suites was to

compare their sieve analyses to one another to see what possible effect differing voltages had on disaggregation. Additional samples were processed using EPD. A table showing their settings can be found in Appendix 2.

Sample Name	Gap (mm)	Number of Pulses	Starting Weight (g)	Ending Weight (g)	Total Energy Discharged (J)
DC-1	30	5			
	20	20	152	151.5	$3.842x10^3$
DC-2	30	5			
	20	45	155.4	153.1	$6.866x10^3$
DC-3	30	5			
	20	70	155	150.8	$9.969x10^3$
DC-4	30	5			
	20	95	152	149	$1.282x10^4$
DC-5	30	5			
	20	120	153.6	150.6	$1.578x10^4$
DC-6	30	5			
	20	145	150.9	148.9	$1.728x10^4$
DC-7	30	5			
	20	170	152	149.2	$2.072x10^4$
DC-8	30	5			
	20	195	153.5	151.2	$2.264x10^4$

Table 4.3 EPD settings for suite of samples from the Duluth Complex Mesaba deposit; along with starting and ending sample weights and total energy discharged by the machine. The gap is the distance between the anode and cathode which discharge the electric pulses. All samples had the additional settings of their voltage being set at 120 kV and frequency set to 5 Hz, meaning there were 5 pulses discharged every second.

Sample Name	Gap (mm)	Number of Pulses	Starting Weight (g)	Ending Weight (g)	Total Energy Discharged (J)
DC-9	30	5			
	20	20	151.4	149.4	7.075×10^3
DC-10	30	5			
	20	45	154.5	152.4	1.351×10^4
DC-11	30	5			
	20	70	154	151.4	1.788×10^4
DC-12	30	5			
	20	95	154.7	152.3	2.195×10^4
DC-13	30	5			
	20	120	151.2	148.7	3.069×10^4
DC-14	30	5			
	20	145	150.4	147.6	3.556×10^4
DC-15	30	5			
	20	170	153.7	150.9	3.910×10^4
DC-16	30	5			
	20	195	153.9	150.2	4.632×10^4

Table 4.4 EPD settings for suite of samples from the Duluth Complex Mesaba deposit; along with starting and ending sample weights and total energy discharged by the machine. The gap is the distance between the anode and cathode which discharge the electric pulses. All samples had the additional settings of their voltage being set at 200 kV and frequency set to 5 Hz, meaning there were 5 pulses discharged every second.

To determine the efficacy of EPD technology at liberating ore from its surrounding gangue a grain mount was made from the disaggregated and sieved material for each sample. The resulting ten grain mounts were then scanned using EDS in an SEM equipped with an MLA software package (see Table 5.2). Before results are discussed, it is important to explain the decisions that went into creating the grain mounts that were scanned. After each sample was processed using the SELFRAG EPD the disaggregated

material was sieved. Each sample was sorted using a sieve set consisting of 10 different sieves (Table 4.1) and after samples were separated, a grain size range needed to be selected for the creation of the grain mounts. To determine which grain size range was the most appropriate to use in the construction of the grain mounts a visual inspection of all ten sieve sets for each of the ten samples was performed using a binocular microscope. A key factor in determining what grain size was appropriate was to determine the grain size range where the majority of ore grains appear to be completely disconnected from any silicate minerals. Along with the appearance of isolated ore grains another important factor in selecting a grain size was to maintain consistency in testing all the samples in the same manner, even though it may not have been the ideal grain size for all samples. Using these criteria, grain sizes of <250 μm and >150 μm were chosen.

4.2.3 Sieve Analysis

After the samples were processed using EPD, the resulting disaggregated material was dried in a sediment oven at 60°C for 2 hours. The disaggregated material of each sample was weighed and then run through a series of sieves. The sieves that were utilized were ASTM sizes 7, 10, 14, 18, 25, 30, 60, 100, 200, 325 (see Table 4.1 for corresponding mesh sizes in microns). All samples were run through the sieves using a shaker table for 5 minutes. The material captured by each sieve was then weighed so that particle size distribution charts could be created.

In addition to the ten samples that were used in this study, there was also 16 more samples that were processed in the EPD to conduct a parametric study. The 16 additional samples were from the same source boulder that was sampled to acquire DC, the sample

representing material from the Duluth Complex. Because of the regional significance of the Duluth Complex, it was decided to perform an addition experiment on this material. A large boulder of this material was obtained and then broken down into 16 smaller samples that weighted roughly 150 g each, these samples were labeled DC-1 thru DC-16. It was then decided that 8 of these samples would be processed in the SELFRAG EPD set at an operating voltage of 120 kV. The first sample, labeled DC-1was subjected to 25 pulses with each subsequent sample being subjected to 20 more pulses than the previous one, ending with DC-8 which was subjected to a total of 200 pulses (Table 4.3). Next, another set of 8 samples were defined as DC-9 through DC-16 were the same testing regime was followed except that the operating voltage was set to 200 kV. The first sample, DC-9, was subjected to 25 pulses and the final sample, DC-16, was subjected to 200 pulses (Table 4.4).

After all the samples were processed the resulting disaggregated sample and testing waters were placed into 3-gallon buckets where they were allowed to settle for multiple days. Once the sample water in the buckets was completely settled the bulk of the water was removed and the samples were again allowed to sit for multiple days until all the water in the buckets had evaporated out. All the disaggregated material for each of these samples was then processed through the same series of sieves as the 10 main samples were.

4.2.4 Scanning Electron Microscopy (SEM)

A JEOL JSM-G490LV scanning electron microscope located at the Research Instrumentation Lab at the University of Minnesota–Duluth was used to analyze grain

mounts that were made from the 150-250 μm size fractions of the EPD samples. Samples were carbon-coated to an approximate thickness of 15 nm using the bulk carbon coater located in the lab. The settings used for all the samples were an accelerating voltage of 15 kV, an aperture setting of 3, a working distance of 10 mm using the backscatter electron detector, and a variable spot size between 60 to 80 nm. The spot size was varied between the different samples to meet other requirements for setting up the MLA and is described in more detail below. The SEM itself was utilized along with the Energy-Dispersive Spectroscopy EDS detector and the corresponding INCA Point & ID software to identify and confirm the presence of mineral species within the samples. A piece of copper tape was used as a standard for all samples.

4.2.5 Mineral Liberation Analysis (MLA)

MLA is a unique analytical method that is an automated mineral identification and measurement tool. The technique uses specialized software that combines backscattered electrons (BSE) image analysis and mineral identification by using an EDS detector (Fandrich et al., 2007). The concept behind the MLA software it that it allows the user to select various BSE grey scale ranges which inform the software what objects are important and need to be scanned using EDS. Using the data collected by this technique it is possible to evaluate how well specific minerals were liberated from the other minerals present. In this study, liberation of ore minerals is defined as any ore particle that has at least 95 % of its surface perimeter free from any material. If they are not fully liberated, the data can be examined to see if the ore minerals are associated with other ore or silicate minerals.

All MLA scans were performed at the Research Instrumentation Lab at the University of Minnesota – Duluth using the SEM and INCA Mineral, an MLA software package. A typical setup had the SEM running at 15 kV, an aperture setting of 3, and a working distance of 10 mm with the BSE detector enabled. The selected spot size for each sample varied between 60 and 80 nm because as part of the MLA setup a microscope optimization was done to ensure that the EDS had a dead time of roughly 30 % and somewhere between 35 and 45 kilo-counts per second (kcps). At least three grey scale ranges are selected; one to represent the epoxy that is present in-between mineral grains, another that captured as much of the silicate minerals as possible, and a third that identifies all ore minerals of interest. The 30 mm grain mounts are divided into a fixed number of rectangular fields of view determined by the magnification level that is set while the scan is occurring. As the scan proceeds, it disregards grey values representative of the epoxy, while at the same time identifying all silicate minerals as generic "silicates" based on the BSE grey scale. Finally, any mineral grains that fell within the grey scale(s) of interest had their x-ray spectra collected. Any mineral grains that fell on the border of the field of view were discarded to ensure that only whole grains are scanned. Once a mineral grain has had its spectra collected the program compares the result to a list of "recipes" that the user has created for the scan. A recipe is a mineral formula that is crafted to be in the form of an acceptable range of abundances for each element present. For example, a common chalcopyrite recipe might instruct the program to look for 25-35 % Fe, 30-40 % Cu, and 30-40 % S. The recipes need to allow for a certain amount of latitude in the abundances for each element as there is a significant amount of variability in nature.

4.2.6 Reflected Light Microscopy

A petrographic analysis of polished thick sections was performed using reflected light microscopy. The petrographic data obtained include sulfide and oxide ore mineralogy, ore textures, and paragenetic information related to when specific ore minerals may have formed in relation to one another. This information is useful for comparing the textures present within the XRCT reconstructions where ore mineral types could not be distinguished for each other.

5. Results

Data were collected for ten samples that represent a wide range of mineral deposit types and varying depositional environments and conditions. This included sample descriptions for both hand samples and polished thick sections, sieve analysis from material disaggregated by the EPD process, 3D reconstructions of samples using XRCT, representative graphical presentation of quantitative XRCT data, and graphical presentation of liberation derived from MLA. Data for additional samples that were processed using EPD alone can be found in Appendices 1 thru 3.

5.1 Sample Description

This section contains both photographs and written descriptions of hand samples and polished thick sections with a focus on textural and mineralogical information. All photomicrographs were collected using reflected light microscopes at the University of Minnesota – Duluth Economic Geology Microscope Lab.

5.1.1 Hand Samples

Most of the samples used for this project were taken from the economic geology collection at UMD. However, a few samples were donated by outside sources. Steven Hauck, retired Director of Economic Geology at UMD's NRRI, donated material from the Mesaba deposit of the Duluth Complex. Bob Mahin, Exploration Manager at Eagle Mine, donated mineralized samples. Professor Latisha Brengman from the Earth and Environmental Sciences department donated a mineralized sample from an MVT deposit.

EG-181

This sample consists of only two observable materials: one ore mineral with a silicate rock matrix. The sample is phaneritic and the color is two toned, the ore mineral is black, and the silicate is tan colored. In addition to the ore mineral being colored black, it left behind a brown streak, has submetallic luster, and is granular in habit, with no observable cleavage. The ore mineral was determined to be chromite and because of that, the silicate rock matrix was concluded to be weathered dunite. Unfortunately, the specific location where this sample was collected is unknown, as the records for the sample have gone missing.

Figure 5.1 Hand sample of EG-181. The black submetallic mineral is chromite, which dominates the sample with weathered dunite filling in the matrix. The chromite exhibits cumulate texture with intercumulate olivine.

Eagle-1

This sample came from Eagle Mine in Marquette Michigan and represents a portion of their tailings that still contains ore mineralization. Based on visual inspection alone this rock appears to be a black very fine-grained, but still phaneritic, ultra-mafic rock that contains three distinct ore minerals. There is a dark brass yellow metallic mineral that leaves behind a greenish-black streak that was determined to be chalcopyrite. One of the other ore minerals is a bronze colored metallic mineral, which leaves a black streak, and is slightly magnetic; it was therefore determined to be pyrrhotite. The final ore mineral observed is a yellowish bronze color with a metallic luster that leaves behind a light brown streak; it was determined to be pentlandite. The mineral composition of the ultra-mafic portion cannot be well defined based solely on a visual inspection because of its very fine grain size making it unclear whether this rock is a gabbro, peridotite, etc. After reviewing literature on this deposit, this rock is identified as a peridotite, this identification was made by petrographic inspections of thin sections (Ding et al., 2010).

Figure 5.2 Hand sample of Eagle-1. The black gangue material is peridotite while the yellowish metallic portion is a mixture of chalcopyrite, pentlandite, and pyrrhotite which are all occurring as a disseminated texture.

DC

This sample is a phaneritic coarse-grained gabbroic rock containing observable plagioclase, pyroxene, and sporadic but medium-grained plates of biotite. Disseminated throughout the silicate material are coarse-grained blebs of two different sulfide ore minerals. The first sulfide is dark brass yellow in color, has a metallic luster, and its steak color is greenish-black. This allowed for the determination of this mineral as chalcopyrite. The second sulfide mineral is a yellowish-bronze color, has a metallic luster, left a light brownish-bronze streak, and was determined to be pentlandite.

Figure 5.3 Hand sample of DC, a gabbroic rock that contains sulfide blebs of both chalcopyrite and pentlandite. The ore minerals here have a clotted texture or a mix of both fine- and coarse-grained disseminated ore.

Bag-1

This sample comes from the Bagdad copper mine located in Bagdad Arizona; this is a porphyry deposit. The sample is a phaneritic medium-grained quartz monzonite that contains disseminated sulfide ore mineralization. The overall bulk of the rock contains observable plagioclase, orthoclase, quartz, hornblende, and minor biotite. The only observed ore mineral was dark brass yellow in color, left a greenish-black streak, with a metallic luster. It was determined that this was chalcopyrite and throughout the sample it is finely disseminated and is very fine-grained. The chalcopyrite also occurs with pyrite, which is more abundant, while not an ore mineral it was distinguished from chalcopyrite by its paler color and cubic crystal habit.

Figure 5.4 Hand sample of Bag-1, a quartz monzonite that contains very fine-grained disseminated chalcopyrite.

V-1

This sample comes from a porphyry deposit and represents a highly altered zone; unfortunately, there is no further information as to the provenance. This sample is mainly gangue material consisting mostly of sericite, the product of altered feldspars, quartz, and some minor chlorite. The only ore mineral is a dark yellow color, with a metallic luster, that leaves a greenish-black streak; this mineral was identified as chalcopyrite. There is also pyrite present within this sample, and it is distinguished from the chalcopyrite by is cubic crystal habit and a duller brass color, not being nearly as yellow as chalcopyrite occurs. Both the chalcopyrite and pyrite only occur as very fine grains.

Figure 5.5 Hand sample of V-1, a highly altered portion of a porphyry deposit. Show here is highly altered gangue material, mostly sericite, quartz, with minor chlorite. Not pictured because of the small size are both chalcopyrite and pyrite which are sparsely disseminated throughout.

O-219

This sample represents a Cu-Mo porphyry deposit and comes from the Continental/Butte Montana Cu-porphyry deposit. The gangue portion of this sample is a quartz monzonite; being composed of mostly plagioclase and orthoclase with anywhere from 5 to 20% quartz. There is also significant iron staining on the surface of this rock giving it a reddish-brown coloration. While this deposit is known for its copper ores, there were none observed within this hand sample. The only ore mineral present was silvery-grey in color, has a metallic luster, left a bluish-grey streak, has a hardness of less than 2, a basal cleavage, and was thereby identified as molybdenite.

Figure 5.6 Hand sample of O-219, an iron stained quartz monzonite with silver-grey molybdenite smeared on the surface. The texture of the ore in this sample appears as interconnected clots.

SLC-55

This sample came from the Mattabi mine in Ontario, Canada, and is part of a VHMS deposit. It comes from a portion of the deposit that experienced significant quartz flooding. The gangue of this sample is principally composed of quartz, followed by chlorite and chloritoid. The ore present within this sample was fine-grained, dark brass yellow in color with a metallic luster, left a greenish-black streak, and was determined to be chalcopyrite. There was also abundant fine-grained pyrite, which was mainly distinguished from chalcopyrite by its duller brassy-yellow color. The typical cubic crystal habit of pyrite was not observed because this sample came in the form of drill core.

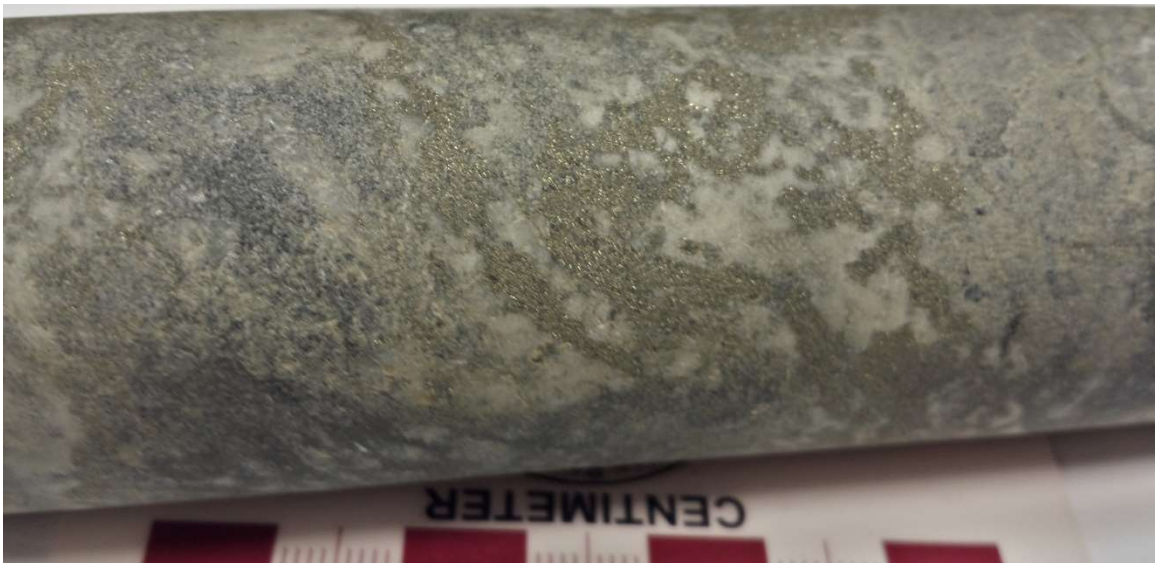

Figure 5.7 Hand sample of SLC-55, a quartz flooded portion of drill core that also contained chlorite and chloritoid in the gangue. The ore mineral present was chalcopyrite that occurred alongside pyrite and occur well disseminated throughout.

SLC-2476

This sample also came from the Mattabi mine in Ontario, Canada, and is part of a VHMS deposit. This specific sample comes from a stringer zone and is highly altered. The gangue in this sample appears to be completely composed of chlorite while the ore present is chalcopyrite. The chalcopyrite was identified by its dark brass yellow color, metallic luster, and the greenish-black streak it made. There was also abundant pyrite present within this sample that was distinguished from chalcopyrite by pyrite's cubic crystal habit and duller yellow color.

Figure 5.8 Hand sample of SLC-2476, chlorite stringer containing fine-grained pyrite and chalcopyrite.

MVT-1

As the sample name suggests, this comes from an MVT deposit. This sample comes from a brecciated zone where large angular clasts of host rock have been broken apart and infilled with alteration and ore minerals. The gangue is composed of two different materials; limestone, which is dark grey and massive, and calcite which is medium to coarse-grained and milky white. Both react vigorously to the application of hydrochloric acid (HCl). There are two ore minerals present in this sample. The first, which is very abundant, is coarse-grained, light yellow (almost honey colored), has an adamantine luster, and leaves a very pale-yellow streak. This mineral was identified to be sphalerite. The second ore mineral, which only occurs very rarely and is very fine-grained, has a dark brass yellow color, a metallic luster, leaves a greenish-black streak, and was therefore identified as chalcopyrite.

Figure 5.9 Hand sample of MVT-1, a brecciated limestone (dark grey) that has had sphalerite (light yellow), chalcopyrite (not pictured), and calcite (milky white) fill in the void space.

1716

This sample came from the White Pine mine in Ontonagon County in the Upper Peninsula of Michigan. This sample comes from a specific rock unit called the Nonesuch Shale and is therefore principally composed of shale with chalcocite and native copper occurring throughout. Because of oxidation of the ore its presence is indicated by the greenish-blue and black oxidation colors. The ore all appears to be occurring in a stratiform pattern, being localized within certain layers of the shale.

Figure 5.10 Hand sample of 1716, Nonesuch Shale with chalcocite and native copper, represented by greenish-blue and black oxidation, occurring in a stratiform pattern.

Additional Samples

Hand sample photos for additional samples that were processed using the EPD can be found in Appendix 1

5.1.2 Thick Sections

All photographs displayed in this section were taken using cross-polarized light

EG-181

The only ore mineral present in EG-181 is chromite. Chromite dominates this sample, being far more abundant than the gangue, appearing as granular masses that have been heavily fractured (fig. 5.11). Based on hand sample identification the gangue is - highly weathered olivine grains and occurs as interstitial grains.

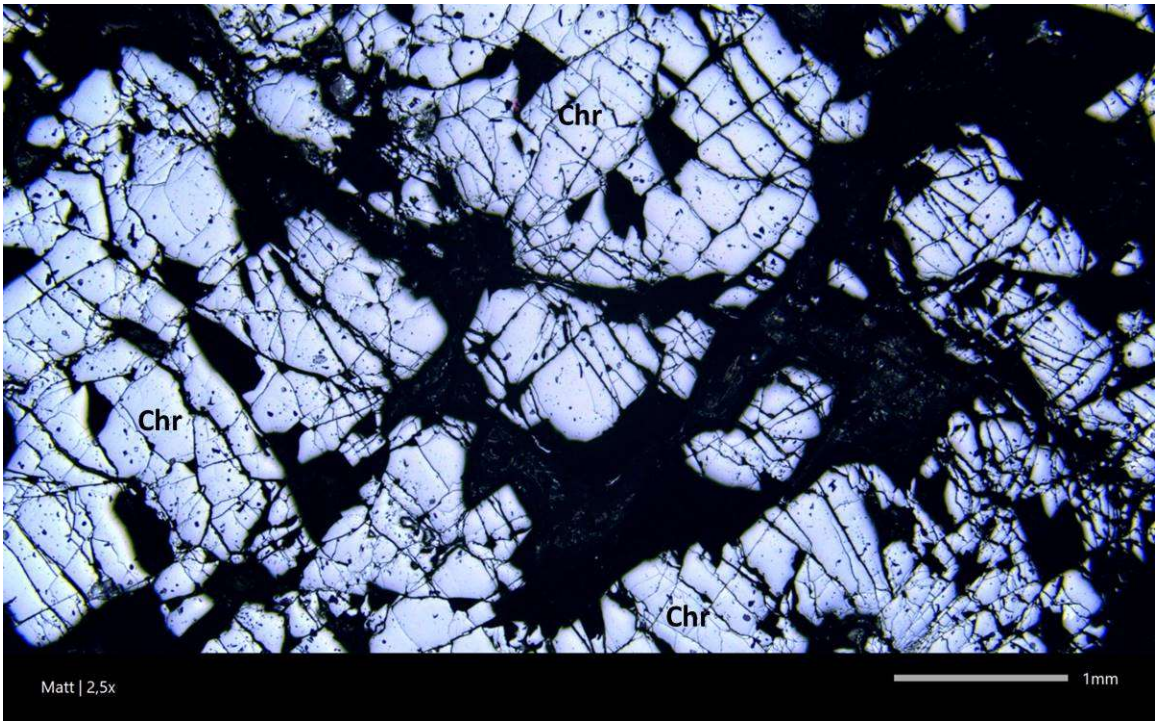

Figure 5.11 EG-181 at 2.5x magnification, chromite (Chr) reflectance is grey with brownish tint, granular habit, and uneven fracture.

Eagle-1

Eagle-1 contains three principle ore minerals; chalcopyrite, pyrrhotite, and pentlandite (not present in fig. 5.12) this sample also includes pyrite and ilmenite (fig. 5.12). The sulfides in this sample show a disseminated texture in some locations. However, the abundance of ore minerals is so great that the sample appears to have more of a net texture, where the ore minerals are surrounding the smaller grained gangue

material. Based on hand sample identification and literature review the gangue was classified as peridotite can be assumed that the gangue is composed of olivine and pyroxenes.

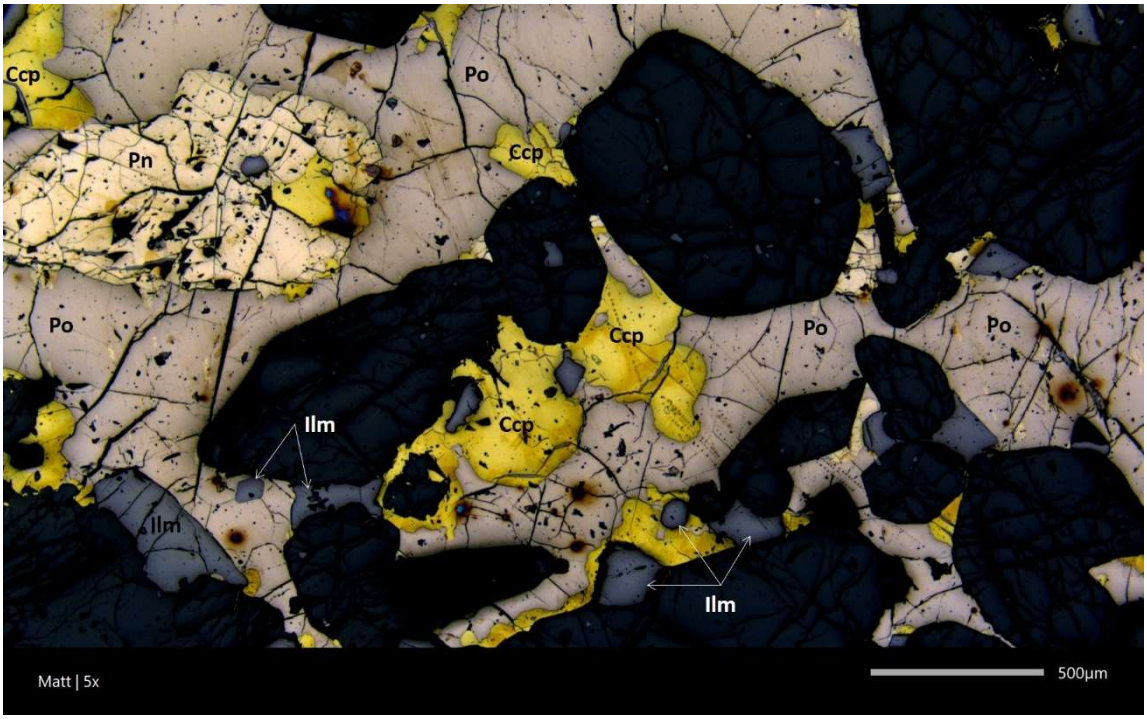

Figure 5.12 Sample Eagle-1at 5x magnification, chalcopyrite (Ccp) reflectance is a dark yellow color, anhedral, no cleavage evident. Pyrrhotite (Po) reflectance is a light brownish color, anhedral, no cleavage evident, uneven fracture. Pyrite (Py) reflectance is cream color, anhedral, no cleavage evident, uneven fracture. Ilmenite (Ilm) reflectance is dark grey, anhedral, no cleavage evident, sub-conchoidal fracture.

DC

The sample from the Duluth Complex contained two principle ore minerals, chalcopyrite and pentlandite (fig. 5.13). The sample also contained ilmenite and pyrite. The overall texture for this sample is disseminated, with the shape of some of the chalcopyrite grains suggesting a secondary replacement texture.

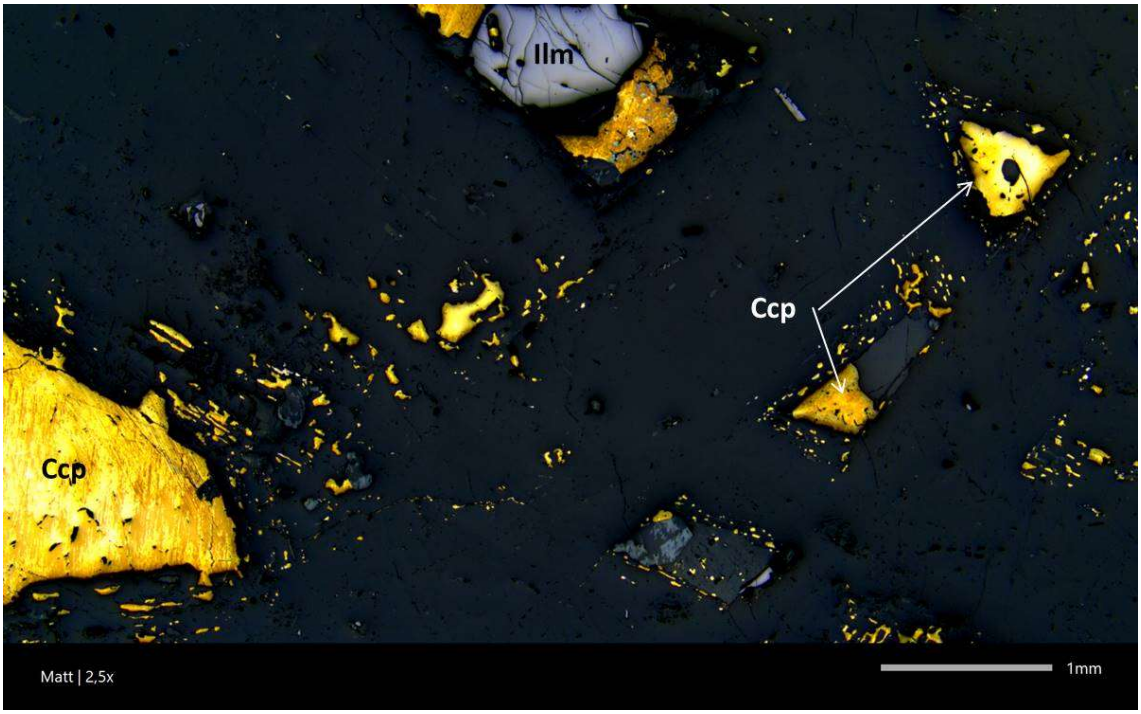

Figure 5.13 Sample DC at 2.5x magnification, chalcopyrite (Ccp) reflectance is a dark yellow color, some are anhedral while some appear euhedral, no cleavage evident. Ilmenite (Ilm) reflectance is grey, anhedral, no cleavage evident, sub-conchoidal fracture. Shape for some chalcopyrite grains suggests possible replacement texture. Other chalcopyrite grains are elongated blebs that surround a larger grain (not necessarily chalcopyrite).

Bag-1

Sample Bag-1 contains a single ore mineral, chalcopyrite as well as non-economic sulfide minerals such as pyrite, and ilmenite, with chalcopyrite being very finely disseminated. Chalcopyrite and pyrite commonly occur together with chalcopyrite frequently being interstitial within the pyrite, but both minerals also occur as separates (fig. 5.14). Gangue is composed of quartz and feldspar.

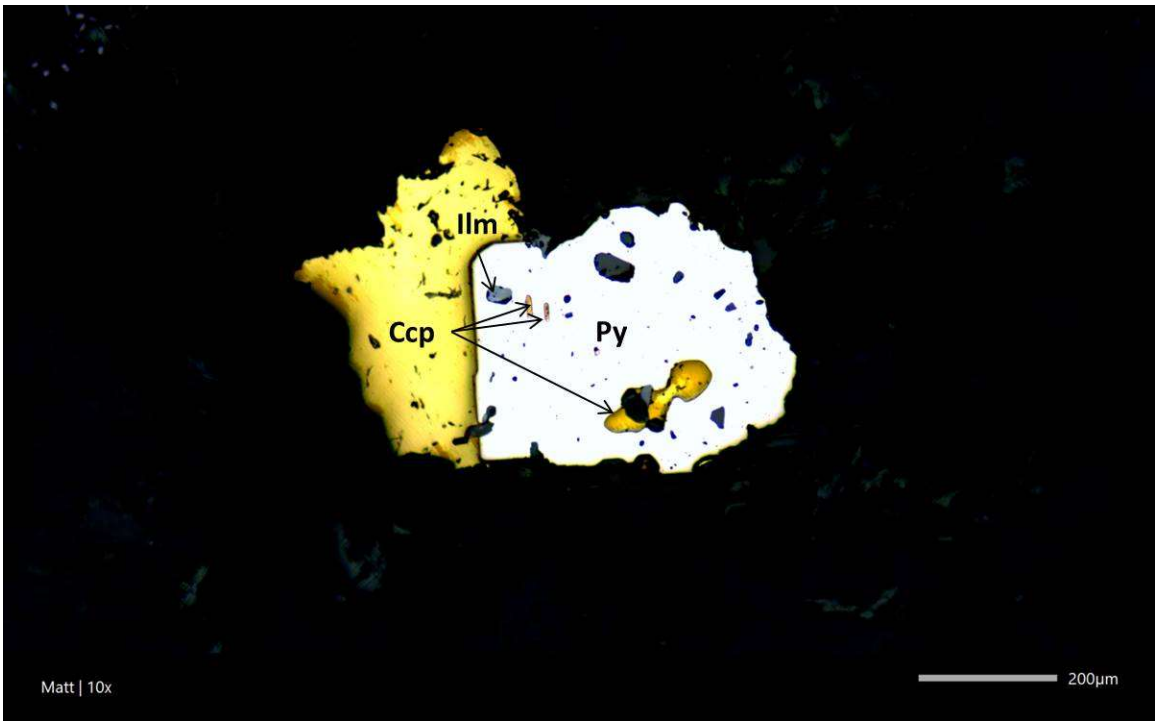

Figure 5.14 Sample Bag-1 at 10x magnification, pyrite (Py) reflectance is white color, anhedral, no cleavage evident. Chalcopyrite (Ccp) reflectance is a dark yellow color, anhedral, no cleavage evident, sometimes occurs as blebs within pyrite. Ilmenite (Ilm) reflectance is grey, anhedral, no cleavage evident, occurs interstitial within pyrite.

V-1

Sample V-1 contains only chalcopyrite based on hand sample identification. However, no chalcopyrite was observed in thick section. The only metallic mineral observed is pyrite, which occurs as very finely disseminated with crystal habits both granular and cubic (fig. 5.15). The gangue material within this sample was identified by inspection of hand sample to be sericite, quartz, and chlorite.

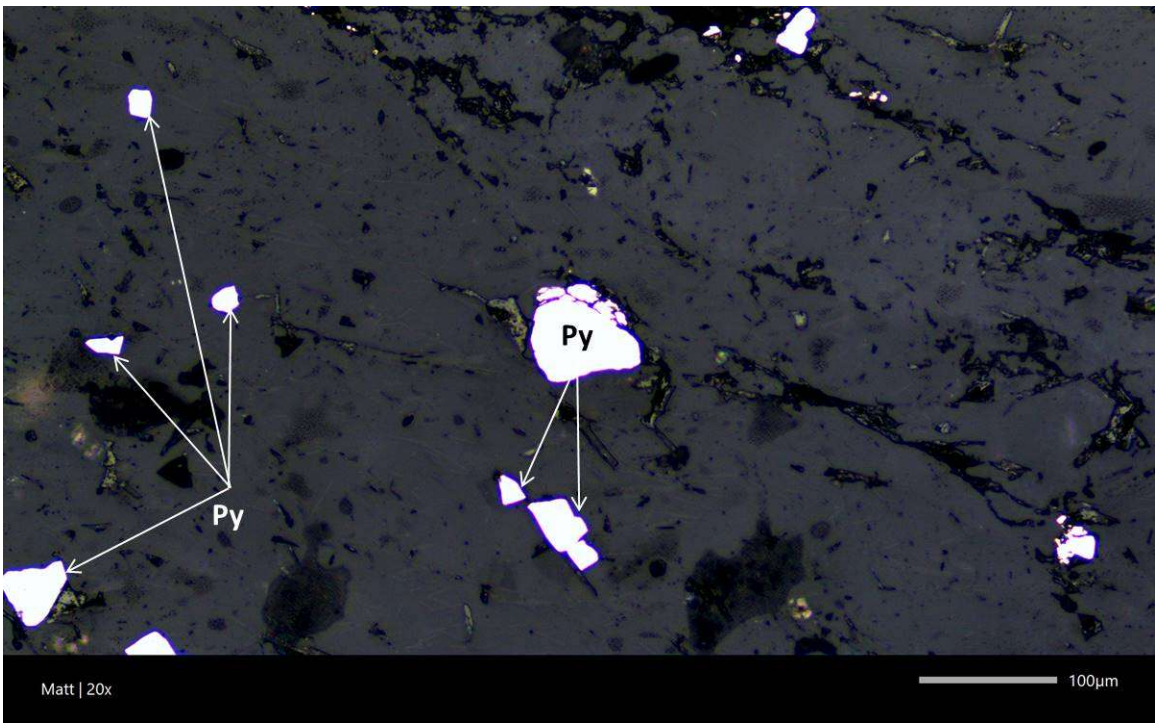

Figure 5.15 Sample V-1 at 20x magnification, pyrite (Py) reflectance is white color, anhedral to euhedral, no cleavage evident, granular habit.

O-219

Sample O-219 came from a Cu-Mo porphyry deposit, but there were no observable Cu-ore minerals within the thick section. The only ore mineral observed under reflective light was molybdenite as anhedral blobs (fig. 5.16). The hand sample indicated far more abundant molybdenite than the thick section yielded. Gangue was identified by inspection of the hand sample and determined to consist of mostly feldspar with some quartz.

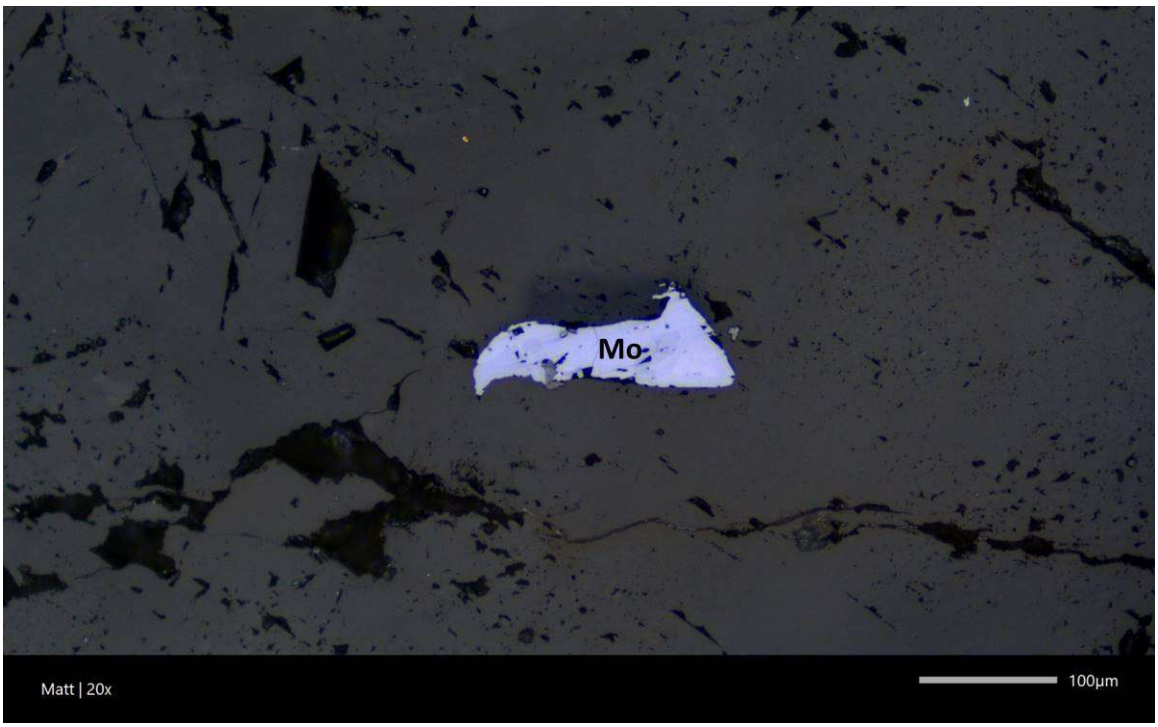

Figure 5.16 Sample O-219 at 20x magnification, molybdenite (Mo) reflectance is a medium to blueish-grey color, anhedral, strong bireflectance.

SLC-55

The only ore mineral within SLC-55 that was observable in the thick section is sphalerite. The sphalerite found is very fine-grained and largely anhedral, typically occurring as interstitial aggregates within much larger masses of pyrite (fig. 5.17). However, based on the hand sample identification, chalcopyrite is also an ore mineral present within this sample but unrepresented within the thick section. The hand sample was utilized for the identification of gangue minerals, which were determined to be quartz, chlorite, and chloritoid.

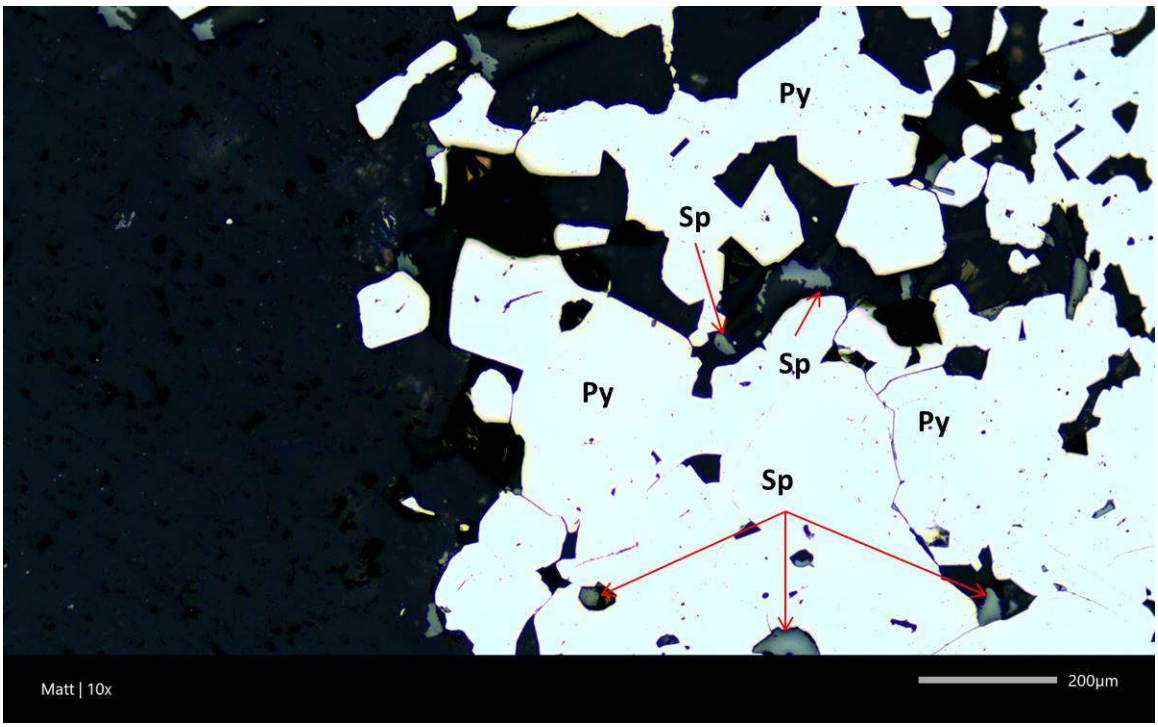

Figure 5.17 Sample SLC-55 at 10x magnification, pyrite (Py) reflectance is white color, sub-euhedral to euhedral, no cleavage evident, massive to granular habit. Sphalerite (Sp) reflectance is medium grey color, anhedral, sometimes occurring interstitial within pyrite.

SLC-2476

Like SLC-55 there was only one ore mineral present within the thick section for SLC-2476, which is chalcopyrite. The chalcopyrite occurs as fine to medium-grained sand sized particles that are disseminated throughout the sample and are typically anhedral in shape (fig. 5.18). Pyrite can also be found near where chalcopyrite is found; it is very fine to fine-grained sand sized particles and is also anhedral in shape. Identification of the gangue material was accomplished by hand sample inspection where it was determined that, within this highly altered sample, the gangue consisted of chlorite.

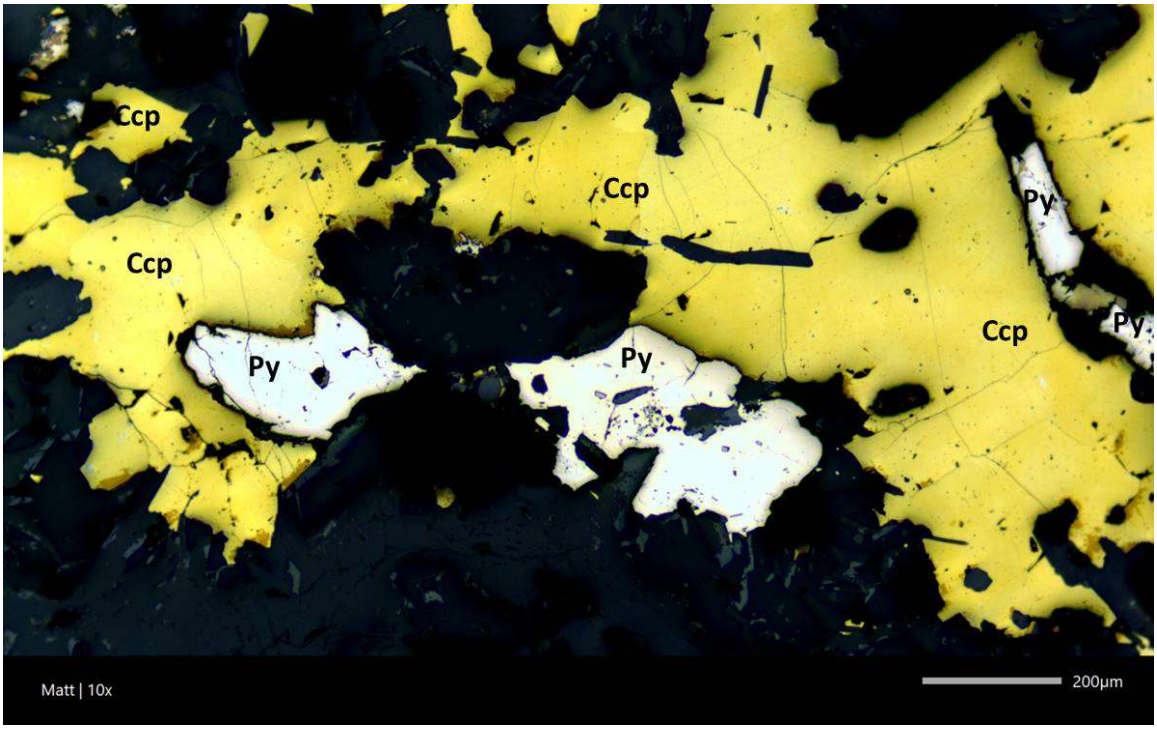

Figure 5.18 Sample SLC-2476 at 10x magnification, chalcopyrite (Ccp) reflectance is a dark yellow color, anhedral, no cleavage evident. Pyrite (Py) reflectance is white color, anhedral, no cleavage evident.

MVT-1

This sample contains sphalerite and chalcopyrite, with the sphalerite being much more abundant than the chalcopyrite. Sphalerite fills very wide veins or brecciated zones and is very coarse sand to very fine pebble sized crystals. The chalcopyrite typically occurs at the edges of sphalerite aggregates and its abundance is sparse compared to sphalerite (fig. 5.19). Chalcopyrite occurs as very fine sand sized crystals or smaller and is anhedral in shape. Pyrite also occurs throughout this sample; like chalcopyrite, pyrite occurs frequently on the fringes of sphalerite but also as inclusions within sphalerite crystals. Pyrite shows very fine sand sized crystals at their largest and are anhedral in shape. Gangue material was identified as calcite based on thick section and hand sample identification.

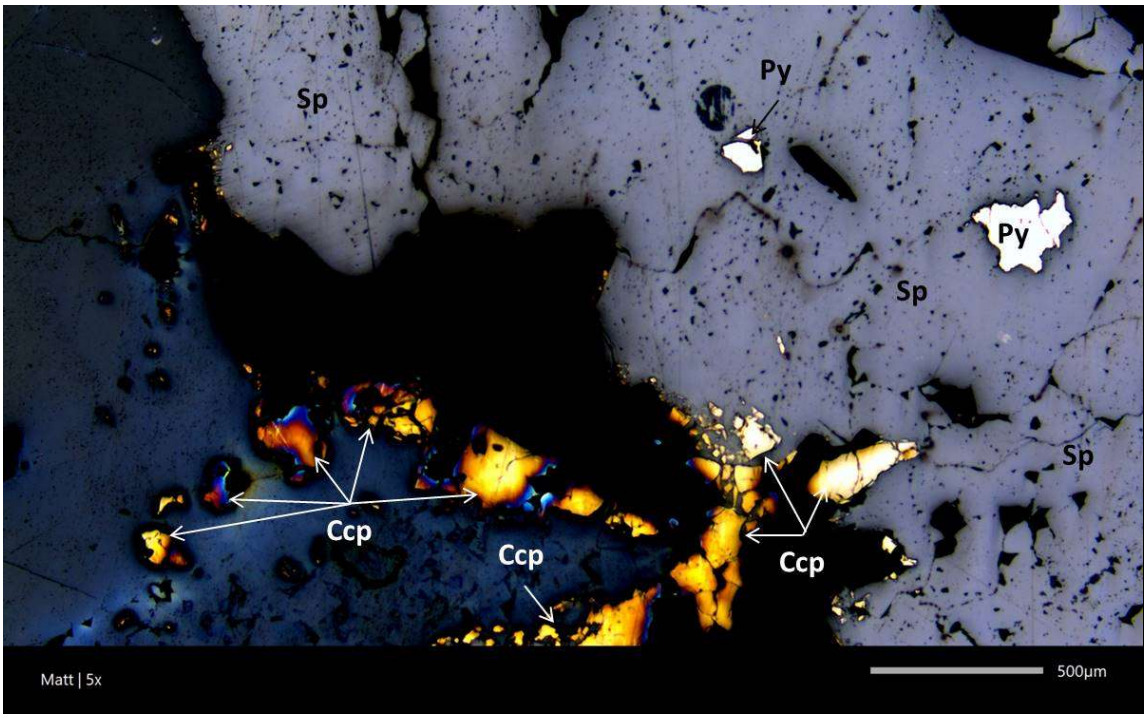

Figure 5.19 Sample MVT-1 at 5x magnification, sphalerite (Sp) reflectance is medium grey color, anhedral, massive in habit. Chalcopyrite (Ccp) reflectance is a dark yellow color, anhedral, no cleavage evident. Pyrite (Py) reflectance is white color, anhedral, no cleavage evident, sometimes occurring interstitial within sphalerite.

1716

This sample contains native copper. The Cu-ore makes up silt to very fine sand sized anhedral particles (fig. 5.20). The ore is highly disseminated with some stratiform characteristics making their occurrence within certain layers of the gangue much more abundant than others. The gangue material was identified as shale, based on the hand sample identification.

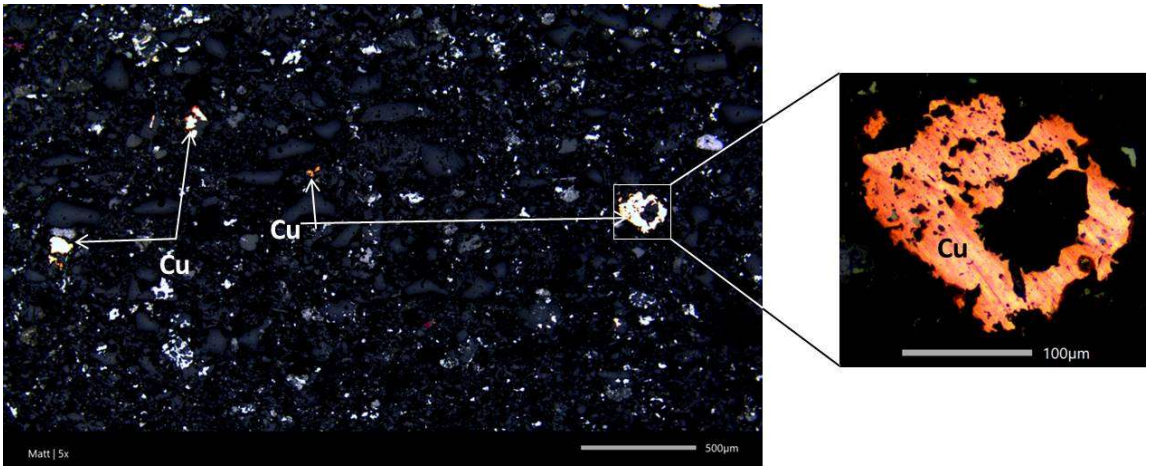

Figure 5.20 Sample 1716 at 5 and 20x (inset) magnification, native copper (Cu) reflectance is distinct copper color to pinkish brown, anhedral, occurring in a stratiform texture on the macro-scale.

5.1.3 Grain Stacks

Figure 5.21 shows the constructed grain stacks that were scanned by XRCT. EPD processing of sample material yielded disaggregated individual mineral grains of various sizes undisturbed by mechanical forces such as grinding or crushing. Inspection of this material using XRCT was expected to produce very high-resolution images of a range of individual ore grains to evaluate if their size and morphology was being preserved or destroyed by the EPD process.

Figure 5.21 Photograph of the three grain stacks that were constructed.

Upon inspection of the imagery, it quickly became clear that the data would be unusable. What were expected to be clear boundaries between different layers of tape, defined by the tape thickness of 2.5 mm, were in fact undulating and complex because of the unexpected gel-like nature of the double-sided tape. Therefore, when attempting to inspect 3D grain reconstructions in Avizo software, it was no longer clear which layer (and by extension which sample) was being viewed.

5.2 Sieve Analyses

Shown below are results of the sieve analyses performed on the disaggregated material resulting from EPD processing. These analyses were performed to characterize material allowing it to be compared with conventional crushing. The sieve sizes used for these analyses can be found in Table 4.1.

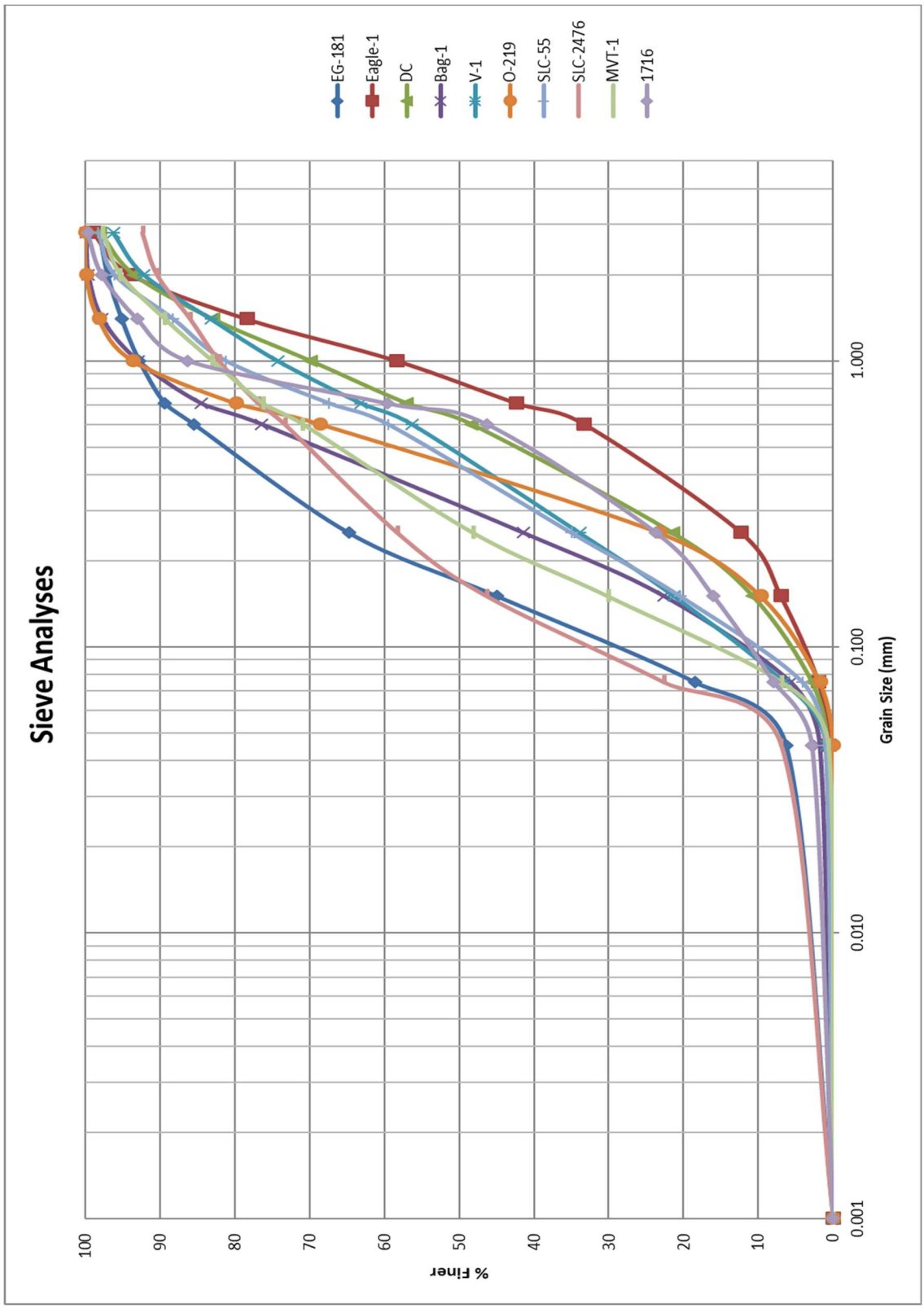

Figure 5.22 Sieve analyses for EG-181, Eagle-1, DC, Bag-1, V-1, O-219, SLC-55, SLC-2476, MVT-1, and 1716

DC-1 thru DC-8

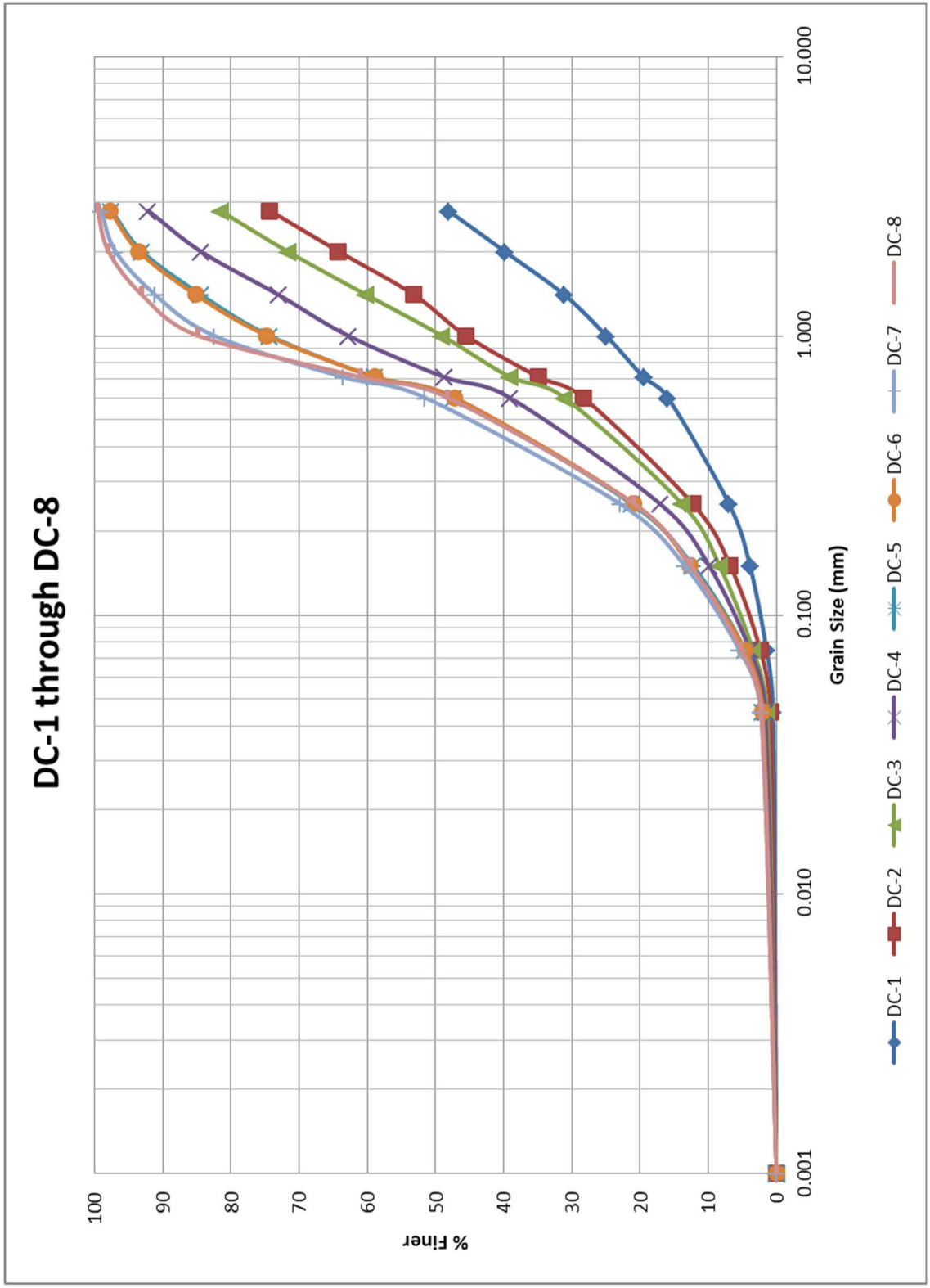

Figure 5.23 Sieve analyses of samples DC-1 through DC-8, processed at 120 kV starting at 25 pulses with DC-1 and increasing by increments of 25 pulses with each subsequent sample.

DC-9 thru DC-16

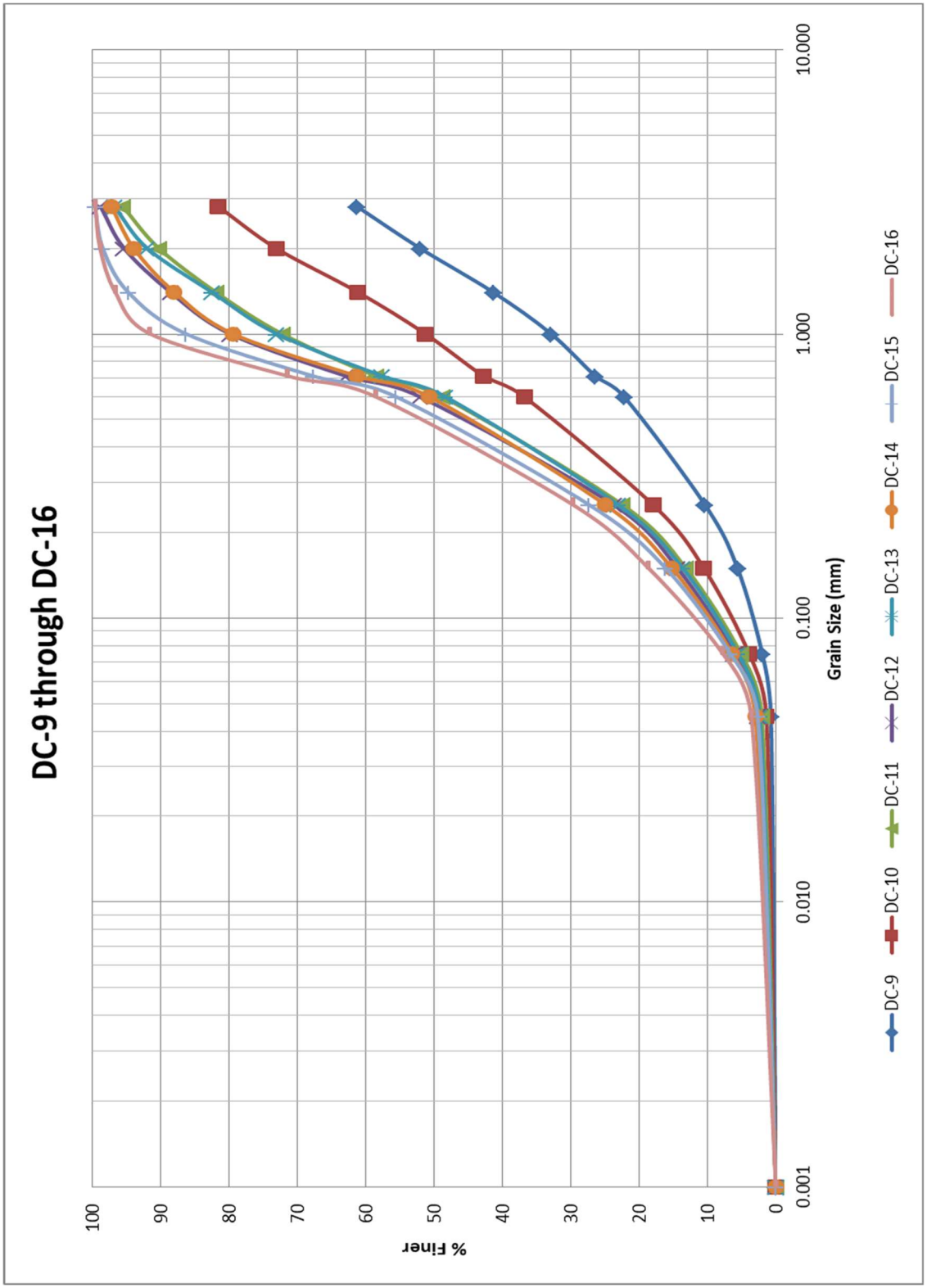

Figure 5.24 Sieve analyses of samples DC-9 through DC-16, processed at 200 kV starting at 25 pulses with DC-9 and increasing by increments of 25 pulses with each subsequent sample.

Direct Comparison of the Two Sample Suites

These figures were constructed to illustrate the effect of increasing the voltage of the EPD with respect to how fine the resulting material is at set intervals of pulses laid out in Tables 4.3 and 4.4.

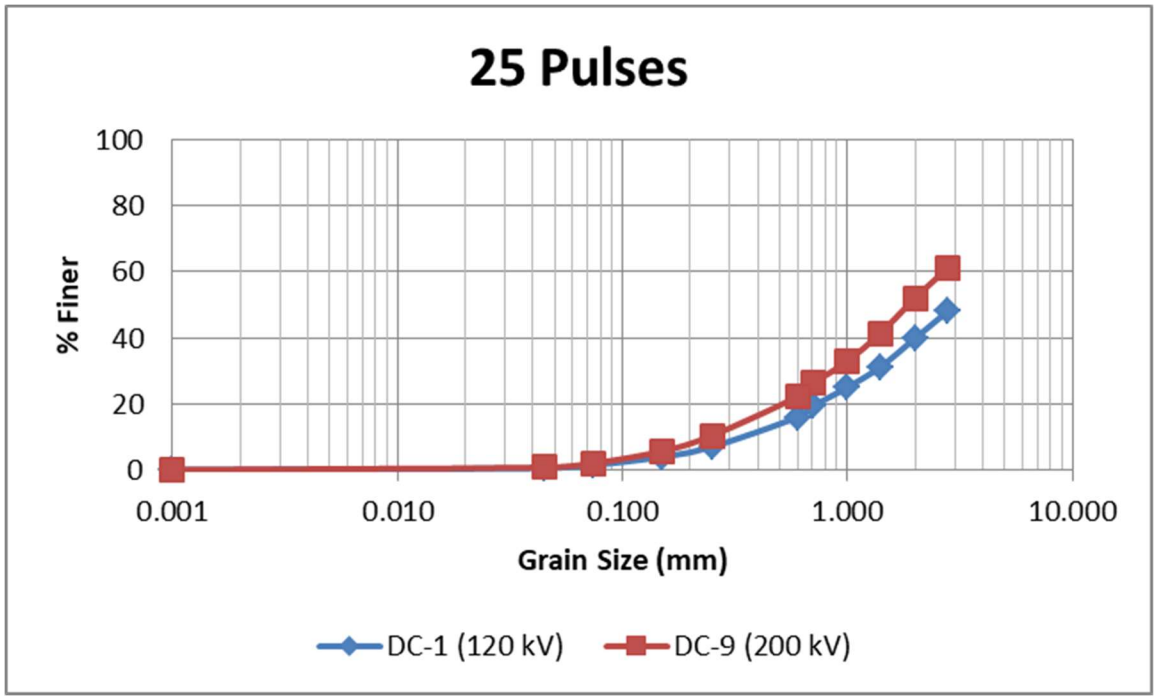

Figure 5.25 Comparison of DC-1 to DC-9, both subjected to 25 pulses at 120 and 200 kV, respectively.

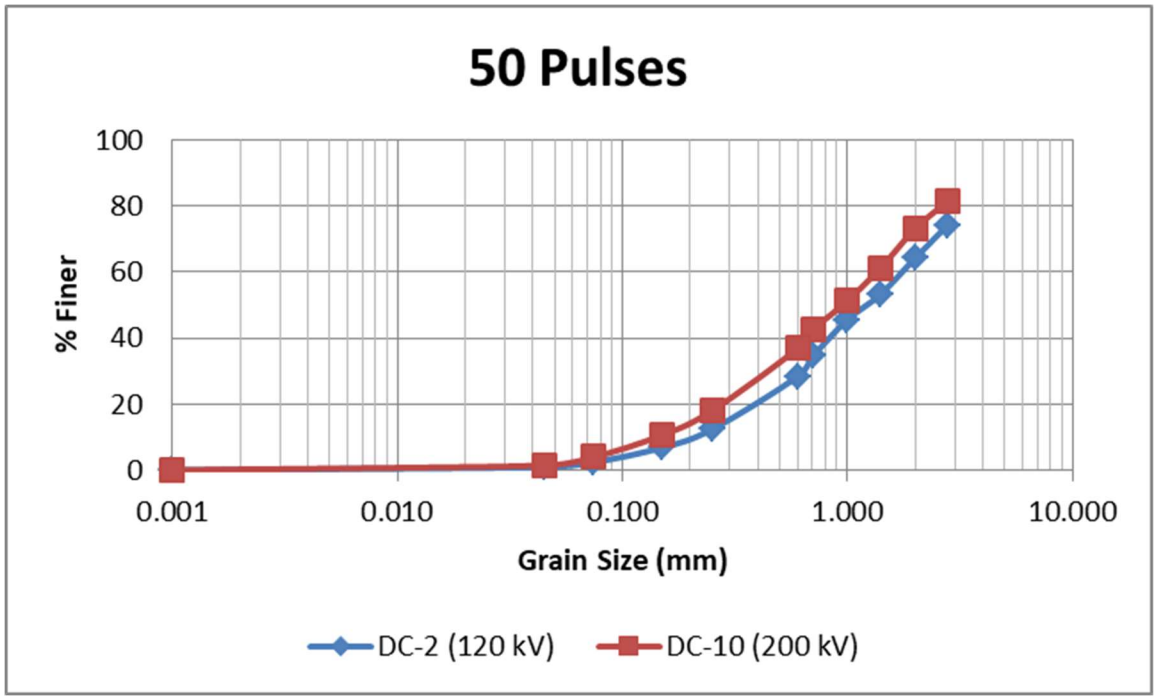

Figure 5.26 Comparison of DC-2 to DC-10, both subjected to 50 pulses at 120 and 200 kV, respectively.

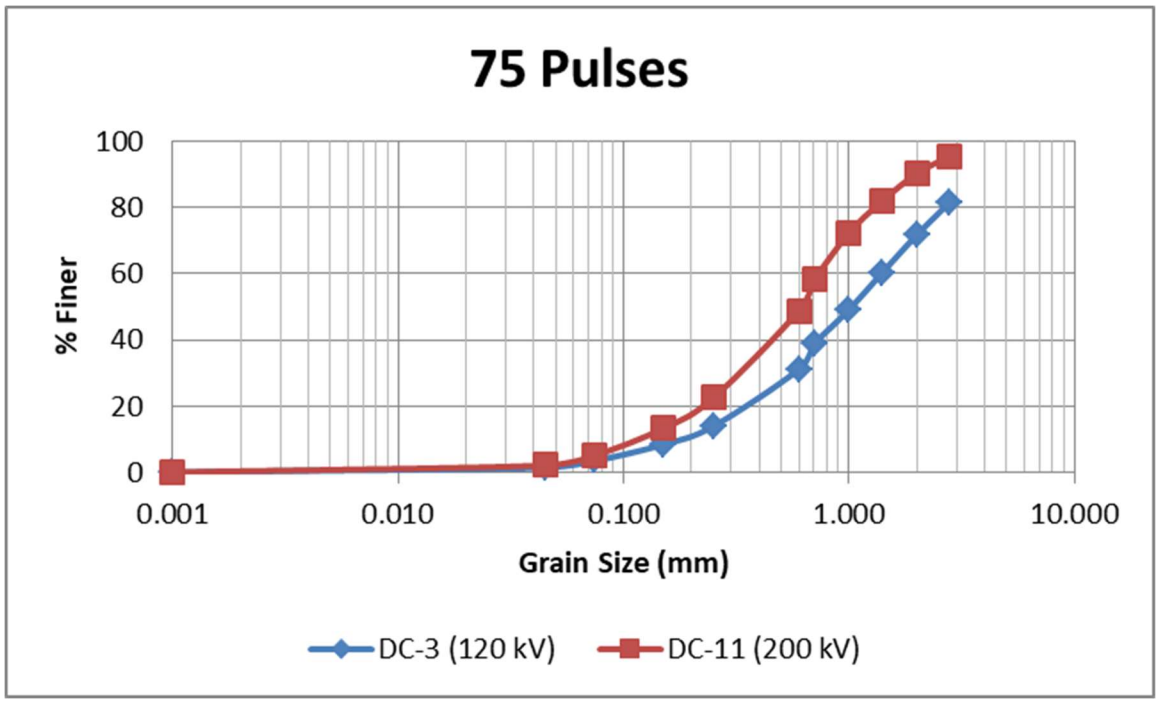

Figure 5.27 Comparison of DC-3 to DC-11, both subjected to 75 pulses at 120 and 200 kV, respectively.

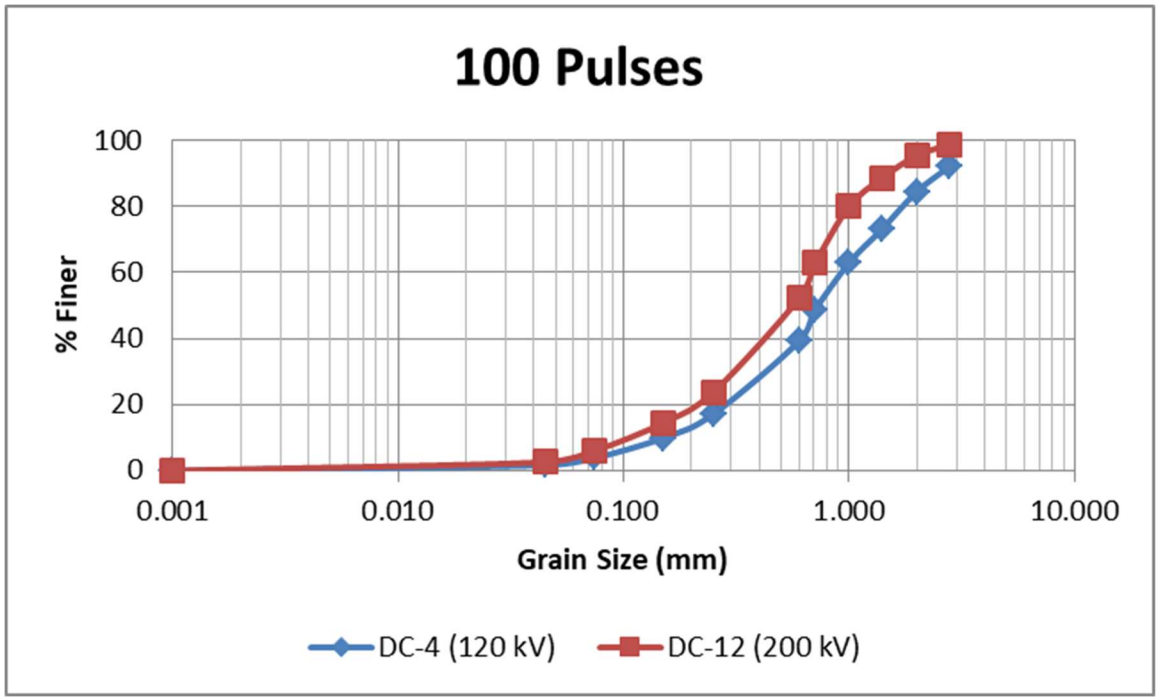

Figure 5.28 Comparison of DC-4 to DC-12, both subjected to 100 pulses at 120 and 200 kV, respectively.

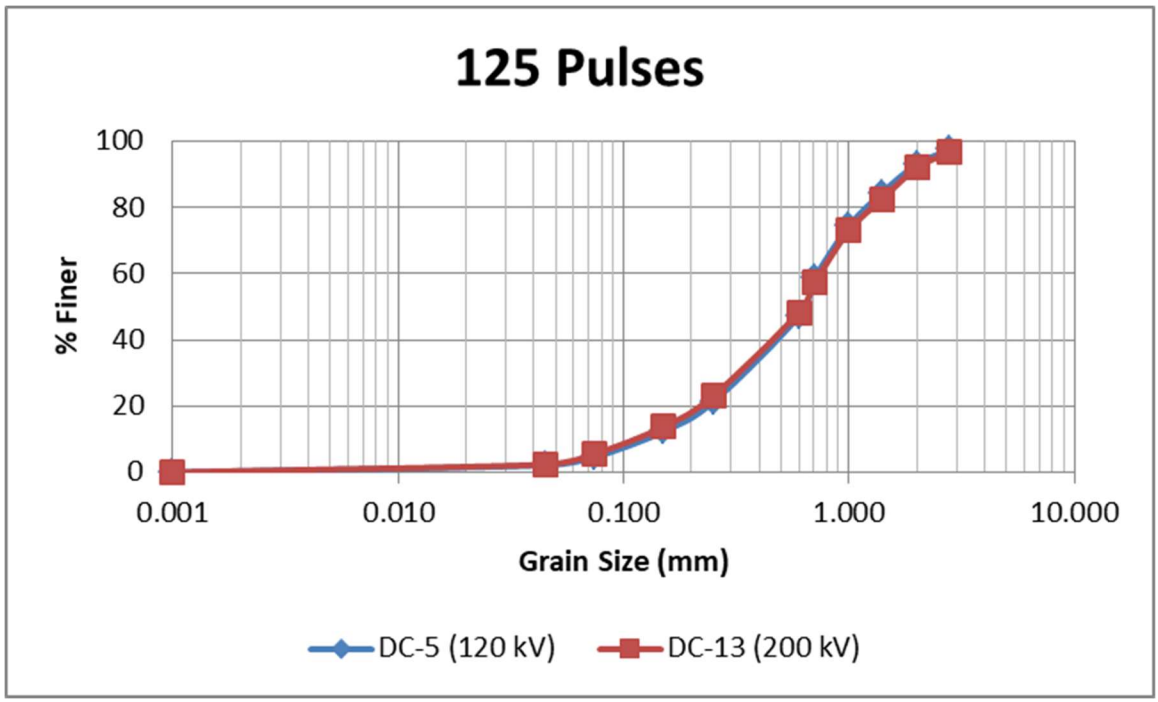

Figure 5.29 Comparison of DC-5 to DC-13, both subjected to 125 pulses at 120 and 200 kV, respectively.

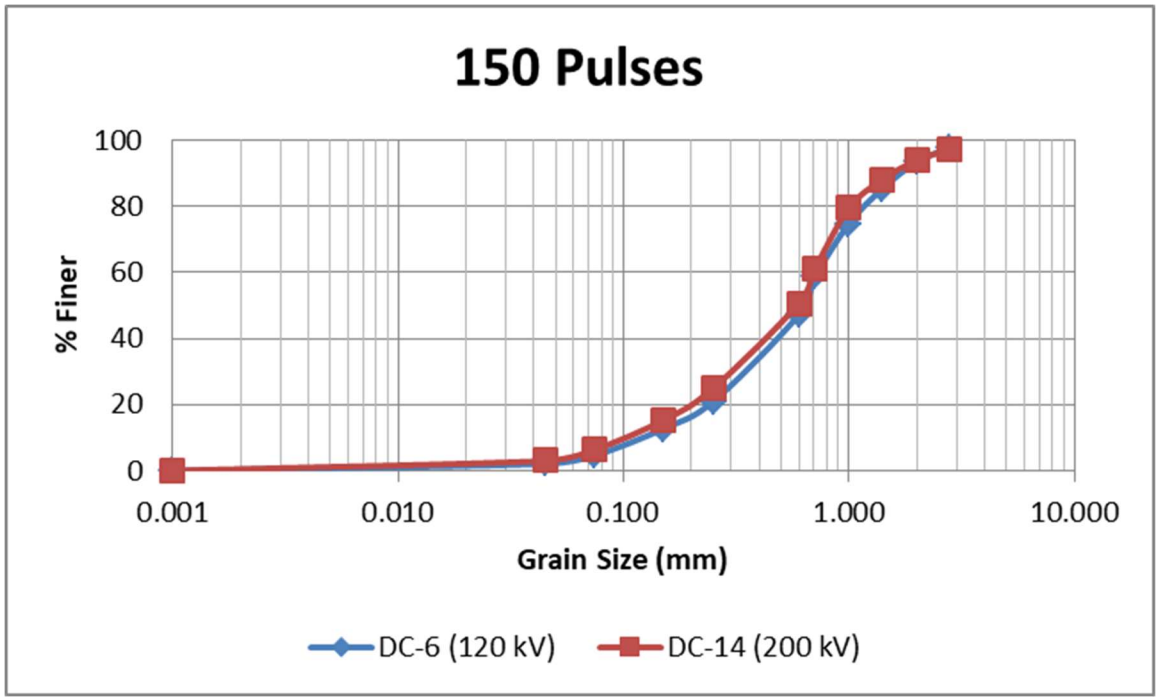

Figure 5.30 Comparison of DC-6 to DC-14, both subjected to 150 pulses at 120 and 200 kV, respectively.

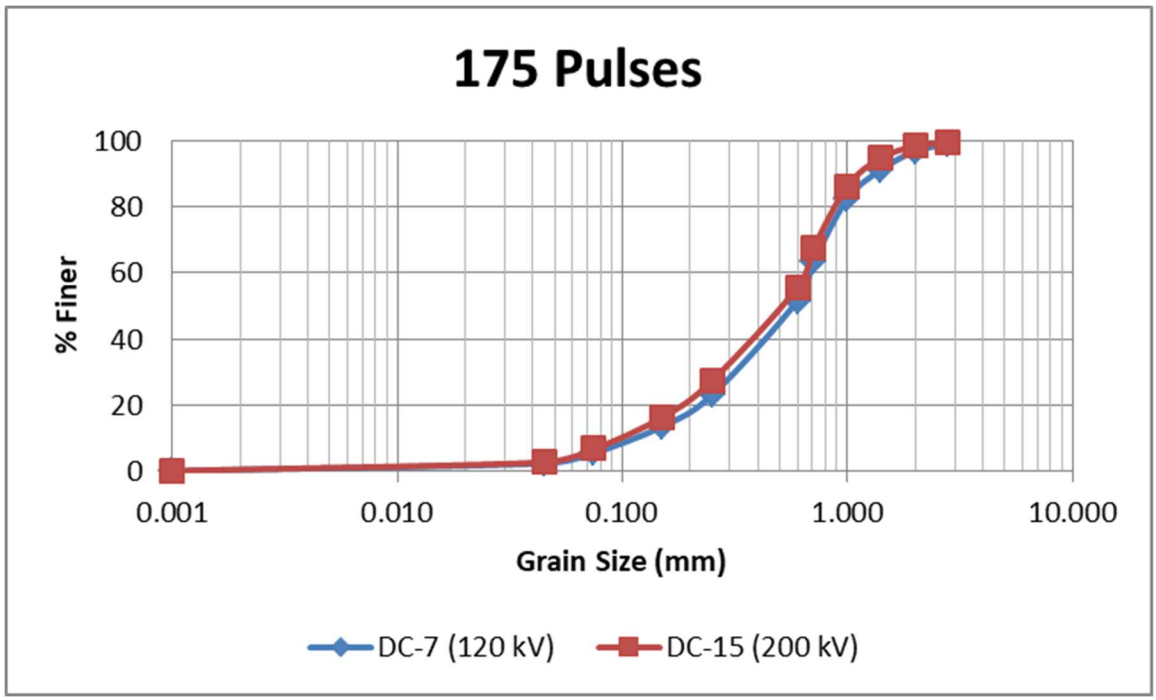

Figure 5.31 Comparison of DC-7 to DC-15, both subjected to 175 pulses at 120 and 200 kV, respectively.

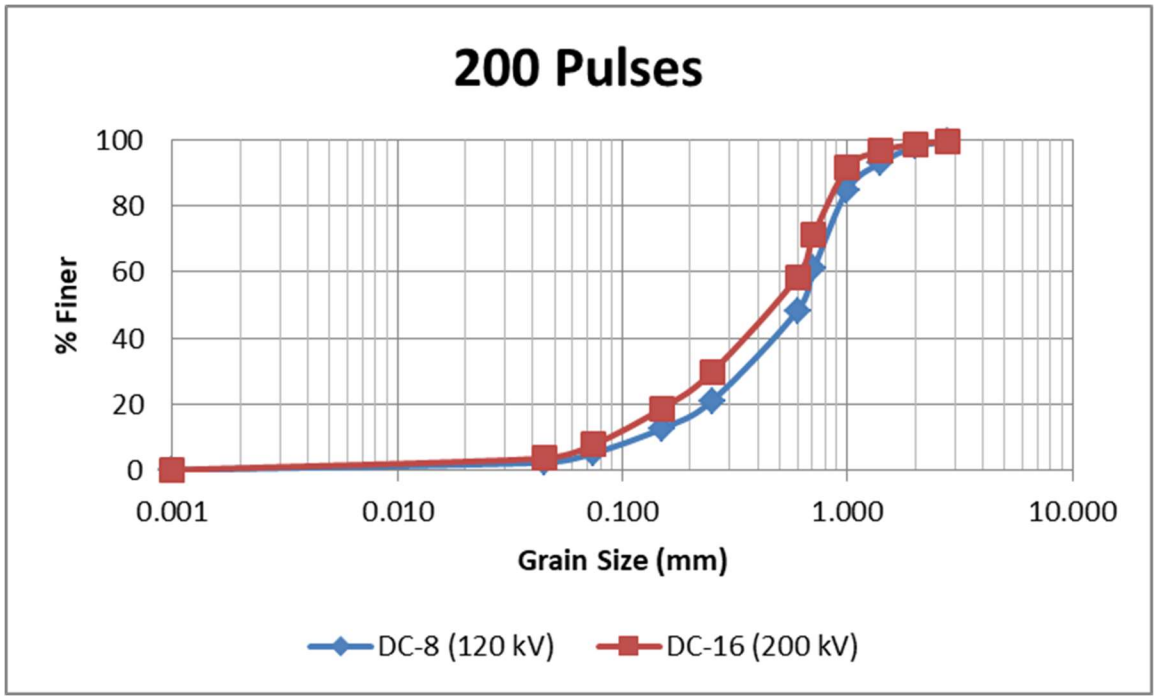

Figure 5.32 Comparison of DC-8 to DC-16, both subjected to 200 pulses at 120 and 200 kV, respectively.

Additional Samples

The sieve analysis results for samples processed through the EPD but not scanned in the XRCT or MLA can be found in Appendix 3.

5.3 X-ray Computed Tomography

Following are the results gathered from scanning each of the samples within an XRCT. The main techniques used to collect results were visual observation of 3D sample reconstructions, grain size distributions, and shape analysis of individual grains.

5.3.1 3D Reconstructions

For each sample, a full sample reconstruction oriented in the (Y, Z) directions is provided along with other images useful for highlighting sample specific features or textures. For each sample, there are additional reconstructions that are oriented in both

the (X, Z) and (X, Y) directions that can be found in Appendix 4, subsection 3. The explanation for how these figures were created can be found in 4.2.1.

EG-181

This sample only has a single 3D reconstruction presented because there was little ore material present to visualize. The ore present within EG-181 is easily described as semi-massive from the reconstruction (fig. 5.33). It almost entirely consists of ore mineralization with only a small amount of gangue present, as represented by the void space. Since all the ore material appears to be interconnected it is impossible to make a comment on grain size or shape based on visualization alone.

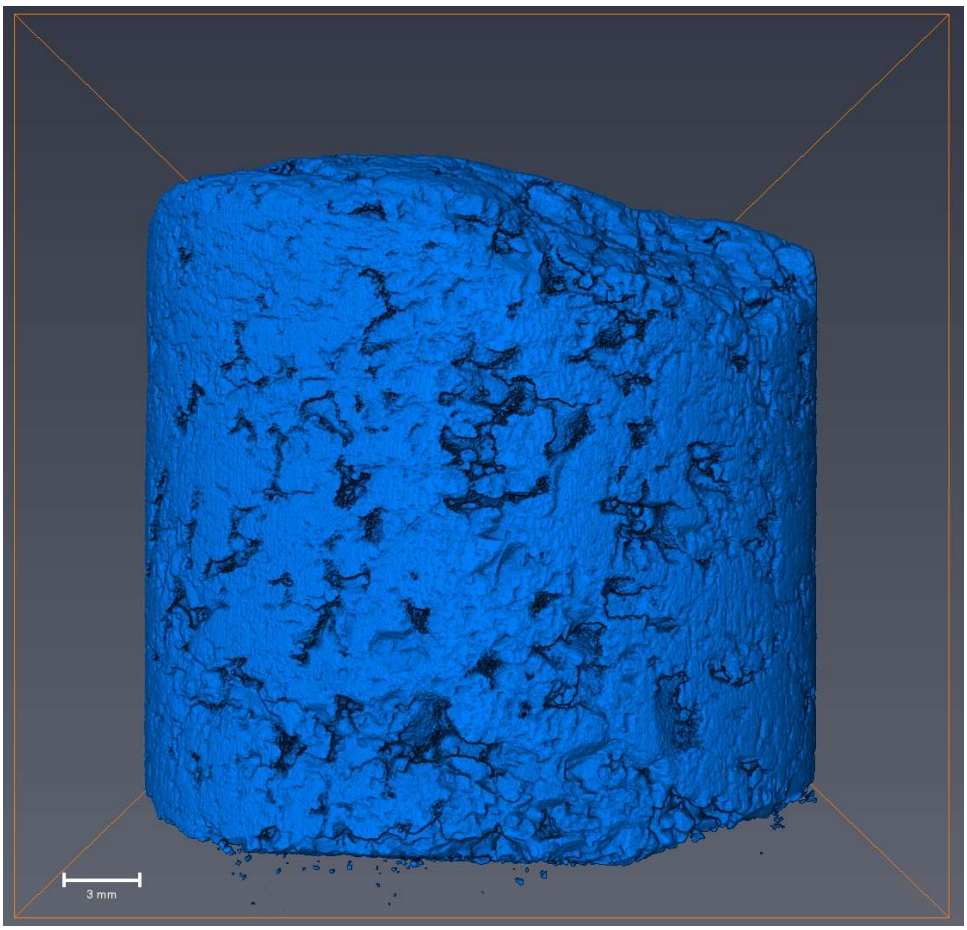

Figure 5.33 A full sample 3D reconstruction of EG-181 with an (Y, Z) display orientation.

Eagle-1

Because of the complex nature of how much ore mineralization is present, along with how it is associated with gangue material, represented by void space; the sample reconstructions for Eagle-1 was cut in half. The stack for Eagle-1 was composed of 2363 images used for 3D reconstructions. Processing the entire stack would have exceeded the available modeling computer's CPU. To avoid this, the stack was divided into two datasets; one that utilized slices 0 through 1182 and a second one that utilized slices 1183 through 2362. The reconstruction presented here is that of slices 0 through 1182 presented in the (Y, Z) direction (fig. 5.34). Results of images of slices 0 through 1182 in the (X, Z) and (X, Y) directions and reconstructions of slices 1183 through 2362 in the (Y, Z), (X, Z), and (X, Y) directions can be found in Appendix 4, subsection 3. While figure 5.34 only represents half of the sample it is obvious that the Eagle-1 sample presents a semi-massive ore (chalcopyrite, pyrrhotite, and pentlandite) with a distinctive net texture. Based on visual observation, the grain sizes are mostly sub-2 mm, but because of the interconnectivity of grains no shape characterization is possible.

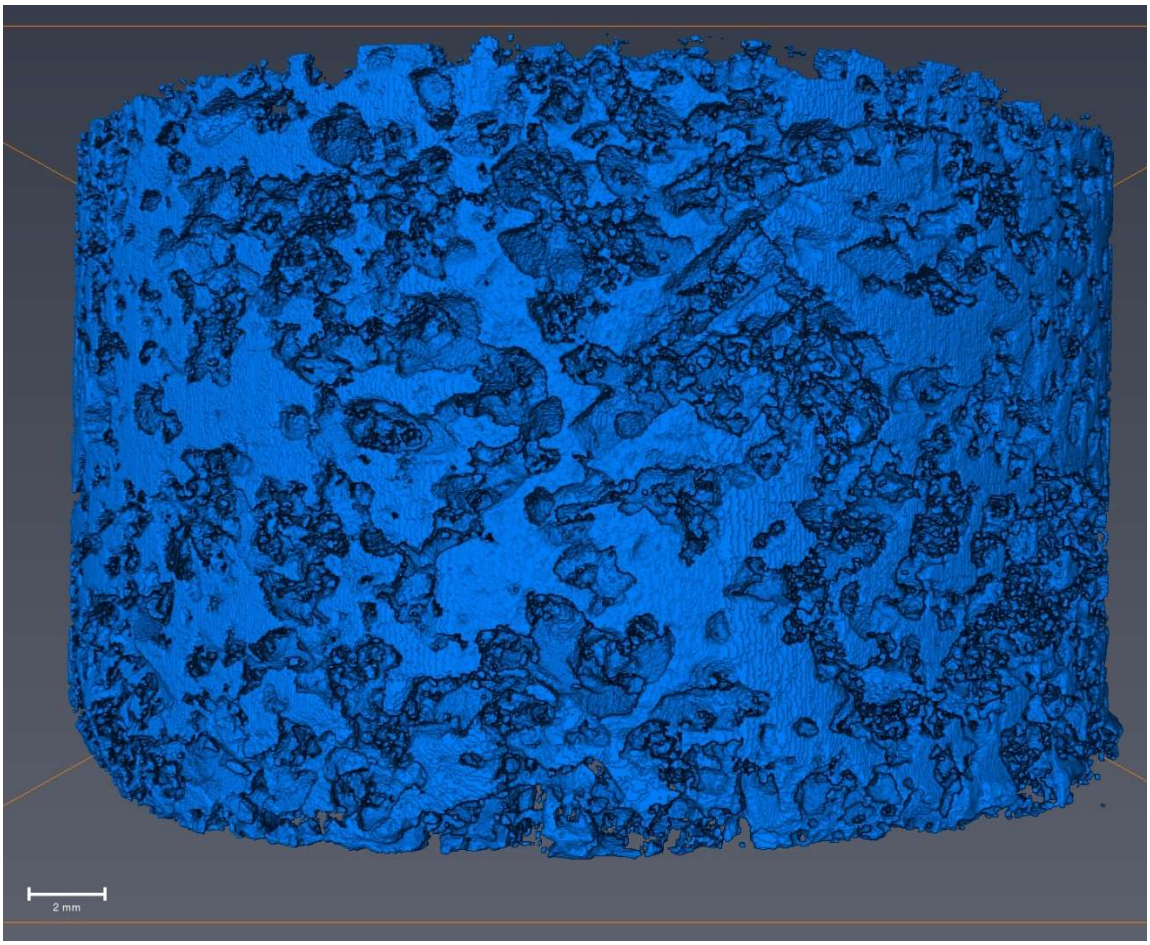

Figure 5.34 A half sample 3D reconstruction of Eagle-1 with an (Y, Z) display orientation. This reconstruction utilizes slices 0 through 1182 out of a total 2363 slices. The voids in this reconstruction represent silicate minerals.

DC

This sample reconstruction shows that ore mineralization is abundant and occurs in a disseminated texture (fig. 5.35). There appears to be at least two distinct grain size populations. While many of the grains appear spheroid there also is a distinct population of grains that appear elongated. Figure 5.36 also highlights what appears to be a rope-like feature that occurs within the DC sample, roughly 10 mm in length with a diameter of 5 mm.

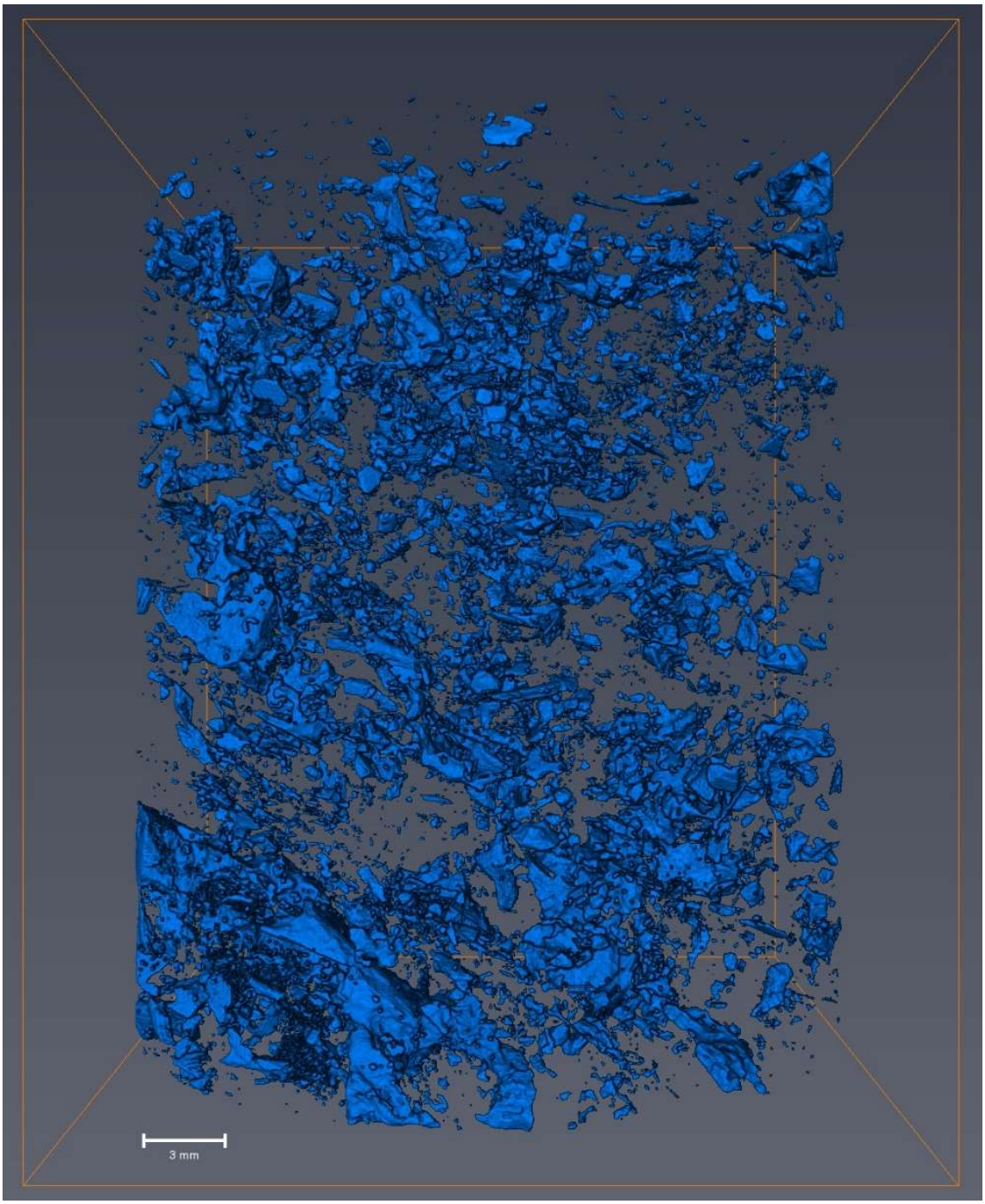

Figure 5.35 A full sample 3D reconstruction of DC with an (Y, Z) display orientation.

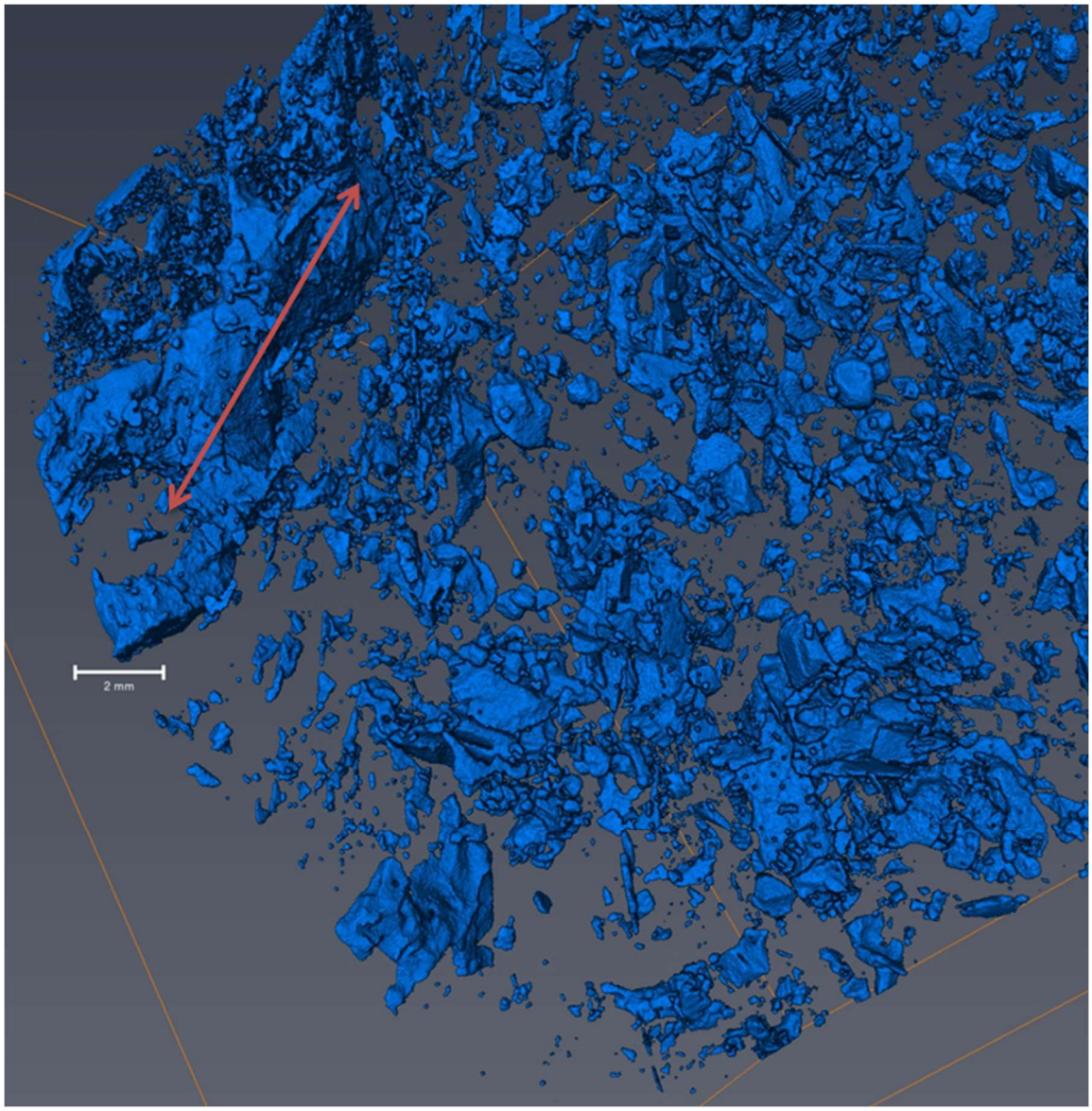

Figure 5.36 A 3D reconstruction of DC magnified and oriented to highlight a rope-like feature present.

Bag-1

The ore within Bag-1 is very finely disseminated with only a small portion of the sample containing ore mineralization (fig. 5.37). The majority of ore grains appear to be in the sub-millimeter size and are mostly spheroid in shape (fig. 5.38) with a few notable exceptions (fig. 5.39). While not always easy to observe there does appear to be a planar feature present. Ore grains, when oriented, appear to be linear in distribution until the

orientation is shifted and it becomes evident that the grains are laid out in a planar sheet-like fashion that has a thickness that is sub-millimeter (fig. 5.40).

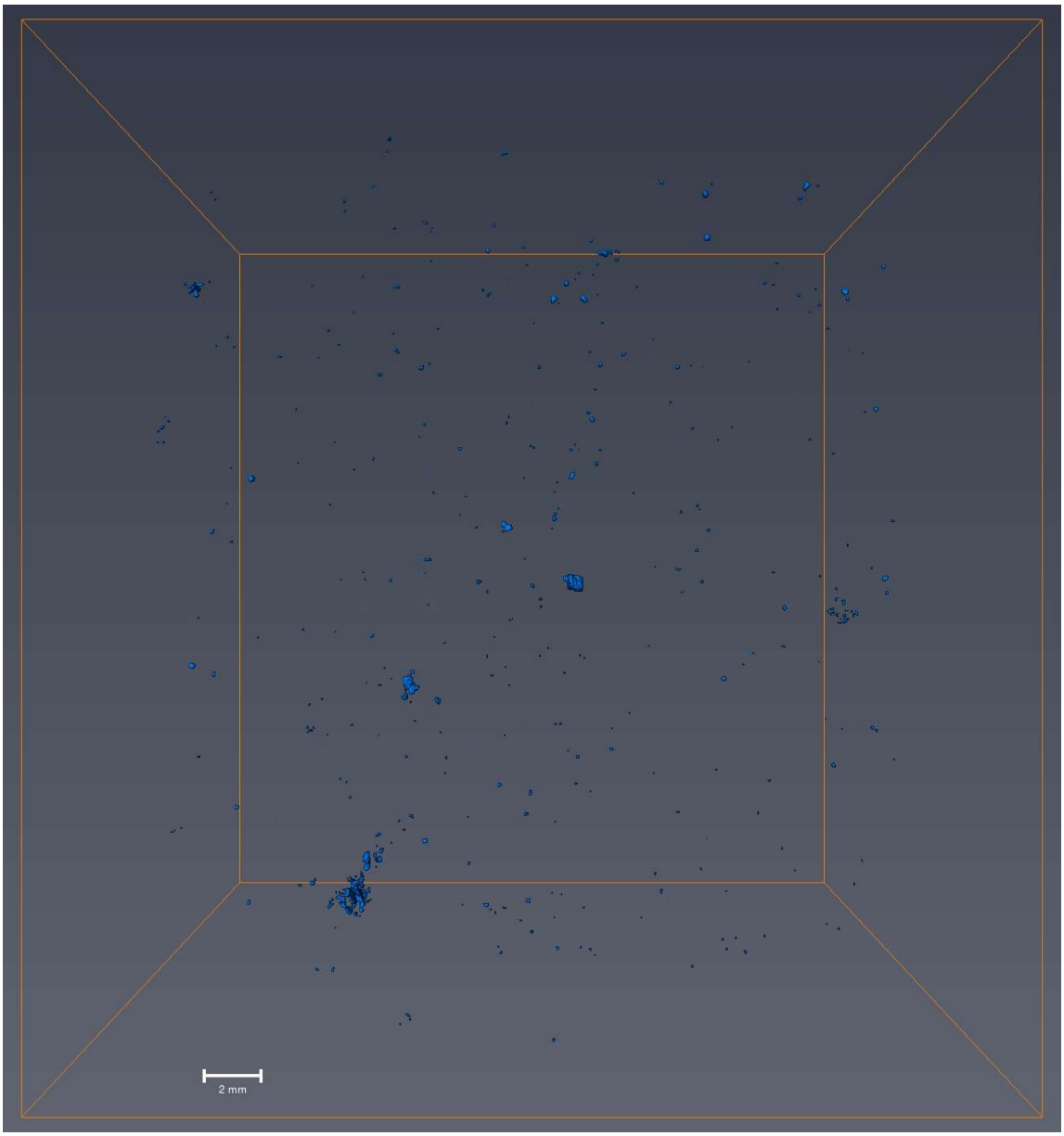

Figure 5.37 A full sample 3D reconstruction of Bag-1 with an (Y, Z) display orientation.

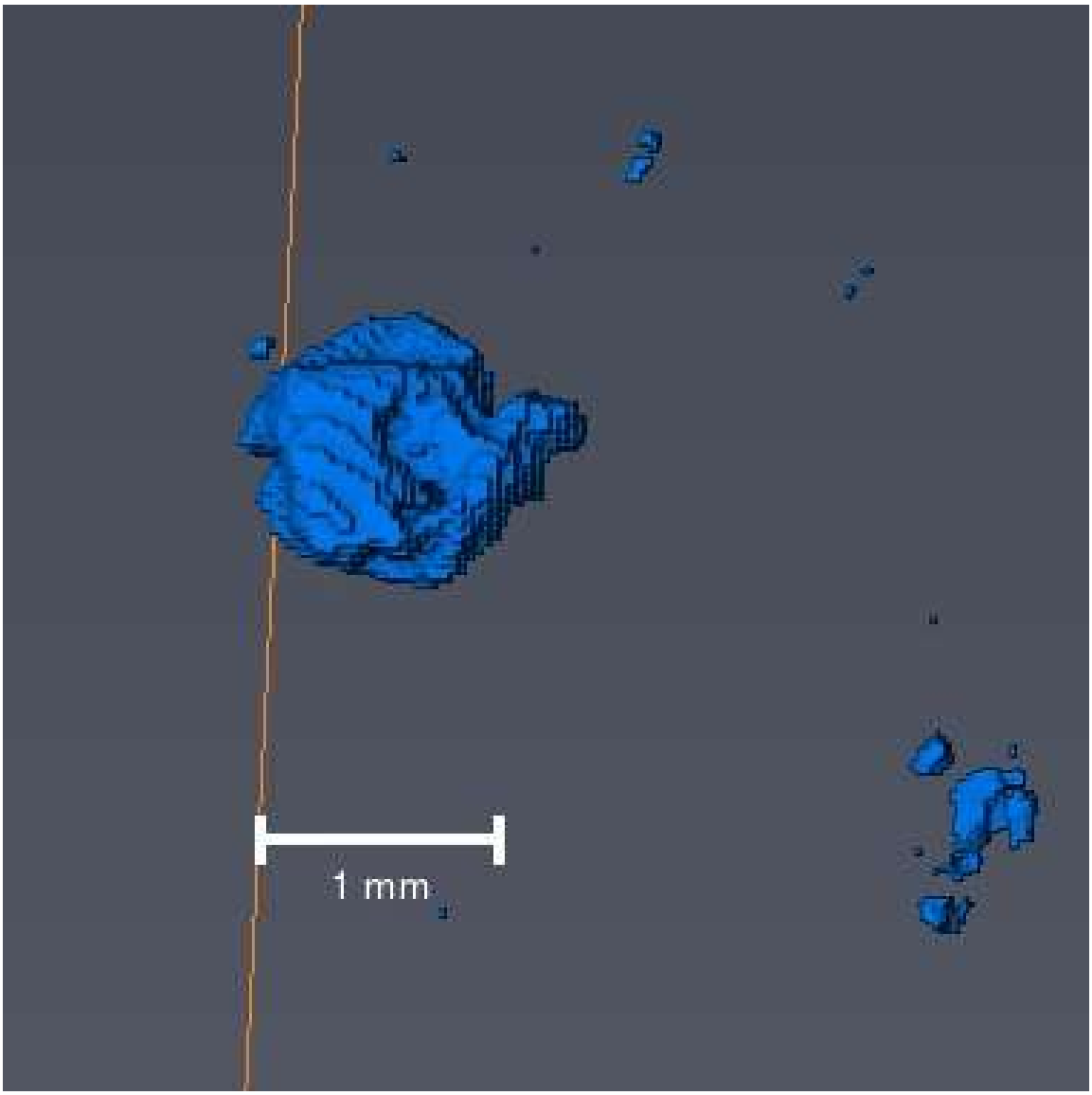

Figure 5.38 A 3D reconstruction of Bag-1 magnified to show the distinct sphericity of individual grains.

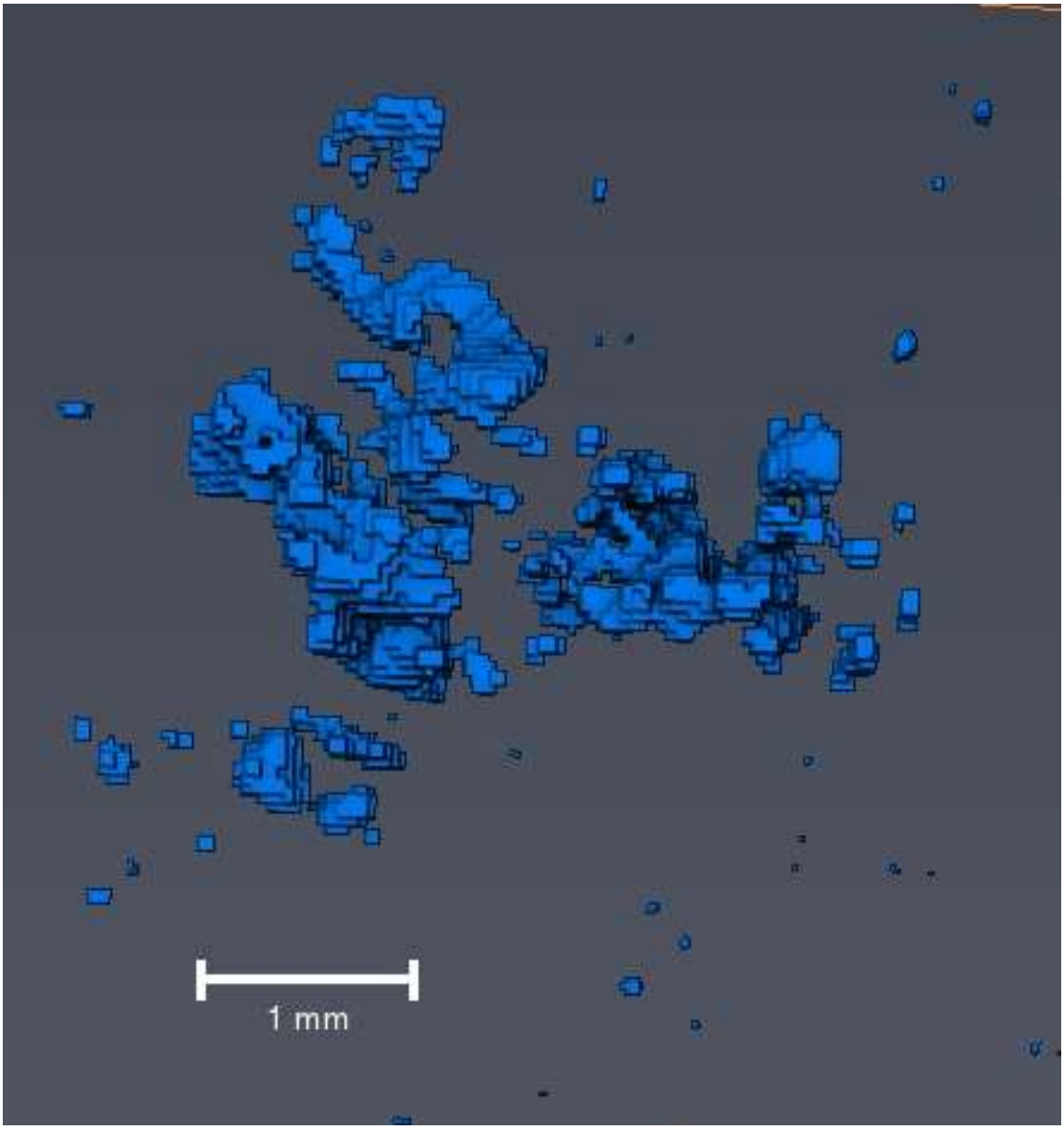

Figure 5.39 A 3D reconstruction of Bag-1 magnified to focus on a cluster of very small grains that appear almost amorphous.

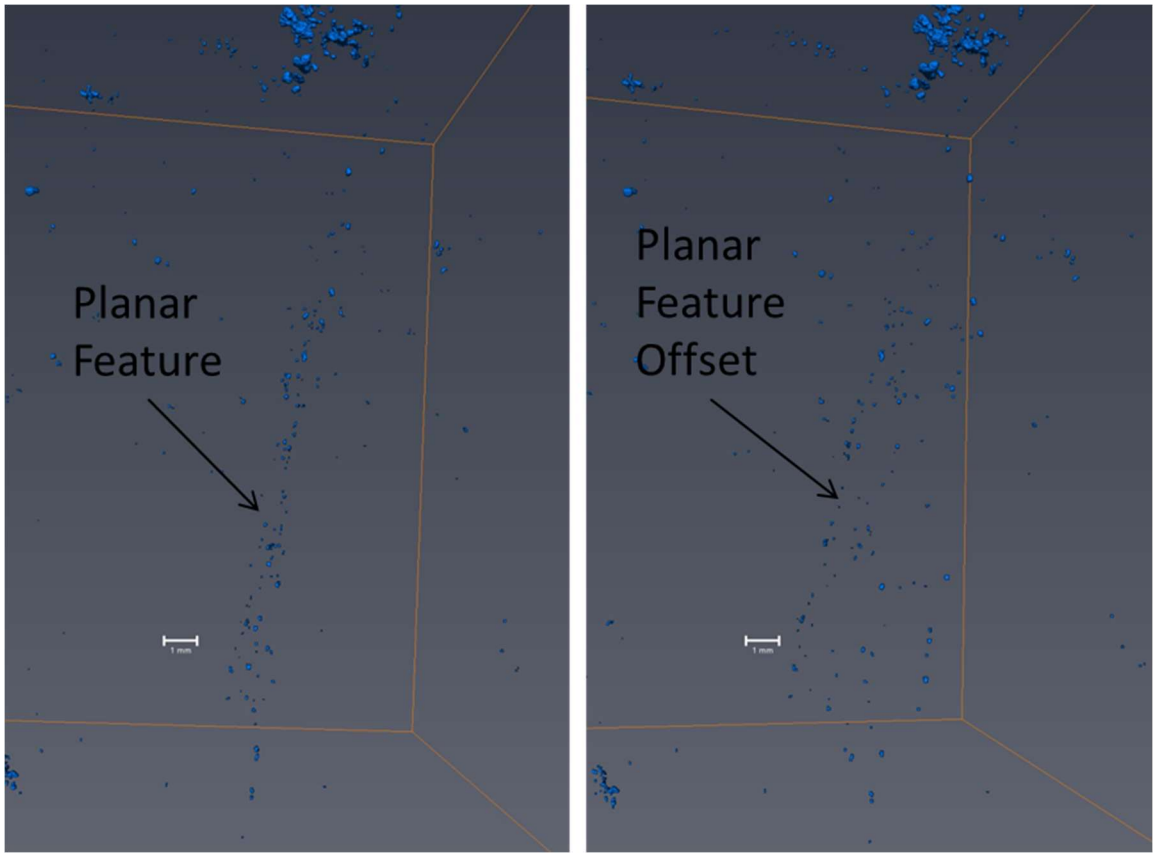

Figure 5.40 A 3D reconstruction of Bag-1 magnified to focus on a planar feature found with adjustments in orientation to highlight it. The thickness of this planar feature is sub-millimeter.

V-1

The ore mineralization present within V-1 all falls within the sub-millimeter size parameter and it occurs in a disseminated texture, albeit at a highly abundant concentration of ore versus gangue (fig. 5.41). There are not many ore grains larger than 2 mm. Many of the ore grains appear to have an elongated shape (fig. 5.42).

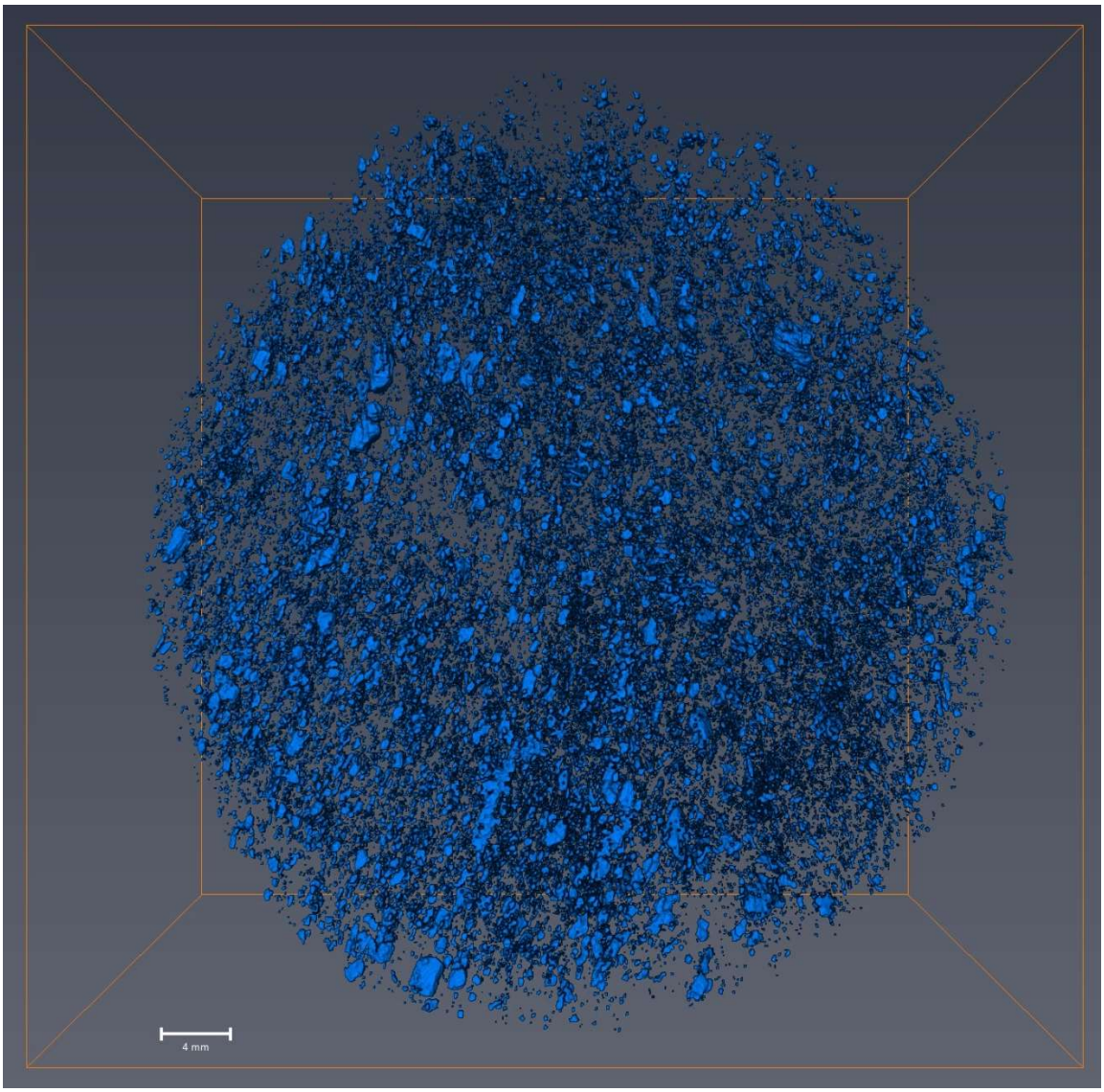

Figure 5.41 A full sample 3D reconstruction of V-1 with an (Y, Z) display orientation.

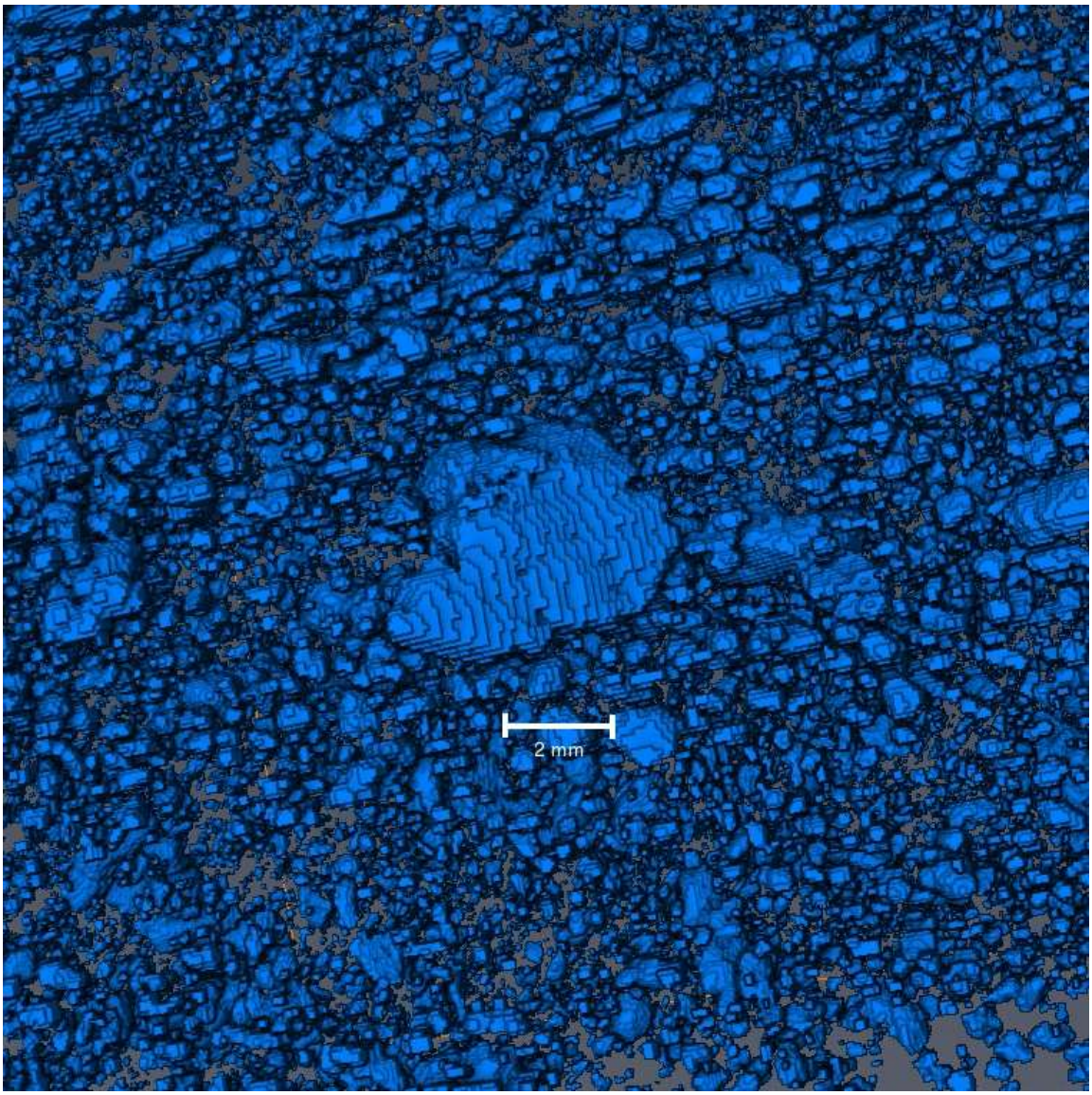

Figure 5.42 A 3D reconstruction of V-1 that has been magnified and reoriented to better display a large ore grain, roughly 4-5 mm in diameter. Smaller grains can range from sub-millimeter to 2 mm in diameter.

O-219

Ore mineralization within O-219 occurs as a disseminated texture (fig. 5.43). The majority of ore grains occur in the sub-millimeter size, but there is a small population of grains that fall into a larger 3 mm plus size fraction. These grains, when magnified, while somewhat elongated appear mostly amorphous suggesting that they may represent some later stage residuum mineralization (fig. 5.44).

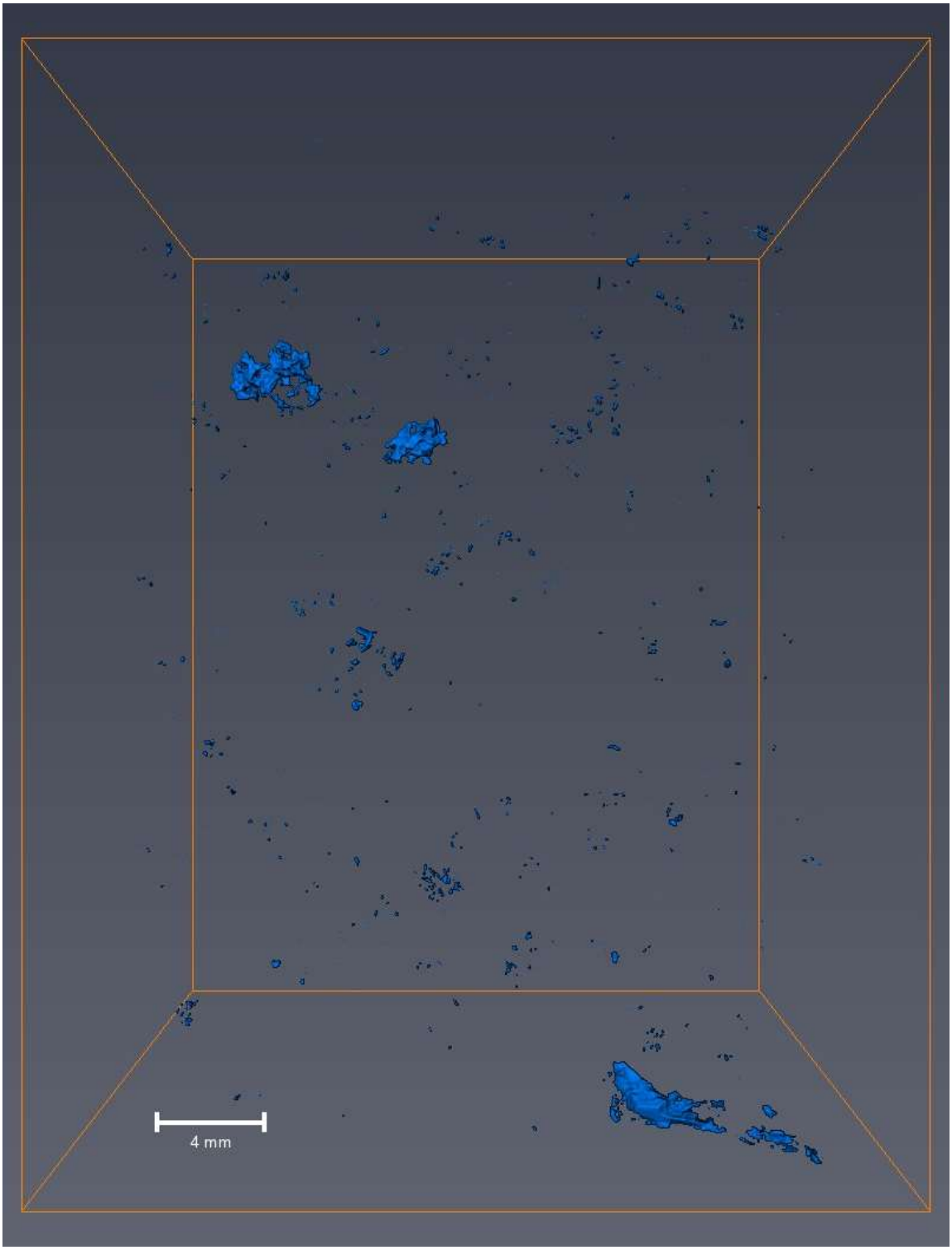

Figure 5.43 A full sample 3D reconstruction of O-219 with an (Y, Z) display orientation.

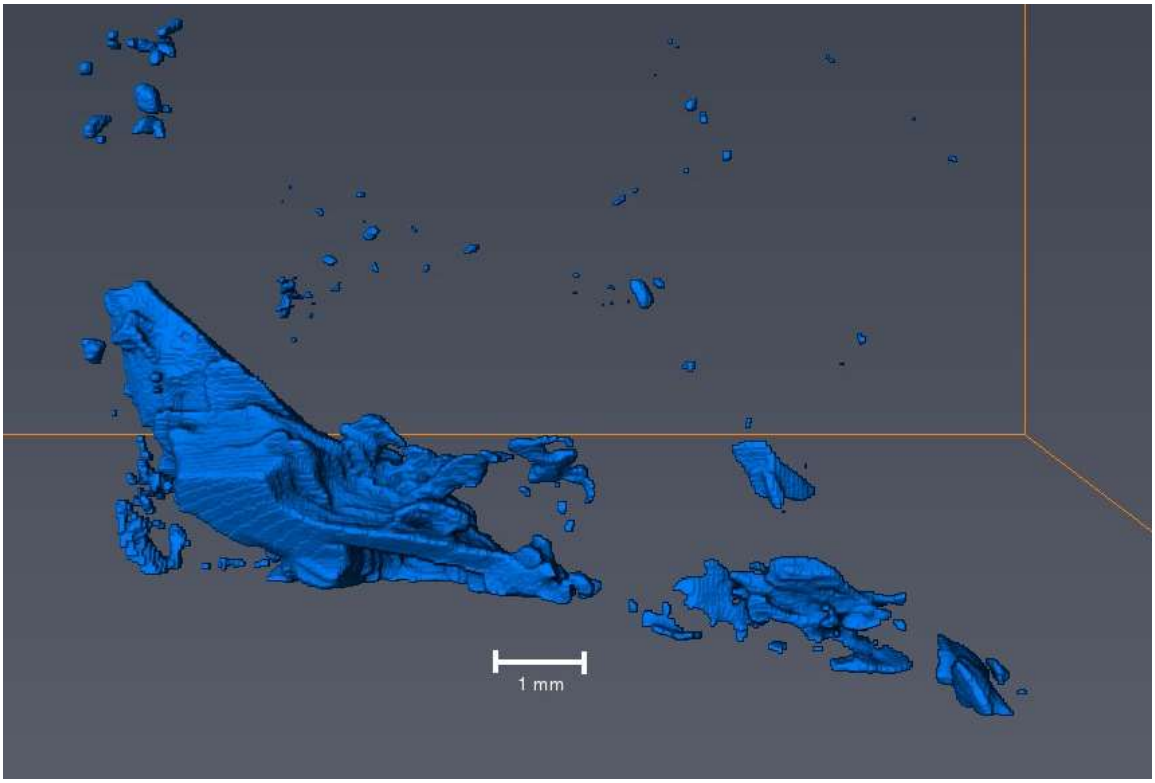

Figure 5.44 A 3D reconstruction of O-219 that has been magnified and oriented to display an amorphous ore grain characteristic.

SLC-55

There appear to be two distinct ore populations within SLC-55. In figure 5.45, the lower left portion contains ore mineralization that has a disseminated texture and appears to be sub-millimeter in size. The upper right portion of figure 5.45 contains ore mineralization that is semi-massive with a distinct net texture (fig. 5.46) and grain sizes that are more in the range of 1-2 mm. The more semi-massive portion of the sample appears to have a planar boundary separating much of the more massive ore mineralization from the disseminated material (fig. 5.47).

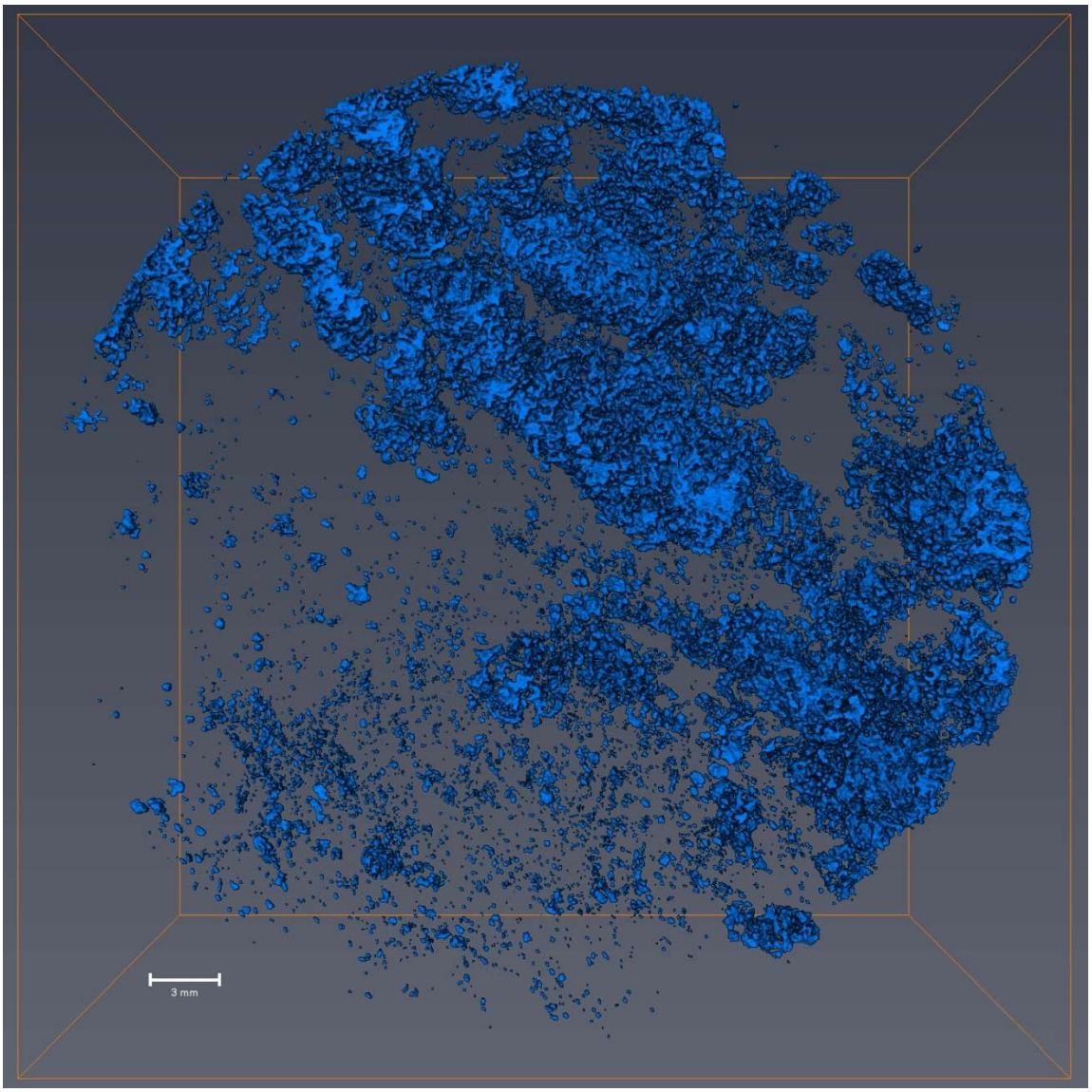

Figure 5.45 A full sample 3D reconstruction of SLC-55 with an (Y, Z) display orientation.

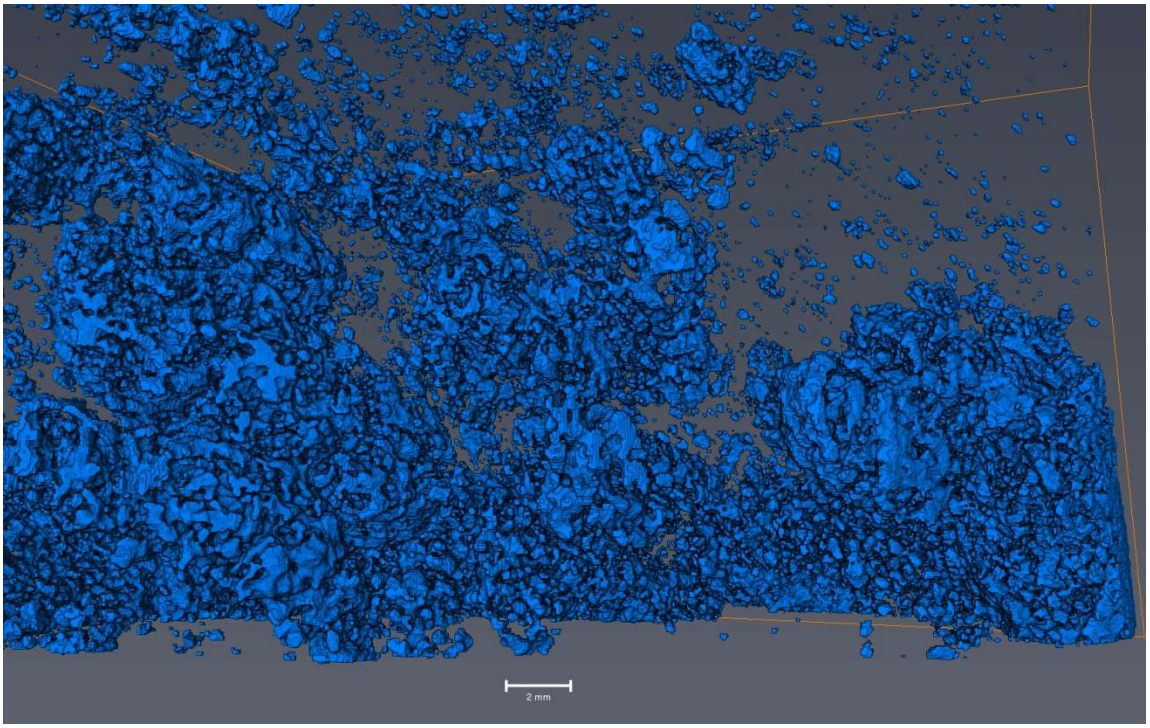

Figure 5.46 A 3D reconstruction of SLC-55 that has been magnified and oriented to display the net texture present.

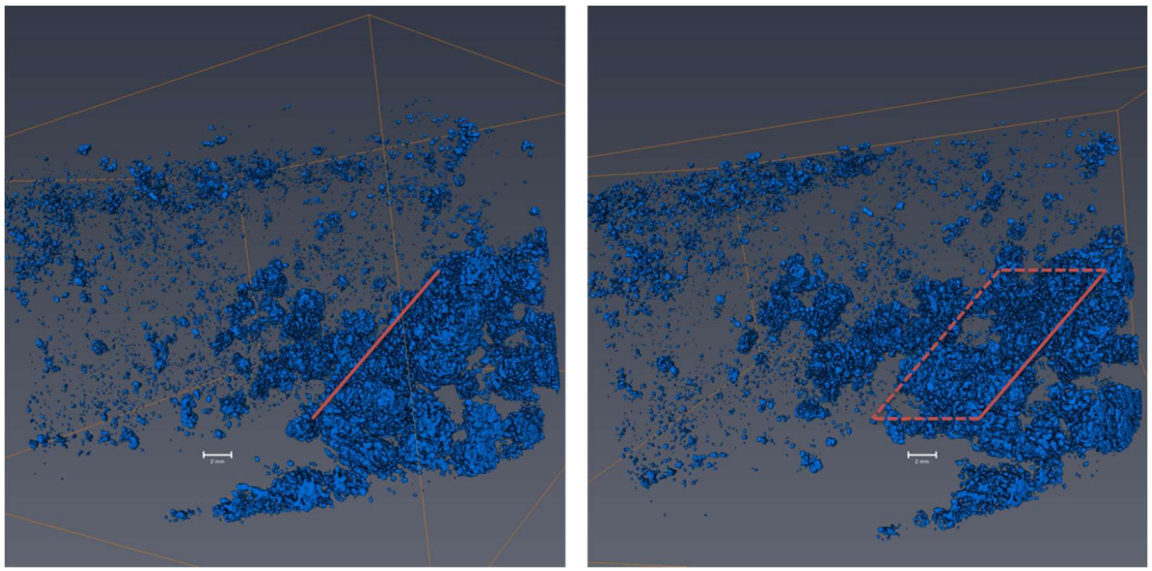

Figure 5.47 A 3D reconstruction of SLC-55 that has been magnified and oriented to display a planar feature. First aligned then offset by rotation to highlight the planar nature.

SLC-2476

The ore mineralization for sample SLC-2476 is highly concentrated with a disseminated texture that could be considered semi-massive if the ore grains were more

interconnected with each other (fig. 5.48). There are two very distinct size populations: an 1-2 mm size fraction, representing roughly a third of the ore mineralization, and a sub-millimeter size fraction which represents roughly two thirds of the ore mineralization (fig. 5.49). Most of the grains appear spheroid in shape; however, there are some grains that appear more elongated, many of which appear near what appears to be a planar boundary of some kind (fig. 5.50).

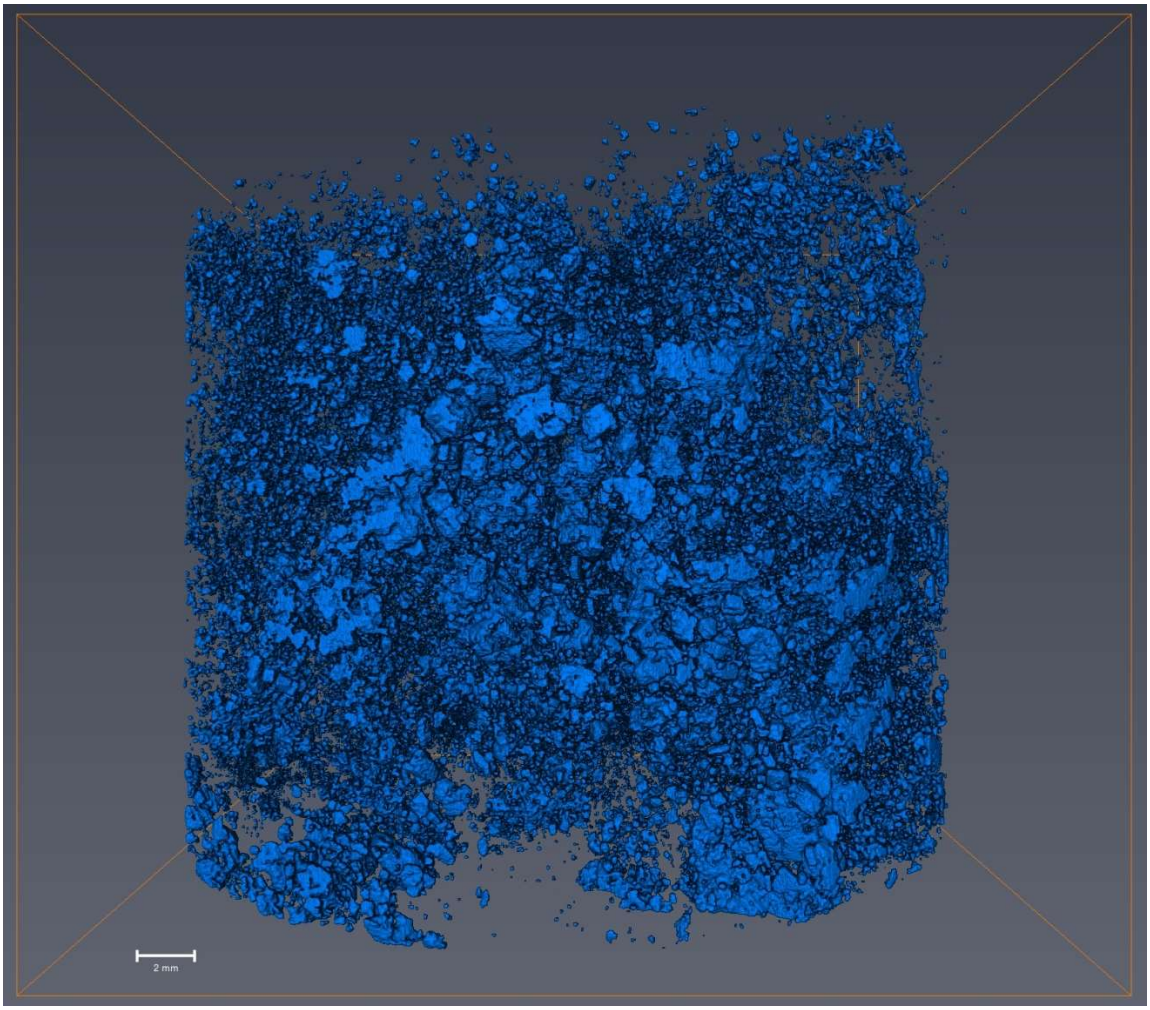

Figure 5.48 A full sample 3D reconstruction of SLC-2476 with an (Y, Z) display orientation.

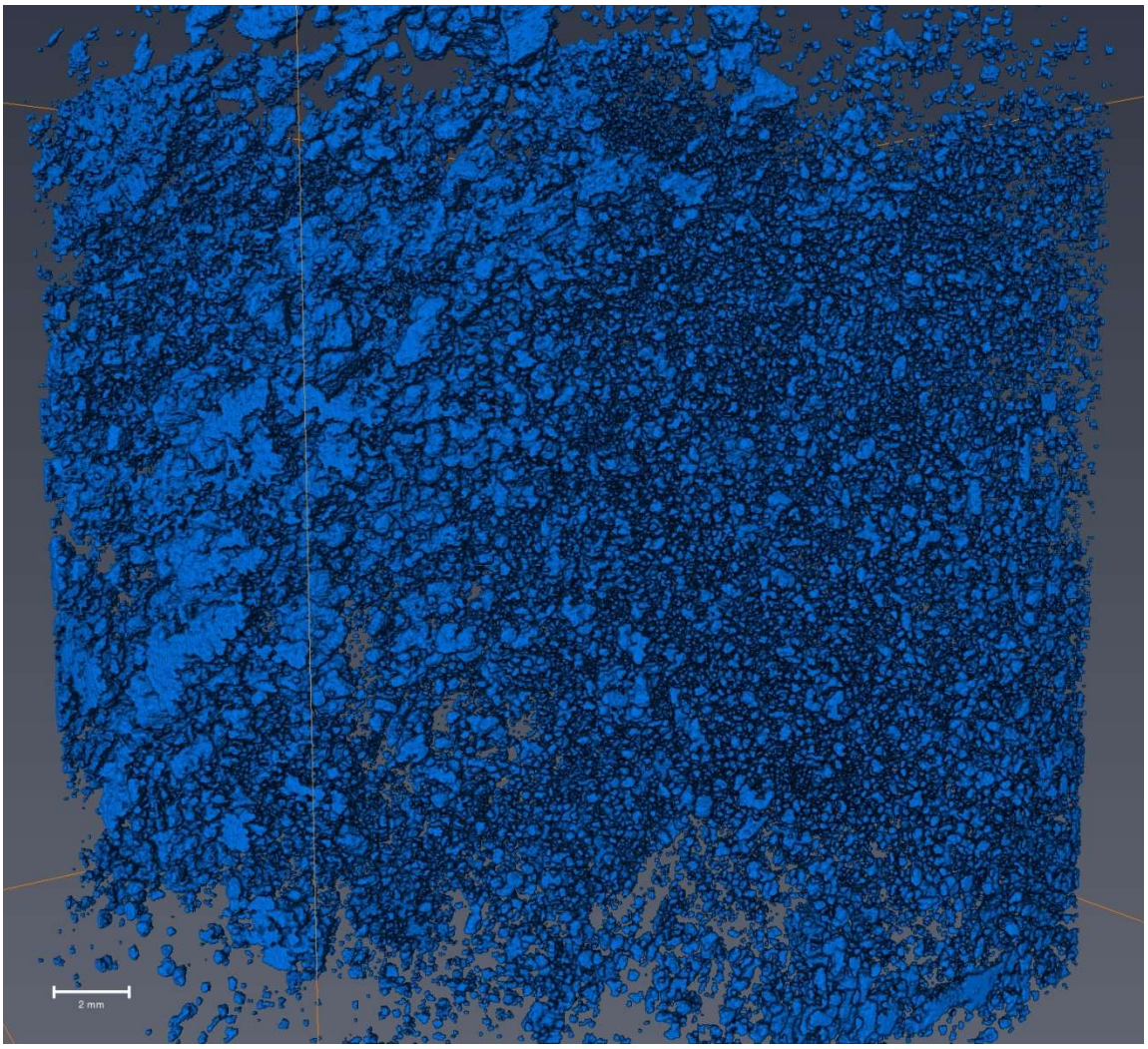

Figure 5.49 A 3D reconstruction of SLC-2476 that has been magnified and oriented to display a portion of the sample where the ore grain size grades from coarse (upper left) to a much finer grain size (lower right).

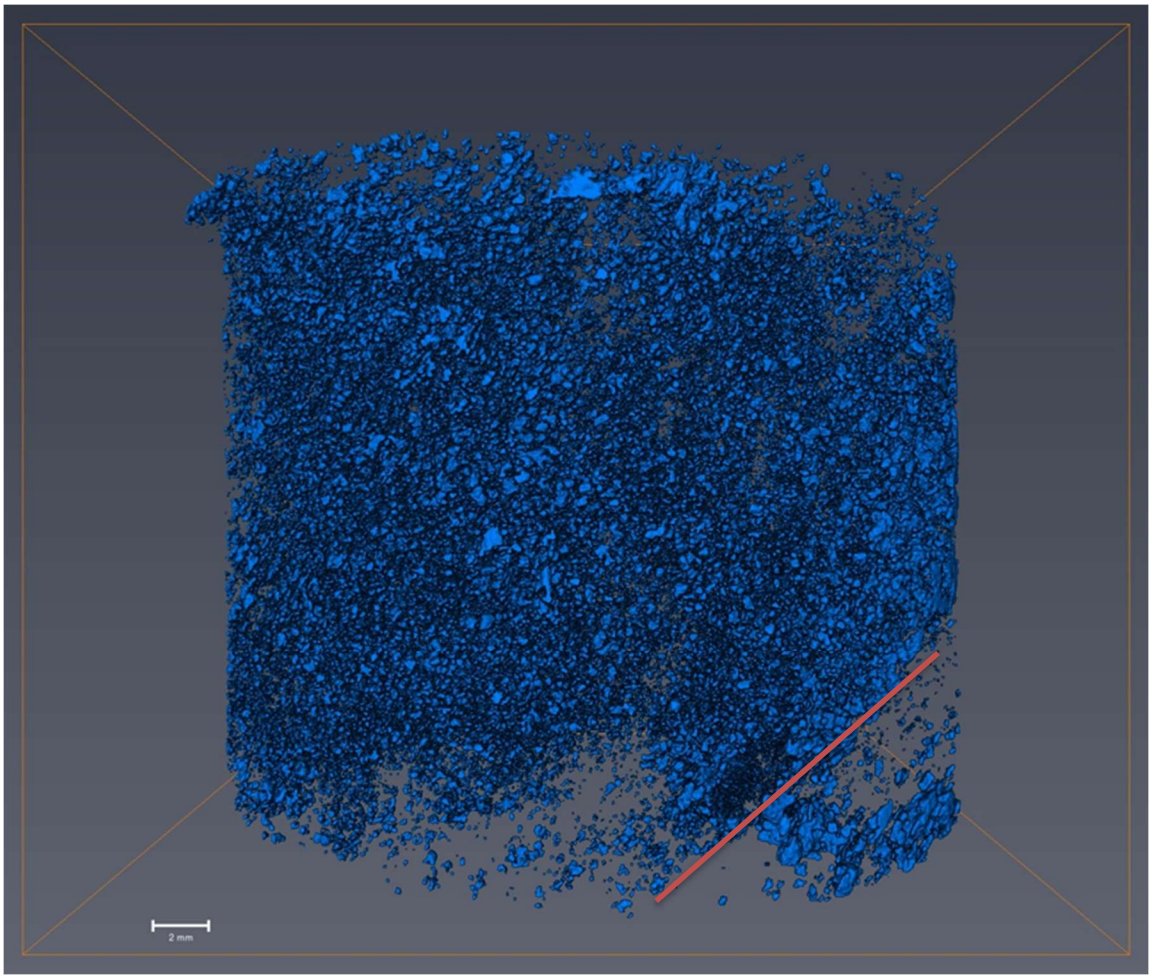

Figure 5.50 A full sample 3D reconstruction of SLC-2476with an (X, Z) display orientation. There a slight planar boundary that may be present within the lower right-hand portion of the image.

MVT-1

The ore mineralization for MVT-1 is a massive vein fill that occurs within a brecciated host rock. Because of the high connectivity of the ore mineralization it is difficult to decipher the size and shape of individual ore grains (fig. 5.51). The thickness of the veins being filled with ore mineralization range from as small as 1 mm in places to as large as 5 mm; average thickness appeared to be roughly 3 to 4 mm. (fig. 5.52).

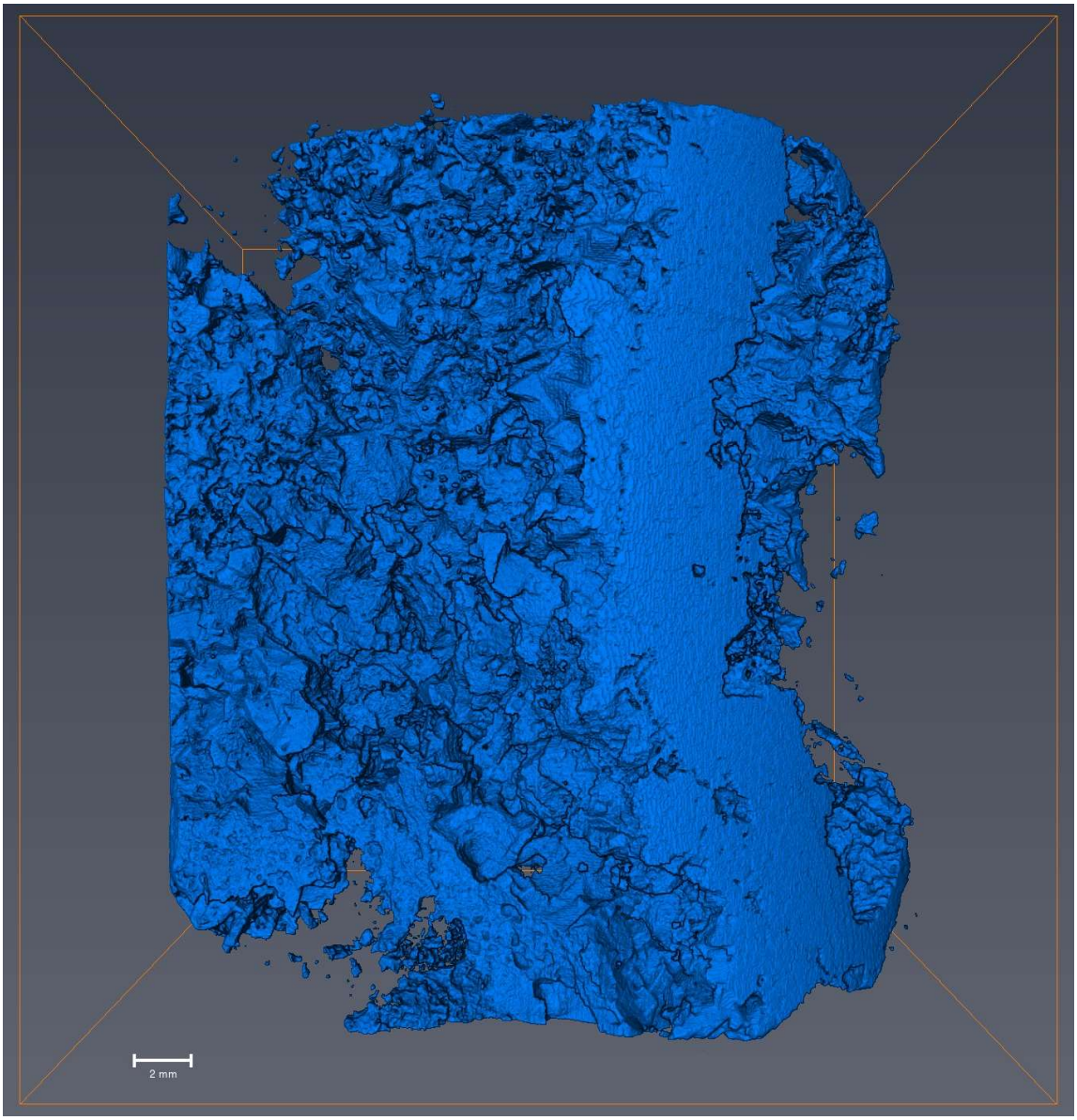

Figure 5.51 A full sample 3D reconstruction of MVT-1 with an (Y, Z) display orientation.

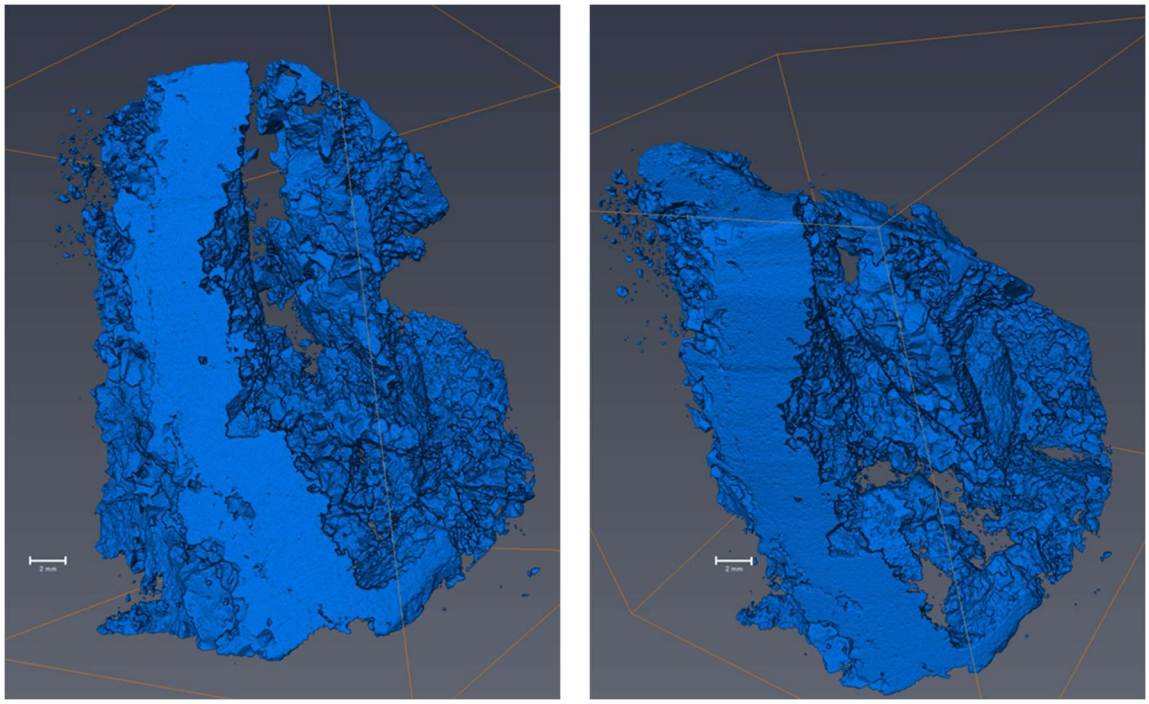

Figure 5.52 A full sample 3D reconstruction of MVT-1 that has been slightly magnified and presented in two different orientations to highlight the ore veins occurring in this brecciated zone.

1716

The ore mineralization within sample 1716 is disseminated with a distinct stratiform texture (fig. 5.53 and 5.54) where ore grains are concentrated in specific layers of the host rock. Most ore grains are spheroids that fall within a sub-millimeter size fraction. However, there are a few ore grains that appear to have a more elongated shape to them and fall into a much larger size fraction, 6 mm or larger (fig. 5.55).

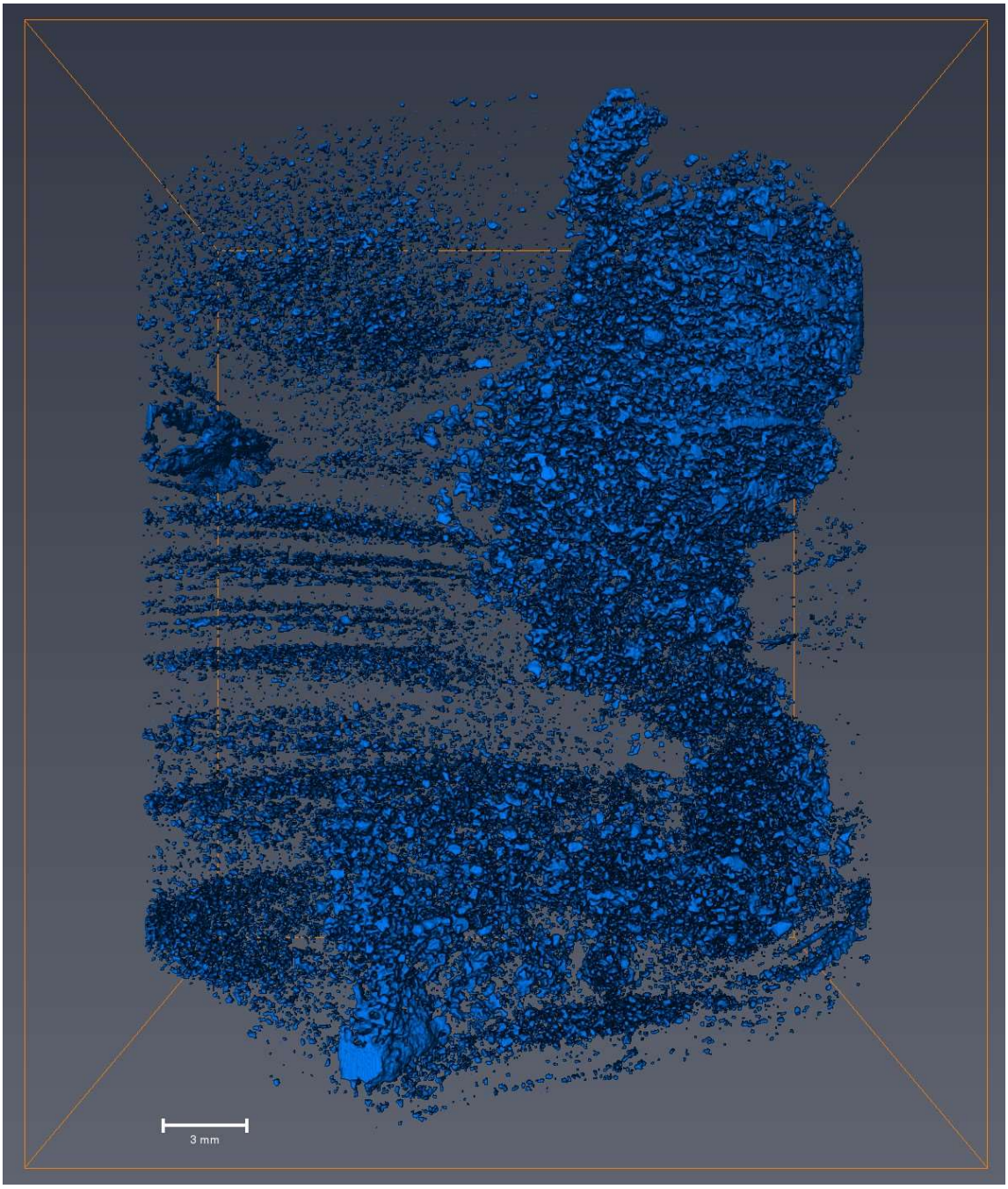

Figure 5.53 A full sample 3D reconstruction of 1716 with an (Y, Z) display orientation.

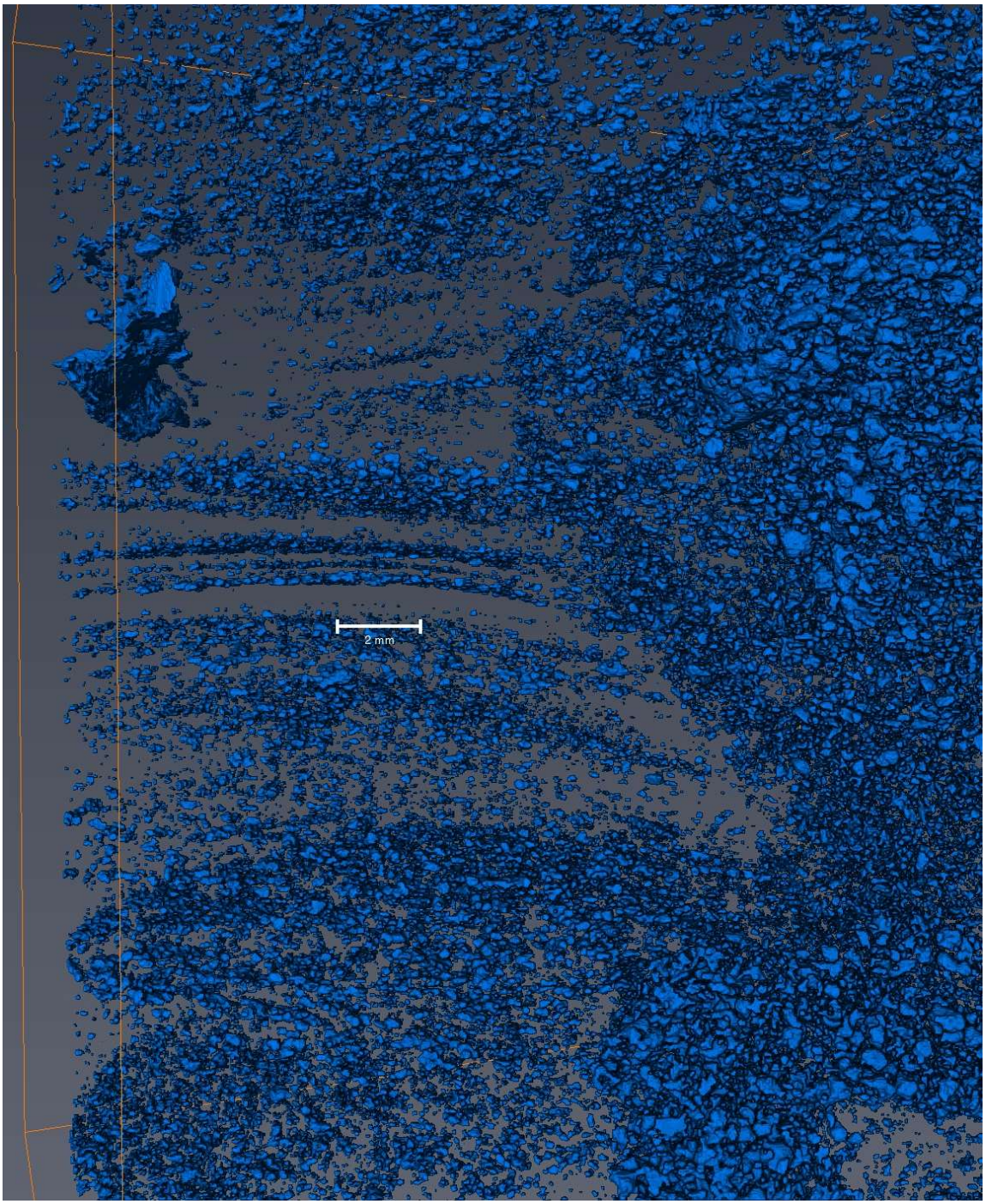

Figure 5.54 A 3D reconstruction of 1716 that has been magnified and oriented to better highlight the stratiform ore texture present within portions of this sample

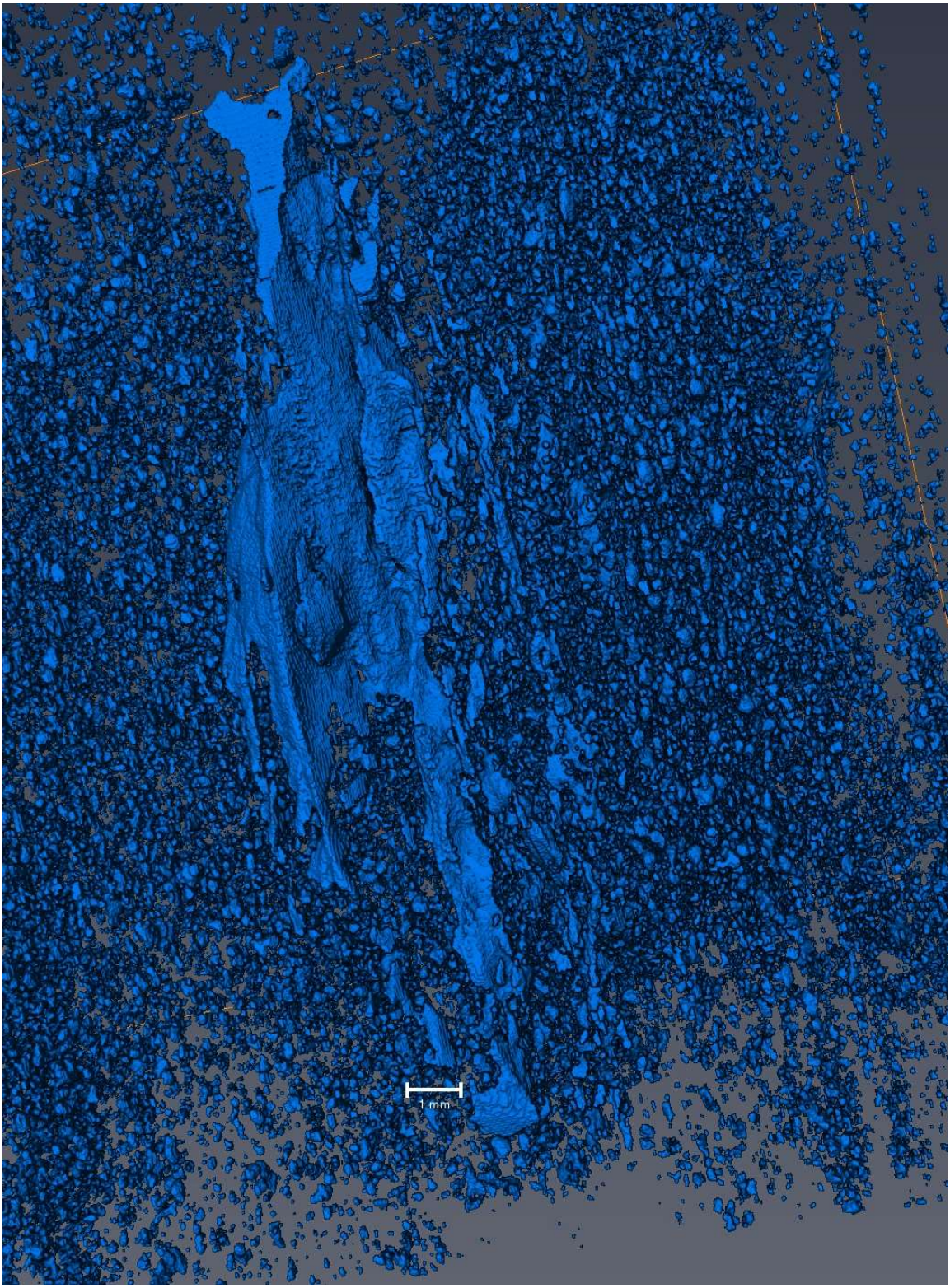

Figure 5.55 A 3D reconstruction of 1716 that has been magnified and oriented to highlight an ore grain that is significantly large than the surrounding ore.

5.3.2 Grain Size Distributions

Grain size distributions were analyzed by collecting the 3D volume information for every ore grain within a sample and then dividing the data range into 1000 bins. Bins in this case refers to smaller sub-sets of data, this allows for values of data within specific ranges to be grouped together and allow more data to be presented at one time in a more condensed form. The high number of bins was necessary to avoid the data being lumped into inappropriately sized bins, because of the extreme range of particle sizes represented. All the samples had the vast majority of grains fall within a very small set of sizes. However, every sample also contained grains that were several orders of magnitude larger than the typical grains creating the need for such a high number of bins.

EG-181

Sample EG-181 required one data point to be removed to display the grain size distribution (fig. 5.56). The removed grain was 4 orders of magnitude larger than the displayed largest grain because of the semi-massive nature of the ore. Even though XRCT counted it as a single grain it likely consists of many grains that are all interconnected making it appear as one grain to the XRCT.

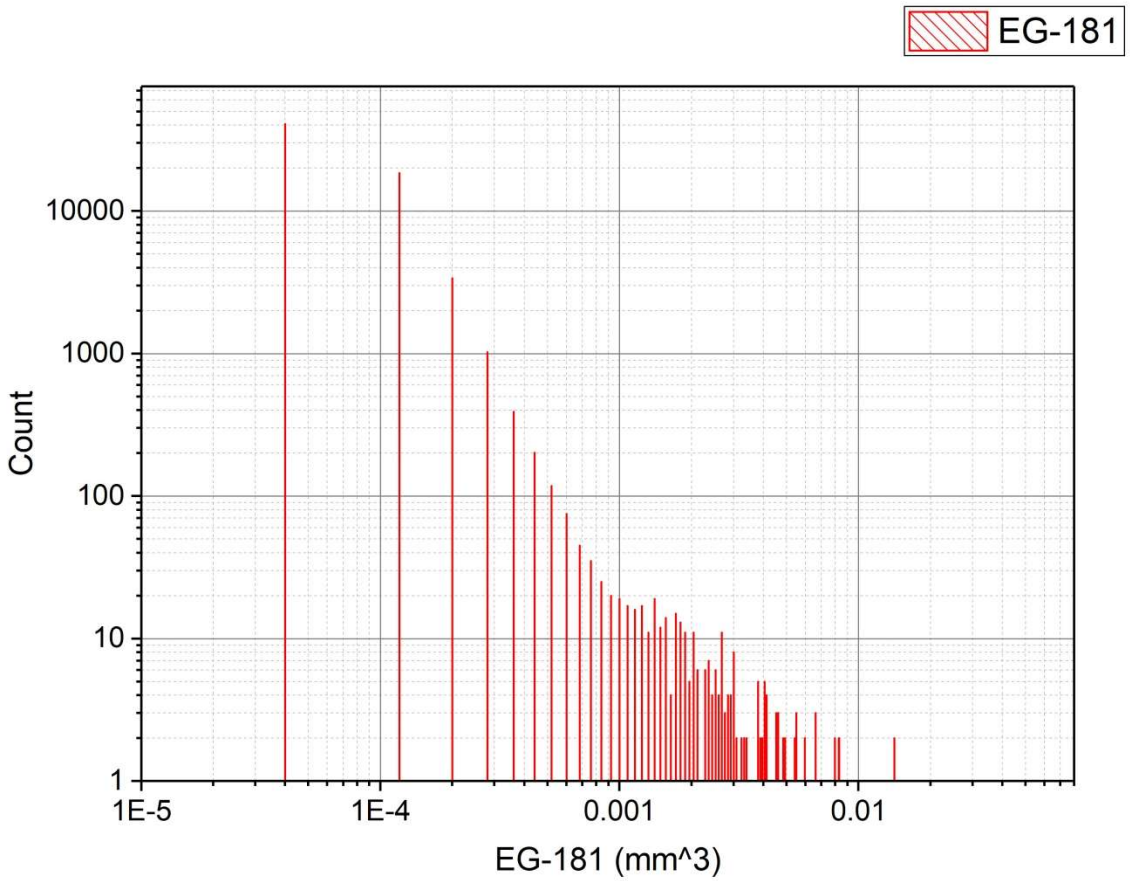

Figure 5.56 Grain size distribution of ore grains within sample EG-181. One large data point was removed to allow for a better visualization of size distribution. Data was separated into 1000 bins.

Eagle-1

The sample Eagle-1 had to have two data points removed to display the grain size distribution (fig. 5.57). The removed grains were 5 orders of magnitude larger than the displayed largest grain. Like EG-181, Eagle-1 also displayed a semi-massive ore texture. Like EG-181, the XRCT counted two grains within Eagle-1 as individual grains when they actually consisted of many interconnected grains.

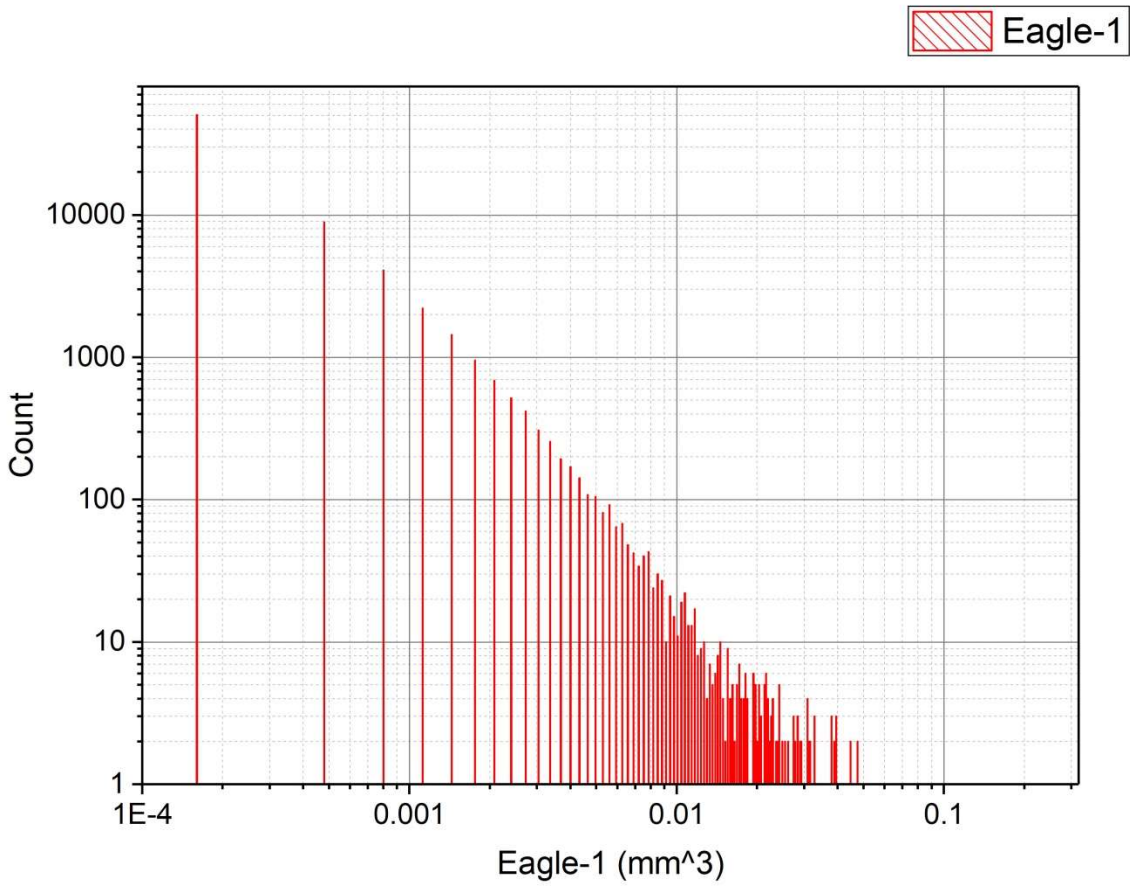

Figure 5.57 Grain size distribution of ore grains within sample Eagle-1. Two large data points were removed to allow for a better visualization of size distribution. Data was separated into 1000 bins.

DC

Sample DC did not require any data to be excluded from the dataset (fig. 5.58). The disseminated nature of the ore within this sample lends itself better to having its grain size measured using an XRCT.

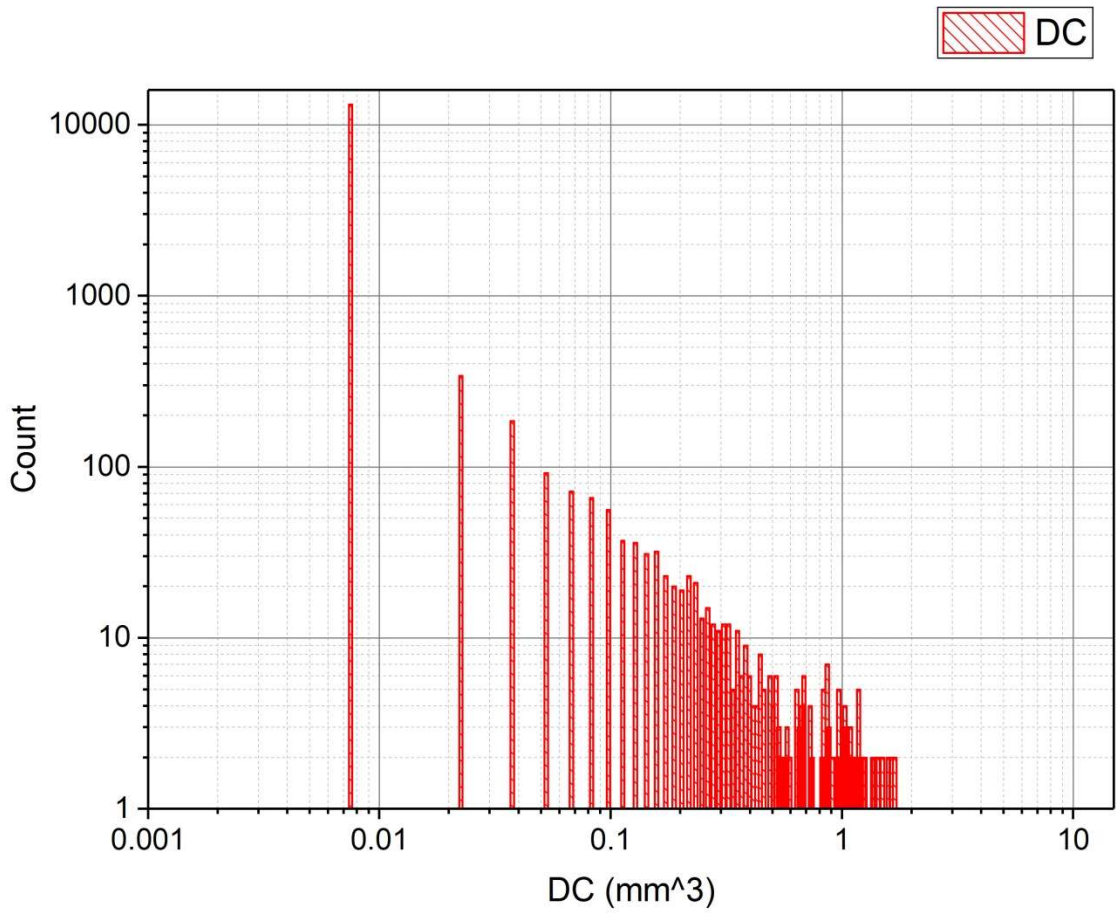

Figure 5.58 Grain size distribution of ore grains within sample DC. Data was separated into 1000 bins.

Bag-1

Compared to other samples tested, Bag-1 did not contain nearly as many ore particles. However, since this sample originated from a porphyry deposits the highly disseminated nature of the ore grains lends itself well to this type of data analysis (fig. 5.59).

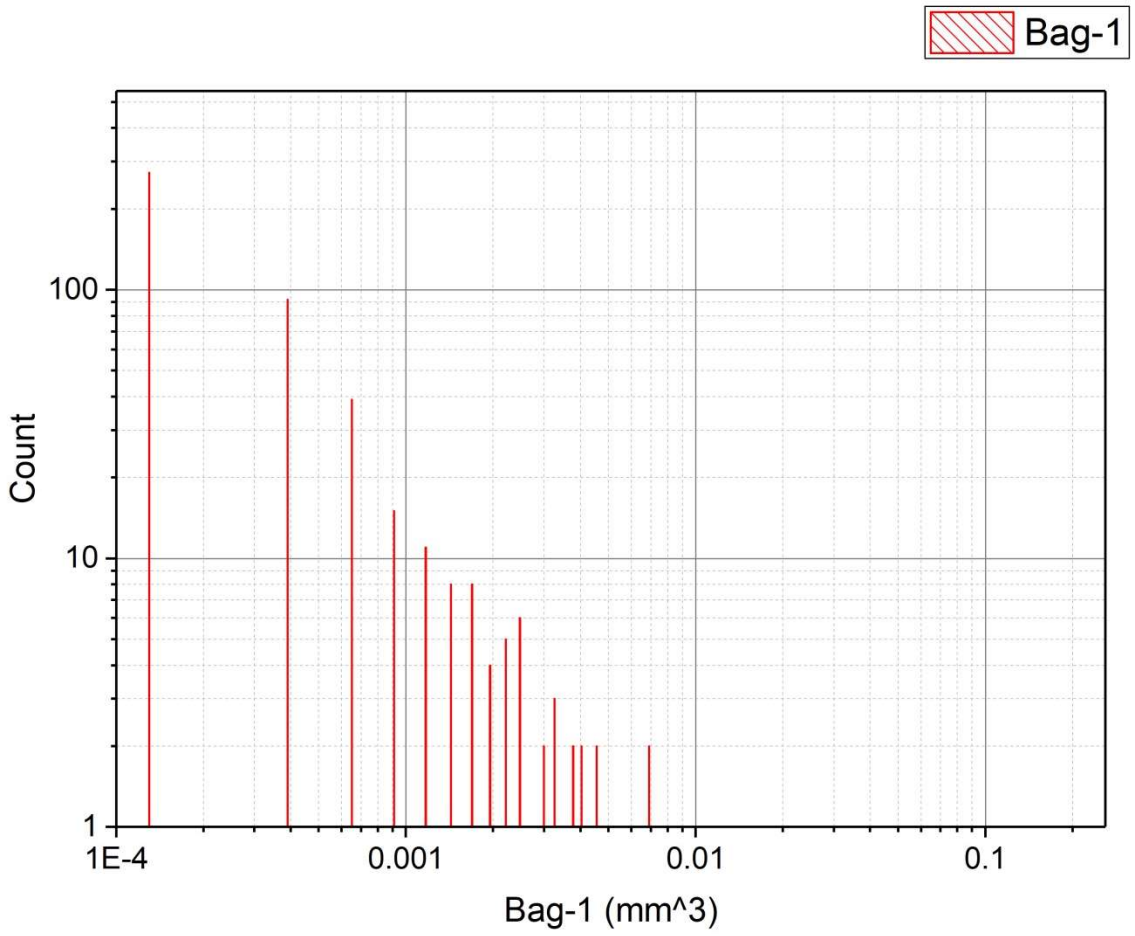

Figure 5.59 Grain size distribution of ore grains within sample Bag-1. Data was separated into 1000 bins.

V-1

Like Bag-1, sample V-1 also originated from a porphyry deposit and also contains highly disseminated ore. However, V-1 has a much more abundant concentration of ore particles and also contains grains that are at least an order of magnitude larger than those present in Bag-1 or in O-219, the other example of porphyritic material (fig. 5.60).

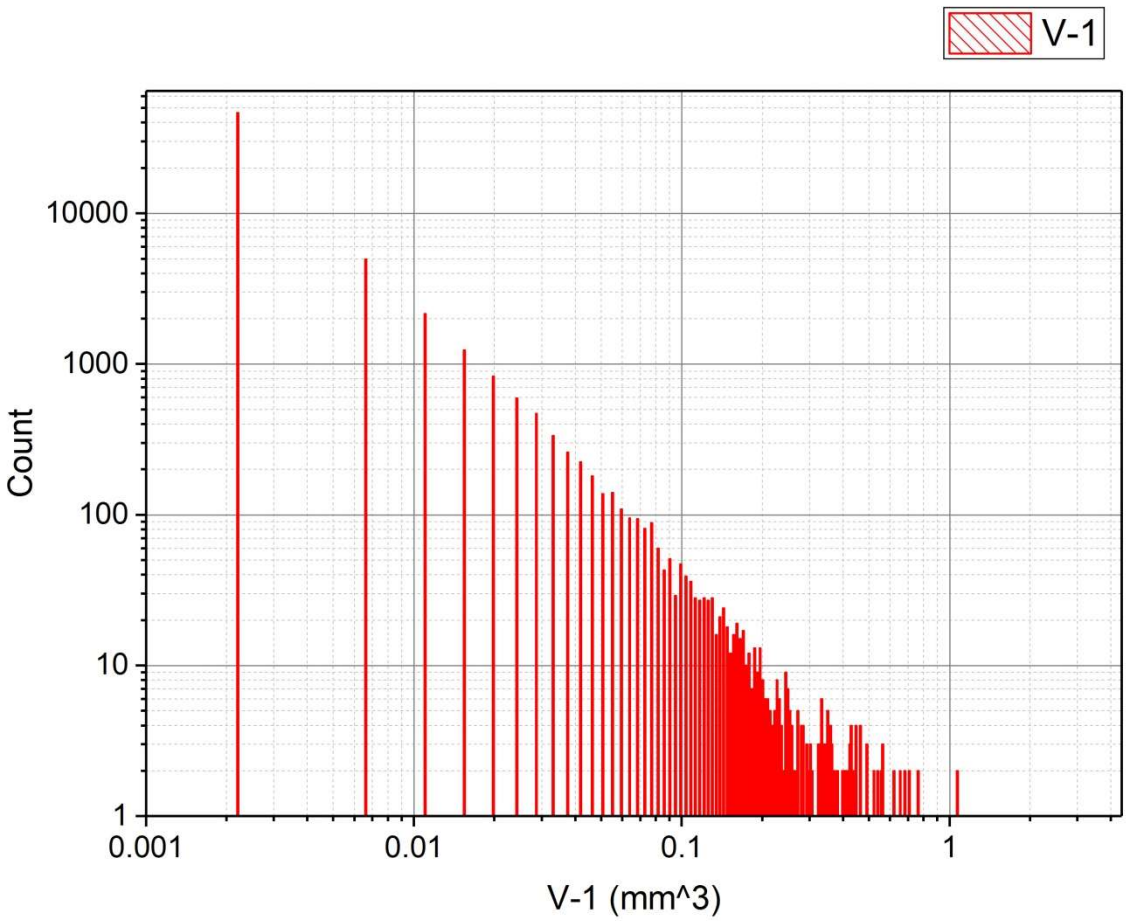

Figure 5.60 Grain size distribution of ore grains within sample V-1. Data was separated into 1000 bins.

O-219

O-219 is the final sample that came from a porphyry deposit and as with the others displayed a highly disseminated texture which allowed for the entire dataset to be displayed without curation (fig. 5.61). O-219 appears to contain a similar abundance of ore grains as does the Bag-1 sample.

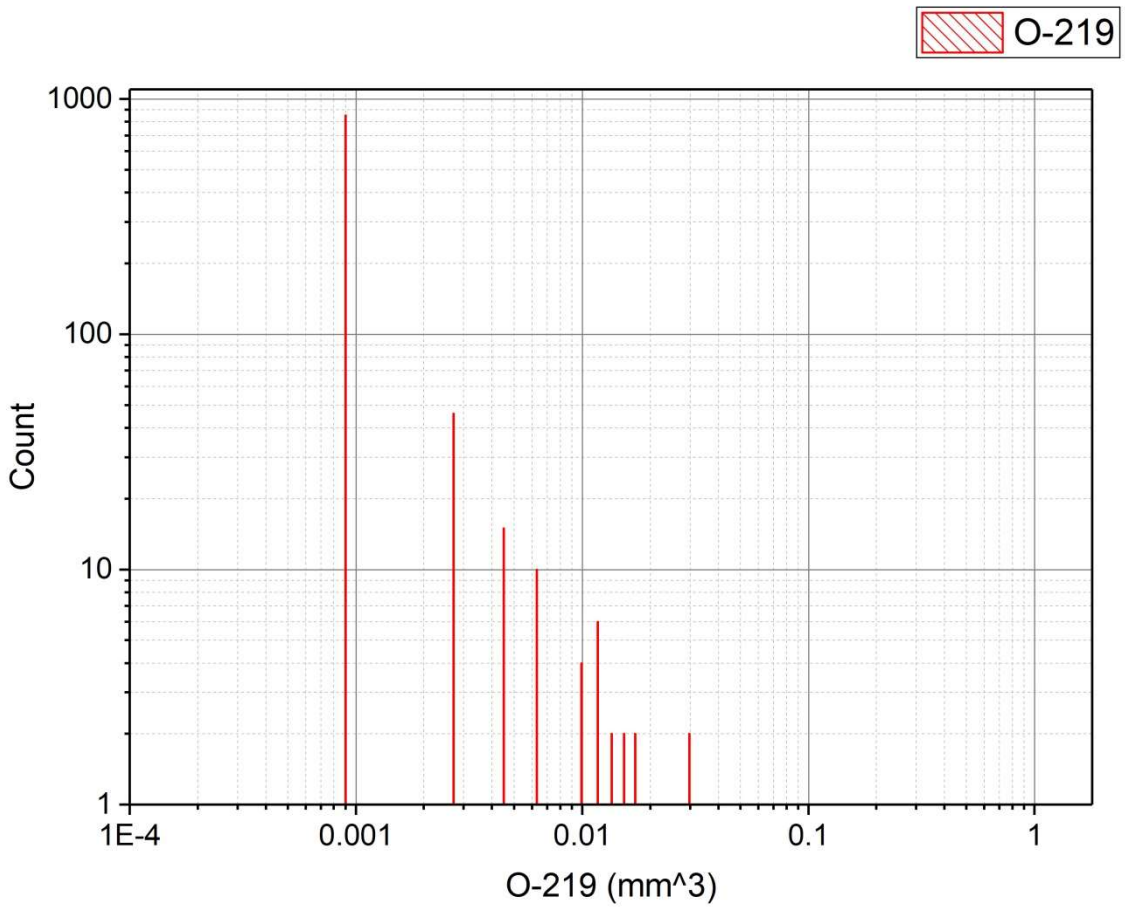

Figure 5.61 Grain size distribution of ore grains within sample O-219. Data was separated into 1000 bins.

SLC-55

SLC-55 is a sample that originated from a VHMS deposit. Since the grain size distribution for this sample was not clustered together, there were no data points that needed to be removed from the dataset (fig. 5.62). The grain size distribution of SLC-55 appears to bear a resemblance to DC, the sample from a liquid-magmatic deposit in both the ranges of grain sizes and the relative abundances of those sizes present.

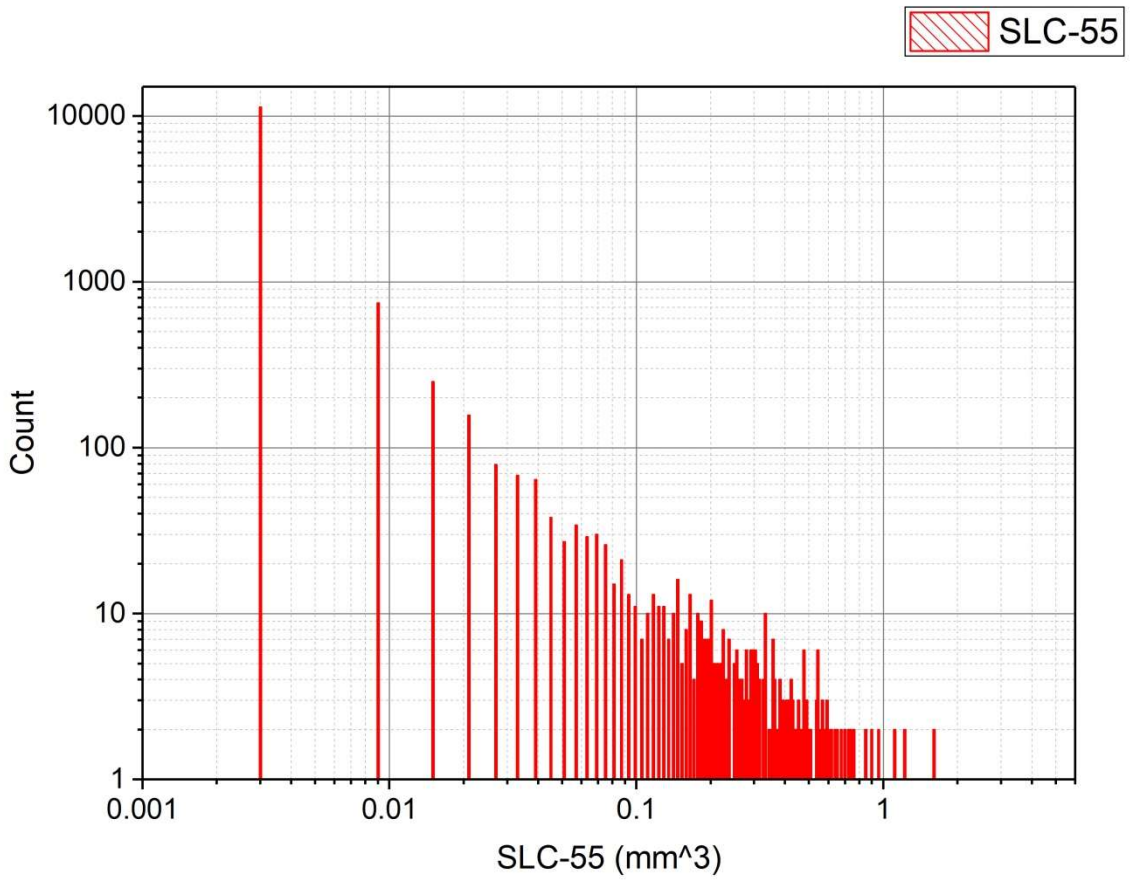

Figure 5.62 Grain size distribution of ore grains within sample SLC-55. Data was separated into 1000 bins.

SLC-2476

Sample SLC-2476 came from the same VHMS deposit that SLC-55 came from but they differ in that SLC-55 came from a location much closer to the main massive ore body whereas SLC-2476 came from a stringer zone that resided in a lower portion of the VHMS deposits structure below the main ore body. The grain size distribution for SLC-2476 (fig. 5.63) has a greater abundance of smaller sized particles occurring than does SLC-55, which could be considered to be representative of its distance from the main ore body.

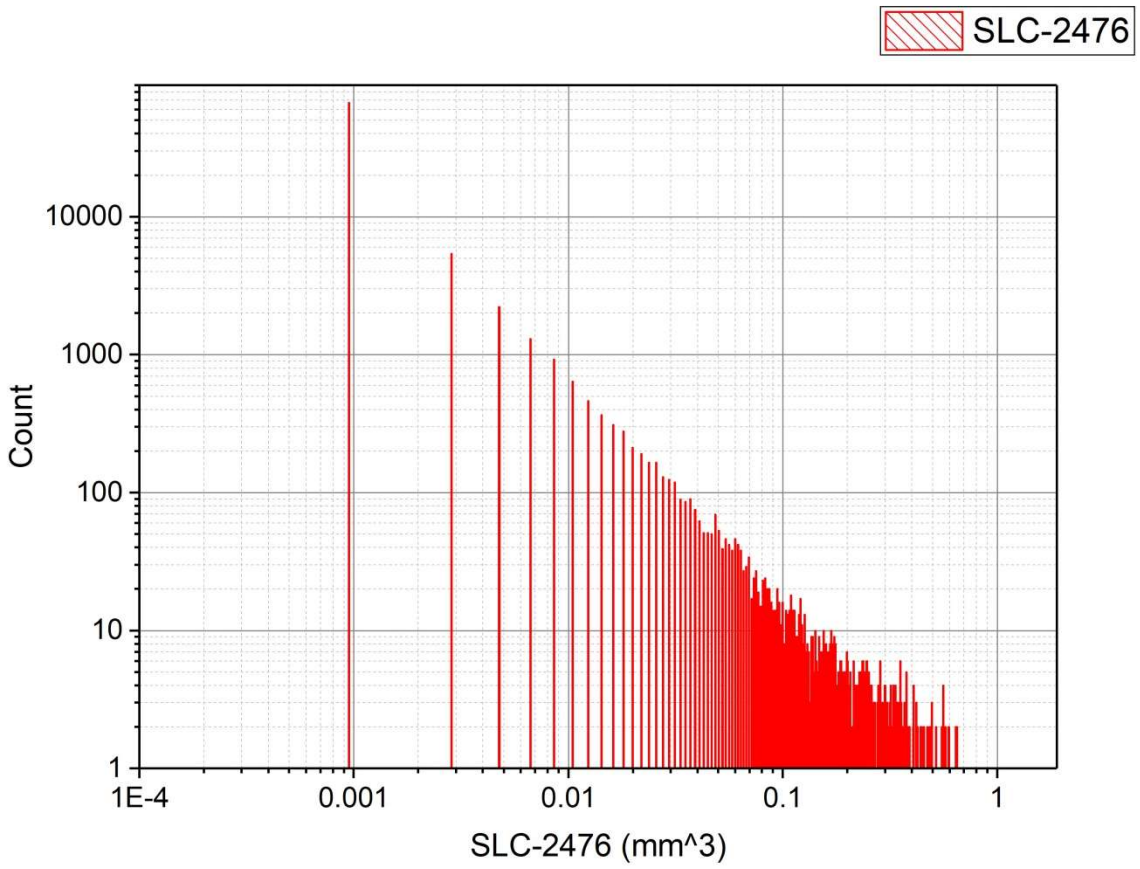

Figure 5.63 Grain size distribution of ore grains within sample SLC-2476. Data was separated into 1000 bins.

MVT-1

For the grain size distribution of MVT-1 to be displayed effectively, one grain had to be removed from the dataset (fig.5.64). The grain that was removed was 4 orders of magnitude lager than the material currently displayed. MVT-1 is a sample that originated from an MVT style deposit and came from a brecciated zone. The brecciated zone allowed for large portions of ore to crystalize out in a localized area. Like with EG-181 and Eagle-1 this had the effect of creating a very large ore grain that likely consists of many interconnected ore grains that the XRCT views as one single object.

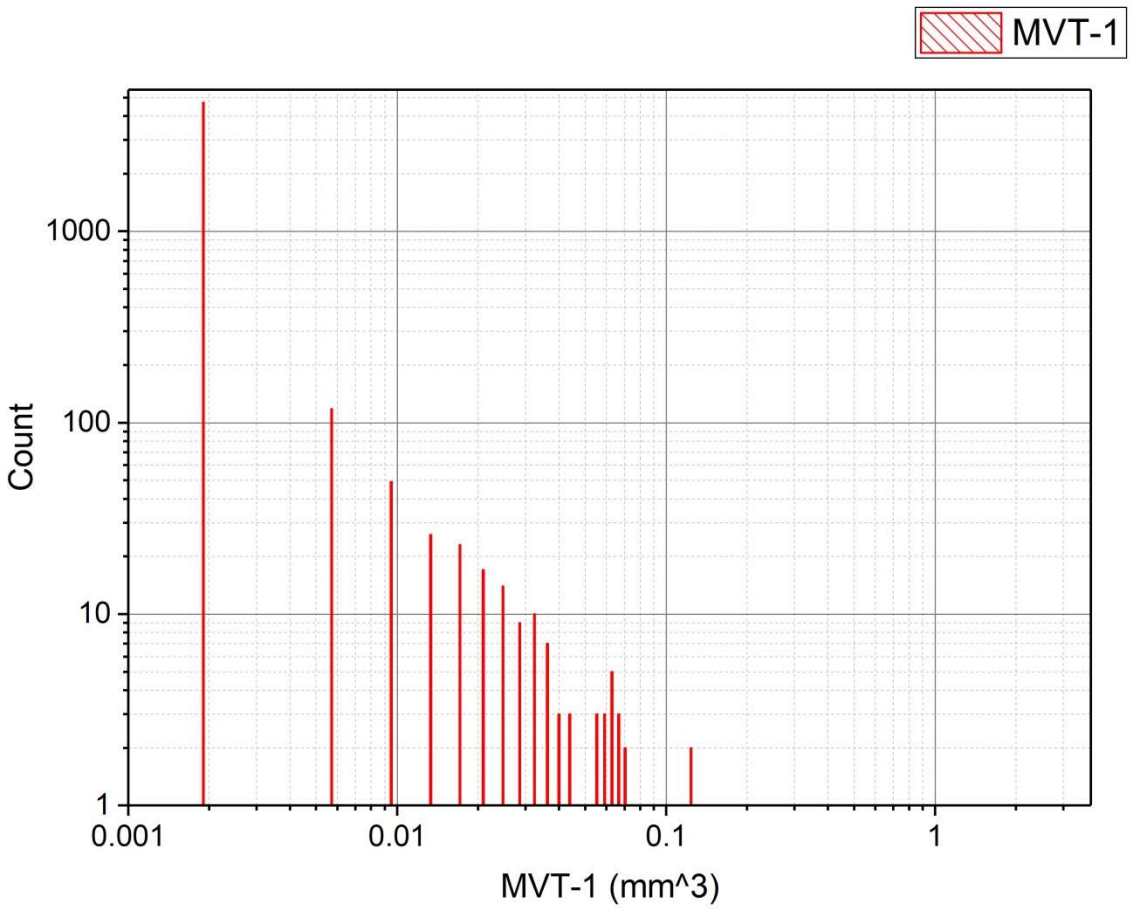

Figure 5.64 Grain size distribution of ore grains within sample MVT-1. One large data point was removed to allow for a better visualization of size distribution. Data was separated into 1000 bins.

1716

For a grain size distribution for sample 1716 to be successfully displayed two data points needed to be removed from the overall dataset (fig. 5.65). The two grains that were removed were only slightly larger than the data currently presented but had the adverse effect of causing a significant portion of the distribution to be lumped together creating a skewed presentation. 1716 comes from an SSC deposit that contains very small and highly disseminated ore grains that are stratigraphically controlled. Based on the visual inspection of the sample the few large grains that were required to be removed did appear

to be anomalously large grains and not instance where the XRCT was considering interconnected grains to be one.

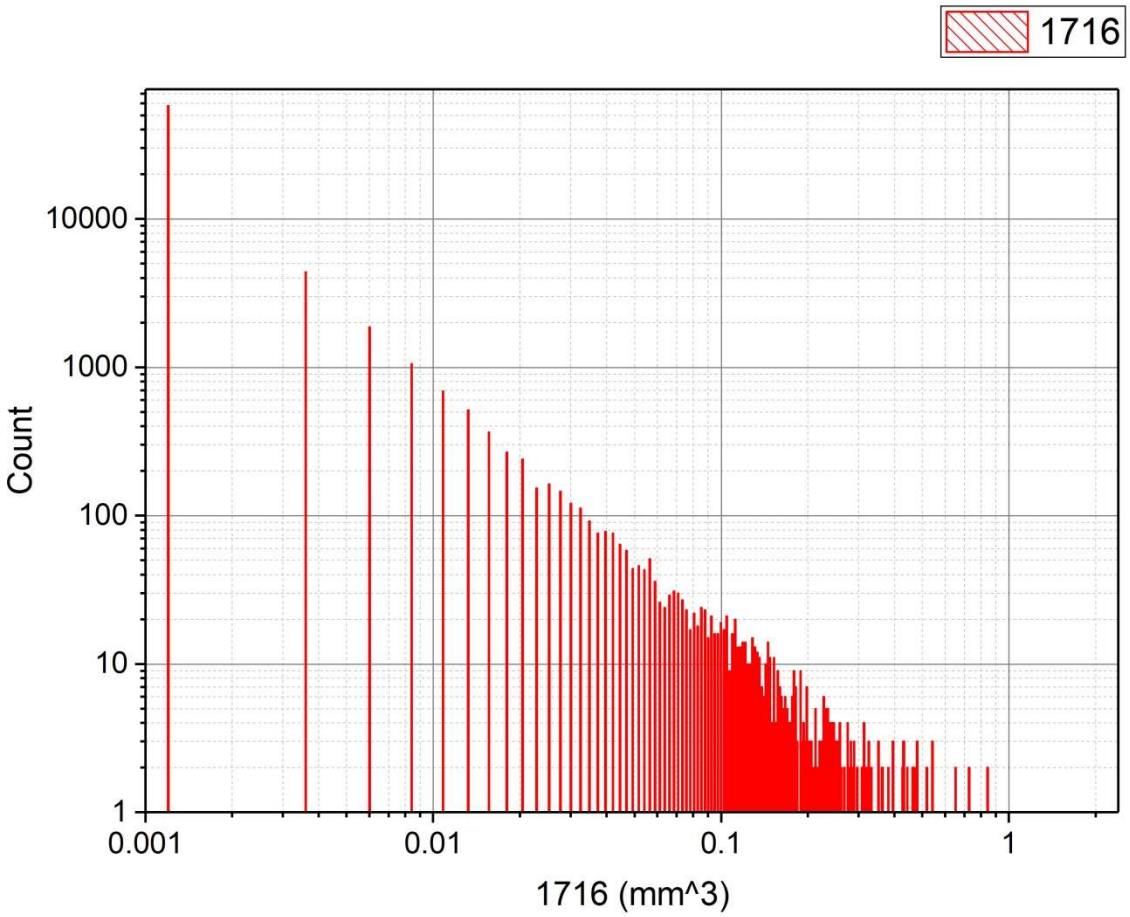

Figure 5.65 Grain size distribution of ore grains within sample 1716. Two large data points were removed to allow for a better visualization of size distribution. Data was separated into 1000 bins.

5.3.3 Shape Analysis Graphs

Shape analysis graphs were created to visualize trends with regards to the overall shape of ore grains and the types of ore deposits that they originated from. To create these graphs, three pieces of data were extracted from the XRCT data using the Avizo 3D data analysis software. These are the 3D volumes, long axis lengths, and short axis lengths for each ore grain within each sample. The long and short axes were extracted in

the form of diameters, so each of those values was then converted to a radius. Using this datum, the three values were plotted on a 3D graph where the long and short radii represented the x and y axes and the 3D volume represented the z axis. What follows in figures 5.66 through 5.75 are the graphs for each of the samples; the red dots represent the data points for every ore grain within the sample, the blue dots represent an ideal spherical shape, and the pink and green dots represent increasingly more elongated ellipsoidal shapes. Table 5.1 displays the percentages of the shapes within each sample. The 1 to less than 1.5 column represent spheroidal shapes, the 1.5 to less than 2.5 column a 2:1 elongated shape, and 2.5 and greater column a 4:1 elongated shape.

Sample Name	Aspect Ratio %		
	1 to <1.5	≥1.5 to <2.5	≥2.5
EG-181	78.30	20.52	1.17
Eagle-1	54.96	41.70	3.34
DC	38.75	46.81	14.44
Bag-1	55.05	41.24	3.71
V-1	51.89	40.53	7.58
O-219	39.48	49.42	11.10
SLC-55	41.89	52.38	5.73
SLC-2476	45.95	50.29	3.75
MVT-1	50.42	44.42	5.16
1716	37.37	54.74	7.88

Table 5.1 Percentages of aspect ratio ranges grains within each sample. The aspect ratio range of 1 to <1.5 represent spheroidal grains, ≥1.5 to <2.5 are 2:1 shaped grains, and ≥2.5 are 4:1 shaped grains.

EG-181

The distribution of shapes within EG-181 correspond most significantly to spherical shapes, with 78 % falling into the classification of spheroidal and 22 % being elongated to some degree (fig. 5.66 and Table 5.1). The vast majority of the elongated grains would fall within the 2:1 classification rather than the 4:1.

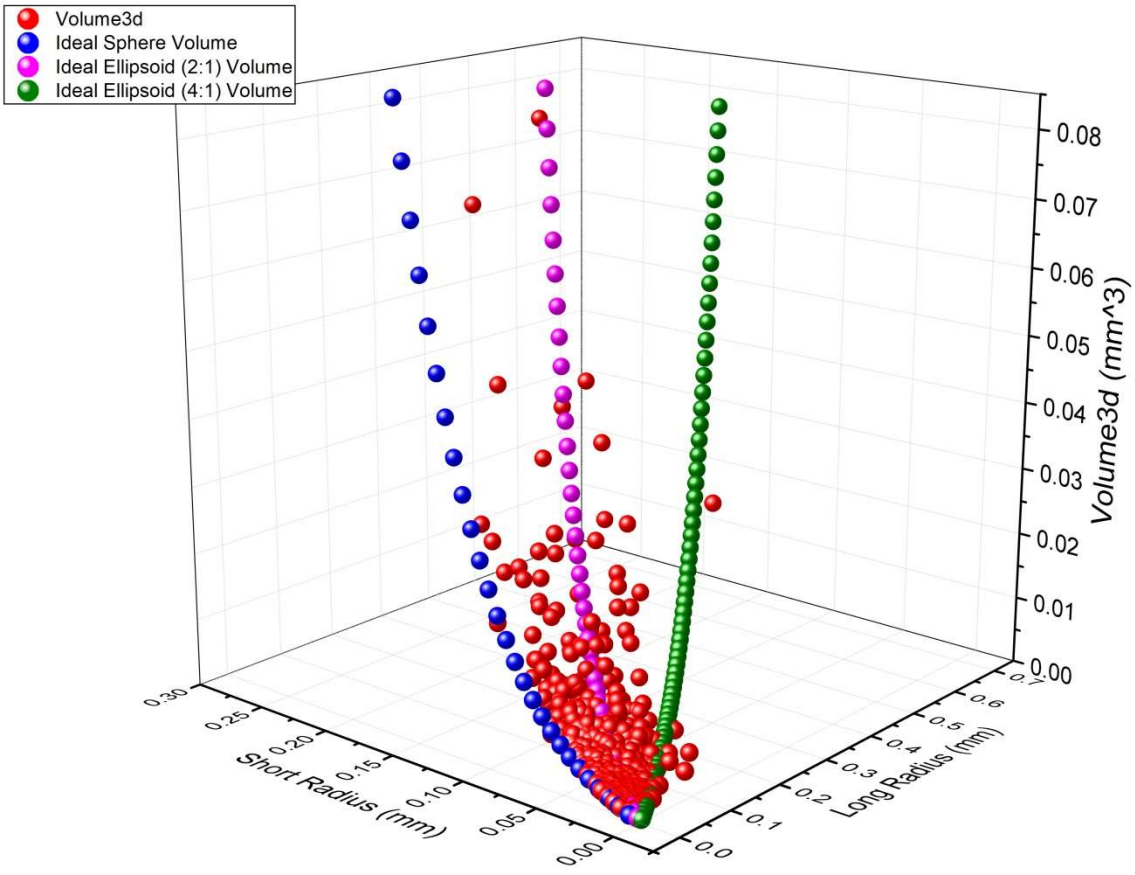

Figure 5.66 Shape analysis graph plotting the long and short radius against the 3D volume for sample Eagle-1. Ideal shape distributions appear as the blue, pink, and green data points.

Eagle-1

The distribution of shapes within Eagle-1 corresponds to a mixture of grain shapes, with 55 % falling into the classification of spheroidal and 45 % being elongated

to some degree (fig. 5.67 and Table 5.1). Most of the elongated grains would fall within the 2:1 classification rather than the 4:1.

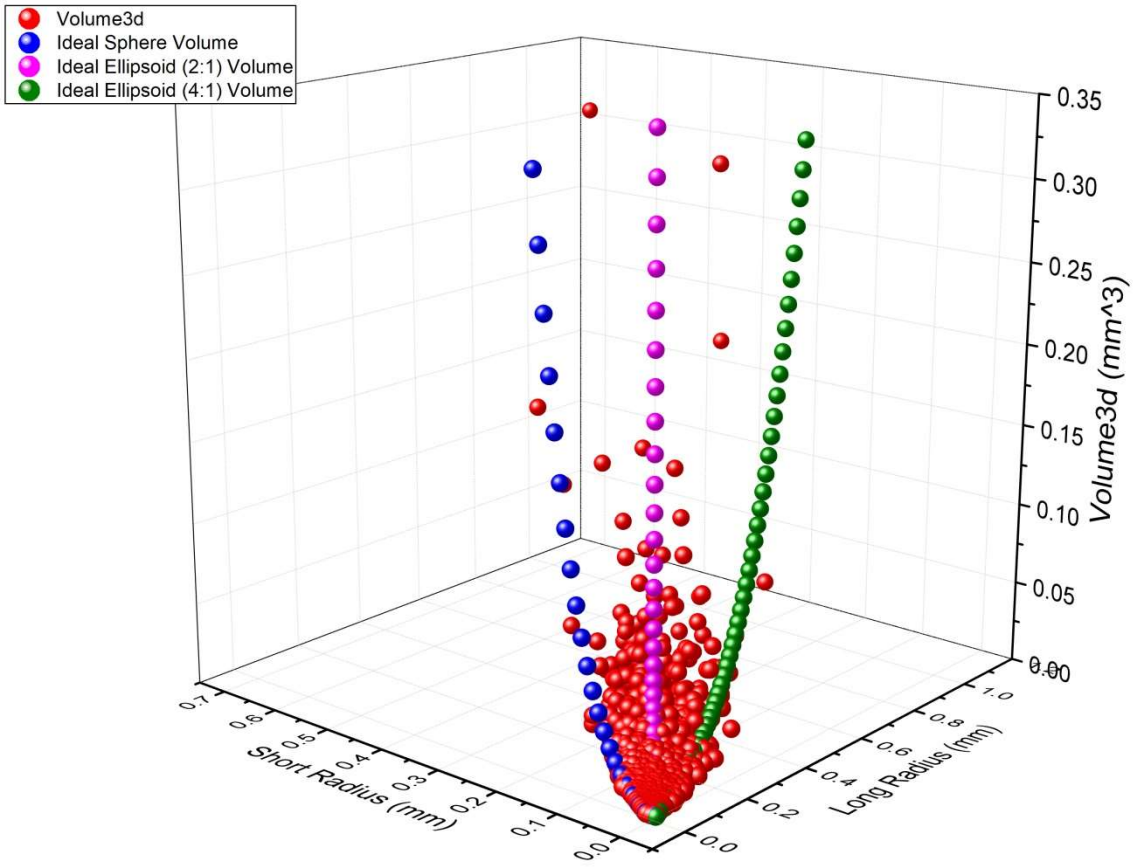

Figure 5.67 Shape analysis graph plotting the long and short radius against the 3D volume for sample Eagle-1. Ideal shape distributions appear as the blue, pink, and green data points.

DC

The distribution of shapes within DC correspond more significantly to elongated shapes, with 61 % falling into the classification of ellipsoidal and 39 % being spheroidal to some degree (fig. 5.68 and Table 5.1). Most of the elongated grains fall within the 2:1 classification but it is worth noting that 14 % of the total number of grains falls into the 4:1 category, which is the highest percentage of 4:1 grains of any of the samples.

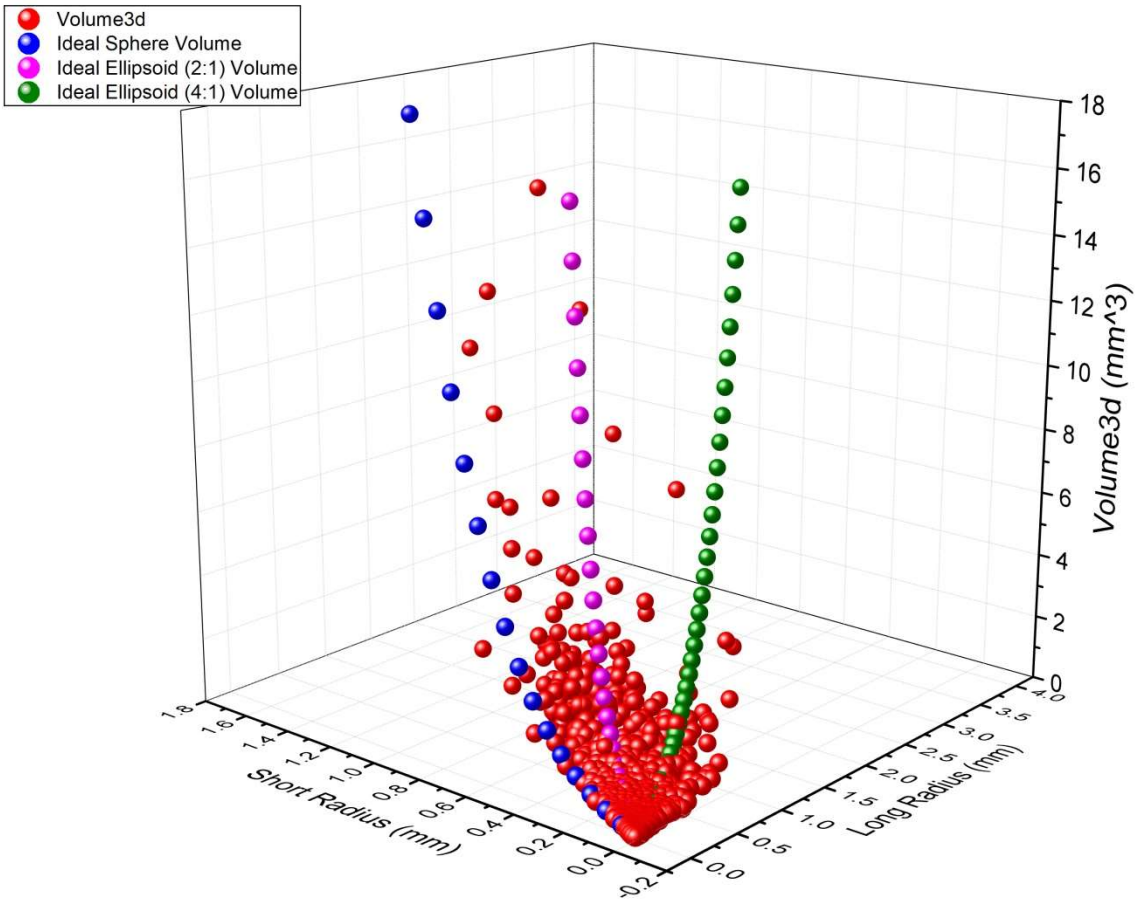

Figure 5.68 Shape analysis graph plotting the long and short radius against the 3D volume for sample DC. Ideal shape distributions appear as the blue, pink, and green data points.

Bag-1

The distribution of shapes within Bag-1 corresponds to a mixture of grain shapes, with 55 % falling into the classification of spheroidal and 45 % being elongated to some degree (fig. 5.69 and Table 5.1). Many of the elongated grains would fall within the 2:1 classification rather than the 4:1.

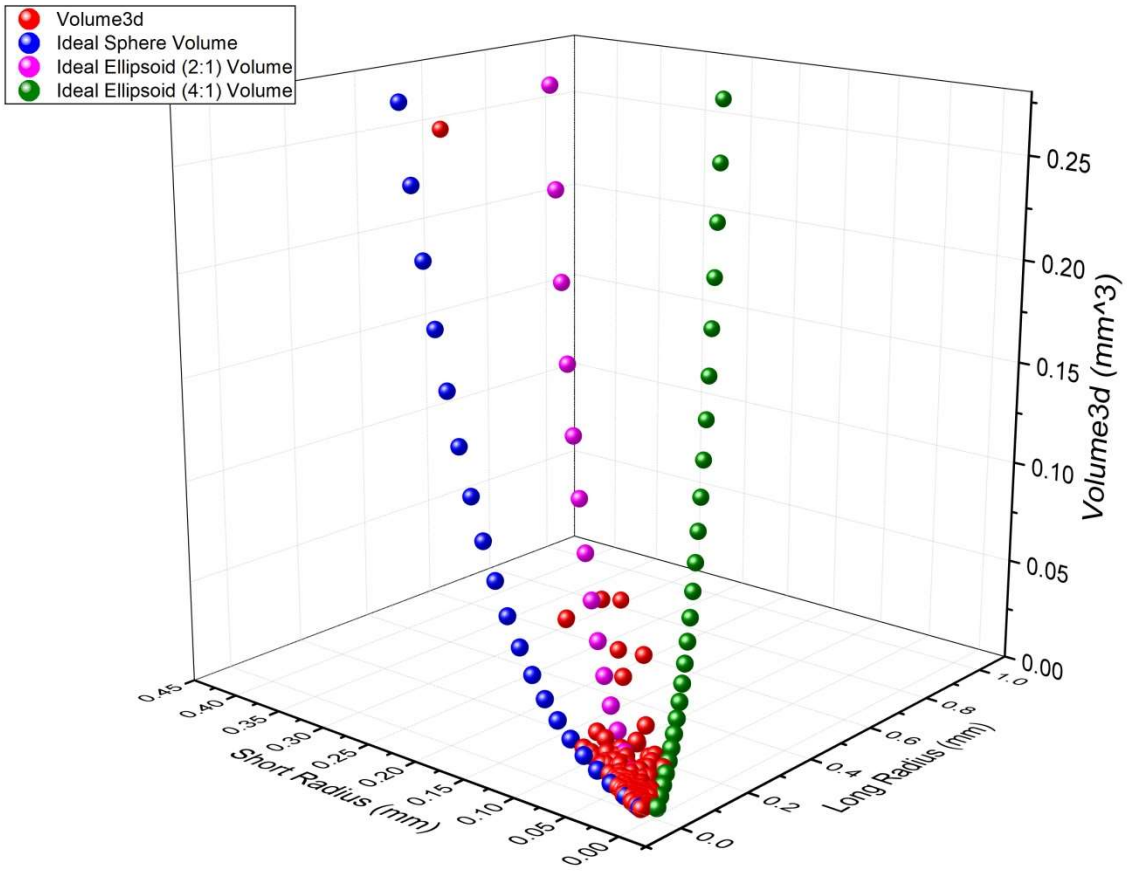

Figure 5.69 Shape analysis graph plotting the long and short radius against the 3D volume for sample Bag-1. Ideal shape distributions appear as the blue, pink, and green data points.

V-1

The distribution of shapes within V-1 corresponds to an almost even mixture of grain shapes, with 52 % falling into the classification of spheroidal and 48 % being elongated to some degree (fig. 5.70 and Table 5.1). While most of the elongated grains would fall within the 2:1 classification (84 %) there are still 16 % of those elongated grains that are classified as 4:1.

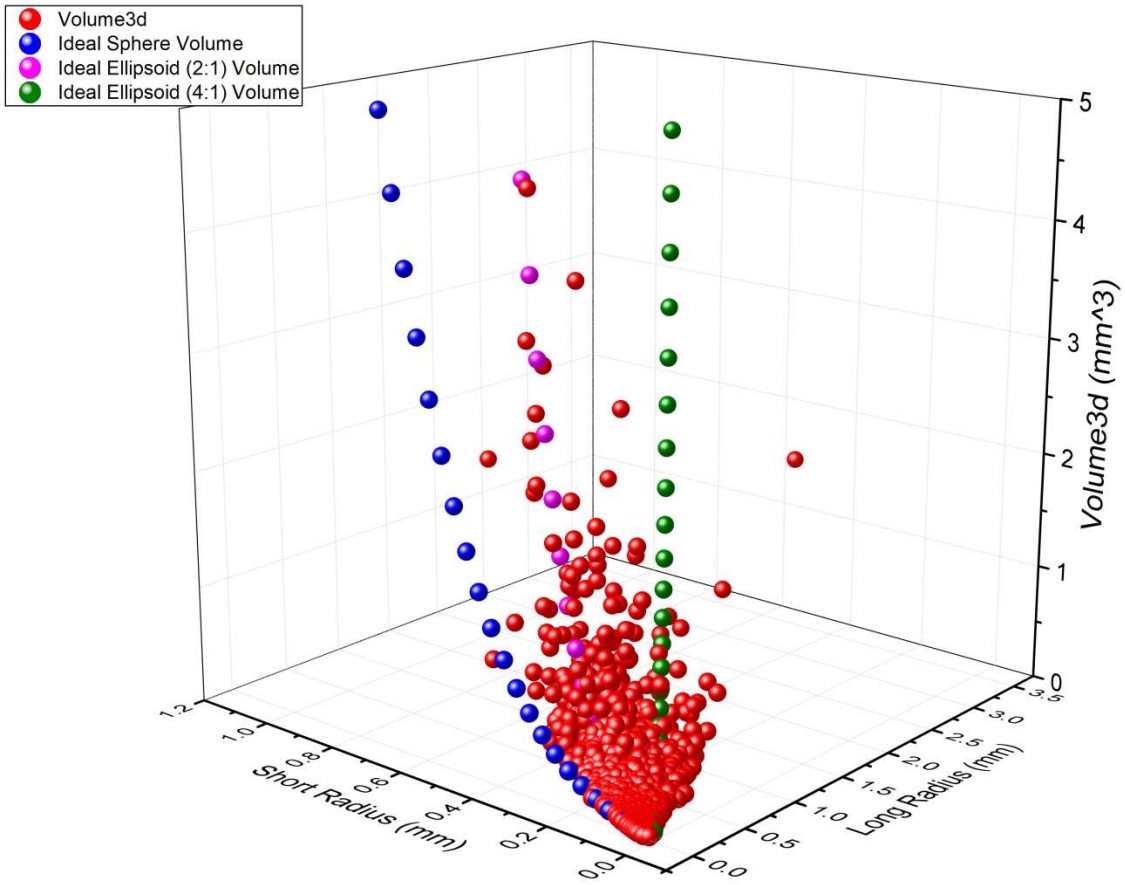

Figure 5.70 Shape analysis graph plotting the long and short radius against the 3D volume for sample V-1. Ideal shape distributions appear as the blue, pink, and green data points.

O-219

The distribution of shapes within O-219 correspond more significantly to elongated shapes, with 60 % falling into the classification of ellipsoidal and 40 % being spheroidal to some degree (fig. 5.71 and Table 5.1). Most of the elongated grains fall within the 2:1 classification (82 %) but it is worth noting that 18 % of the ellipsoidal grains fall into the 4:1 category.

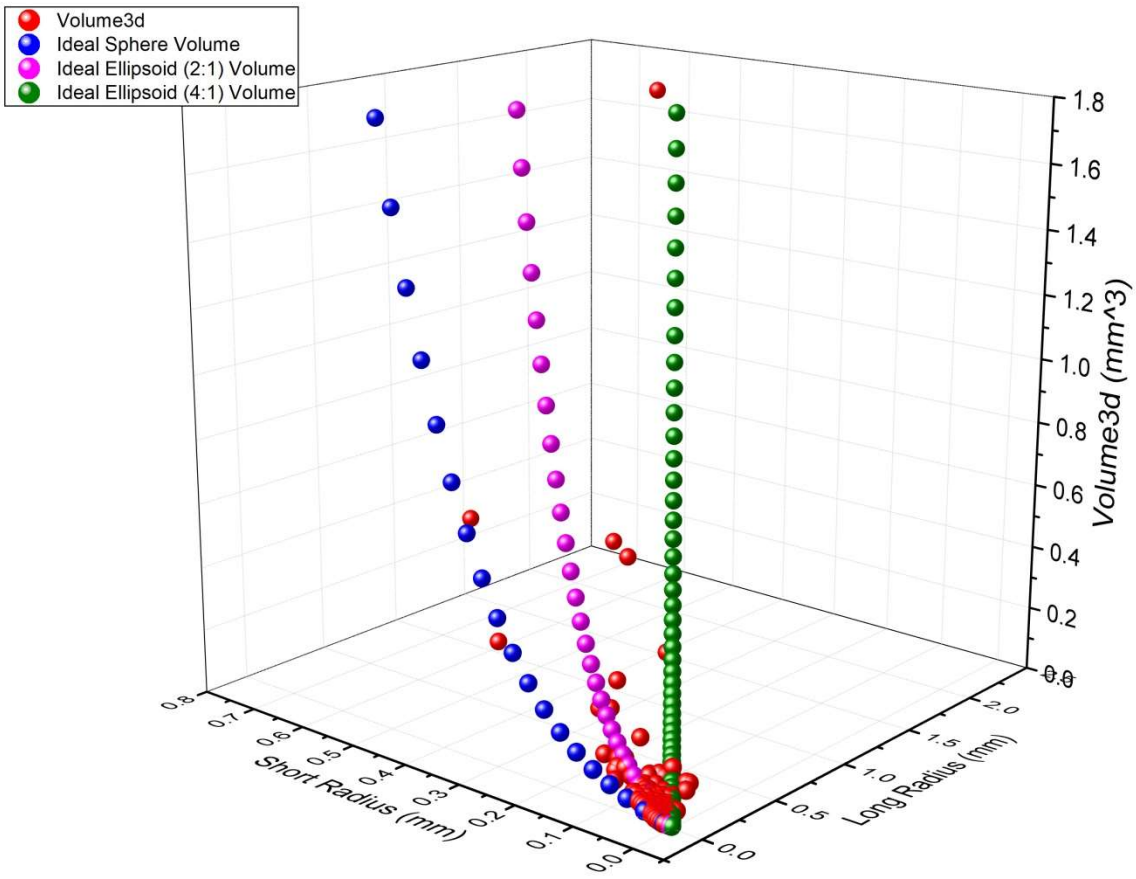

Figure 5.71 Shape analysis graph plotting the long and short radius against the 3D volume for sample O-219. Ideal shape distributions appear as the blue, pink, and green data points.

SLC-55

The distribution of shapes within SLC-55 correspond slightly more to elongated shapes, with 58 % falling into the classification of ellipsoidal and 42 % being spheroidal to some degree (fig. 5.72 and Table 5.1). Many of the elongated grains would fall within the 2:1 classification rather than the 4:1.

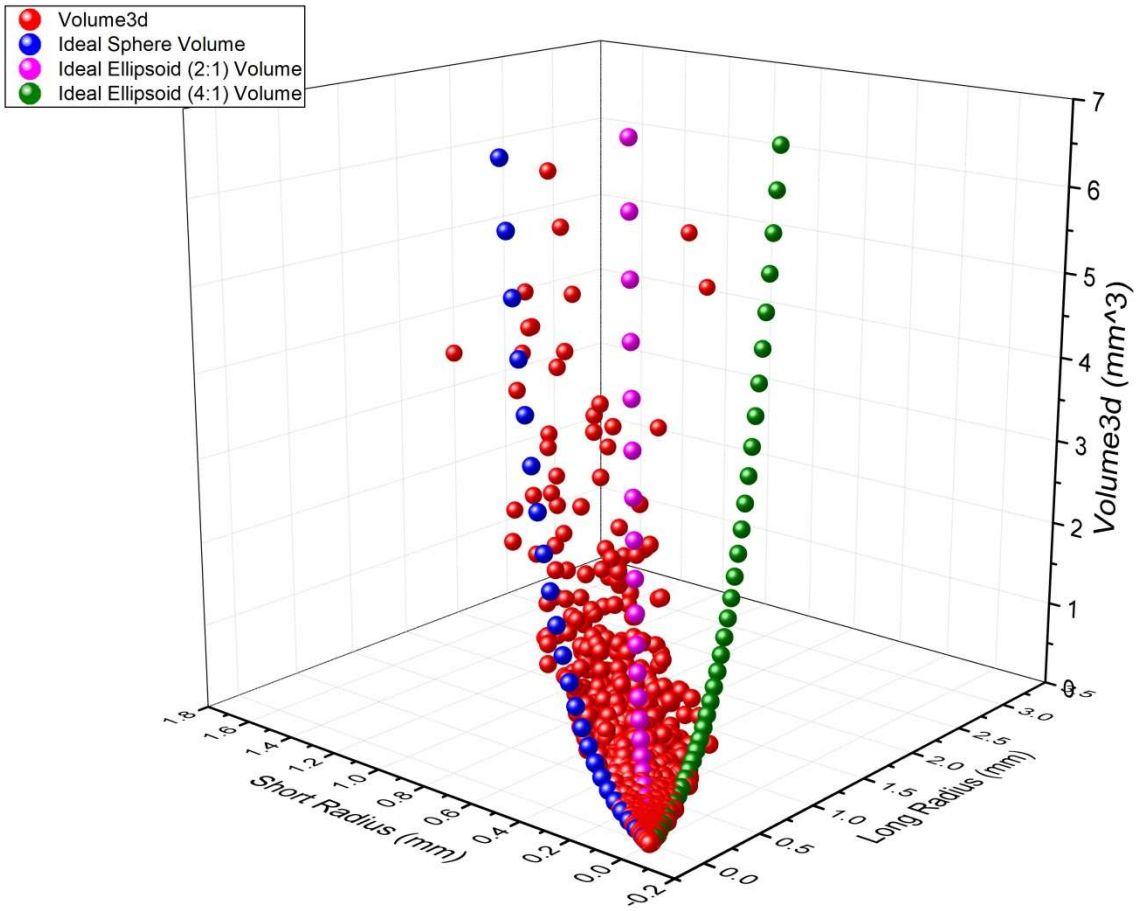

Figure 5.72 Shape analysis graph plotting the long and short radius against the 3D volume for sample SLC-55. Ideal shape distributions appear as the blue, pink, and green data points

SLC-2476

The distribution of shapes within SLC-2476 correspond to an almost even mixture of grain shapes, with 54 % falling into the classification of ellipsoidal and 46 % being spheroidal to some degree (fig. 5.73 and Table 5.1). Most of the elongated grains would fall within the 2:1 classification rather than the 4:1.

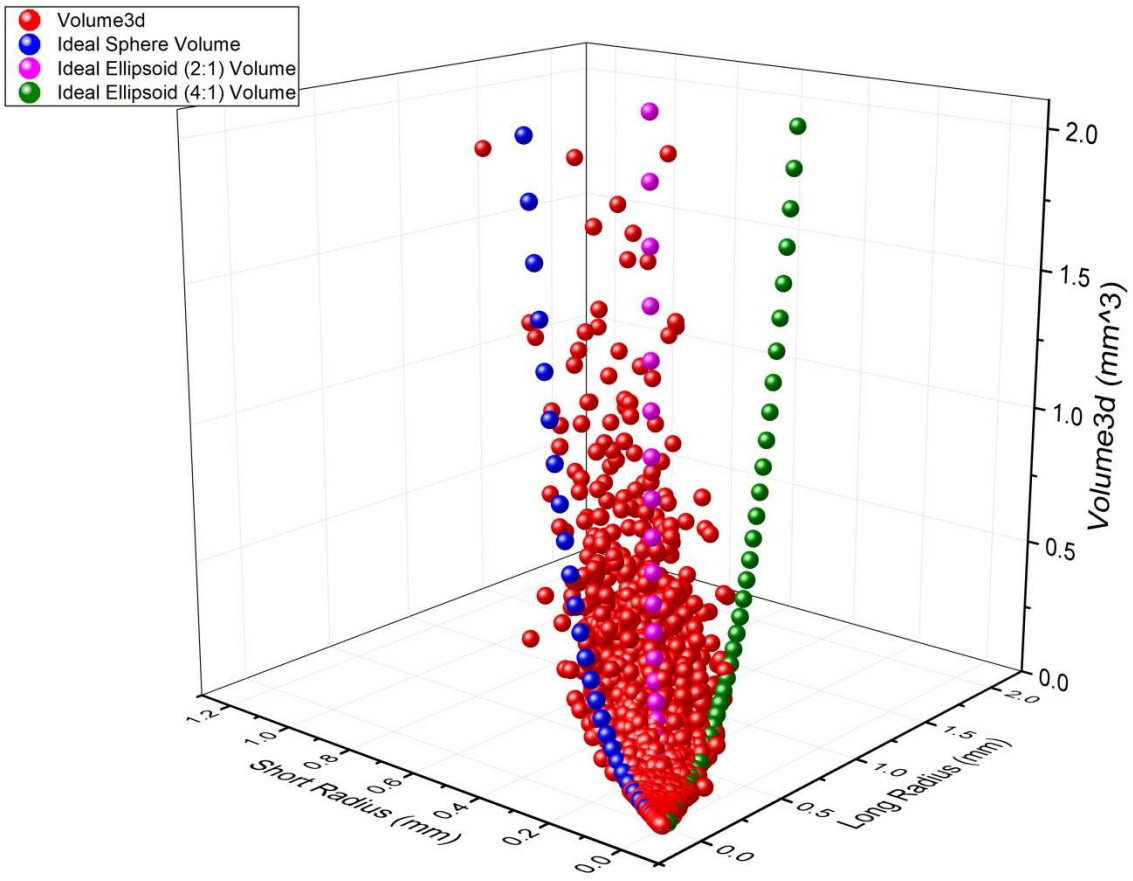

Figure 5.73 Shape analysis graph plotting the long and short radius against the 3D volume for sample SLC-2476. Ideal shape distributions appear as the blue, pink, and green data points

MVT-1

The distribution of shapes within MVT-1 also corresponds to an almost even mixture of grain shapes, with 50.4 % falling into the classification of spheroidal and 49.6% being ellipsoidal to some degree (fig. 5.74 and Table 5.1). Many of the elongated grains would fall within the 2:1 classification (90 %), but 10 % of those elongated grains do correspond to the 4:1 classification.

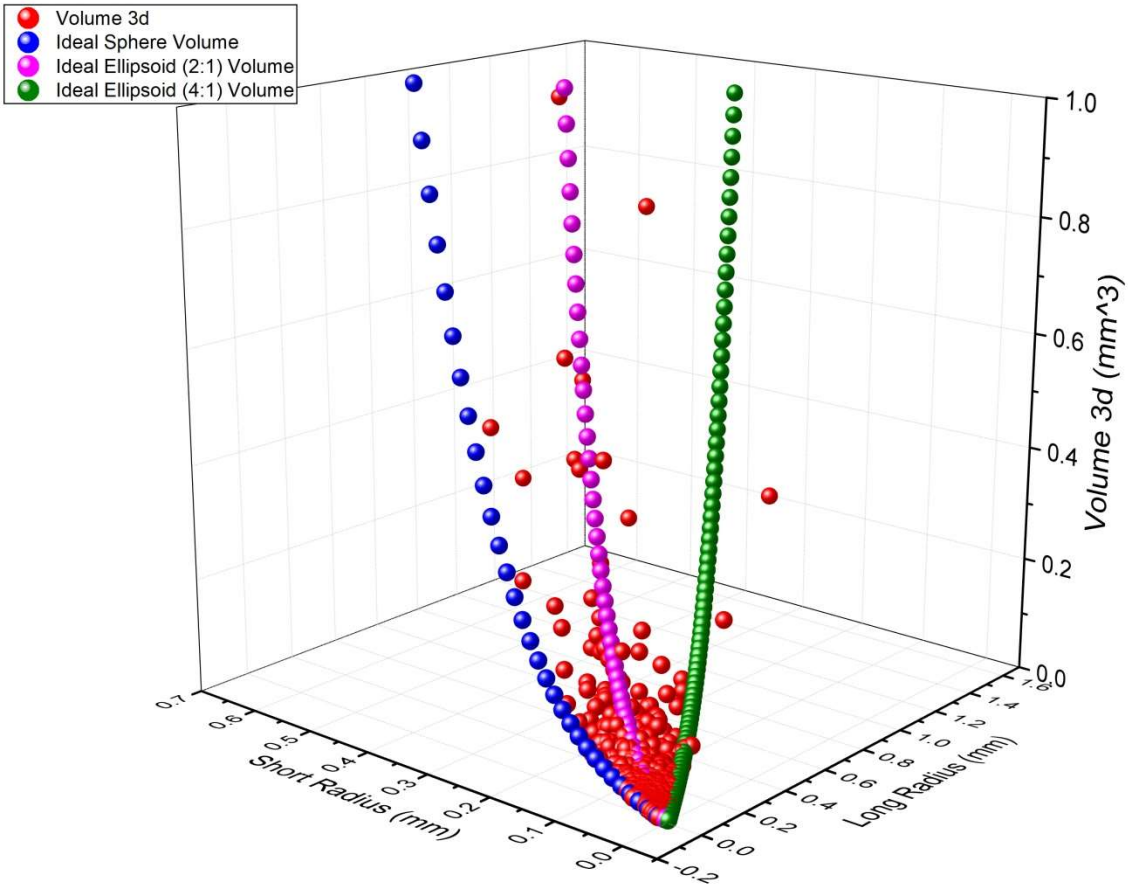

Figure 5.74 Shape analysis graph plotting the long and short radius against the 3D volume for sample MVT-1. Ideal shape distributions appear as the blue, pink, and green data points.

1716

The distribution of shapes within 1716 corresponds most significantly to elongated shapes, with 63 % falling into the classification of ellipsoidal and 37 % being spheroidal to some degree (fig. 5.75 and Table 5.1). Most of the elongated grains fall within the 2:1 classification. Of all the elongated grains 87 % of them correspond to the 2:1 classification, while 13 % of the elongated grains can be classified as a 4:1 grain.

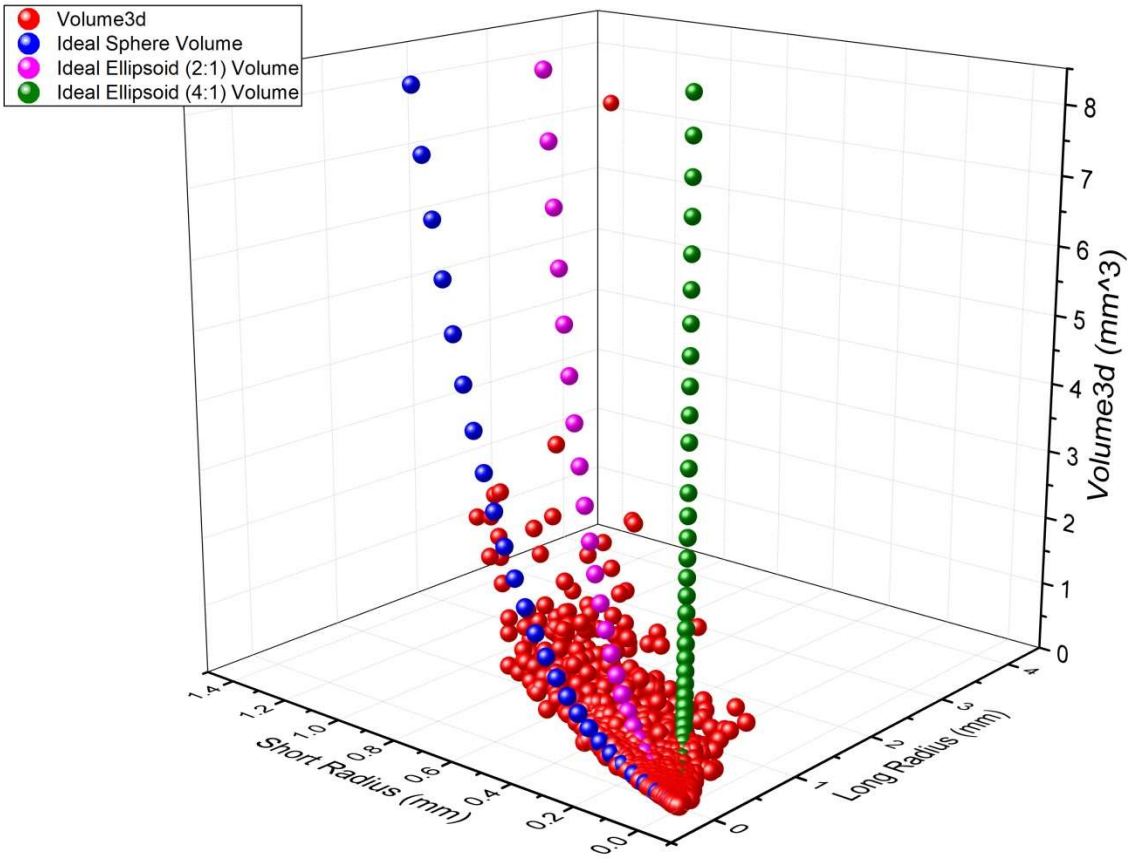

Figure 5.75 Shape analysis graph plotting the long and short radius against the 3D volume for sample 1716. Ideal shape distributions appear as the blue, pink, and green data points.

5.3.4 Ore Grain Long Axis Orientation Vector Graphs

The orientation of the long axis for ore grains within these samples was of interest as this information could inform on whether there was any potential flow direction to the fluids or magmas present as ore minerals were crystalizing. To create the grain orientation vector graphs six pieces of data were exported from the XRCT scans using the Avizo 3D data analysis software. The first three pieces of data were simply the x, y, and z coordinate data so that each individual grain within a sample could be plotted in its appropriate place in space. The other three pieces of data were x, y, and z components of the eigenvector that represents the long axis of the ore grains. This data allowed for the

location of every ore grain within a sample to be plotted in 3D space with an attached arrow that would point the in direction that the long axis of each grain propagated.

Most of the samples scanned with XRCT contained far too many data points so that graphs containing an entire data set are simply solid cylinders of symbols. To display the data effectively, the datasets were initially sorted by aspect ratios. As the datasets for certain aspect ratio ranges for some samples were still too large, they were subsequently sorted again, this time by volume size of the ore grains. 3D vector graphs were created for these data subsets and analyzed to determine if any patterns in ore grain long axis orientations are present.

EG-181

For sample EG-181 a representative 3D vector graph is shown in figure 5.76. The graph displays a portion of the dataset that corresponds to ore grains that have an aspect ratio greater than 1 but less than or equal to 2. Figure 5.76 does not appear to show any preferred orientation for the ore grains and this figure is representative of every other subset of the data that also had vector graphs created and inspected.

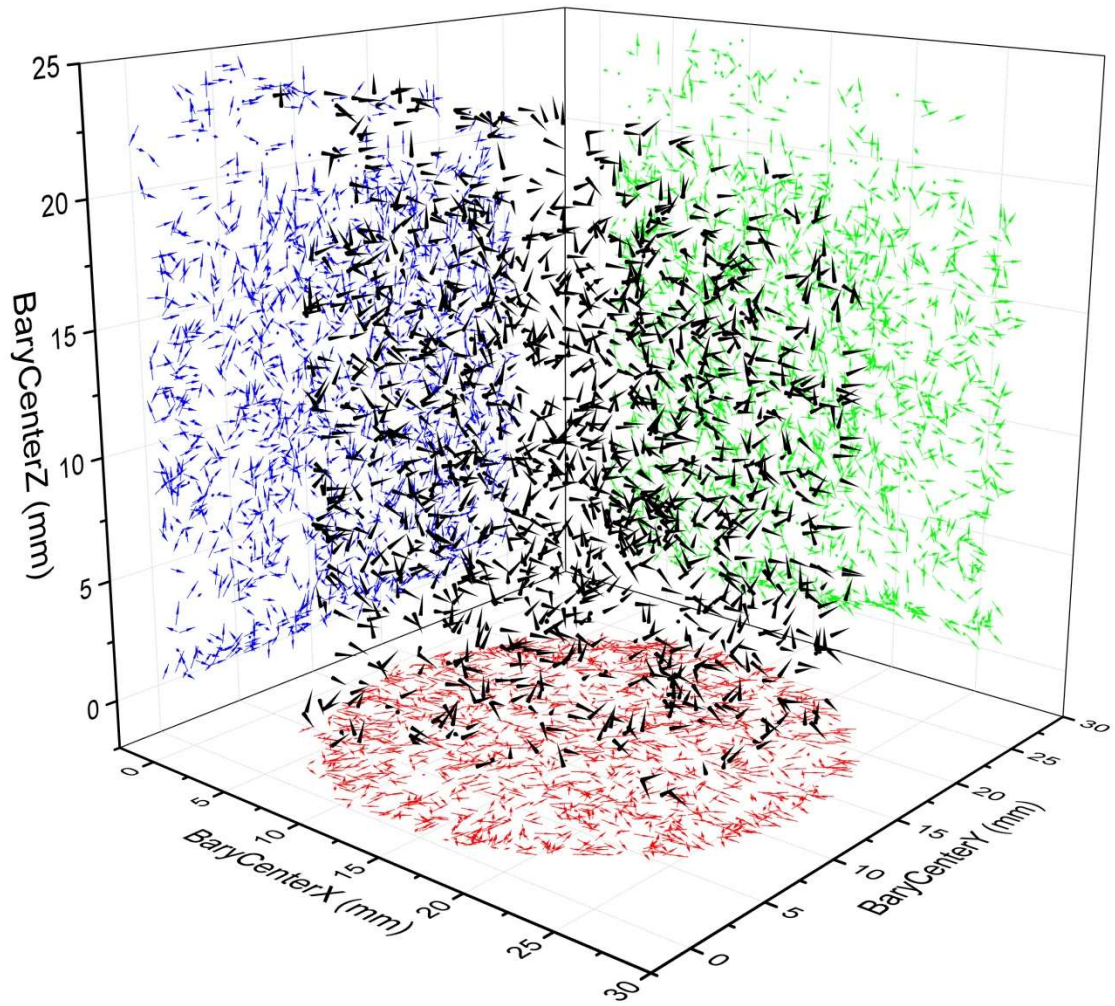

Figure 5.76 Vector graph of the long axis orientations of ore grains within sample EG-181; displaying a subset of grains with an aspect ratio greater than 1 and less than or equal to 2. This sample appears to be randomly oriented.

Eagle-1

For sample Eagle-1 (fig. 5.77) the graph displays a portion of the dataset that corresponds to ore grains that have an aspect ratio greater than 2 but less than or equal to 4. Figure 5.77 appears to display a preferred general orientation for the ore grains present in the z direction. This preferred "up, down" orientation can be seen throughout most of the data subsets that were created but is most pronounced within the subsets that contained the larger grain sizes.

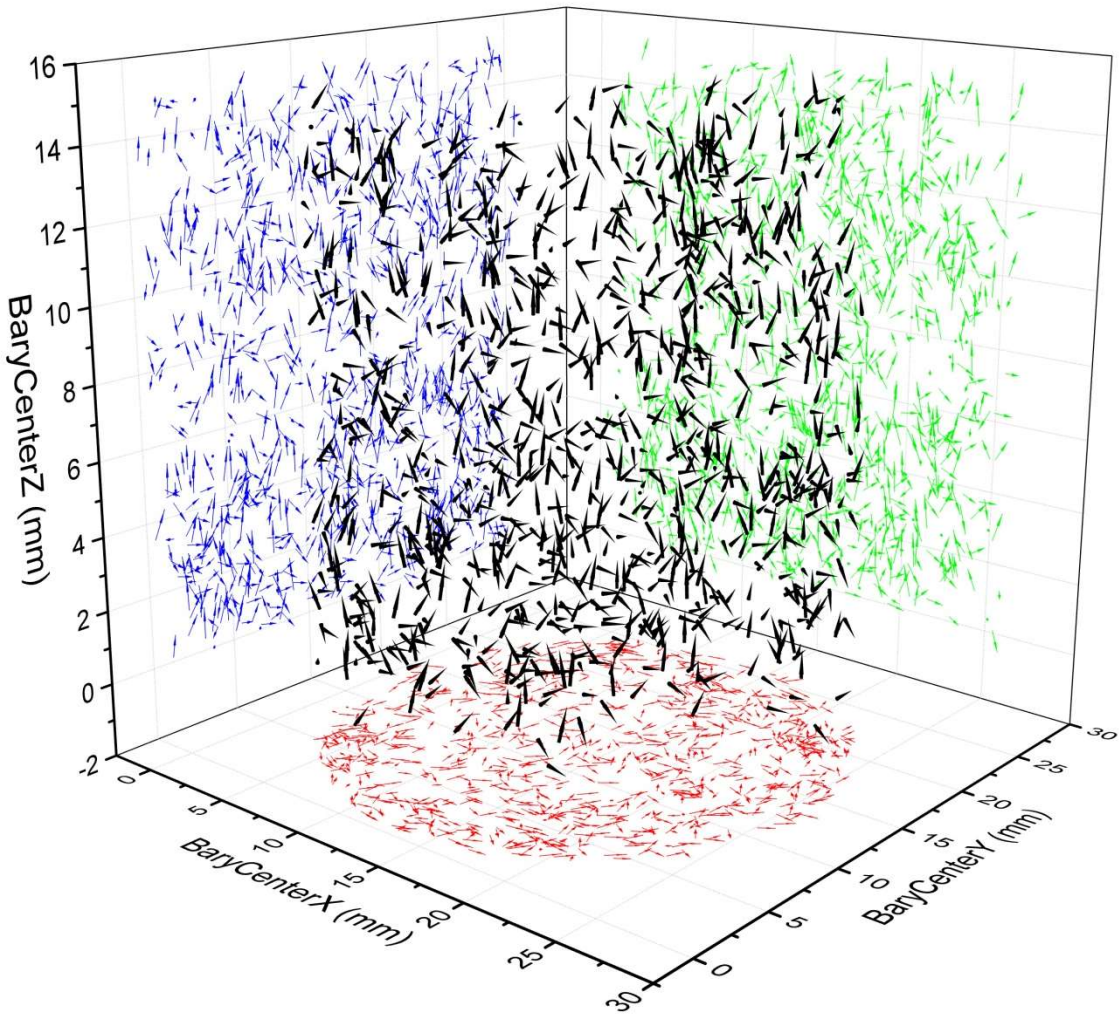

Figure 5.77 Vector graph of the long axis orientations of ore grains within sample Eagle-1; displaying a subset of grains with an aspect ratio greater than 2 and less than or equal to 4.

DC

A representative 3D vector graph for sample DC can be seen below (fig. 5.78). The graph displays a portion of the dataset that corresponds to ore grains that have an aspect ratio greater than 2 but less than or equal to 4. The graph in figure 5.78 displays a preferred orientation for the majority of ore grains in positive x and positive y direction. This preferred "diagonally rightward trending" orientation can be seen throughout most

of the data subsets that were created. It is most clearly seen within the subsets that contained the small to medium sized grains that make up the rope-like feature near the bottom of the sample.

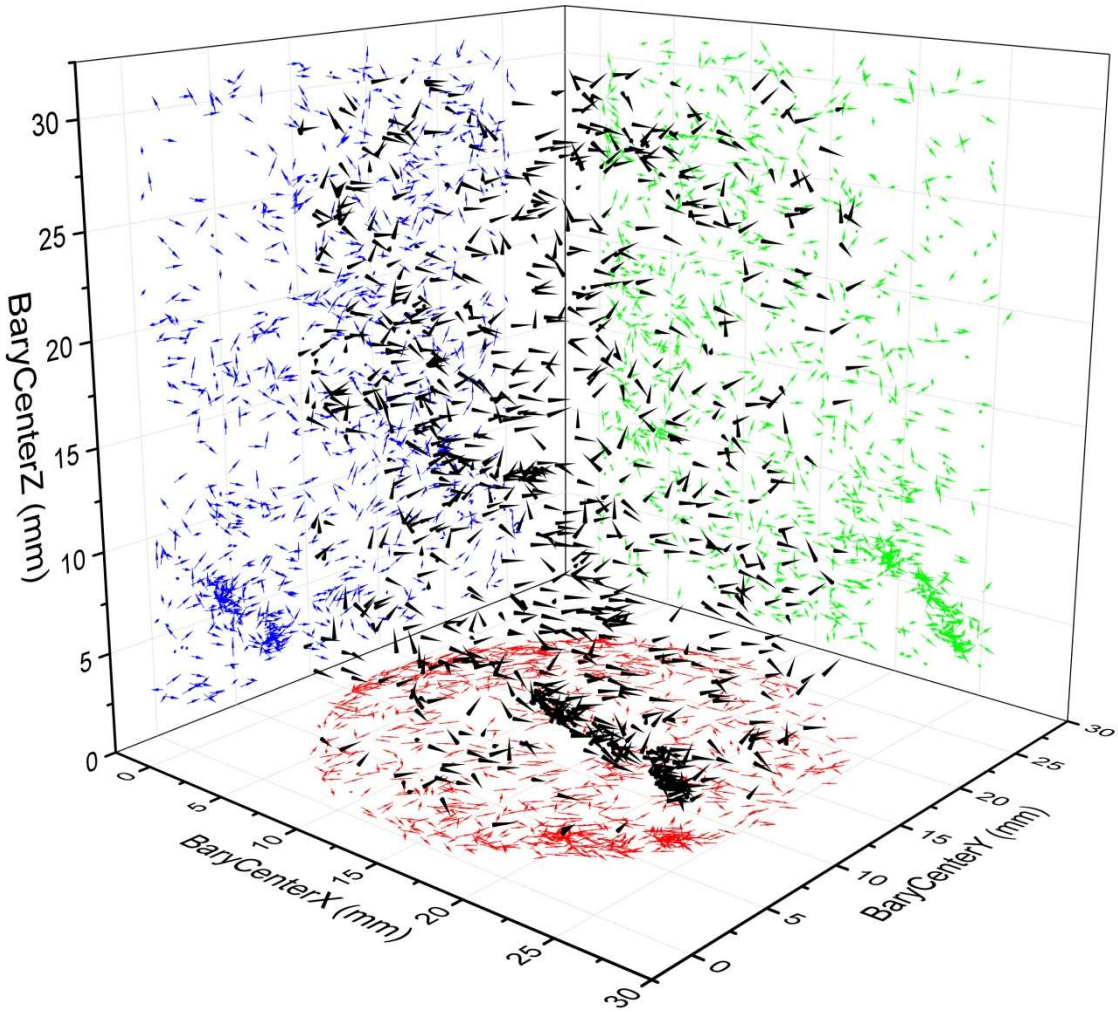

Figure 5.78 Vector graph of the long axis orientations of ore grains within sample DC; displaying a subset of grains with an aspect ratio greater than 2 and less than or equal to 4.

Bag-1

The graph for Bag-1 displays a portion of the dataset that corresponds to all ore grains that have an aspect ratio greater than 1 but less than or equal to 2. Overall, there

does not appear to be a preferred orientation to all the grains, but a planar feature can be observed most effectively by observing the light green (x, z) projection (fig. 5.79). This planar feature, when inspected using the (x, z) projection, appears to have a positive z orientation, and when inspecting the red (x, y) projection had a general orientation in the positive y direction. There are also a few clusters of grains that appear together, and these also have a preferred orientation in the positive x, y, and z directions.

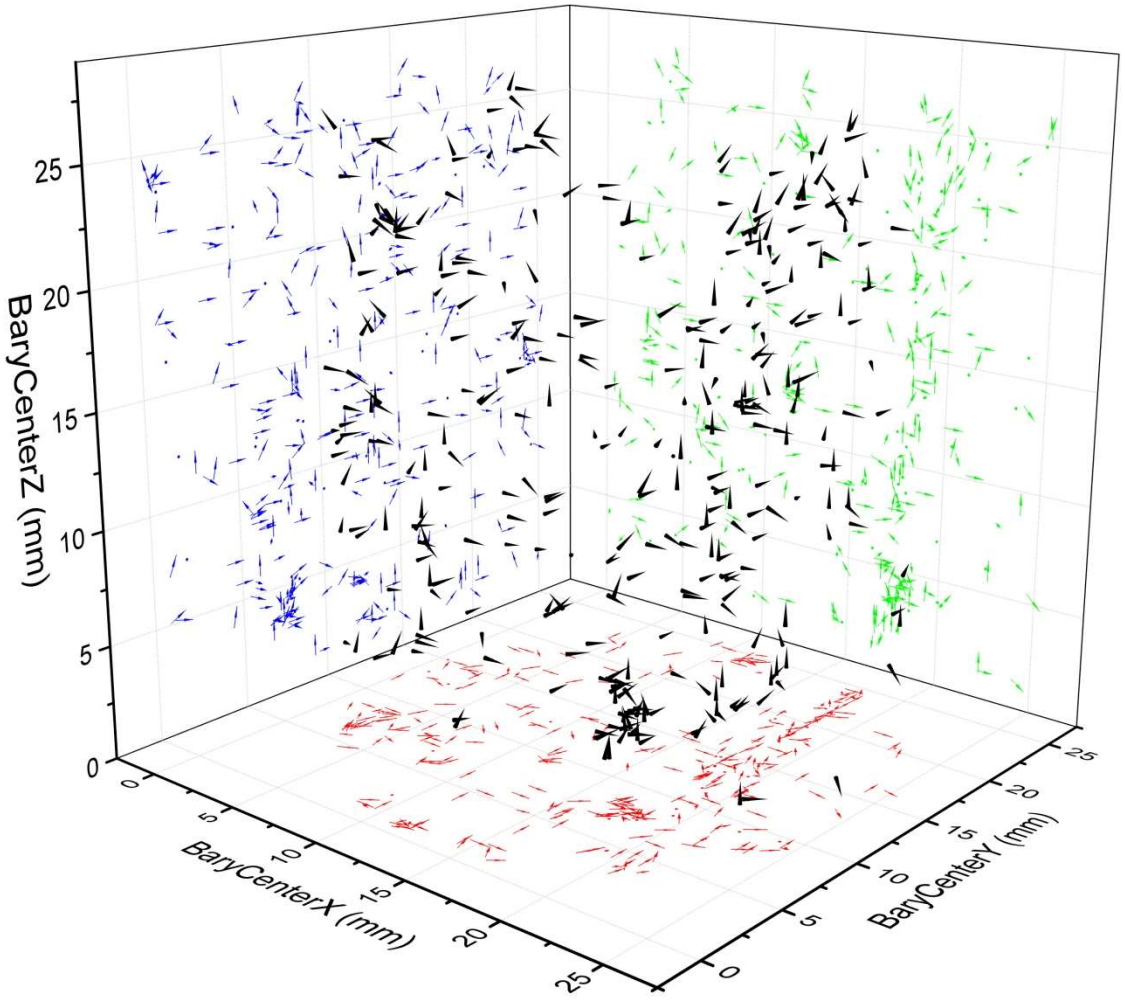

Figure 5.79 Vector graph of the long axis orientations of ore grains within sample Bag-1; displaying all grains with an aspect ratio greater than 1 and less than or equal to 2.

V-1

A representative 3D vector graph for sample V-1 can be seen below (fig. 5.80). The graph displays a portion of the dataset that corresponds to ore grains that have an aspect ratio greater than 2 but less than or equal to 4. The V-1 sample represents a highly altered portion of a porphyry deposit (fig. 5.5) and this can be seen in the almost spiral like pattern to the ore grain orientations. Figure 5.80 displays in portions a positive z and y orientation. In other regions of the sample there is a positive x orientation that is most easily observed in the red (x, y) projection.

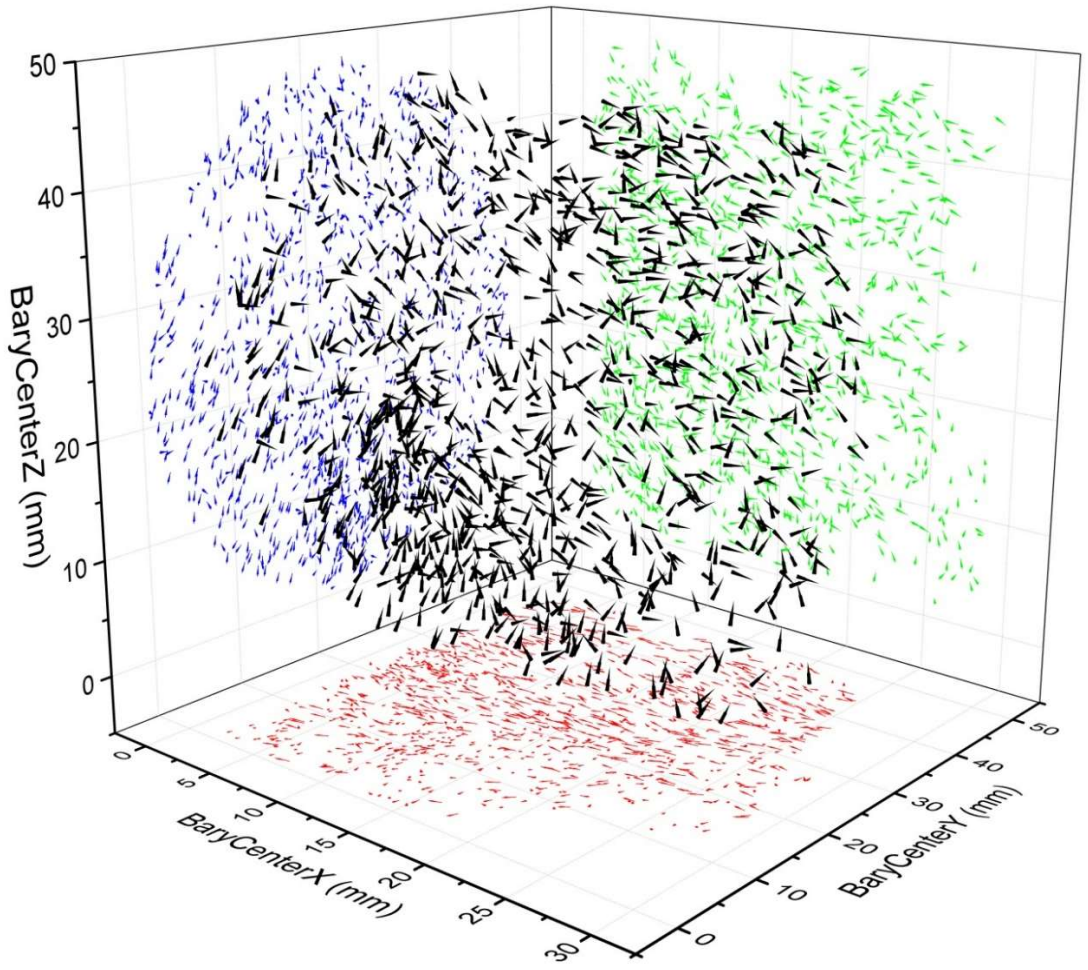

Figure 5.80 Vector graph of the long axis orientations of ore grains within sample V-1; displaying a subset of grains with an aspect ratio greater than 2 and less than or equal to 4.

O-219

For sample O-219 a representative 3D vector graph can be seen below (fig. 5.81). The graph displays a portion of the dataset that corresponds to all ore grains that have an aspect ratio greater than 1 but less than or equal to 2. Figure 5.81 does not appear to display a preferred orientation for all ore grains. However, there are several clusters of grains visible that all appear to share an overall orientation. The clusters all appear to have a positive trend in the x, y, and z directions.

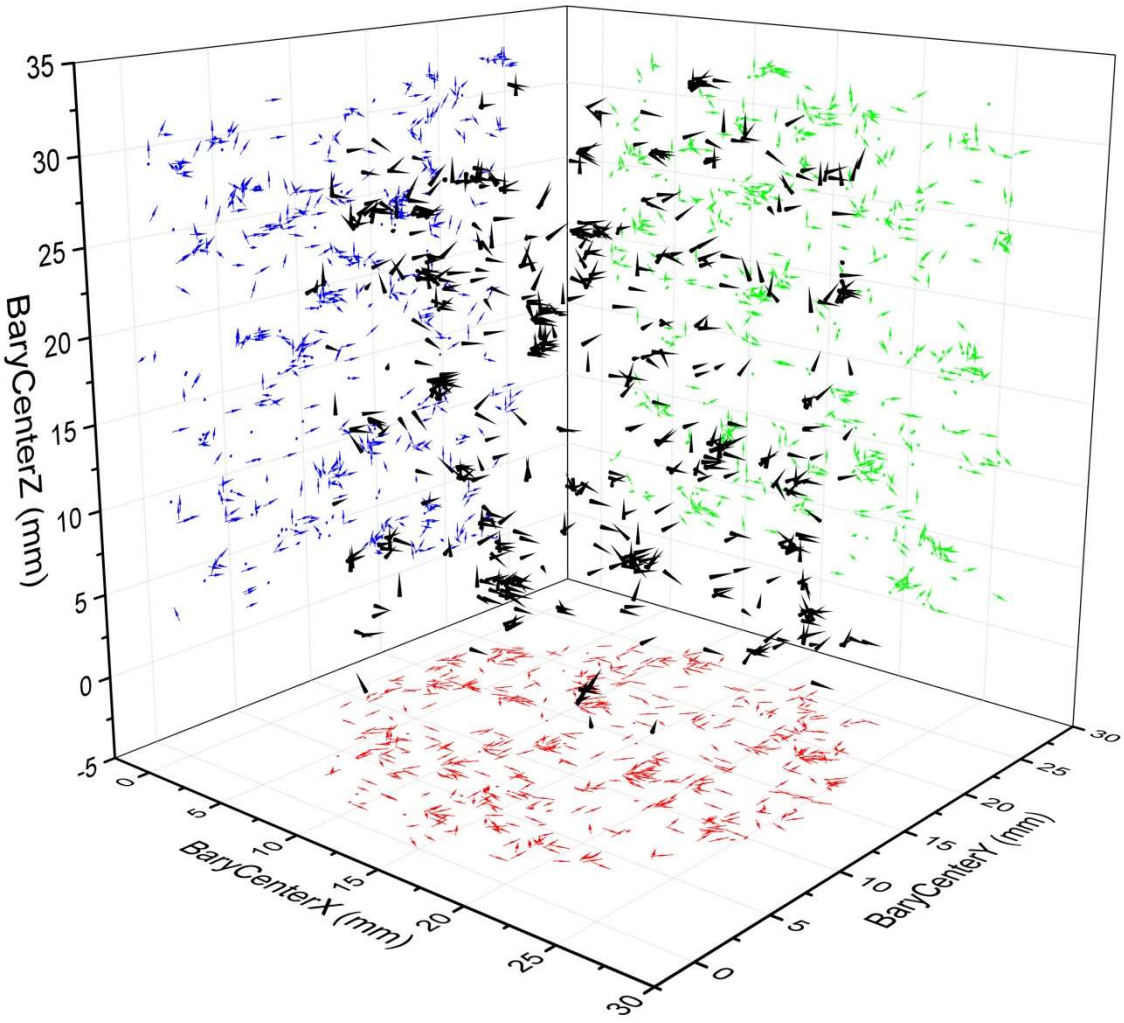

Figure 5.81 Vector graph of the long axis orientations of ore grains within sample O-219; displaying all grains with an aspect ratio greater than 1 and less than or equal to 2.

SLC-55

A representative 3D vector graph for sample SLC-55 can be seen in figure 5.82. The graph displays a portion of the dataset that corresponds to ore grains that have an aspect ratio greater than 1 but less than or equal to 2. All of subsets of data that were graphed display a preferred orientation of grains that point in the positive x direction.

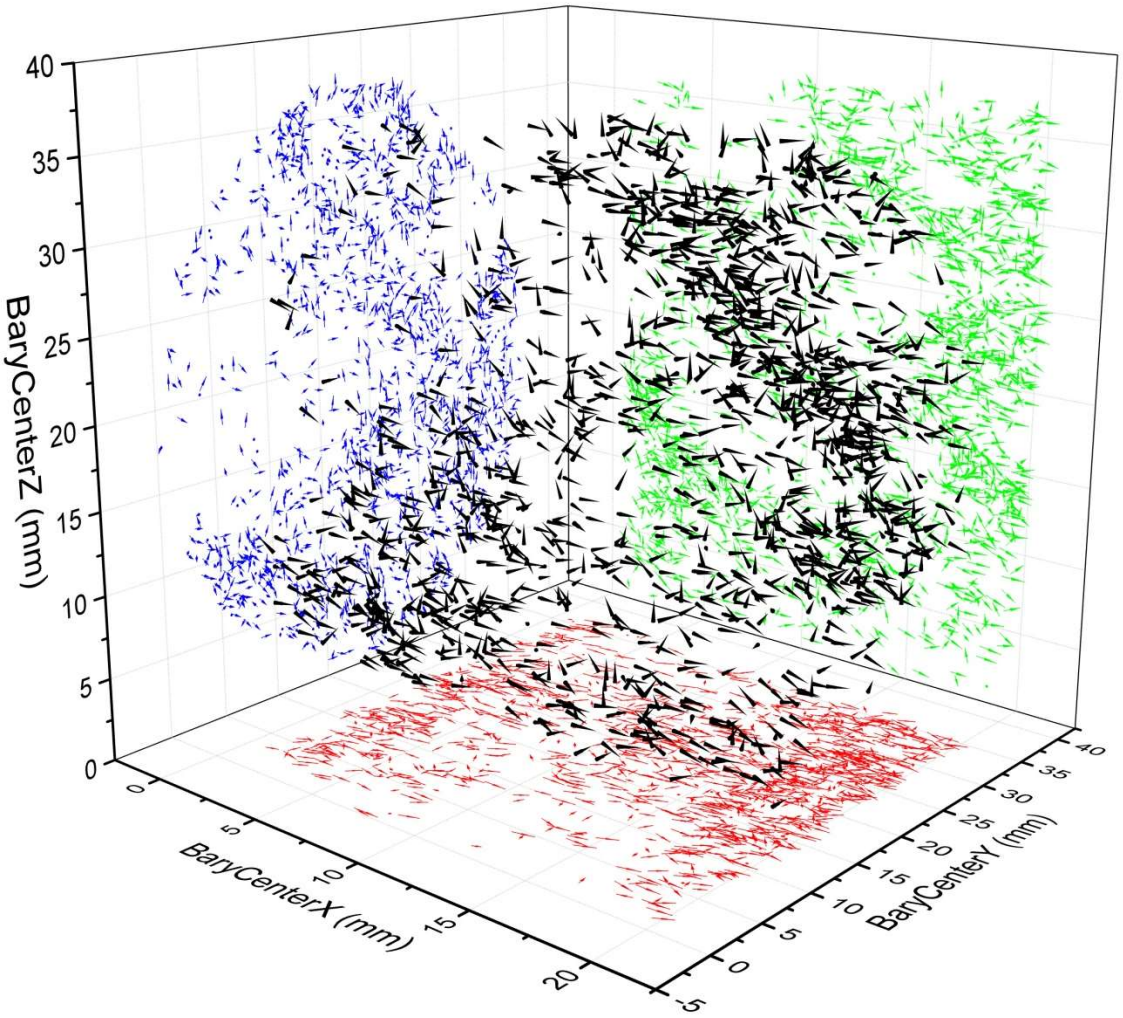

Figure 5.82 Vector graph of the long axis orientations of ore grains within sample SLC-55; displaying a subset of grains with an aspect ratio greater than 1 and less than or equal to 2.

SLC-2476

A representative 3D vector graph for sample SLC-2476 can be seen in figure 5.83. The graph displays a portion of the dataset that corresponds to ore grains that have an aspect ratio greater than 2 but less than or equal to 4. Most of the grains within this sample do not appear to share an orientation. However, there are two large clusters of grains; one which occurs near the bottom of the sample and the other that occurs near the top of the sample. Both clusters of grains share the same orientation which trends in the positive z and y directions. The trends are best observed by inspecting the blue (z, y) projection and the red (x, y) projection.

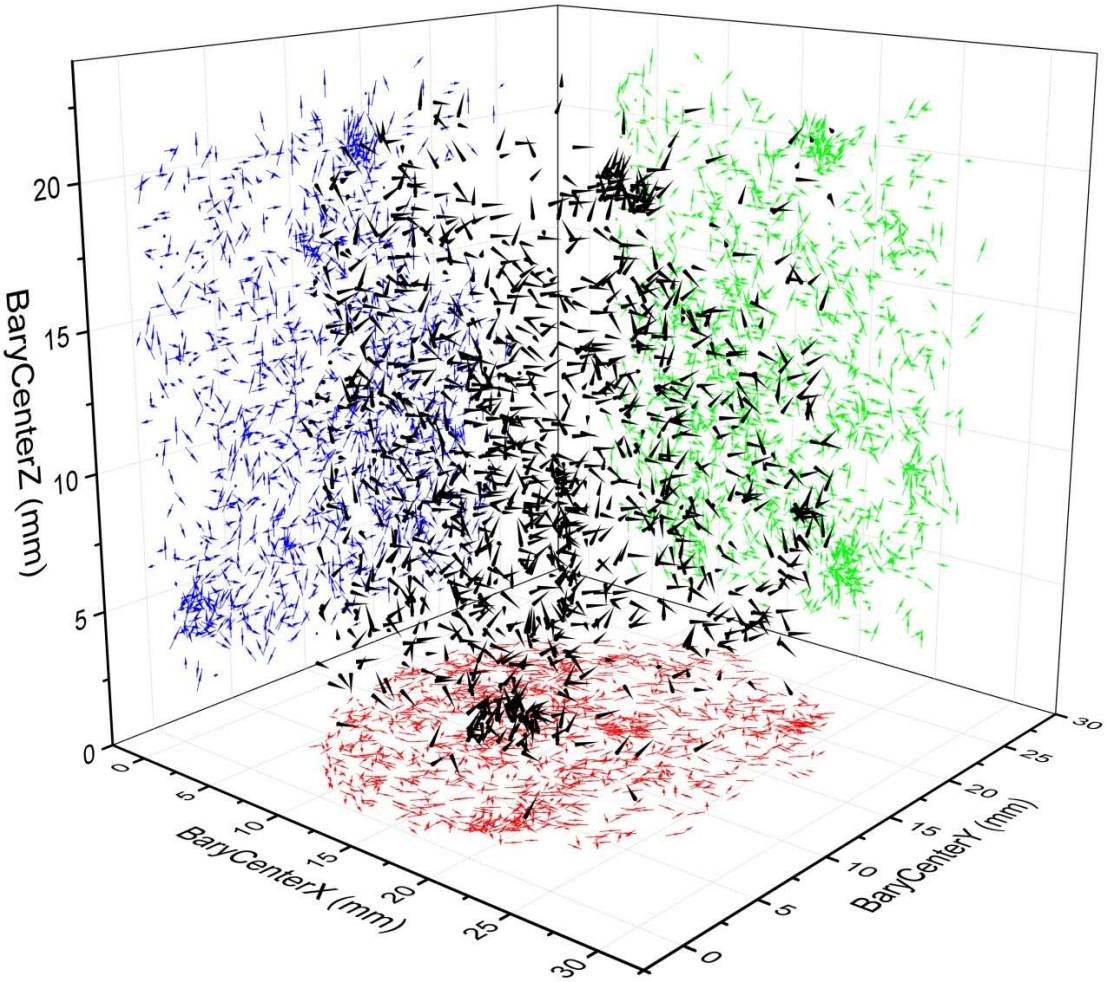

Figure 5.83 Vector graph of the long axis orientations of ore grains within sample SLC-2476; displaying a subset of grains with an aspect ratio greater than 2 and less than or equal to 4.

MVT-1

A representative 3D vector graph for sample MVT-1 can be seen below (fig. 5.84). The graph displays a portion of the dataset that corresponds to all ore grains that have an aspect ratio greater than 1 but less than or equal to 2. Figure 5.84 does not appear to display any preferred orientation for the ore grains present and that is representative of every subset of the data that was created and inspected.

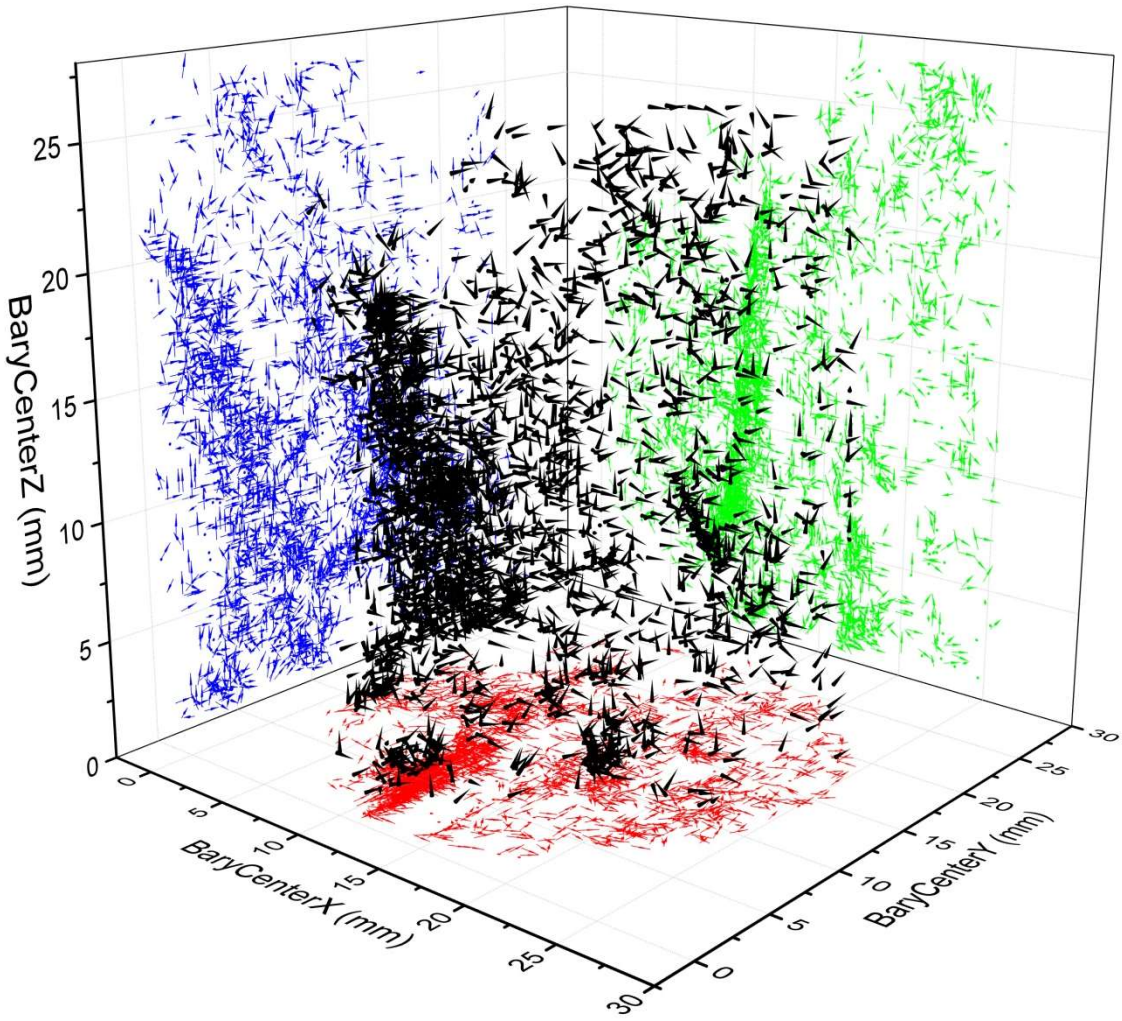

Figure 5.84 Vector graph of the long axis orientations of ore grains within sample MVT-1; displaying all grains with an aspect ratio greater than 1 and less than or equal to 2.

1716

For sample 1716 a representative 3D vector graph can be seen below (fig. 5.85). The graph displays a portion of the dataset that corresponds to ore grains that have an aspect ratio greater than 2 but less than or equal to 4. 1716 is a sample that originated from an SSC deposit and is stratiform in nature. Within the layers where the ore occurs there is an apparent preferred orientation in the positive x and y directions. There is a

portion of the sample where the ore is penetrating through otherwise ore-barren layers and within these areas there does not appear to be any preferred orientation.

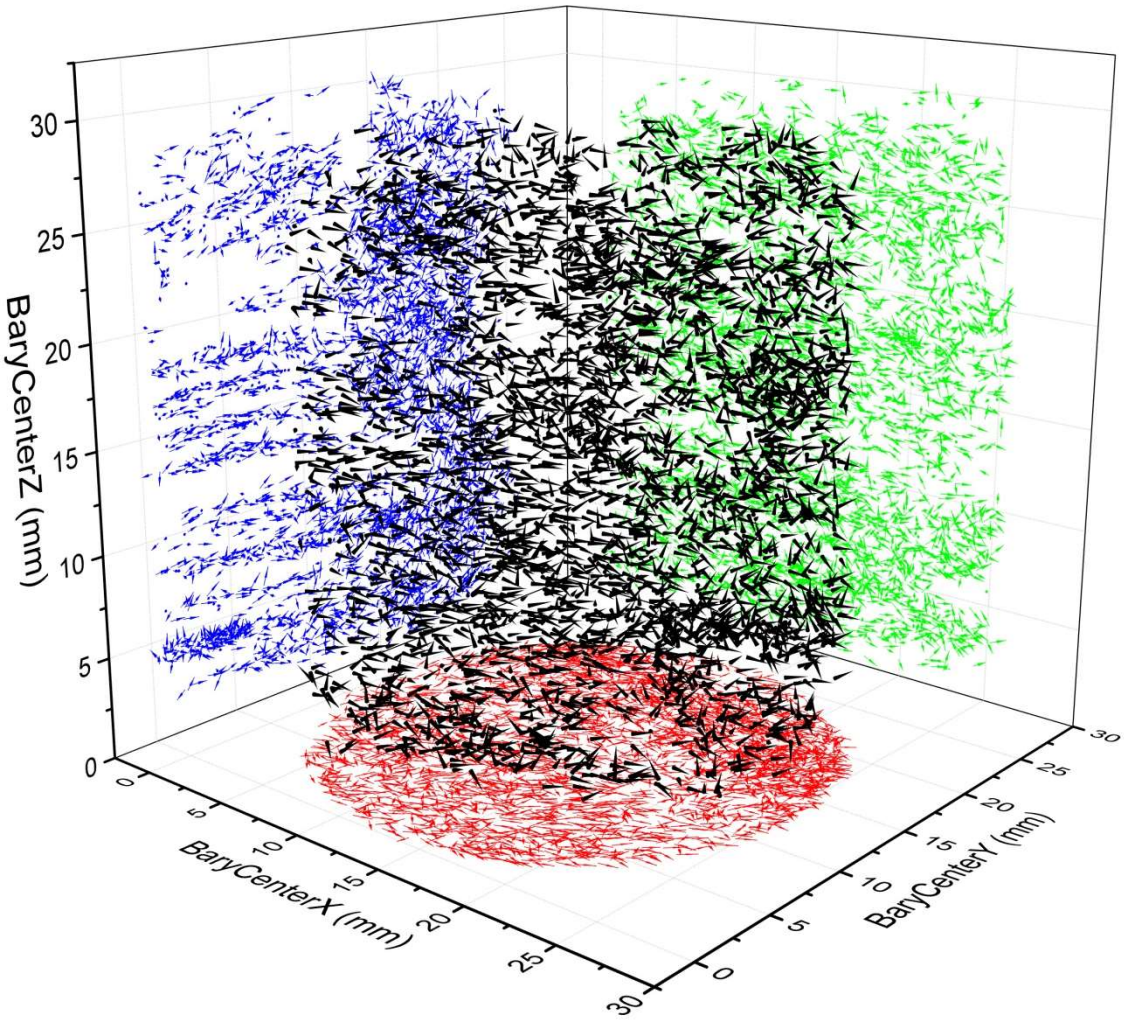

Figure 5.85 Vector graph of the long axis orientations of ore grains within sample 1716; displaying a subset of grains with an aspect ratio greater than 2 and less than or equal to 4.

5.3.5 Sieve Analysis: Comparison of EPD Material to In-situ Ore Grains

In order compare material processed within the EPD and XRCT with one another; sieve analyses comparisons for both the EPD and XRCT material were constructed. In figures 5.86 through 5.95 the blue lines conform to the sieve analyses for material that was processed using EPD technology while the red lines represent a simulated sieve

analysis for ore grains scanned by XRCT. To achieve the simulated sieve analysis, the volumetric data of all the ore grains within the samples were converted to an equivalent circular diameter (ECD) and then sorted to fit within the same sieve set that was used for the EPD sieve analyses. Then using an average ore density for each sample, the volumetric data was converted into mass and processed as a typical sieve analysis would.

EG-181

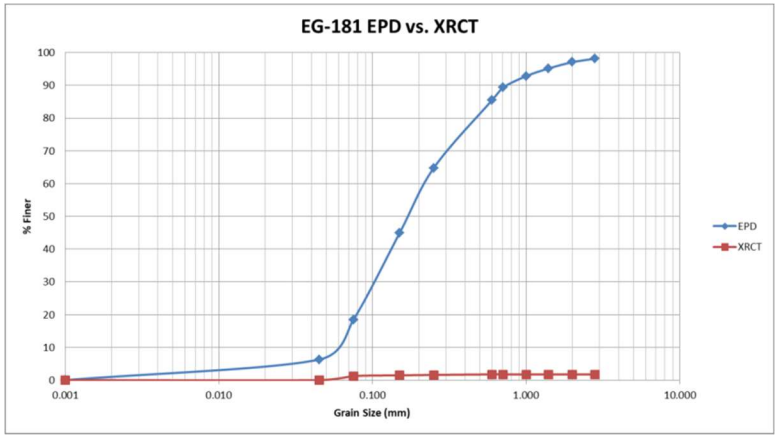

Figure 5.86 Sieve analysis comparison of EPD and XRCT material from sample EG-181.

Eagle-1

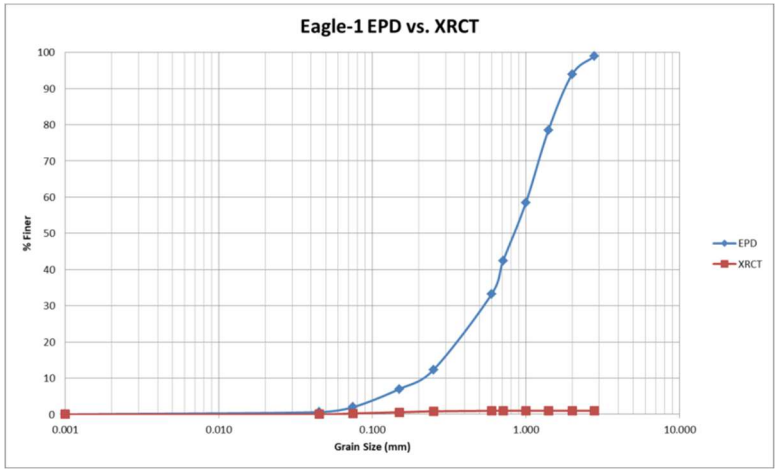

Figure 5.87 Sieve analysis comparison of EPD and XRCT material from sample Eagle-1.

DC

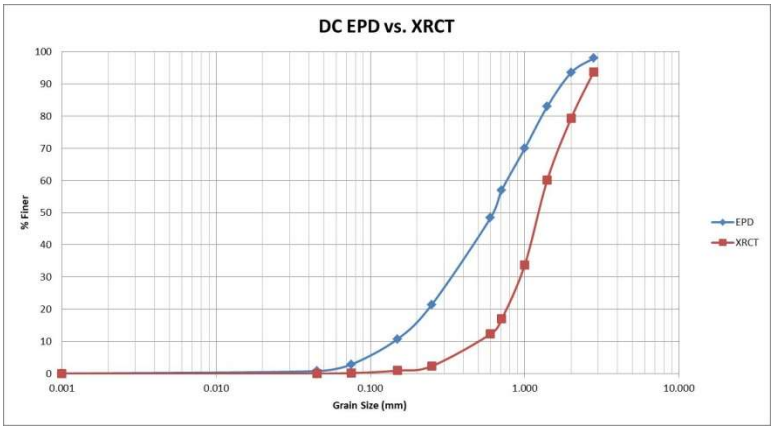

Figure 5.88 Sieve analysis comparison of EPD and XRCT material from sample DC.

Bag-1

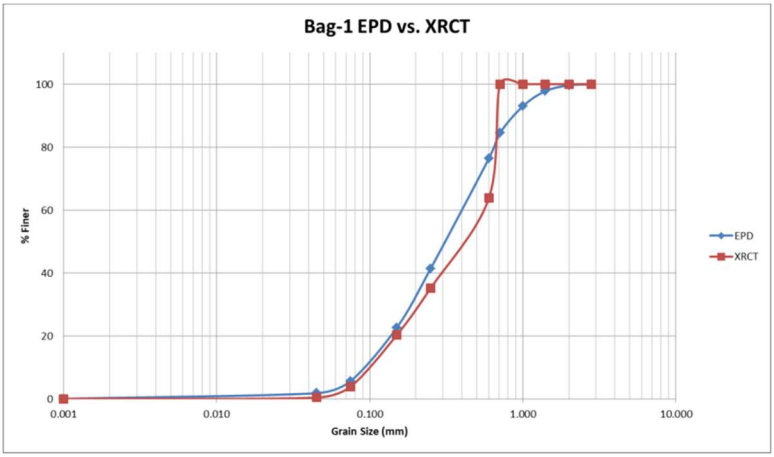

Figure 5.89 Sieve analysis comparison of EPD and XRCT material from sample Bag-1.

V-1

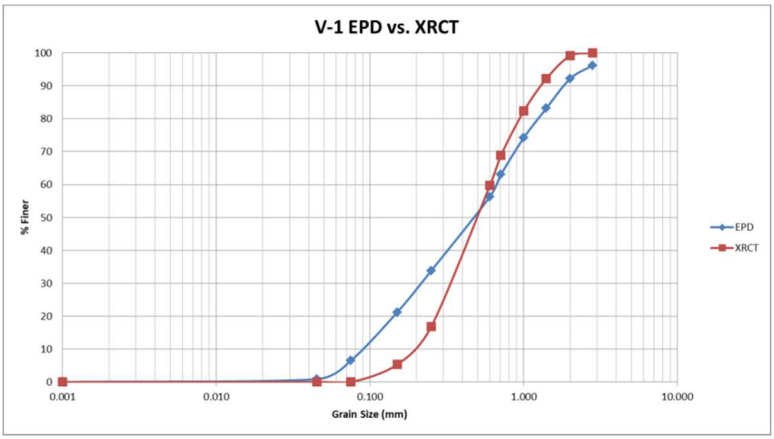

Figure 5.90 Sieve analysis comparison of EPD and XRCT material from sample V-1.

O-219

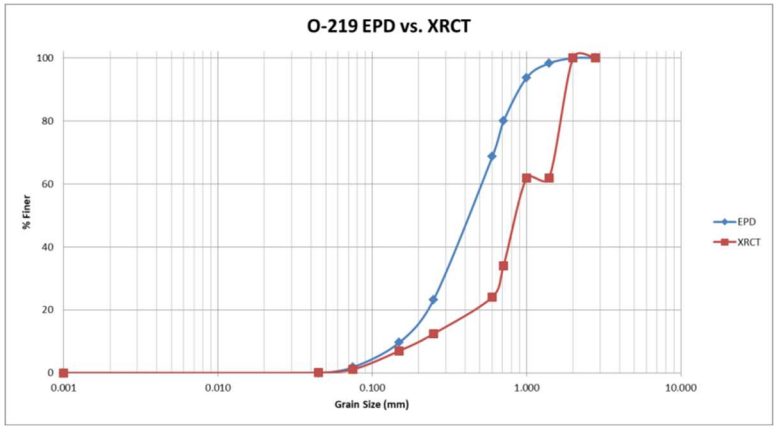

Figure 5.91 Sieve analysis comparison of EPD and XRCT material from sample O-219.

SLC-55

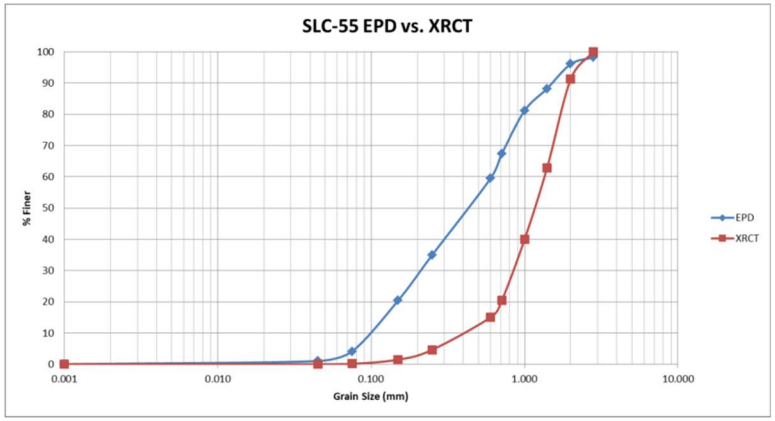

Figure 5.92 Sieve analysis comparison of EPD and XRCT material from sample SLC-55.

SLC-2476

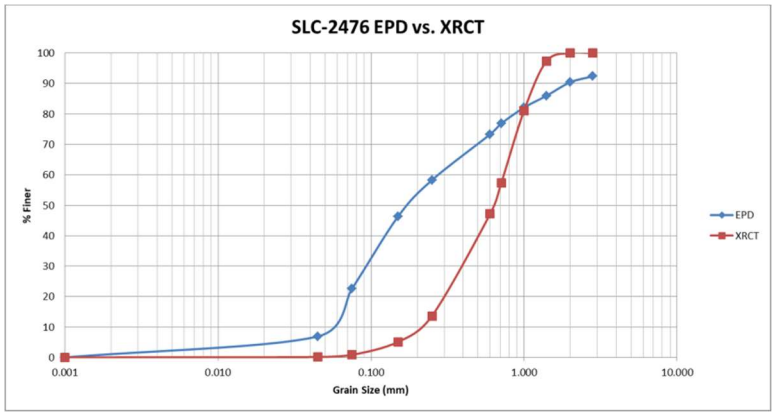

Figure 5.93 Sieve analysis comparison of EPD and XRCT material from sample SLC-2476.

MVT-1

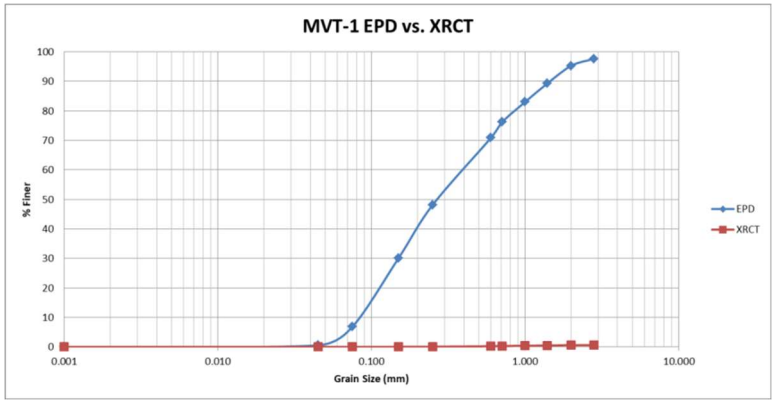

Figure 5.94 Sieve analysis comparison of EPD and XRCT material from sample MVT-1.

1716

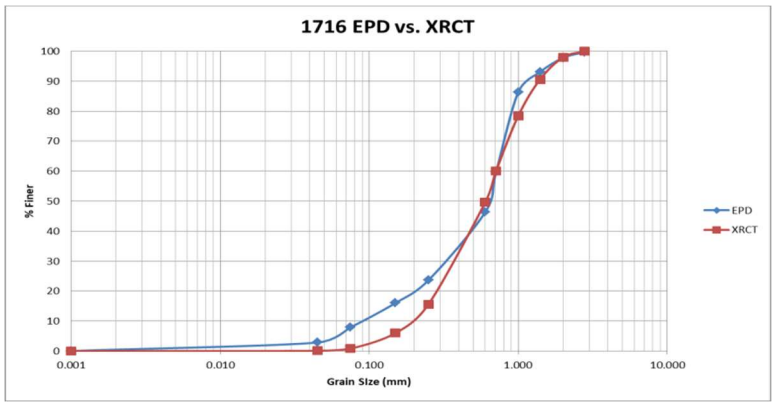

Figure 5.95 Sieve analysis comparison of EPD and XRCT material from sample 1716.

5.3.6 Grain Size Distribution: Comparison of EPD to In-situ Ore Grains

Another way to compare results from EPD and XRCT analysis is to compare grain size distributions for both the EPD material and XRCT material. In figures 5.96 through 5.105 the blue bars represent material that was processed using EPD technology, while the red lines represent material scanned by XRCT. To plot the XRCT data, the volumetric data of all of the ore grains within the samples were converted to an equivalent circular diameter (ECD) and then sorted to fit within the same sieve set that was used for the EPD sieve analyses. Then using an average ore density for each sample,

the volumetric data was converted into mass. This allowed the grain size distribution to be plotted as their weight percentages for each of the sieve sizes used to get an idea of the overall size distribution within a sample.

EG-181

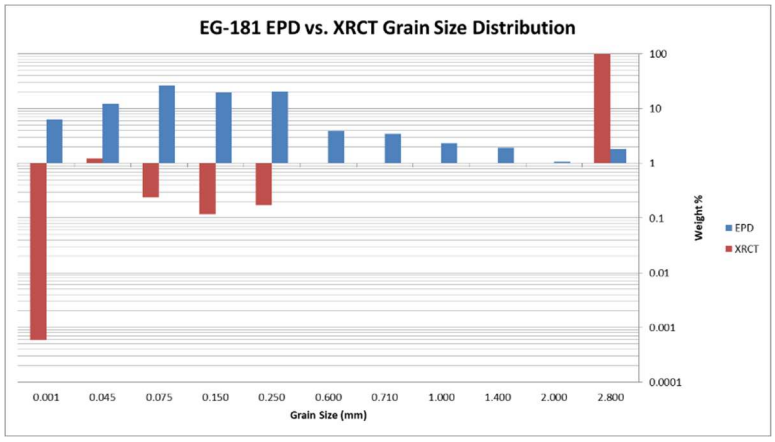

Figure 5.96 Grain size distribution comparison of EPD and XRCT material from sample EG-181. The EPD data does still contain silicate material whereas the XRCT data only contains ore grain information.

Eagle-1

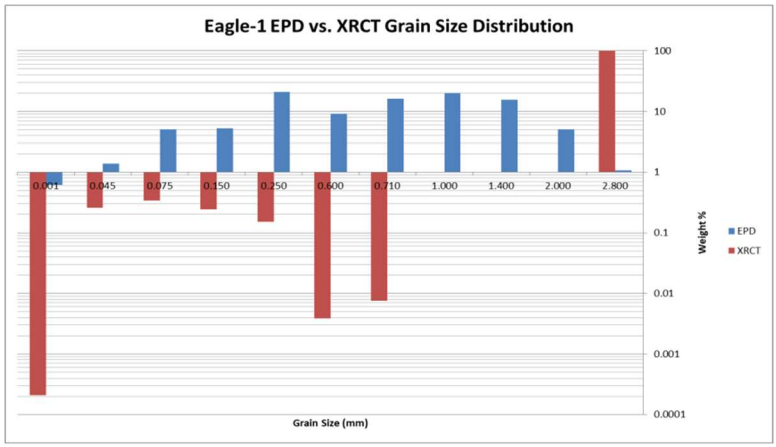

Figure 5.97 Grain size distribution comparison of EPD and XRCT material from sample Eagle-1. The EPD data does still contain silicate material whereas the XRCT data only contains ore grain information.

DC

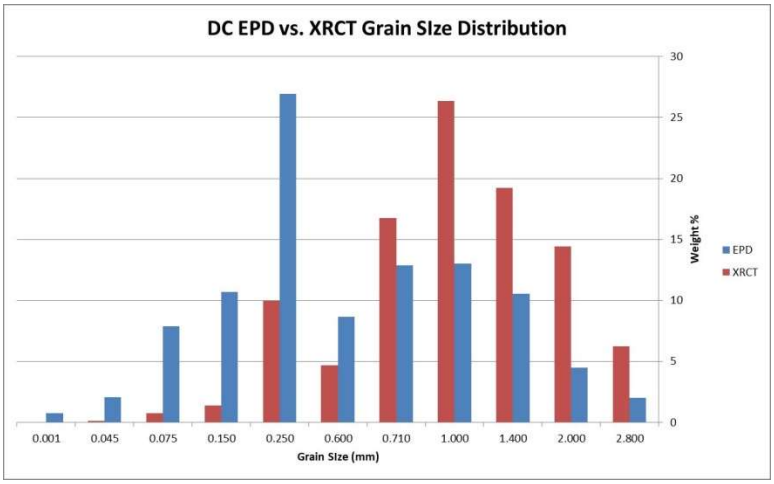

Figure 5.98 Grain size distribution comparison of EPD and XRCT material from sample DC. The EPD data does still contain silicate material whereas the XRCT data only contains ore grain information.

Bag-1

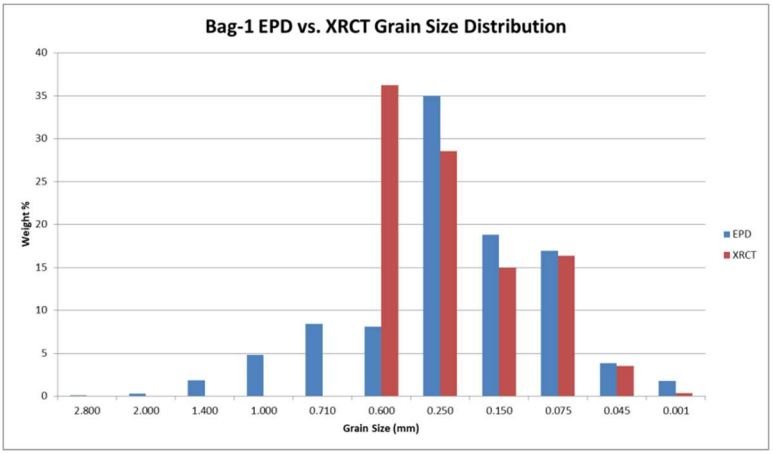

Figure 5.99 Grain size distribution comparison of EPD and XRCT material from sample Bag-1. The EPD data does still contain silicate material whereas the XRCT data only contains ore grain information.

V-1

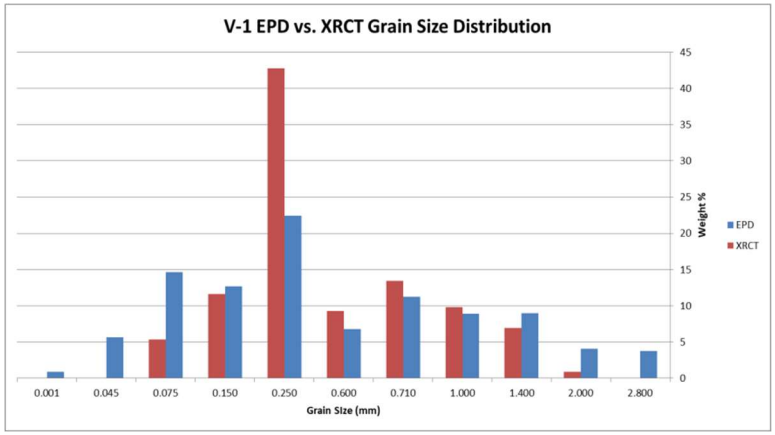

Figure 5.100 Grain size distribution comparison of EPD and XRCT material from sample V-1. The EPD data does still contain silicate material whereas the XRCT data only contains ore grain information.

O-219

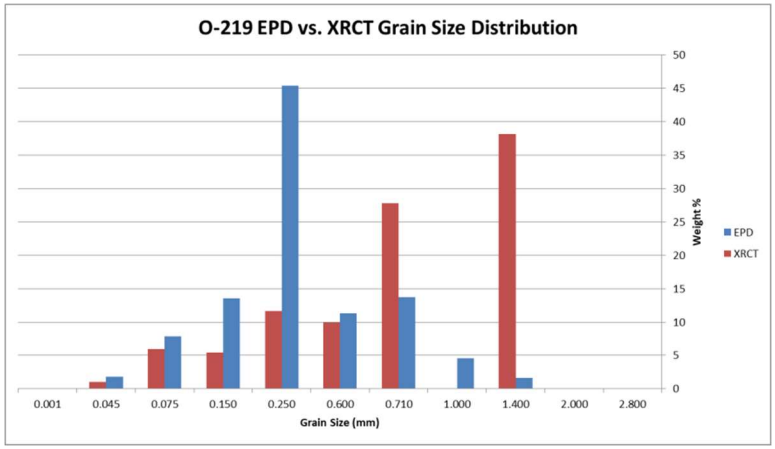

Figure 5.101 Grain size distribution comparison of EPD and XRCT material from sample O-219. The EPD data does still contain silicate material whereas the XRCT data only contains ore grain information.

SLC-55

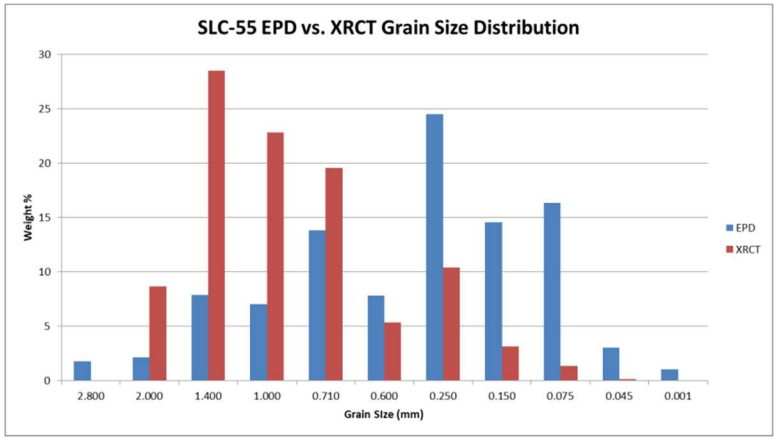

Figure 5.102 Grain size distribution comparison of EPD and XRCT material from sample SLC-55. The EPD data does still contain silicate material whereas the XRCT data only contains ore grain information.

SLC-2476

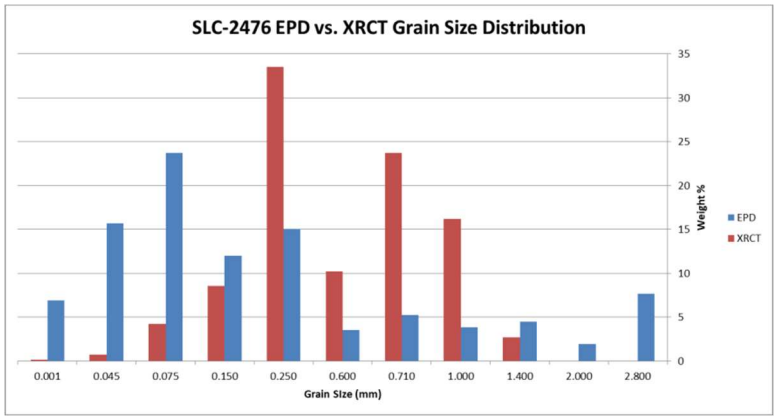

Figure 5.103 Grain size distribution comparison of EPD and XRCT material from sample SLC-2476. The EPD data does still contain silicate material whereas the XRCT data only contains ore grain information.

MVT-1

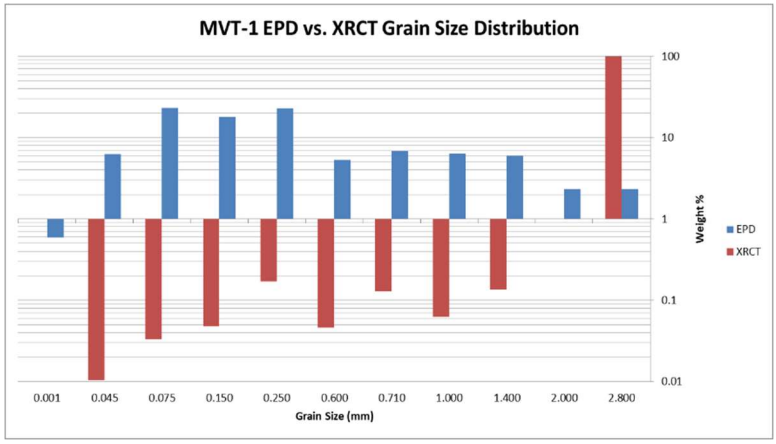

Figure 5.104 Grain size distribution comparison of EPD and XRCT material from sample MVT-1. The EPD data does still contain silicate material whereas the XRCT data only contains ore grain information.

1716

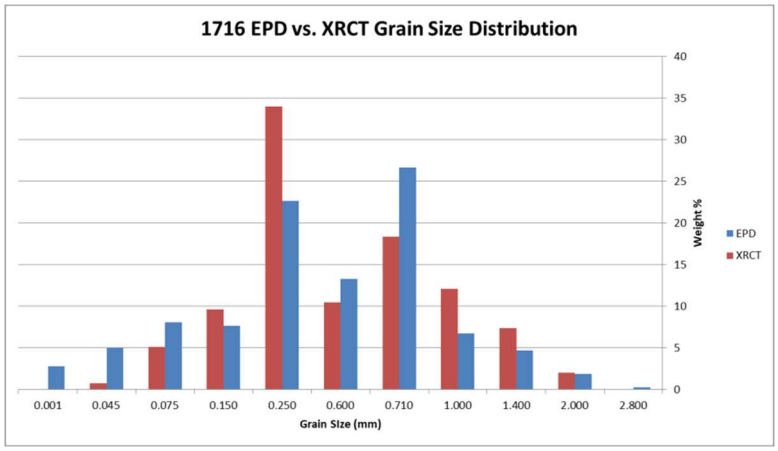

Figure 5.105 Grain size distribution comparison of EPD and XRCT material from sample 1716. The EPD data does still contain silicate material whereas the XRCT data only contains ore grain information.

5.4 Scanning Electron Microscopy and Mineral Liberation Analysis

Table 5.2 displays the results from the MLA scans, listing each sample, what deposit type it originated from, the principle mineralogy, ore mineralogy, total number of ore grains analyzed by the software, and how well it was liberated. As stated previously, liberated grains are grains that have over 95 % of their perimeter free from any other mineral. Also listed are binary and ternary associations. A binary association is a grain

that it attached to one other mineral, while a ternary association is a grain that is attached to two or more different minerals.

Deposit Type	Sample Name	Sample Mineralogy	Ore Mineral	Number of Grains	% Efficiency (Liberation)	Binary Association (Other Sulfides)	Ternary Association
Si-differentiation (Liq-Mag)	Eg-181	Ol, Cpx, Opx, Chr	Chromite	4637	34.78	7.59 (N/A)	57.62
Immiscible S melt (Liq-Mag)	Eagle-1	Ol, Cpx, Opx, Ilm, Py, Ccp, Pn, Po	Chalcopyrite	1100	72.91	9.29 (0)	17.8
			Pentlandite	88	69.57	8.65 (0)	21.77
	DC	Pl, Px, Bt, Ilm, Py, Ccp, Pn	Chalcopyrite	694	69.7	11.00 (0)	19.3
			Pentlandite	52	68.16	11.31 (0)	20.53
Porphyry (Hydrothermal)	Bag-1	Qtz, Pl, Or, Hbl, Ilm, Py, Ccp	Chalcopyrite	61	58.49	27.21 (0)	14.3
	V-1	Ser, Qtz, Chl, Py, Ccp	Chalcopyrite	3	97.16	2.84 (0)	0
	O-219	Pl, Or, Qtz, Mo	Molybdenite	11	0	54.51 (N/A)	45.49
VHMS (Hydrothermal)	SLC-55	Qtz, Chl, Cld, Py, Ccp, Sp, Gn	Chalcopyrite	7	0	48.45 (0)	51.55
			Sphalerite	4	0	92.65 (0)	7.35
			Galena	1	0	0 (N/A)	100
	SLC-2476	Chl, Py, Ccp, Sp	Chalcopyrite	748	88.67	5.80 (0)	5.53
			Sphalerite	43	67.35	2.00 (0)	30.66
MVT (Sedimentary)	MVT-1	Cal, Ccp, Sp	Chalcopyrite	4	37.27	41.55 (0)	21.18
			Sphalerite	2577	90.89	4.44 (0)	4.68
SSC (Sedimentary)	1716	Clay Minerals (Shale), Cu, Cc	Native Cu	1935	9.03	8.51 (0)	82.46
			Chalcocite	289	31.03	0 (N/A)	68.97

Table 5.2 A table presenting the results from MLA. Reports on the efficiency of EPD at separating constituent minerals from a sample as based on the overall percentage of ore mineral liberation. Also reports the percentage of binary mineral association (two different minerals still connected) and ternary mineral associations (three or more different minerals still attached to one another). The number of grains listed provides a basis on which the liberation percentage stands. Sample mineralogy: olivine (Ol), clinopyroxene (Cpx), orthopyroxene (Opx), plagioclase (Pl), pyroxene (Px), biotite (Bt), quartz (Qtz), orthoclase (Or), hornblende (Hbl), sericite (Ser), chlorite (Chl), chloritoid (Cld), calcite (Cal), ilmenite (Ilm), pyrite (Py), pyrrhotite (Po), chromite (Chr), chalcopyrite (Ccp), pentlandite (Pn), molybdenite (Mo), sphalerite (Sp), galena (Gn), chalcocite (Cc), native copper (Cu).

6. Discussion

Ten samples have been examined from a wide range of deposit environments such as magmatic, hydrothermal, and sedimentary. These samples have been processed and

examined using various technologies like EPD, XRCT, and MLA in addition to reflected light microscopy, sieve analysis, grain size distributions, 3D reconstructions, vector graphs, and shape analysis graphs. Results will be discussed with the primary objective of determining the efficacy of EPD technology at liberating various ore types from gangue material and its potential implications for ore comminution. Secondary questions that will be addressed are how well does EPD technology preserve mineral grain morphology/shape and what is the utility of using the technologies and techniques presented in this work with regards to characterizing ore minerals and mineralization styles within individual ore deposit types.

6.1 Effectiveness of EPD at Liberation of Ore

For the results displayed in Table 5.2 the most important column is "% Efficiency (Liberation)." This column represents the percentage of grains for each specific ore mineral within a sample that the MLA software classified as "liberated." based on overall grain area. The term liberated, in this case, is defined as any ore grain that has at least 95% of its perimeter free of any other minerals. This is also the classification that is utilized within the field of ore processing, as an ore grain that has over 95% of its perimeter free of gangue is more easily recovered downstream in the processing circuit by some other method such as floatation (Wang et al., 2012b).

The results illustrated by the % Efficiency column in Table 5.2 have a wide range of values. The highest liberation results (97 %) occurred in the V-1 sample with chalcopyrite. It should be noted that there were only 3 grains recovered from sieving in the chosen size range. The V-1 sample also show a binary association of ~3% and no

ternary associations, based on the 3 ore grains scanned. This is explained by a single small grain with a binary association compared to 2 much larger liberated grains. On the other end of the spectrum, two samples show liberation values of zero. Sample O-219 had no liberation for 11 grains of molybdenite while sample SLC-55 had no liberation for 7 chalcopyrite, 4 sphalerite, and 1 galena grains. The average liberation for all ten samples is 54% and 68 % when the two samples with null liberation values are excluded. However, the higher value for the average liberation cannot be considered valid, as explained below.

6.1.1 Explanations for the Variability in Efficiency of Liberation

Before considering the likely causes for the variability in liberation a few caveats to the data and how it was collected should be discussed. EPD and XRCT data are frequently compared to each other but it should be made clear that these data sets cannot be considered true 1 to 1 comparisons. For example, section 5.3.5 contains sieve analysis comparisons and section 5.3.6 contains grain size distribution comparison between EPD material and in-situ XRCT ore data. While these comparisons are useful, they are not true 1 to 1 comparisons, because the XRCT data represents only ore grains while the EPD material still contains all the silicates originally present within the rock. A heavy liquid separation was not performed to isolate the ore because of safety considerations and the lack of proper facilities. Another limitation of the XRCT data is that if a sample was poly-metallic there was no way to separate the different ore minerals from one another because of the samples being scanned at high-voltages. All the samples in this study were scanned at 150 kV. For different ore minerals to be separated from one another in an

XRCT scan the minerals must have attenuation coefficients that vary from one another enough so that their grey values will occur as identifiable peaks on the grey scale. As can be seen in figure 6.1 as the voltage used to perform a scan increases the attenuation coefficients become more and more similar, essentially lumping multiple peaks into one. For the ores present in this study to be differentiated within each sample the scanning voltage would have needed to be at or below 50 kV. Scans run at these lower voltages are called high-resolution XRCT scans and require a much smaller sample to be scanned. Typically micro cores of ~8 mm diameter are used compared to the 25 mm cores used in this study; this is because of the X-rays not being able to penetrate as deeply with lower energies (Godel, 2013).

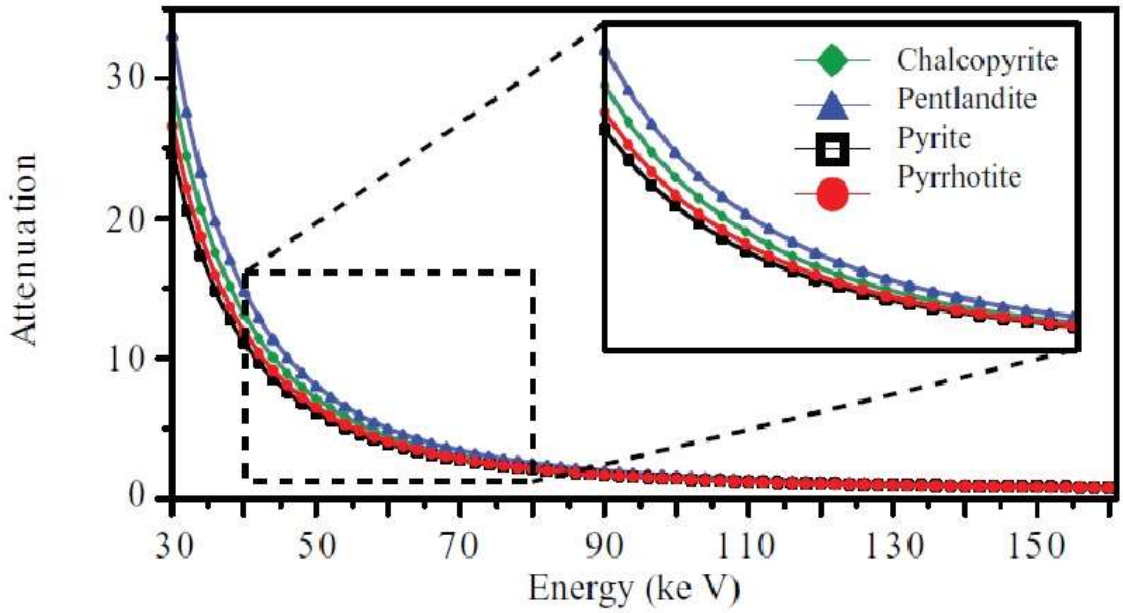

Figure 6.1 Common sulfide minerals and their calculated theoretical linear attenuation coefficients with increasing energy (Godel, 2013).

There has been research that shows that ore bearing rocks processed in an EPD create a coarser ore concentrate than those processed in a mechanical crusher and also that there is a higher occurrence of whole and unbroken mineral crystals (Rudashevsky et al., 1995; Cabri et al., 2008; Wang et al., 2012a). The higher abundance of unbroken crystals suggests that EPD technology preserves in-situ grain size. Following this line of reasoning, the in-situ ore grain sizes for the samples that had no liberation were examined to see if the -250 µm to +150µm size fraction was the appropriate choice. The two samples that contained no liberated ore grains were O-219 and SLC-55.

Comparisons of the grain size distributions for EPD material and XRCT ore grains, which is considered to be in-situ grain size, is shown in section 5.3.6. For sample, O-219 figure 5.101 shows that ~87 wt% of ore grains fell into size fractions that were larger than the one selected for this study. This may explain why there were only 11 molybdenite grains that were scanned by the MLA for this sample. Upon closer inspection of the individual particle XRCT data, out of 955 ore grains identified within this sample only 73 grains would be classified in the size fraction in question. This amounts to just ~8% of the overall abundance of ore grains being present within the -250 µm to +150 µm size fraction. For sample SLC-55 figure 5.102 indicates that ~95 wt% fell into larger size fractions but the particle data from the XRCT showed that there were 2788 ore grains classified in this size fraction, which represents ~21% of the ore grains within this sample. The fact that 21% of ore grains should be represented within this size fraction and the MLA only contained a total of 12 ore grains suggests some other issue with SLC-55. This discrepancy is attributed to the way the sample material was handled.

When preparing grains mounts for MLA, sample material was extracted out of the vessel containing the appropriate size fraction with no consideration of potential gravity settling of the heavier ore minerals. It is likely that the grain mount predominantly contains silicates that were closer to the surface of the sample container. After inspecting the raw data from the MLA this theory appears to be validated as there were 6,553 particles scanned, but only 12 of them were ore grains.

It initially appeared that the samples with zero liberation could be at least partially explained by either poor sampling technique or by scanning a much smaller grain size than the average within the sample. The reasoning was that the larger grains would liberate more efficiently because of their increased size. These observations proved invalid when some of the better liberated samples were inspected in a similar fashion. DC had ~70% of chalcopyrite and ~68% of pentlandite liberated, but it also had over 97 wt% of ore occurring in larger size fractions. The XRCT data showed that the size fraction chosen represented ~10% of ore particles present within the sample; this amounted to 1532 ore grains. SLC-2476, which comes from the same deposit as SLC-55, had ~88% of chalcopyrite and ~67% of sphalerite liberated with over 86 wt% of ore being coarser in size. XRCT data showed that ~12% of ore grains fall within the -250 μm to +150 μm size fraction or a total of 9864 ore grains. V-1, which, like the zero value samples also had a low number of particles scanned, had ~97% of chalcopyrite liberated with over 82 wt% of ore being coarser. XRCT data indicates that ~24% of ore grains fall within this size fraction. While it is reasonable to assume that V-1 also had a fair amount of sampling error as only 3 grains were scanned by the MLA: it is also clear there is no link between

liberation value and number of particles scanned. In addition, it also seems that all the samples in the study contained most of their wt% in larger particle sizes and that this has no bearing on how well sample ore was liberated. Therefore, another factor must play a role in determining how well ore is liberated from gangue.

It useful to consider if the type of ore deposit played a role in how well ore from different deposit types were liberated. Table 5.2 shows deposit type and in parentheses the deposit environment. Sample EG-181 (fig. 5.1) is the sole example of a Si-differentiation liquid-magmatic deposit examined. Because it was the only one of its type, it will be compared to the two other samples (DC and Eagle-1), albeit of different deposit types, that originated from liquid-magmatic environments. While both DC and Eagle-1 have high liberation values in the 60% and 70% range, EG-181 only had liberation of 34% of its chromite grains. This could be because of the fact that chromite, the ore mineral present within EG-181, is an oxide while both DC and Eagle-1 contain only sulfide ore minerals. In an attempt to understand why there was such a significant difference between these liberation values the various properties of these minerals were examined. It was noted that they possess differing electric conductivities. Silicate minerals have an average electrical conductivity of 1.0×10^{-14} S/m while sulfide minerals, such as pyrite, has a conductivity of 0.9 S/m (Wang et al., 2012b). It is possible that the conductive properties of different minerals present within a sample play a major role in how well they are disaggregated from each other by EPD technology. The idea behind this thought is that the electrical pulse from the EPD will travel through the silicate rock but that its pathway will pass through materials of higher conductivity and therefore

lower resistivity. The conductivity of chromite is reported to be from 0.001 to 0.1 S/m while the conductivity of chalcopyrite, taken as proxy for sulfide ore minerals in general, has a conductivity of 75 S/m (Lu et al., 2005; Wang et al., 2012a). It is possible that conductivity plays a significant role in determining the efficiency of liberation, but it is difficult to say for certain considering EG-181 was monomineralic with respect to ore minerals.

Samples Eagle-1 and DC can be compared to each other since both of these samples came from deposits that are representative of immiscible sulfide melts. Based on the hand sample descriptions Eagle-1 (fig. 5.2) contained three ore minerals chalcopyrite, pentlandite, and pyrrhotite while DC (fig 5.3) only contained two; chalcopyrite and pyrrhotite. It can be seen in Table 5.2 that both samples only had chalcopyrite and pentlandite scanned in the MLA. Even though pyrrhotite was present in Eagle-1 the MLA software was unable to identify it successfully. This is mostly likely because of the fact that the sample also contained pyrite which has a very similar mineral formula and since it is the chemical formulas that determines the MLA process the program was unable to differentiate between the two. MLA results indicate a high percentage of liberation in the two ore minerals identified for each sample. While this represents only two data points it suggests that liquid-magmatic immiscible sulfide ore deposits may lend themselves well to being processed by EPD technology.

The next group of samples compared is Bag-1 (fig. 5.4), V-1 (fig. 5.5), and O-219 (fig. 5.6) as all these samples originate from a hydrothermal depositional environment and are samples from porphyry deposits. As can be seen in Table 5.2 the ore mineralogy

for both Bag-1 and V-1 contained chalcopyrite and O-219's ore was molybdenite, but between the three samples all of the ore minerals represent sulfide ores. It can also be observed that all three samples had relatively low ore grains counts identified by the MLA, but there is a huge range of liberation results represented by these three. Bag-1 had liberation of ~58%, V-1 had liberation of ~97%, and O-219 had no ore grains liberated at all. When the raw XRCT data were examined it was determined that the -250 μm to +150 μm size fraction chosen for the MLA scans contained 6.6% of the ore grain present in Bag-1, 24.9% of ore grains in V-1, and 7.6% of the ore grains in O-219. These values illustrate that there were enough ore grains present within this size fraction to rule out the possibility that this size fraction was an inappropriate one to sample. The likely cause of the low ore grain occurrence in the grain mounts likely originated from sampling error. It is worth noting that the Bag-1 grain mount represented a sample that likely contained ore grains of the size fraction -250 μm to +75 μm, essentially two different sieve fractions. This was discovered when examining the raw XRCT data and it indicated that there were only 32 ore particles that fit into the -250 μm to +150 μm but the MLA results showed that 61 ore grains were scanned.

Samples SLC-55 (fig. 5.7) and SLC-2476 (fig. 5.8) both come from that same deposit and therefore both represent samples that originated from a VHMS deposit. Table 5.2 indicates that both of these samples essentially have the same ore mineralogy, chalcopyrite and sphalerite, with the exception of a single grain of galena that was identified in SLC-55. Aside from the similar mineralogy the results of the MLA were vastly different. SLC-55 had no liberated grains at all while SLC-2476 had ~88% of

chalcopyrite and ~67% of sphalerite liberated. There is also a huge difference in the number of grains identified by the MLA; SLC-55 had only 12 grains identified from its three different ore minerals while SLC-2476 had 791 between its two ore minerals. Based on the raw XRCT data the size fraction used for these grain mounts contained 20.9% of ore grains for SLC-55 and 11.96% of ore grains for SLC-2476. The low ore grain identification for SLC-55 is most likely caused again by sampling material for the construction of its grain mount. The issue of the vast difference between the liberation values of the two samples is not easily resolved. One would expect that because these sample came from the same deposit that they would have very similar liberation values, but they do not. It is possible that the different degrees of ore liberation were the result of each sample coming from a different portion of the deposit and therefore being subjected to differing alteration styles. As described in hand sample (see 5.1.1), SLC-55 came from a portion of the ore body were there was significant quartz flooding with minor chlorite and chloritoid. SLC-2476 came from the stringer portion of the deposit and aside from its ore mineralogy is almost entirely composed of chlorite.

Samples Bag-1, V-1, O-219, SLC-55, and SLC-2476 were all compared to each other on the basis that they all originate from hydrothermal depositional environments. Examining them as a group it appears that only two samples had very high liberation values: V-1 and SLC-2476. Sample Bag-1 has a moderately high liberation value (58.5%) while O-219 and SLC-55 had no liberation at all. When comparing these results to the mineralogy for each sample, as described in section 5.1.1, a possible pattern emerges. Samples that were richer in quartz, plagioclase, and orthoclase (or silicates in general)

appeared to have either worse or no liberation at all, while samples that contained chlorite and sericite had much better liberation. These observations again point to the material property of electric conductivity. Silicates have a conductivity of $1.0x10^{-14}$ S/m, whereas the conductivity of chlorite is $6.3x10^{-10}$ S/m and sericite is $4.6x10^{-13}$ S/m (Durand et al., 2000; Wang et al., 2012b). The improved liberation values for Bag-1 and SLC-2476 could be explained by chlorite being significantly more conductive than silicates and sericite slightly more so. Since sericite is the identified phyllosilicate in Bag-1 and is only slightly more conductive than silicates this might explain why Bag-1 had only a moderate liberation of ~58%. This could potentially mean that the effectiveness of EPD technology is not only dependent on the presence of highly conductive ore minerals but also on the coverall conductivity of the whole sample. The more highly conductive minerals there are present within a sample the better EPD technology will liberate any ore present while samples with abundant low conductivity silicates, but still containing ore minerals, will have a lower efficiency of liberation for said ore.

The final comparison to be made is between samples MVT-1 (fig. 5.9) and 1716 (fig. 5.10). These two samples come from different deposit types: with MVT-1 originating from a Mississippi Valley Type (MVT) deposit and 1716 originating from a Sediment-Hosted Stratabound Copper (SSC) deposit. However, both samples do share a common depositional style and environment, hydrothermal deposition in a sedimentary environment. Both samples contain a good number of ore grains identified by MLA, except for chalcopyrite in MVT-1. There were only 4 grains of chalcopyrite scanned in MVT-1 but based on the observations made while performing reflected light microscopy

in section 5.1.2 (fig. 5.19) chalcopyrite occurs very fine-grained and sparsely distributed. The ore mineralogy is different between both samples, with MVT-1 containing chalcopyrite and sphalerite while 1716 contained native-Cu and Cc. Liberation appear to vary significantly between the minerals in each of the samples. For MVT-1, sphalerite had an extremely high liberation of ~90% while the few chalcopyrite grains present only had liberation of ~37%. For 1716 Cc had liberation of ~31% while the native-Cu only had liberation of ~9%. Looking specifically at MVT-1 the poor liberation of chalcopyrite can likely be explained by its low abundance and very fine grain size compared to sphalerite. Keeping the idea of extremely high liberation connected to overall rock electric conductivity in mind, the conductivity of limestone is $3.3x10^{-4}$ S/m and the conductivity of sphalerite ranges from 370 to $3.7x10^{-13}$ S/m (Pearce et al., 2006; Nordiana et al., 2013). sphalerite can be very conductive but it is only slightly more conductive than silicates, so overall this rock is likely much more conductive than a silicate rich one. This supports the previous assertion that the overall conductivity of a rock is a controlling factor in the effectiveness of EPD technology at liberating ore minerals. Appling this same hypothesis to sample 1716 does not work as well since both ore and gangue materials have similar conductivity values. The conductivity of a shale slate is $2x10^{-3}$ S/m, native Cu is $5.8x10^{7}$ S/m, and chalcocite ranges from $1.0x10^{4}$ to $4.3x10^{-4}$ S/m, all of which are much more conductive than silicates at $1.0x10^{-14}$ S/m (Pearce et al., 2006; Parkhomenko, 2012; Wang et al., 2012a). To help explain this divergence from the otherwise observed trend a few points can be made. First, the rock that contains the ore minerals is shale and may contain microscopic quartz that would not have been identified in reflected light microscopy (fig. 5.20) and would also lower the overall conductivity of

the sample. The Cc contained within this sample is likely very finely distributed as it was not observed in hand sample and only discovered through the use of MLA, where it was reexamined in the SEM using EDS and then identified by the MLA. Finally, it has been reported that the pulse of electricity that travel through the sample during EPD processing preferentially follows mineral grain boundaries; since native Cu does not conform to a crystal morphology it is at least possible that the electrical pulses are actually being transmitted through the Cu much like it would in electrical wiring and not just passing along boundaries (Sperner et al., 2014).

6.1.2 Comparison with Published Literature

Comparing the work of this study to existing published material is difficult for two reasons. All published material relating to the effectiveness of EPD technology at liberating ore minerals features data sets of material processed using EPD and material processed with mechanical crushing equipment. These data sets lend themselves readily for an easy comparison of improvement in liberation by using EPD technology. The other reason is that most other research also investigated some other aspect that may have affected the results from the perspective of a pure liberation efficiency result. For example, Wang et al. (2012a) focused on comparing material processed through and EPD with material processed through a jaw crusher, while making sure to maintain that each process consumed equal amounts of energy.

Lastra et al. (2003) processed a single sample that originated from the Merensky Reef, a magmatic ore deposit, through both an EPD process and a mechanical jaw crusher and then compared the two data sets using image analysis software similar to MLA that

allowed for the determination of liberation percentages. Results of this study are shown in figure 6.2. For this work the definition of liberation is taken to mean minerals grains that had > 95% of their perimeter free of any other mineral. Because of this definition only two groupings of results in figure 6.2 are important (columns EP-D 90 to free and jaw 90 to free) and they are the only results that are considered since these represent the portions closest to the definition of liberation used here. Column labeled "ga" refers to silicates, "cr" to chromite, "po" to pyrrhotite, "cp" to chalcopyrite, and "pn" to pentlandite. Lastra et al. (2003) saw an increase in liberation for chromite of ~50%, pyrrhotite of ~23%, and pentlandite of ~49%. Interestingly, they saw a decrease of ~50% for the liberation of chalcopyrite, and their explanation is that EPD technology may not be universally good at liberating all ore minerals.

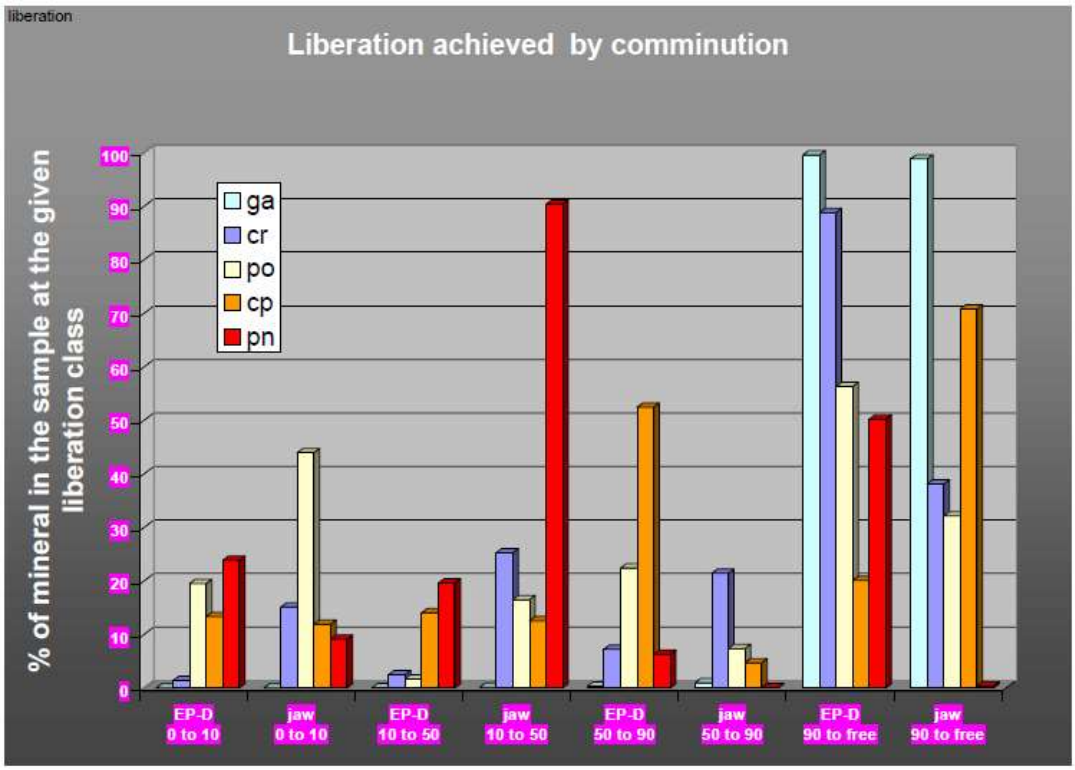

Figure 6.2 Liberation achieved by EPD and conventional jaw crusher of a sample from the Merensky Reef, sorted on the x-axis by percentage of liberation achieved (Lastra et al., 2003)

In order to relate results of Lastra et al. (2003) to what factors play a role in EPD effectiveness the mineralogy is examined. The sample material was determined to have the following mineralogy, in order of decreasing abundance: serpentine, anorthite, enstatite, chromite, olivine, mica, and talc. The mineralogy of this sample was determined by use of x-ray diffraction (Lastra et al., 2003). If, as hypothesized in the previous section, the overall conductivity of a sample is an important factor in how effective EPD technology is then this sample appears support that hypothesis. Pyroxenes, in this case enstatite, are reported to have conductivities in the range of $1x10^{-4}$ to $1x10^{-5}$ S/m, olivine ranges from $1x10^{-2}$ to $1x10^{-4}$ S/m along with clays and micas that range from $1x10^{-8}$ to $1x10^{-13}$ S/m (Duba et al., 1973; Constable and Duba, 1990; Durand et al., 2000). The previously stated gangue conductivity taken into account with the very highly conductive ore minerals would suggest that this sample should liberate very well. Sample EG-181 in this study can provide a point of comparison, while it does not contain the range of ore minerals like the Merensky Reef sample from Lastra et al. (2003). The degree of liberation achieved with EG-181 was not as efficient as that of Lastra et al. (2003), but this may be explained by the gangue mineralogy of EG-181. The only identified gangue mineral in EG-181 was dunite with a conductivity of $1x10^{-5}$ S/m (Constable and Duba, 1990). The overall conductivity, potentially being lower than the Merensky reef sample from Lastra et al. (2003), could account for the difference of ~34% chromite liberation in EG-181 to ~88% chromite liberation in the Merensky Reef sample.

An investigation by Wang et al. (2012a) looked at three different ores which were processed both using EPD technology and conventional mechanical crushing while

making sure that equivalent energies were used to process both sample sets. In Wang's study, each ore was represented by a specific ore mineral deemed to be the most important to each deposit. The first ore was defined by chalcopyrite and came from a Cu-Au mine with major silicate minerals of quartz, orthoclase, hornblende, and chlorite. The second ore was defined by pyrite and came from a low-grade Au deposit with the major silicate minerals of calcite and ankerite. The third ore was defined by pyrrhotite and came from a platinum group metal mine with major silicate minerals of pyroxene, amphibole, and feldspar (Wang et al., 2012a). The results of this study are shown below for each of the key indicator minerals for both a 5 kWh/t and a 10 kWh/t test (fig. 6.3). For these graphs, the red bar is the EPD results while the white bar represents the mechanical crushing results. The error bars represent a 95% confidence interval, and the results report mineral deportment percentages which are synonymous with liberation percentages.

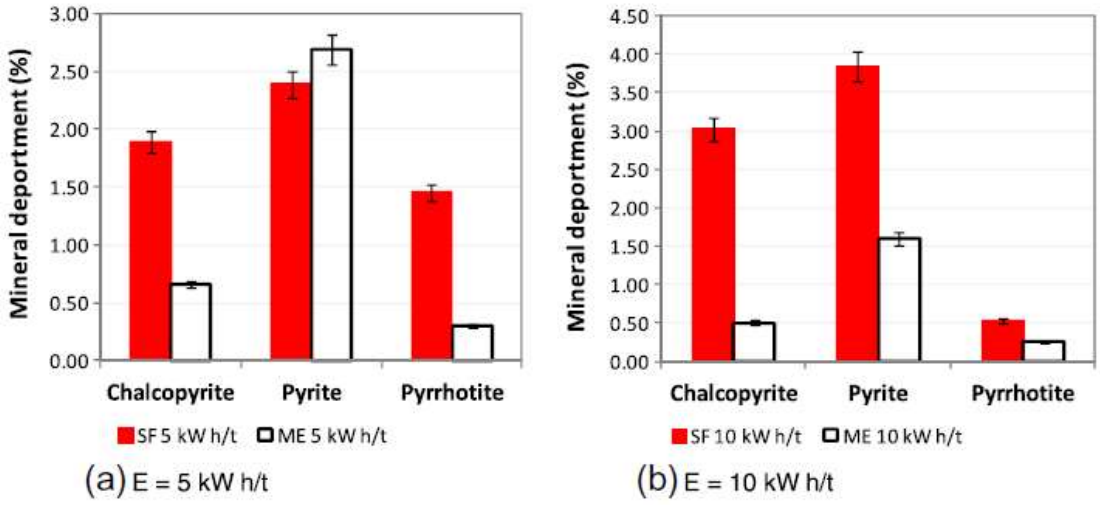

Figure 6.3 Greater than 95% liberation values for the indicator minerals for 3 different ore samples that were processed using two different specific energy levels. White bars represent material that was mechanically comminuted while the red bars represent material that was comminuted in an EPD, error bars represent 95% confidence interval (Wang et al., 2012a).

The results from Wang et al. (2012a) show that for the 5 kWh/t test both the chalcopyrite and pyrrhotite ores had better liberation than their mechanical counterpart, but the pyrite ore had better liberation with the mechanically processed material. However, for the 10 kWh/t test all three ores had better liberation when processed using EPD technology, though the pyrrhotite result is not as good as it was for the 5 kWh/t test. When comparing these results to the ones from this study only the chalcopyrite ore appears to match. Since the chalcopyrite sample, as defined by its silicate mineralogy, appears very similar to Bag-1, O-219, and SLC-55 which also had either moderate liberation, in the case of Bag-1, or no liberation at all. This may support the hypothesis that quartz and feldspar rich rocks, which have the general conductivity of $1x10^{-14}$ S/m, liberate more poorly than rocks that contain other more conductive minerals (Wang et al., 2012b). However, other samples from Wang et al. (2012b) do not support that hypothesis. Both the pyrite and pyrrhotite samples only resulted in ~3.75% and ~1.5% liberation, respectively. The pyrite sample came from an ore deposit rich in calcite; an equivalent sample from this study would be MVT-1 that is also dominated by calcite as its dominant gangue mineral. In the case of MVT-1 the principle ore mineral, sphalerite, was liberated to ~90% which is far better than ~3.75% liberation that Wang et al. (2012b) achieved. For the pyrrhotite ore sample there is no obvious comparison to make. Since the pyrrhotite samples main gangue mineralogy is mafic in composition it might be comparable to either Eagle-1 or DC, both of which are predominately composed of mafic minerals. This comparison does not support the previous hypothesis; all samples contain more highly conductive gangue minerals such as Pyx and Ol. Liberation was much better for Eagle-1 (~72%) and DC (~69%) compared to the pyrrhotite ore sample (~1.5%). It is

entirely possible however that because Wang et al. (2012a) was focused on matching the amount of energy utilized between EPD and mechanical crushing and that there was simply not enough energy used to get the liberation values that were achieved by this experiment.

A third study compared EPD technology to mechanical crushing with respect to Au and Ag deposits (Andres, 2010). In their investigation, samples from an unknown American Au deposit were processed using both EPD technology and mechanical crushing. Each sample was processed by their respective methods down to sub-3 mm, at which point both samples were further process to sub-50 μm by a ball mill. Results show that the crushing method was able to achieve an average metal extraction, equivalent to liberation, of only 30% that was stated to be insufficient to be profitable (Table 6.1). With EPD processing the average metal extraction increased to 54.2%; it is unclear whether or not this would make the mine profitable or not (Andres, 2010). There was also a single test performed on an Ag ore from Endeavour Mine in Mexico where the use of EPD technology resulted in an increased average metal extraction of 12.3%. Andres (2010) stressed that there was no specific pulse regime that would be effective for all ore types and that each different ore needed to be tested and calibrated to find the specific treatment regime that is most effective. The observations that Andres (2010) made may also help explain some of the fluctuations in liberation effectiveness observed in this study.

Sample	Treatment Type	Number of Tests	Average Metal Extraction
Gold	Mechanical Crushing	3	30.0%
Gold	Electrical Pulse	3	54.2%
Silver	Mechanical Crushing	1	70.5%
Silver	Electrical Pulse	1	82.8%

Table 6.1 Average metal extractions from samples of gold and silver ores that were processed both by mechanical crushing and electrical pulses. Adapted from Andres (2010).

6.1.3 A Special Test Run of DC Samples

The entire set of sieve analyses can be found in chapter 5 (Ch. 5.2, fig. 5.23 - 5.32; sieve analysis in fig. 5.22). In addition to the main sample for DC that was processed there were 16 extra samples processed with EPD by conducting a parametric study. Because of the regional significance of the Duluth Complex, it was decided to perform an addition experiment on this material. Figure 5.23 shows all 8 samples that were processed through the SELFRAG EPD using 120 kV and several observations can be made based on the data. It is clear from the graph (fig. 5.23) that as samples are subjected to more pulses (greater amounts of energy) a finer grained product is the result. There is a threshold where adding more energy has little to no effect (see DC-7 and DC-8). The largest gain in size reduction occurs from DC-1 to DC-2, 25 to 50 pulses, with the second largest gain occurring from DC-3 to DC-4 or 100 to 125 pulses. Samples DC-6 and DC-7 appear to have the exact same size fractionations as both lines overlap one another. Figure 5.24 displays all 8 samples that were processed through the SELFRAG EPD using 200 kV. The largest gain in size reduction for the 200 kV series of samples occurred from DC-9 to DC-10, 25 to 50 pulses, with the second largest seen from DC-10 to DC-11 or 50 to 75 pulses. As with the lower voltage sample series there were samples that had near identical size fractions. However, in the case of the 200 kV sample series,

there were two times that this occurred; DC-11 and DC-13 are near identical as were DC-12 and DC-14. These pairings are interesting and could be attributed to some sort of sample loss either during the EPD processing or subsequent sieve analysis or be the result of human error. Regardless of the error, these results suggest that DC-11 through DC-14 would likely generate very similar grain size plots, meaning processing beyond 75 pulses at a 200 kV operating voltage will not yield any additional advantages with regard to grain size reduction.

It is useful to compare the sieve analyses for each stage of processing. Figures 5.25 through 5.32 display the direct comparisons of the 25 pulses samples and subsequent samples in 25 step increments. Figure 5.29 shows the comparison of the two tests at 125 pulses that appear to almost overlap completely. However, upon comparison with the 100 pulse stage (fig. 5.28) it can be seen that the 200 kV material gets coarser from the 100 pulse to 125 pulse stages and then becomes relatively finer than the 100 pulse samples compared to the 150 pulse stage (fig. 5.30). This could be the result of sample loss, measurement error specifically for the 125 pulse 200 kV material, or that specific sample happened to have larger mineral crystals compared to the others. From the 125 pulse to 150 pulse stages for the 120 kV material there is a fining of size fraction and this is where the 200 kV material re-stabilizes. It appears that at the 150 pulse stage (fig. 5.30) the 120 kV and 200 kV material are almost identical and as can be observed from Tables 5.2 and 5.3 the 120 kV processing uses only 48.6% of the energy required to process the 200 kV version. As Andres (2010) observed, each ore will likely require a tailor-made processing scheme that is tested and determined to be effective, and as such the above test illustrates

one method to achieve this. Testing incremental series of pulses at differing voltages allows the determination of the most effective way to process a given material and gain significant energy savings to an equivalent product produced by using high voltages. It would be a logical extension of this work to perform MLA on all these samples to investigate whether the most energy efficient sample also represented good liberation values.

6.2 EPD and Mineral Characteristics Preservation

One of the secondary questions that arose during this study was how well does EPD technology preserve mineral grain boundaries? This is of interest because a review of the literature related to EPD technology shows that there appears to be differing claims as to grain boundary preservation. In addition, the possibility of producing clean, uncontaminated mineral separates is of great interest to both commercial and academic applications (e.g., ore comminution, single crystal age dating, geochemical analysis). Multiple studies processed samples of kimberlites using EPD technology to liberate diamonds from the kimberlite matrix and then compare them to samples of diamonds liberated by crushing (Andres and Bialecki, 1986; Rudashevsky et al., 1995). It was the conclusion of Andres (1995) that the liberation of diamonds using EPD technology produced unbroken and fracture-free diamonds unlike crushing which damaged all the diamonds. Rudashevsky (1995) recovered a sample of a diamond that had a preserved cubic structure and was able to show multiple examples of grains isoferroplatinum that also had preserved cubic, cuboctahedral, and octahedral crystal forms, along with an example of growth zonation. Another study looked at samples of rubies and sapphires

liberated by EPD technology and concluded that the technology is very efficient at liberating gemstones from very hard rock while preserving their original shapes (Cabri et al., 2008). A study that came to the opposite conclusion looked at samples of apatite crystal that were liberated using EPD technology and determined that while EPD technology does result in a coarser sized product compared to crushing both methods tended to break the elongate crystals into shorter pieces, frequently losing the pyramidal faces at the ends of the crystals (Sperner et al., 2014).

To determine if any data from this study could be used to assess the EPD technology with regards to preserving mineral grains two different types of graphs were made. The first was sieve analysis graphs that compared the material processed using EPD technology with the in-situ ore grain information (Ch. 5.3.5). The second set of graphs made illustrate grain size distributions of both EPD material and XRCT ore grain information on the basis of wt% (Ch. 5.3.6). These graphs will be discussed to determine their validity towards investigating this question.

Figures 5.86 through 5.95 show the sieve comparisons for all ten samples used in this study. The idea behind the creation of these graphs is that if there was a gap between the two curves where XRCT data represented a coarser product (offset to the right of the EPD data), this might suggests that the EPD processing is actually breaking down ore grains and is therefore not preserving mineral grain boundaries. Sample 1716 (fig. 5.95) illustrates the best example of the EPD and XRCT data matching up; it is the only sample where the mid-size fractions (0.4 to 0.8 mm) either line up or closely align. This was the only example that could be interpreted to support the preservation of mineral grains.

Samples DC (fig. 5.88), O-219 (fig. 5.91), and SLC-55 (fig. 5.92) are all examples where the XRCT data is shifted to the right of the EPD data. These results would all suggest that EPD processing does not fully preserve mineral grain boundaries and actually results in the destruction of the in-situ grain size. Samples EG-181 (fig. 5.86), Eagle-1 (fig. 5.87), Bag-1 (fig. 5.89), V-1 (fig. 5.90), SLC-2476 (fig. 5.93), and MVT-1 (fig. 5.94) cannot be used for this analysis for reasons discussed below.

There several issues that became apparent while analyzing these data. For samples EG-181 (fig. 5.86), Eagle-1 (fig. 5.87), and MVT-1 (fig. 5.94) the data cannot be used since these samples were all semi-massive and therefore extremely densely populated with ore grains to the point where most ore grains were interconnected. When interconnected or touching grains are scanned in the XRCT the software treats them as a single particle that had the effect of forcing the XRCT (red) lines on these graphs to be nearly horizontal and placed at the bottom because over 99% of the material falls within the largest bin. There are also issues with samples Bag-1 (fig. 5.89), V-1 (fig. 5.90), and SLC-2476 (fig. 5.93) where the EPD and XRCT line intersect. In all these samples, the XRCT data shows that in the larger size fractions the in-situ ore particles are finer than the EPD data would suggest. At some point, the lines cross which would then suggest that for the smaller size fractions the in-situ ore is coarser and the EPD is breaking apart grains, but both outcomes cannot be true. A key issue with trying to utilize these data is that for all EPD data silicates are still present, so while XRCT data represents only ore grains the EPD data represents ore grains and silicate grains. Another issue is that any sample that was polymetallic had artificially larger grain sizes reported in the XRCT data.

This is because the type of XRCT scan performed on the samples did not allow for the differentiation of ore minerals within the scan. This means that the XRCT data might show that particle X is 250 μm in size but particle X is actually 2 different smaller ore minerals that happen to be touching or formed as part of the same sulfide bleb. For this to be a more useful tool the EPD samples would need a heavy liquid separation so that the comparison could be between ore particles processed with EPD technology and in-situ as scanned by an XRCT. This suggests that only samples that contain disseminated or sufficiently small ore grains may be utilized in this fashion since interconnected or touching grains create an artificially large grain size most of the time.

In section 5.3.6, figures 5.96 through 5.105 show the grain size comparisons for all ten samples. The idea behind these graphs is that if the peaks for wt% distributions between the two data sets were offset with the XRCT data it would indicate a greater wt% of ore grains in coarser size fractions and that the ore grain size is not being preserved. Samples V-1 (fig. 5.100) and 1716 (fig. 5.105) have graphs show peaks that match up quite well. These graphs suggest that ore grain size may indeed be preserved; the EPD data represents both ore and silicate minerals however and in the graph for V-1 the 250 μm XRCT peak is far too large to make sense with the EPD results. Samples DC (fig. 5.98), Bag-1 (fig. 5.99), O-219 (fig. 5.101), SLC-55 (fig. 5.102), and SLC-2476 (fig. 5.103) all have graph that have their EPD and XRCT peaks offset from one another. In all these examples the XRCT peaks fall into coarser size fraction which suggests that ore grain boundaries are being broken down into smaller particles. For samples EG-181 (fig. 5.96), Eagle-1 (fig. 5.97), and MVT-1 (fig. 5.104), like for the previous set of graphs,

have errors that are the result of XRCT scans considering interconnected and touching ore particles as a single massive particle.

As before, there are issues with using the data. The inclusion of silicate material within the EPD data, interconnected or touching particles, and polymetallic ores being counted as single grains are all impacting the interpretation. In addition, because the XRCT scans were unable to identify multiple ore minerals within a single sample an average ore density had to be calculated to convert the XRCT data into wt%. This may potentially skew the data because it is possible that a lower density mineral and a higher density mineral had different size distributions. Treating these two different populations of ore particle as the same likely skewed the wt% peaks.

Because of the issues, discussed above, these tools are of limited use in this study. If the material processed by EPD had their ore minerals separated from the silicates by heavy liquids and only disseminated monometallic ores were used, then these plots may shed some light on the question of whether or not EPD technology preserves mineral grain boundaries. These techniques would also have the bonus of being able to be backed by statistics rather than SEM images that display crystal form.

6.3 Ore Mineral Characterization Using Applied Technologies

Throughout the course of this study a range of tools were utilized, and techniques developed with regards to ore mineral characterization such as 3D reconstructions of in-situ ore distributions, grain size distributions, shape analysis graphing, and ore grain long axis orientation graphing.

6.3.1 3D Reconstructions of In-Situ Ore

Utilizing XRCT to scan small 25 by 30 mm cores samples and then using the Avizo 3D visualization software package is a useful tool for characterizing ore minerals. This technique allows the unique opportunity to observe ore minerals in-situ. The gangue material can then be filtered out so that 3D reconstructions of just ore minerals are possible and illustrate how they occur throughout the scanned core. This can be useful for observing textural patterns within the ore such as small-scale net-textures, dissemination, brecciated vein fill, or stratiform mineralization. There were several good examples of net-texture ores observed in this study. Samples EG-181 (fig.5.33), Eagle-1 (fig. 5.34), SLC-55 (fig. 5.46) all display small scale net-texture (as small as 50 μm); for SLC-55 it only occurs in a portion of the sample. Samples DC (fig. 5.35), Bag-1 (fig. 5.37), V-1 (fig. 5.41), O-219 (fig. 5.43), SLC-55 (fig.5.45), and SLC-2476 (fig. 5.48) are all examples of disseminated ore mineral distribution. Bag-1 is very sparsely disseminated while V-1 is a very dense disseminated ore. DC is a very coarse-grained disseminated ore, while SLC-2476 appears to be bio-modal with two distinct grain sizes. Sample MVT-1 (fig. 5.52) is an example of brecciated vein fill where very coarse-grained ore is filling the gaps between brecciated carbonate gangue. Sample 1716 (fig. 5.55) illustrates an example of a stratiform ore that appears to preferentially occur in discrete layers of gangue, whereas other layers of gangue a merely represented as void space because they contain no ore particles.

These 3D reconstructions can also be used to identify structures within these cores that would be otherwise either obscured or altogether unobservable because of their small

size. Both samples Bag-1 (fig 5.40) and SLC-55 (fig 5.47) illustrate examples of microscopic microstructures that would be otherwise invisible to the naked eye. In both cases, a planar feature can be observed that may represent a small fault or slip surface functioning as fluid flow pathways that likely would go unrecognized using traditional methods of core description. Sample 1716 does exhibit a stratiform ore texture that projects upward into the sample creating a large blob like shape of ore particles that cut through layers that would otherwise be barren of ore (fig. 5.53). This feature appears to be a potential fluid pathway that allowed for the migration of metal-bearing fluids into different strata where they encountered conditions leading to the precipitation of ore.

6.3.2 Ore Grain Size Distributions Using Raw XRCT Data

In section 5.3.2, figures 5.56 through 5.65, ore grain size distributions generated for raw XRCT particle volume information are shown for each sample. All the samples seem to resemble an exponential function with a negative slope, with all the highest peaks in the smallest grains sizes quickly decreasing towards zero as the grain size increases. There were some issues with some samples that had interconnecting or touching particles. The XRCT counts these as one massive particle many magnitudes larger than the next largest grains making it difficult to display the data.

6.3.3 Shape Analysis

Chapter 5.3.3 contains all the shape analysis graphs and data have been summarized in Table 5.4. The purpose of the shape analysis is to see if any trend can be observed connecting the overall shape of ore grains and the types of ore deposits from which they originated. Most of the samples fall into a mixed category, containing roughly

equal portions of spherical and elongated grains (fig. 5.67, fig. 5.69, fig. 5.70, fig. 5.73, and fig. 5.74). The mixed group contained a liquid-magmatic (immiscible S-melt) sample with Eagle-1, two examples of porphyry (Bag-1 and V-1), an example of VHMS (SLC-2476), as well as the MVT sample. The only sample categorized a spherical is EG-181 (fig. 5.66) which represents a liquid-magmatic (Si-differentiation) deposit. There are four samples categorized as elongate (fig. 5.68, fig. 5.71, fig. 5.72, and fig. 5.75). DC represents a liquid-magmatic (immiscible S-melt) deposit, O-219 a porphyry, SLC-55 a VHMS, and 1716 an SSC deposit. Sample SLC-55 was barely categorized as elongate while 1716 was the most elongate of all the samples.

EG-181 is the only sample that can be categorized as spherical and it also represents the only sample that came from a Si-differentiation liquid-magmatic ore deposit. Processing additional examples from this type of deposit may reveal if this characterization is a valid ore deposition characteristic or has another cause. A comparison of EG-181 with Eagle-1 and DC, both of immiscible S-melt type liquid-magmatic origin, does not show any similarity, since Eagle-1 falls into the mixed category while DC falls into the elongate one. Since SLC-55 just falls into the elongate category it could be considered to belong to the mixed category and shares that same category as SLC-2476. Both represent VHMS deposits but originated from different locations with the deposit, with SLC-55 representing massive ore while SLC-2476 is from the stringer zone. 1716 had the most elongated grains of all the samples tested and is the only example of an SSC deposit. There could be potential for these shape analysis graphs to reveal characteristics for different deposit types and associated ore processing,

such as increased grinding requirements and higher energy input but more comprehensive testing needs to be performed to better evaluated the potential usefulness of this type of analysis.

6.3.4 Ore Grain Long Axis Orientation

In section 5.3.4 graphs for ore grain long axis orientations are shown (fig. 5.76 through 5.85). It is common practice in the geosciences to make observations about the orientations of the long axis of samples like stretched grains, or elongate pebbles. These types of observations can inform the careful field researcher as to the direction that shear stress was being exerted upon a region where stretched and aligned mineral grains are found or new mineral growth is observed. Noting a pattern of pebble long axis orientations within a paleo streambed can inform the observer of the paleo flow direction of water. It makes sense that in ore bodies that involve mineralizing fluids or a cooling magma it is possible that ore minerals may crystallize/precipitate with a preferred orientation. Would these moving hydrothermal fluids then orient the ore grains in the direction of the flow? Could these observations inform the researcher as to the direction of fluid flow during mineralization events or the extent of gravitational settling during magma chamber crystallization? This type of observation may not apply in all situations as is the case where larger veins are filled with ore, where crystals will nucleate on the wall of the vein and grow inward towards the center of the vein. What about the case of immiscible S-melts, where there is demixing and separate melts? What if there is still some flow or movement to one of these melts, will the ore grains present in such a

deposit retain an orientation that could potentially indicate the direction of a feeder structure from where the melt migrated?

The graphs can be divided into three different types. Of the ten samples scanned, there are samples that showed no apparent preferred grain orientations, some preferred orientations, and strong preferred orientations. All directions will be described as either positive or negative in x, y, or z direction because these descriptive terms directly apply to the graphs presented and none of samples have known orientations, with respect to sampling.

Samples EG-181 (fig. 5.76) and MVT-1 (fig.5.84) do not appear to display any pattern of preferred ore grain orientation. For EG-181 this result was to be expected since that sample was classified as dominantly spherical (sec.6.3.3). The results for MVT-1 are also expected as this is an example of an infill environment, more specifically filling brecciated zones. Because these brecciated zones are large and poorly defined there is no apparent ore grain orientation is expected.

There were three different samples that appeared to have at least some clusters of grains that were oriented in a preferred direction. Samples Bag-1 (fig. 5.74), O-219 (fig. 5.81), and SLC-2476 (fig. 5.83) all have at least some features that appear to have a preferred orientation. There is a planar feature present within Bag-1 as discussed earlier in section 6.3.1 and visible in the orientation graph. The planar feature is most easily observed if the 2D projections are inspected. If the light green (x, z) projection is inspected a linear feature can be observed where a majority of the grains that comprise this feature point in the positive z direction. If the red (x, y) projection is also inspected

another linear feature can be observed that points in a positive y direction. Both of these features on the 2D projections correspond to the same 3D feature so the planar feature in this case has ore grains that are oriented in an observable positive z and y direction. Sample O-219 has a number of small clusters that occur throughout the sample, and while there is no overall trend to ore grain orientations these clusters did appear to be oriented. The clusters within this sample all appear to have a preferred orientation that points in the positive x and y directions. These clusters could possibly represent an early generation of ore that precipitated while fluids were still moving or perhaps a later stage pulse of fluids that resulted in ore replacement; further research is needed to be able to provide a better interpretation. SLC-2476 contained two larger clusters of grains that appeared to have preferred orientations in the positive y and z directions, but otherwise appeared to be mostly randomly orientated.

Half of the samples that had their data displayed using this method appeared to have well defined preferred orientations to their ore grains. Samples Eagle-1 (fig. 5.77), DC (fig. 5.78), V-1 (fig. 5.80), SLC-55 (fig. 5.82), and 1716 (fig. 5.85) were all good examples of samples with well-defined ore grain orientations. Eagle-1 had a strong trend for its ore grains to be oriented in a positive z direction and this occurred throughout the entire sample, not just one particular region or cluster. This was a surprising result as this sample consisted of ore that formed a net-texture throughout the entire sample. Sample DC displays an overall orientation of grains that point in a positive x and y direction. There is also a rope-like cluster of grains that occurs near the bottom of the sample that has a similar orientation, with a slightly negative trend in the z direction. Sample V-1, as

can been seen in its hand sample (fig. 5.5), is highly altered with a wavy texture throughout the sample. This texture highlights the ore grain orientations (fig. 5.80). There are defined grain orientations in the ore for this sample, but they appear to flow and bend in a way that very closely resembles the alteration patterns of the hand sample. However, this pattern could also be the result of some later stage of deformation that occurred after the rock was hydrothermally altered. SLC-55 has an overwhelming trend that ore grains are oriented in a positive x direction. Within the layers 1716 there are positive x and y trends with no real z orientation. When observing the portion of the core where the layers are disturbed, and ore begins to occur throughout the entire z direction of the core, a huge variability in the z direction appears. There is no obvious trend to these orientations other than that they only appear within the region of the sample were ore begins to precipitate in otherwise barren layers.

The results are promising with respect to this technique having the potential to be a useful tool for the non-destructive determination of grain orientation. It does appear that some ore deposits have ore grains that are oriented in a preferred direction. However, more work needs to be completed to fully evaluate the usefulness of this technique. A key factor in making this technique more useful will be to use oriented core. With additional information it might be possible to discuss the effect that gravity had on any ore grain crystallization and the resulting ore textures.

7. Conclusions

Throughout the research performed during this project, 10 samples were selected that represented 3 different depositional environments and 6 different deposit types. All samples were processed using EPD technology and scanned using both XRCT and MLA. The primary goal of this research was to assess the efficiency at which EPD technology can be used to liberate ore minerals from gangue. There were also secondary goals of trying to determine if EPD processing truly preserves mineral grains boundaries and how these novel technologies could be used to aid in ore mineral characterization.

With respect to the primary goal of this research, there are no tangible conclusions that can be drawn. A review of published literate reveals that there is a consensus within the scientific community that EPD technology can generally liberate ore minerals more efficiently than traditional methods. However, since none of the research performed in this thesis involved traditional processing (e.g., crushing), it is difficult make a direct comparison between the two methods. An attempt was made to determine if there were any patterns to the efficiency of liberation by looking at different deposit types, but no obvious trend emerged that would indicate one deposit type is more efficiently liberated than others. A more comprehensive treatment of this research topic turned out to be beyond the scope of this thesis, but future research can utilize the research plan presented below by breaking down the plan into several BS and MS thesis topics.

With respect to the secondary goal of assessing EPD technology's ability to preserve mineral grain boundaries there is no unique outcome from the results obtained. This topic is also worth pursuing since after a review of published literature there does

not appear to be an overwhelming consensus on the matter. Conclusions could not be drawn because of the issues of XRCT data not being able to distinguish different ore types from one another, XRCT considering interconnected or touching particle to be one object, and the disaggregated material produced by EPD processing still containing silicate material. These data are worth revisiting and being analyzed using additional tools. If all the disaggregated material were to be processed using heavy liquid separation and sieve analyses, they could be compared to the XRCT sieve data. It is predicted that the error caused by XRCT counting multi-ore mineral grains as singular objects would be smaller compared to having all the silicate material included in the EPD sieve analyses. If ore minerals were isolated from the EPD data sets future research may determine if mineral grain boundaries are being persevered by comparing the sieve analyses of both the EPD and XRCT datasets.

In the consideration of the final goal, to observe whether any of these technologies could be useful in characterizing ore minerals, results allow preliminary interpretation. There is some evidence that different ore deposit types can have ore that has preferential shapes. However, more testing and research is needed to verify these overall trends. 3D reconstructions to identify micro-features within ore bodies and plotting ore grain orientations appear to be very useful for identifying potential deposit wide characteristics. In-depth studies on a deposit-wide scale will provide additional information about individual ore types, host rocks, alteration, intensity, and other deposition-related features.

7.1 Future Studies and Speculation

- It appears that the overall conductivity of a rock might play a key role in determining how well ore is liberated from the gangue. Almost all ore minerals are highly conductive but there is a fair amount of conductivity variation of the gangue. It would instructive to test what role conductivity plays by testing samples from the high conductivity ore bodies and lower conductive ore bodies that contained roughly similar ore mineralogy, grain size, and distribution/texture. A high conductivity ore body might contain more micas or pyroxene, while a less conductive one would contain mostly quartz and feldspars. These samples would be processed identical EPD settings and then have the ore liberation measured using MLA.
- Similar to the multi-stage EPD test performed in section 6.1.3, it would be useful to examine sample material from a single ore deposit, preferably monometallic (a chromite deposit is a possibility) and have them scanned using XRCT. With data exported from XRCT, analyze ore grain size information for the in-situ particles and process the samples using EPD technology. Process the samples in a multistage manner were each sample gets subjected to more pulses than the previous. Then scan each stage of the resulting material with MLA to determine if there a specific stage where adding more energy to the system, in the form of additional pulses, no longer results in a better liberation.
- A different study could look at ore deposits genesis. Samples would be collected throughout an entire ore deposit site and all samples scanned using XRCT or potentially high-resolution XRCT. 3D reconstructions of data would be used to

identify characteristic feature or structures that would be otherwise invisible and see if these could affect the genesis theory currently in use for that deposit.

- A shape analysis study where multiple samples are taken from a single deposit to see if there are any trends for the shape of ore grains within this deposit. If there is a pattern within the deposit acquire additional samples from different deposits, but of the same type, to see if there is a pattern to ore grain shape that could be associated with a deposit type. If patterns emerge for one deposit type, expand the research to begin testing other deposit types.

8. Bibliography

Anderson, G.M., 2008. The Mixing Hypothesis and the Origin of Mississippi Valley-Type Ore Deposits. Econ. Geol. Bull. Soc. Econ. Geol. 103, 1683–1690.

Anderson, G.M., 1991. Organic Maturation and Ore Precipitation in Southeast Missouri. Econ. Geol. Bull. Soc. Econ. Geol. 86, 909–926.

Andres, U., 2010. Development and Prospects of Mineral Liberation by Electrical Pulses. Int. J. Miner. Process. 97, 31–38.

Andres, U., 1995. Electrical Disintegration of Rock. Miner. Process. Extr. Metullargy Rev. 14, 87–110.

Andres, U., 1989. Parameters of Disintegration of Rock by Electrical Pulses. Powder Technol. 58, 265–269.

Andres, U., Bialecki, R., 1986. Liberation of Mineral Constituents by High-Voltage Pulses. Powder Technol. 48, 269–277.

Brenner, D.J., Hall, E.J., 2007. Computed tomography—an increasing source of radiation exposure. N. Engl. J. Med. 357, 2277–2284.

Brown, A.C., 1992. Sediment-hosted stratiform copper deposits. Geosci. Can. 19.

Cabri, L.J., Rudashevsky, N.S., Rudashevsky, V.N., Oberthür, T., 2008. Electric-Pulse Disaggregation (EPD), Hydroseparation (HS) and their use in combination for mineral processing and advanced characterization of ores, in: Canadian Mineral Processors 40th Annual Meeting, Proceedings. pp. 211–235.

Constable, S., Duba, A., 1990. Electrical conductivity of olivine, a dunite, and the mantle. J. Geophys. Res. Solid Earth 95, 6967–6978.

Ding, X., Li, C., Ripley, E.M., Rossell, D., Kamo, S., 2010. The Eagle and East Eagle sulfide ore-bearing mafic-ultramafic intrusions in the Midcontinent Rift System, upper Michigan: Geochronology and petrologic evolution. Geochem. Geophys. Geosystems 11.

Duba, A., Boland, J., Ringwood, A., 1973. The electrical conductivity of pyroxene. J. Geol. 81, 727–735.

Duke, J., 1983. Ore deposit models 7. Magmatic segregation deposits of chromite. Geosci. Can. 10.

Durand, C., Cerepi, A., Brosse, E., others, 2000. Effect of pore-lining chlorite on petrophysical properties of low-resistivity sandstone reservoir, in: SPE Annual Technical Conference and Exhibition. Society of Petroleum Engineers.

Fandrich, R., Gu, Y., Burrows, D., Moeller, K., 2007. Modern SEM-based mineral liberation analysis. Int. J. Miner. Process. 84, 310–320.

Galley, A.G., Hannington, M., Jonasson, I., 2007. Volcanogenic massive sulphide deposits.

Giese, J., Seward, D., Stuart, F.M., Wüthrich, E., Gnos, E., Kurz, D., Eggenberger, U., Schreurs, G., 2010. Electrodynamic Disaggregation: Does it Affect Apatite Fission-Track and (U-Th)/He Analyses? Geostand. Geoanalytical Res. 34, 39–48.

Godel, B., 2013. High-resolution X-ray computed tomography and its application to ore deposits: From data acquisition to quantitative three-dimensional measurements with case studies from Ni-Cu-PGE deposits. Econ. Geol. 108, 2005–2019.

González-Jiménez, J.M., Griffin, W.L., Proenza, J.A., Gervilla, F., O'Reilly, S.Y., Akbulut, M., Pearson, N.J., Arai, S., 2014. Chromitites in ophiolites: How, where, when, why? Part II. The crystallization of chromitites. Lithos 189, 140–158.

Hayes, T.S., Cox, D.P., Bliss, J.D., Piatak, N.M., Seal II, R.R., 2015. Sediment-hosted stratabound copper deposit model: Chapter M in Mineral deposit model for resource assessment. US Geological Survey.

Ketcham, R.A., Iturrino, G.J., 2005. Nondestructive high-resolution visualization and measurement of anisotropic effective porosity in complex lithologies using high-resolution X-ray computed tomography. J. Hydrol. 302, 92–106.

Large, R.R., 1992. Australian volcanic-hosted massive sulfide deposits; features, styles, and genetic models. Econ. Geol. Bull. Soc. Econ. Geol. 87, 471–510.

Lastra, R., Cabri, L.J., Weiblen, P.W., Lorenzen, L., Bradshaw, D., 2003. Comparative liberation study by image analysis of Merensky reef samples comminuted by electric-pulse disaggregation and by conventional crusher, in: Proceedings of the XXII International Mineral Processing Congress. pp. 251–260.

Leach, D.L., Taylor, R.D., Fey, D.L., Diehl, S.F., Saltus, R.W., 2010. A deposit model for Mississippi Valley-Type lead-zinc ores: Chapter A in Mineral deposit models for resource assessment. US Geological Survey.

Lu, Z., Zhu, J., Andrew Payzant, E., Paranthaman, M.P., 2005. Electrical conductivity of the manganese chromite spinel solid solution. J. Am. Ceram. Soc. 88, 1050–1053.

Maier, W.D., 2005. Platinum-group element (PGE) deposits and occurrences: Mineralization styles, genetic concepts, and exploration criteria. J. Afr. Earth Sci. 41, 165–191. https://doi.org/10.1016/j.jafrearsci.2005.03.004

Naldrett, A., 2010. Secular variation of magmatic sulfide deposits and their source magmas. Econ. Geol. 105, 669–688.

Naldrett, A.J., Duke, J.M., 1980. Platinum Metals in Magmatic Sulfide Ores. Science 208, 1417–1424.

Nesse, W.D., 2012. Optical Mineralogy, in: Introduction to Mineralogy. Oxford University Press, New York, p. 180.

Nordiana, M., Saad, R., Nawawi, M., Azwin, I., Mohamad, E.T., 2013. Case study: shallow subsurface geology mapping using 2-D resistivity imaging with EHR technique. APCBEE Procedia 5, 134–140.

Parkhomenko, E.I., 2012. Electrical properties of rocks. Springer Science & Business Media.

Pearce, C.I., Pattrick, R.A., Vaughan, D.J., 2006. Electrical and magnetic properties of sulfides. Rev. Mineral. Geochem. 61, 127–180.

Richards, J.P., 2011. Magmatic to hydrothermal metal fluxes in convergent and collided margins. Ore Geol. Rev. 40, 1–26.

Ridley, J., 2013. Ore Deposit Geology. Cambridge University Press, New York.

Rudashevsky, N., Burakov, B., Lupal, S., Thalhammer, O., 1995. Liberation of accessory minerals from various rock types by electric-pulse disintegration-method and application. Trans. Inst. Min. Metall. Sect. C Miner. Process. Extr. Metall. 104.

Saini-Eidukat, B., Weiblen, P.W., 1996. A New Method of Fossil Preparation, Using High-Voltage Electric Pulses. Curator Mus. J. 39, 139–144.

Sillitoe, R.H., 2010. Porphyry copper systems. Econ. Geol. 105, 3–41.

Spandler, C., Mavrogenes, J., Arculus, R., 2005. Origin of chromitites in layered intrusions: Evidence from chromite-hosted melt inclusions from the Stillwater Complex. Geology. 33.

Sperner, B., Jonckheere, R., Pfänder, J.A., 2014. Testing the influence of high-voltage mineral liberation on grain size, shape and yield, and on fission track and 40 Ar/39 Ar dating. Chem. Geol. 371, 83–95.

Sverjensky, D.A., 1986. Genesis of Mississippi Valley-type lead-zinc deposits. Annu. Rev. Earth Planet. Sci. 14, 177–199.

van der Wielen, K., Weh, A., Giese, H., Kappeler, J., 2014. High voltage breakage: A review of theory and applications, in: XXVII International Mineral Processing Congress-IMPC 2014. Gecamin Digital Publications.

Wang, E., Shi, F., Manlapig, E., 2012a. Mineral liberation by high voltage pulses and conventional comminution with same specific energy levels. Miner. Eng. 27, 28–36.

Wang, E., Shi, F., Manlapig, E., 2012b. Factors affecting electrical comminution performance. Miner. Eng. 34, 48–54.

Wang, E., Shi, F., Manlapig, E., 2011. Pre-weakening of mineral ores by high voltage pulses. Miner. Eng. 24, 455–462.

Weh, A., 2013. Pulsed HV fragmentation technology as an alternative treatment method for the glass industry.

Zhou, M.-F., Robinson, P.T., 1997. Origin and tectonic environment of podiform chromite deposits. Econ. Geol. Bull. Soc. Econ. Geol. 92, 259–262.

9. Appendix 1 – Additional Hand Sample Photos

All the photos below were taken because at the outset of this study many more samples were selected and processed through the EPD as this piece of equipment was only available to us for a short period of time. All the samples below had a portion removed and were disaggregated using the EPD. Each of these samples also had a sieve analysis conducted using the resulting disaggregated material. However, because of the financial constraints of this study none of the samples below were scanned in the XRCT.

SLC-1

Figure 9.1 Hand sample photo for SLC-1.

SLC-100

Figure 9.2 Hand sample photo for SLC-100.

O-257

Figure 9.3 Hand sample photo for O-257.

O-357

Figure 9.4 Hand sample photo for O-357.

O-537

Figure 9.5 Hand sample photo for O-537.

O-538

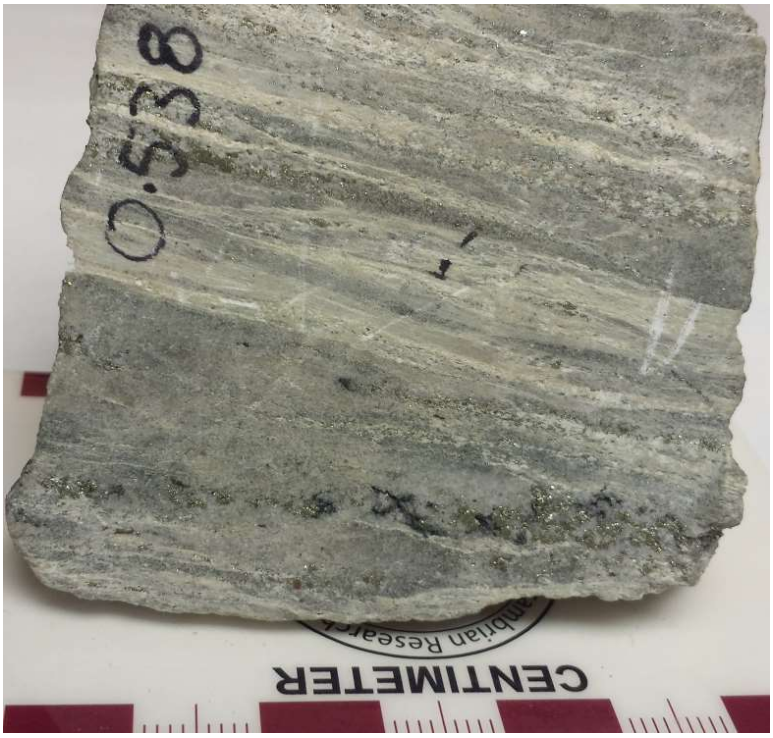

Figure 9.6 Hand sample photo for O-538.

O-551

Figure 9.7 Hand sample photo for O-551.

O-559

Figure 9.8 Hand sample photo for O-559.

O-569

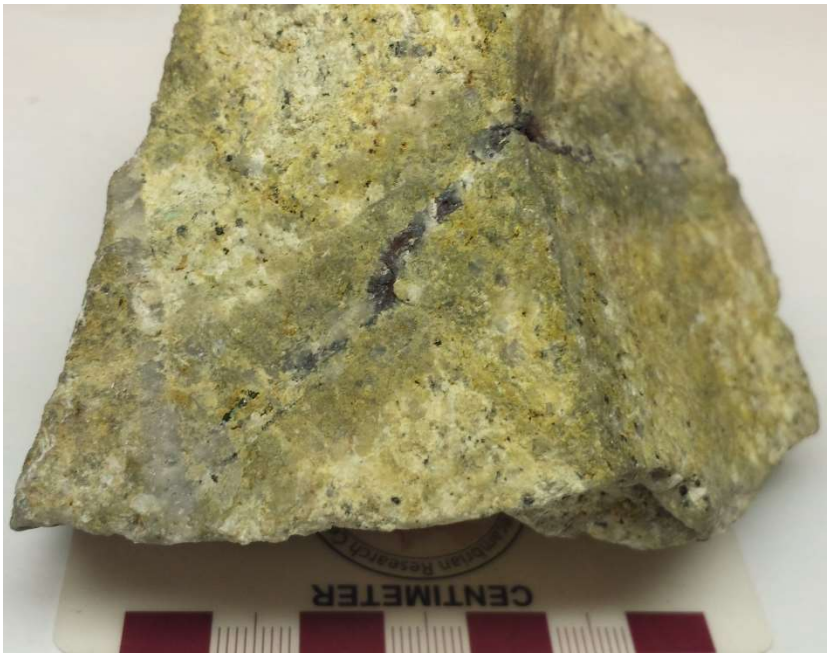

Figure 9.9 Hand sample photo for O-569.

1537

Figure 9.10 Hand sample photo for 1537.

2776

Figure 9.11 Hand sample photo for 2776.

DT-88a

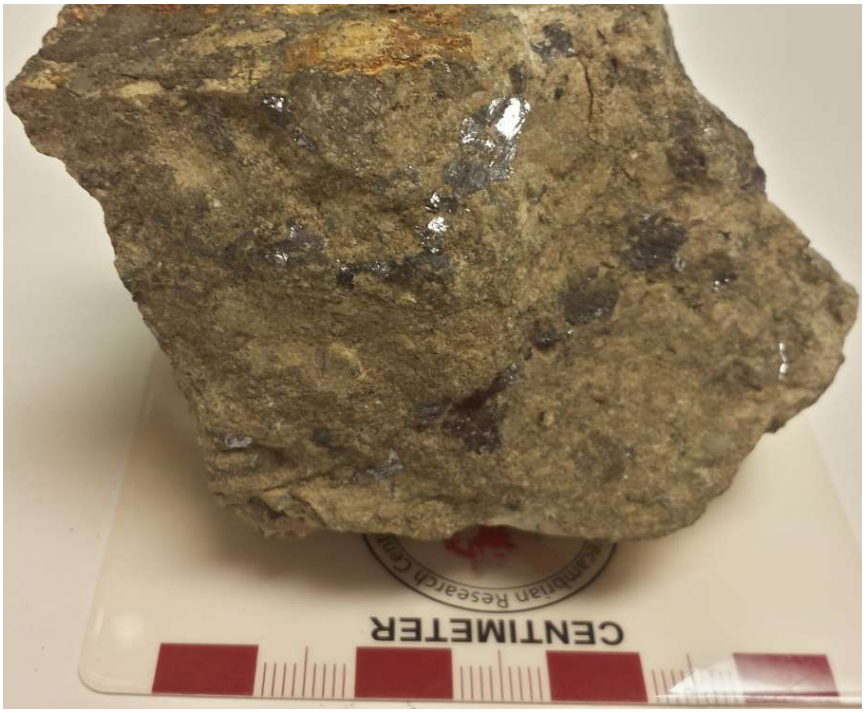

Figure 9.12 Hand sample photo for DT-88a.

Hel-3

Figure 9.13 Hand sample photo for Hel-3.

SOU-IF

Figure 9.14 Hand sample photo for SOU-IF.

G-1

Figure 9.15 Hand sample photo for G-1.

G-2

Figure 9.16 Hand sample photo for G-2

M

Figure 9.17 Hand sample photo for M.

QH-13

Figure 9.18 Hand sample photo for QH-13.

Z-552

Figure 9.19 Hand sample photo for Z-552.

Mica Pegmatite

Figure 9.20 Hand sample photo for Mica Pegmatite.

Sericite Schist

Figure 9.21 Hand sample photo for Sericite Schist.

Lake Ellen Kimberlite

Figure 9.22 Hand sample photo for Lake Ellen Kimberlite.

Slag

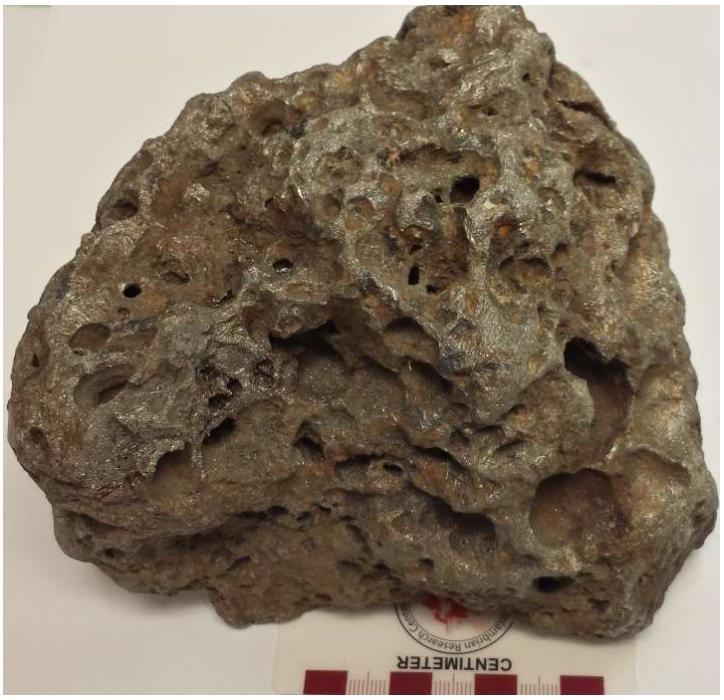

Figure 9.23 Hand sample photo for Slag

10. Appendix 2 – Additional EPD Settings

Tables 10.1 and 10.2 contain the EPD settings for all the additional samples that were processed using EPD but did not have the other procedures (XRCT and MLA) performed on them. The gap represents the distance between the anode and cathode which discharge the electric pulses. A smaller gap is preferred as this results in more consistent discharges. So, to achieve the smallest gap possible sample were initially set with a gap of roughly 40 mm and were then subjected to 20 lower voltage (140 kV) pulses to facilitate in the breakdown of the sample into smaller pieces. The samples then had their gap decreased (ideally to 20 mm but this was not always achieved) so that the main disaggregation could be performed using a higher number of pulses at 180 kV. The starting and ending weights record the loss of sample material either because of being trapped in the sample vessel (an unfortunate issue with how the vessel is designed) or by being suspended in the water bath which was not retained for these samples.

Sample Name	Gap (mm)	Number of Pulses	Voltage (kV)	Starting Weight (g)	Ending Weight (g)	Total Energy Discharged (J)
SLC-1	20	20	140			
	20	400	180	42.3	40.2	9.280×10^4
SLC-100	20	20	140			
	20	178	180	165.5	162.1	3.977×10^4
O-257	40	20	120			
	30	164	180	211.4	209.6	4.205×10^4
O-357	20	20	140			
	20	50	180	75.1	72.9	1.308×10^4
O-537	20	20	140			
	20	125	180	100.5	99.2	1.999×10^4
O-538	30	20	140			
	20	100	180	131.6	130.3	1.666×10^4
O-551	30	20	140			
	20	200	180	153.1	150.5	7.019×10^4
O-559	25	28	120			
	25	200	180	236.4	233.3	6.259×10^4
O-569	35	20	140			
	25	184	180	60.7	58.1	4.113×10^4
1537	40	25	140			
	25	200	180	294.2	292.1	6.171×10^4
2776	25	20	140			
	20	200	180	26.9	25.3	4.080×10^4
DT-88a	30	20	140			
	20	200	180	113.4	111.6	7.533×10^4
Hel-3	20	20	140			
	20	200	180	28.4	26.9	4.125×10^4
SOU-IF	40	25	140			
	40	170	180			
	25	146	180	163.5	160.6	7.801×10^4

Table 10.1) Recorded settings for additional samples processed using EPD along with starting and ending sample weights and total energy discharged by the machine. The gap is the distance between the anode and cathode which discharge the electric pulses. All samples had the additional setting of their frequency being set to 5 Hz, meaning there were 5 pulses discharged every second.

Sample Name	Gap (mm)	Number of Pulses	Voltage (kV)	Starting Weight (g)	Ending Weight (g)	Total Energy Discharged (J)
G-1	40	20	140			
	30	110	180			
	25	129	180	321.1	318.7	6.222×10^4
G-2	25	20	140			
	20	200	180	99.9	97.4	7.794×10^4
M	25	20	140			
	20	200	180	50.7	48.5	4.056×10^4
QH-13	20	20	140			
	20	200	180	62.3	61.4	3.577×10^4
Z-552	30	20	140			
	20	87	180	155	152.1	2.889×10^4
Mica Pegmatite	30	20	140			
	20	179	180	283.2	279.4	3.517×10^4
Sericite Schist	20	20	140			
	20	134	180	68.4	66.6	2.360×10^4
Lake Ellen Kimberlite	35	25	140			
	25	200	180	175.8	172.2	4.67×10^4
Slag	40	205	140			
	25	800	180	408.4	402.1	1.885×10^5

Table 10.2) Continued recorded settings for additional samples processed using EPD.

11. Appendix 3 – Additional Sieve Analyses

As referred to above in Appendix 1 there were several additional samples that were selected a processed through the EPD but ultimately not selected to be scanned in the XRCT. Below are sieve analyses for samples that were processed using the EPD but did not have any further analyses performed.

SLC-1

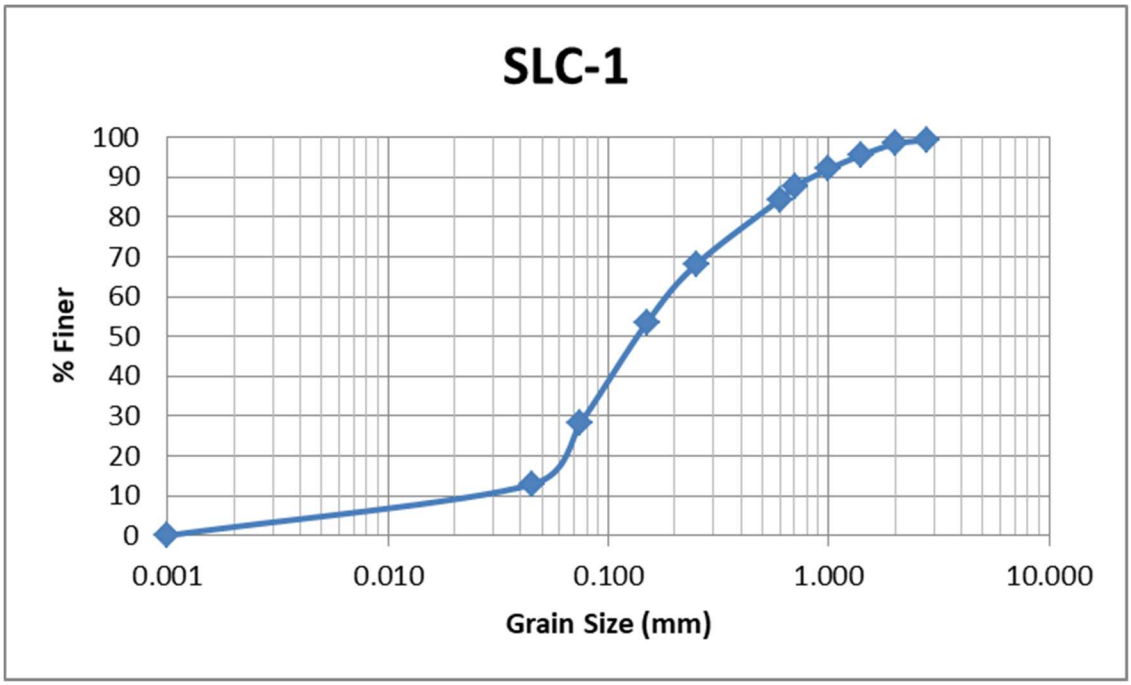

Figure 11.1 Sieve analysis for SLC-1.

SLC-100

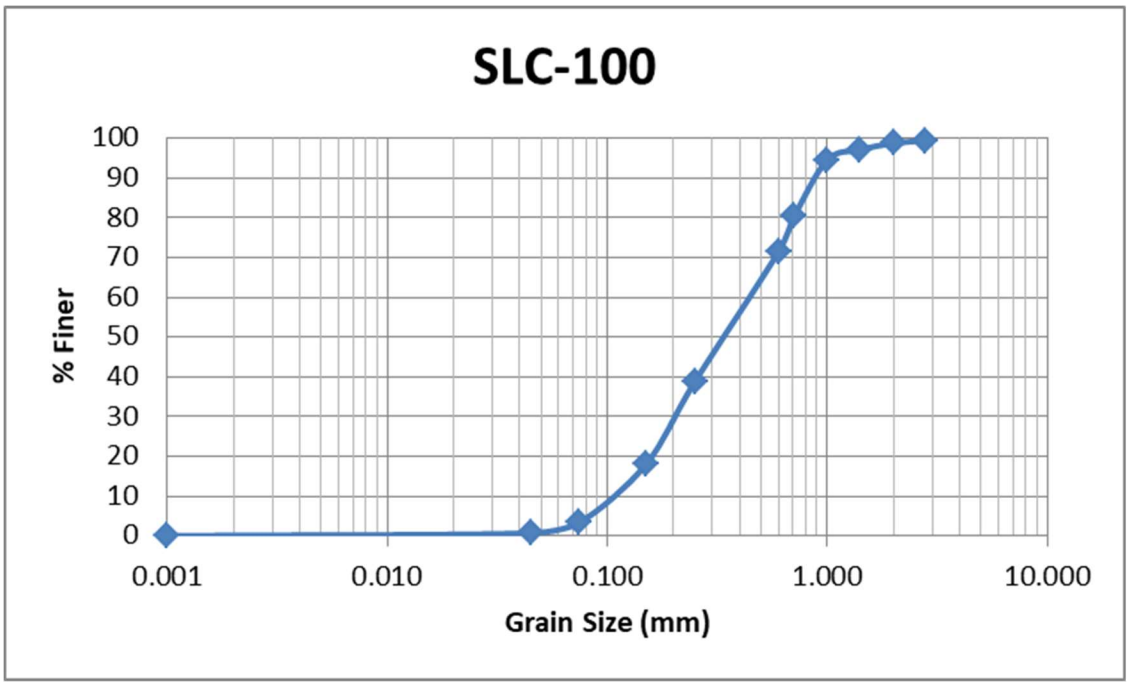

Figure 11.2 Sieve analysis for SLC-100.

O-257

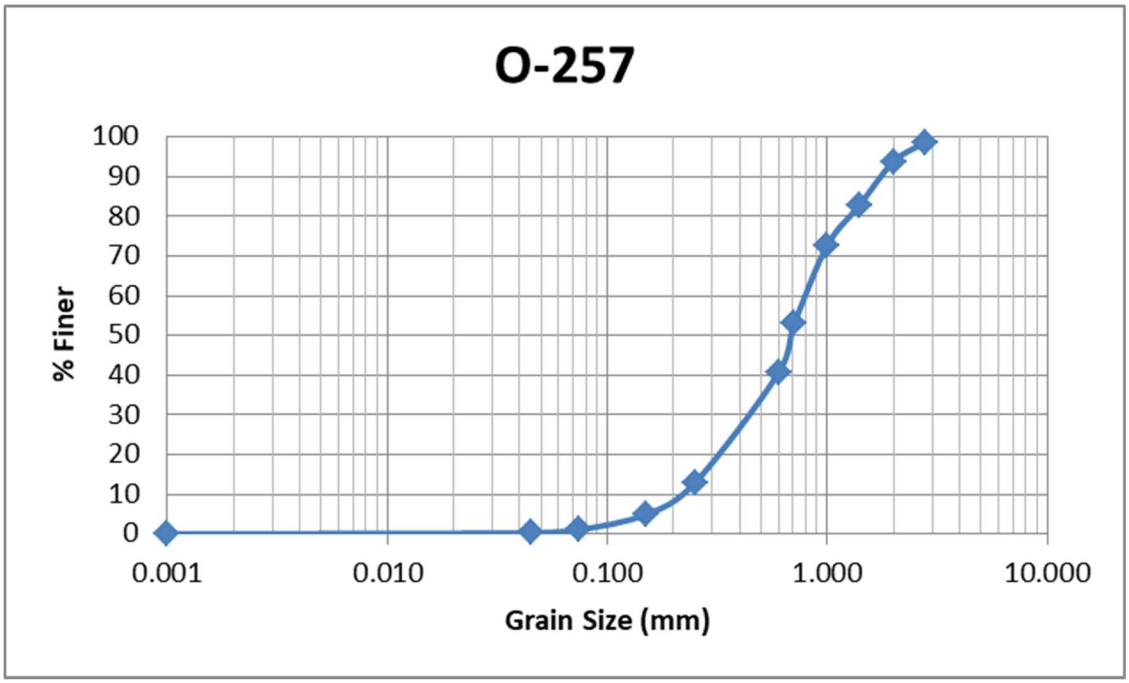

Figure 11.3 Sieve analysis for O-257.

O-357

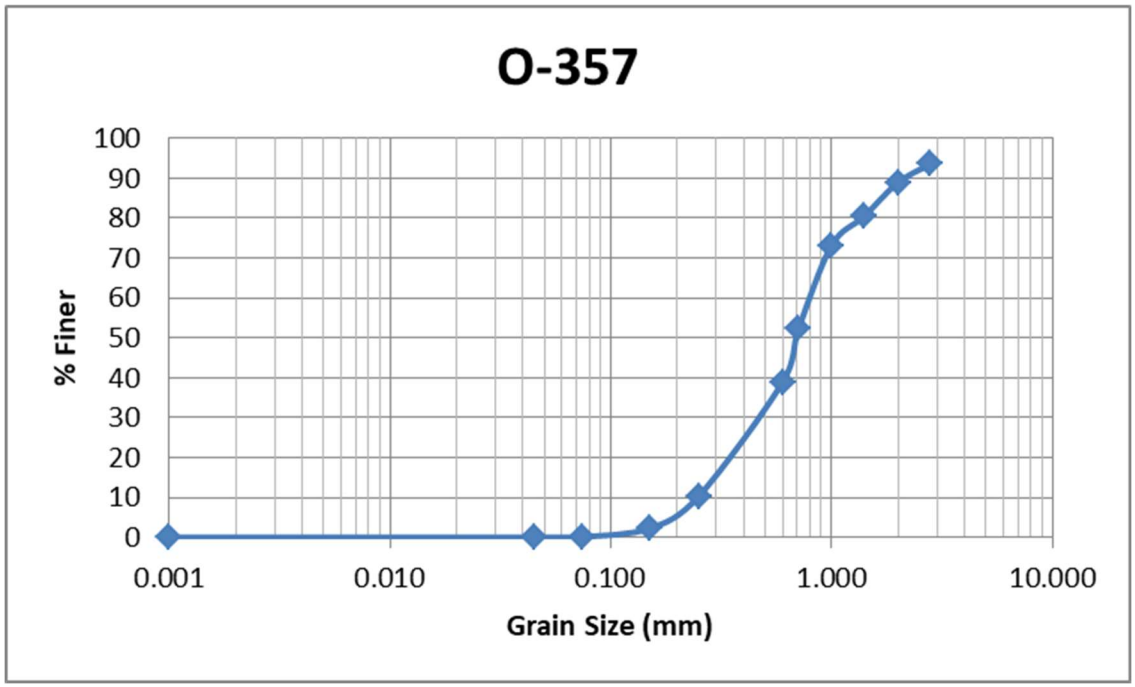

Figure 11.4 Sieve analysis for O-357.

O-537

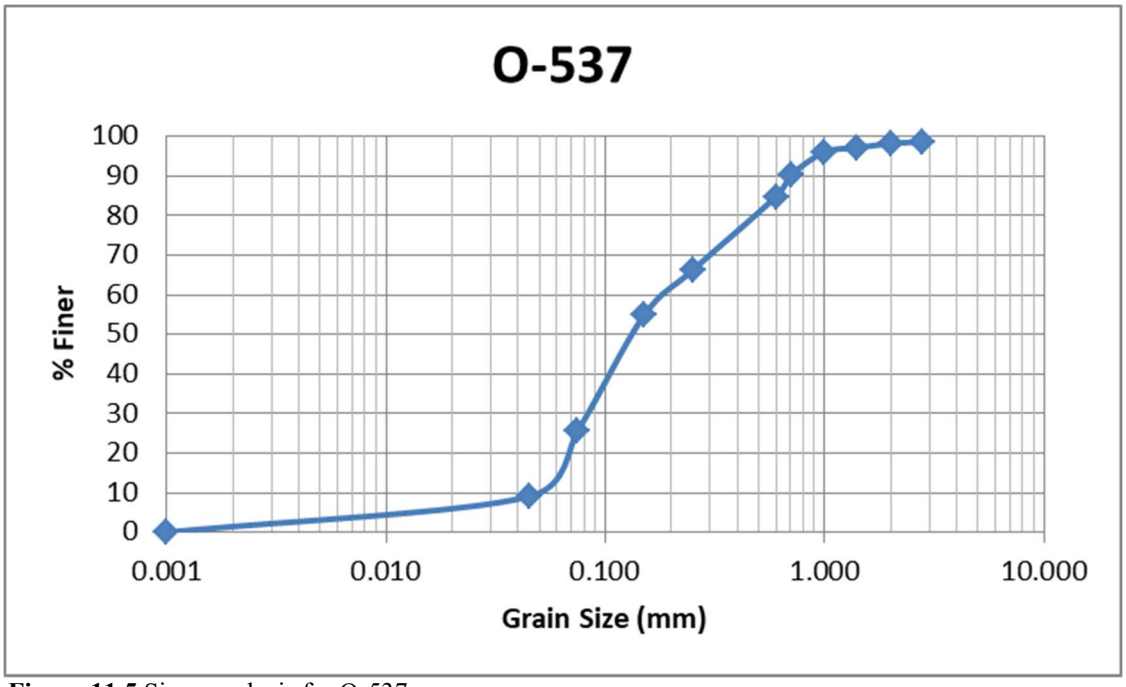

Figure 11.5 Sieve analysis for O-537.

O-538

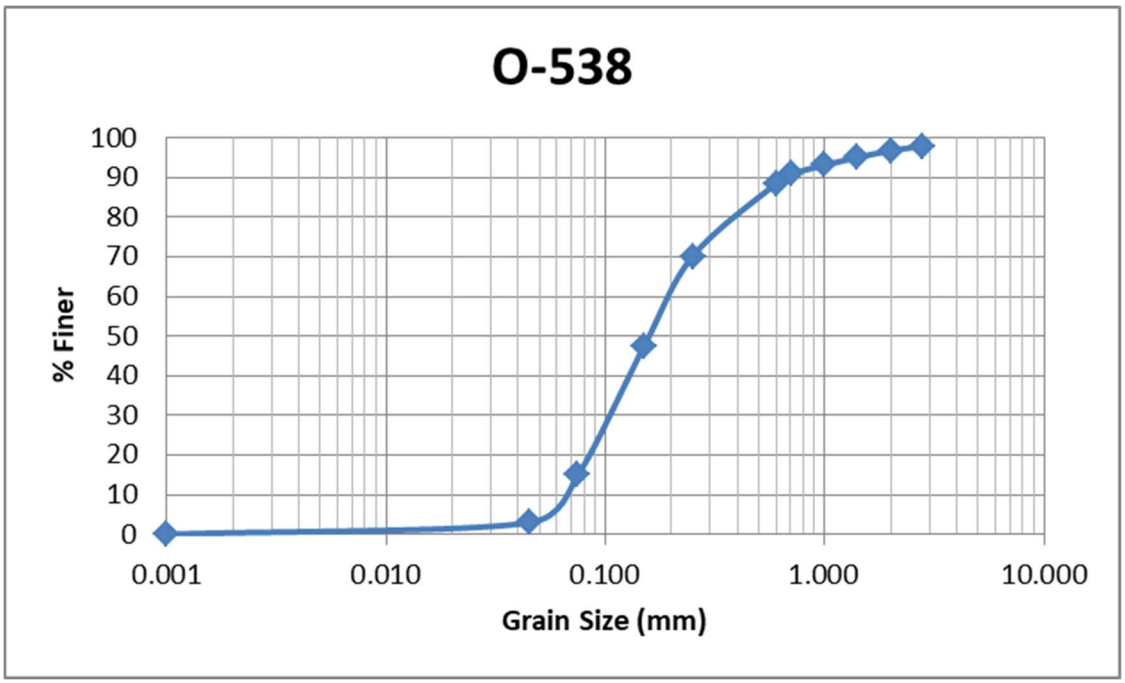

Figure 11.6 Sieve analysis for O-538.

O-551

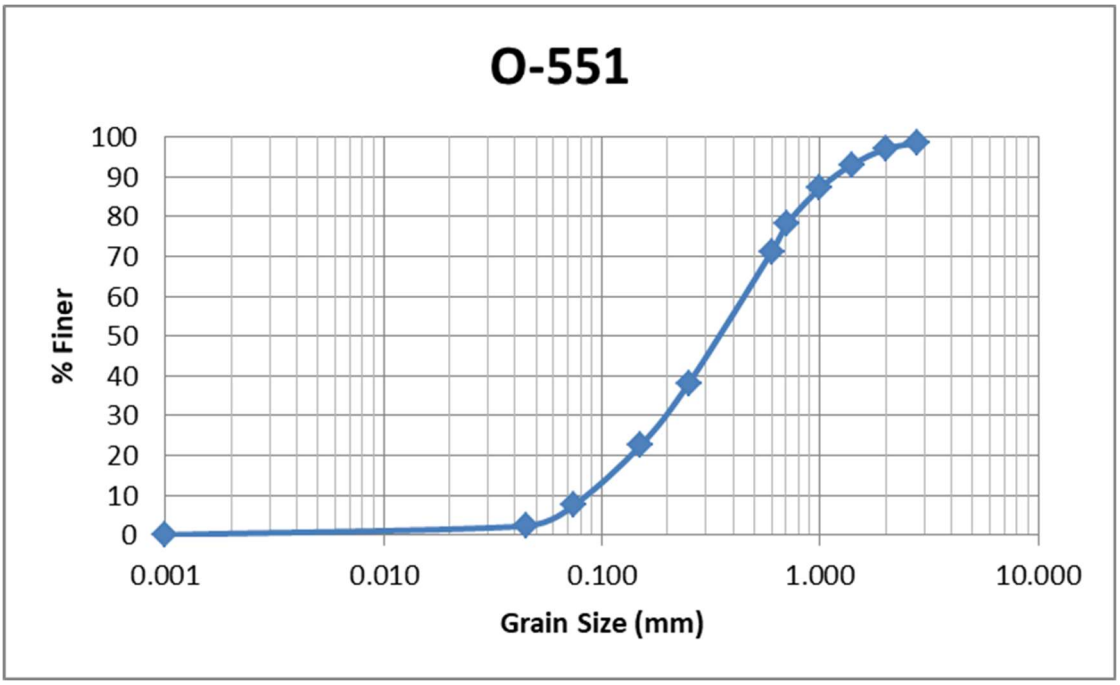

Figure 11.7 Sieve analysis for O-551.

O-559

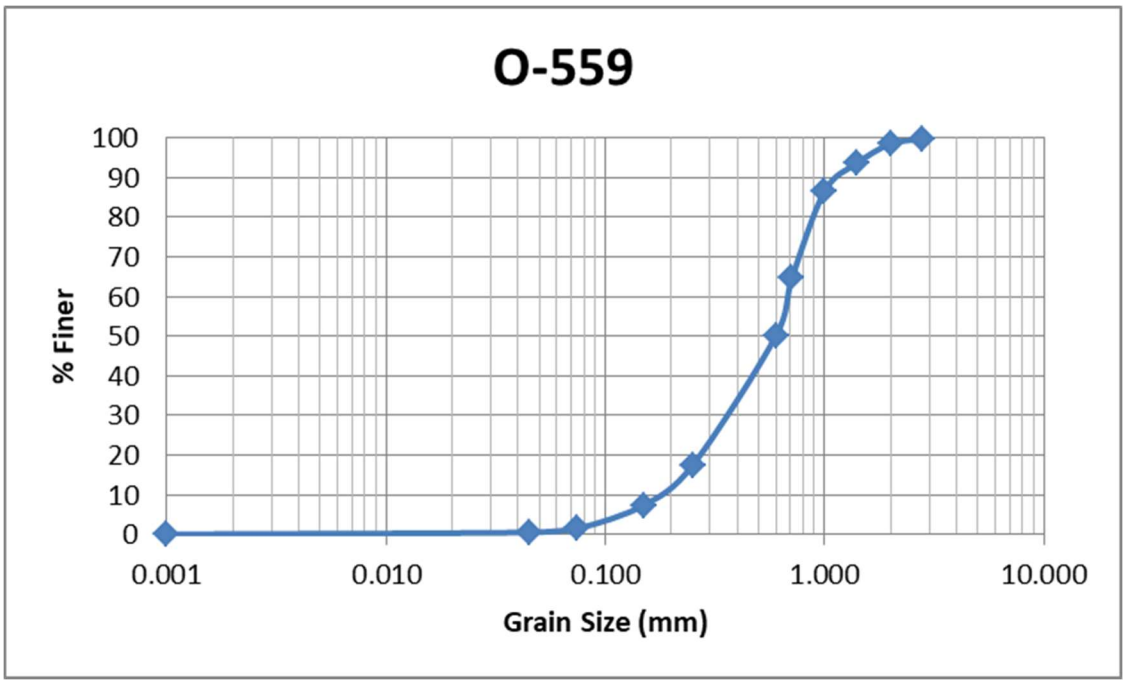

Figure 11.8 Sieve analysis for O-559.

O-569

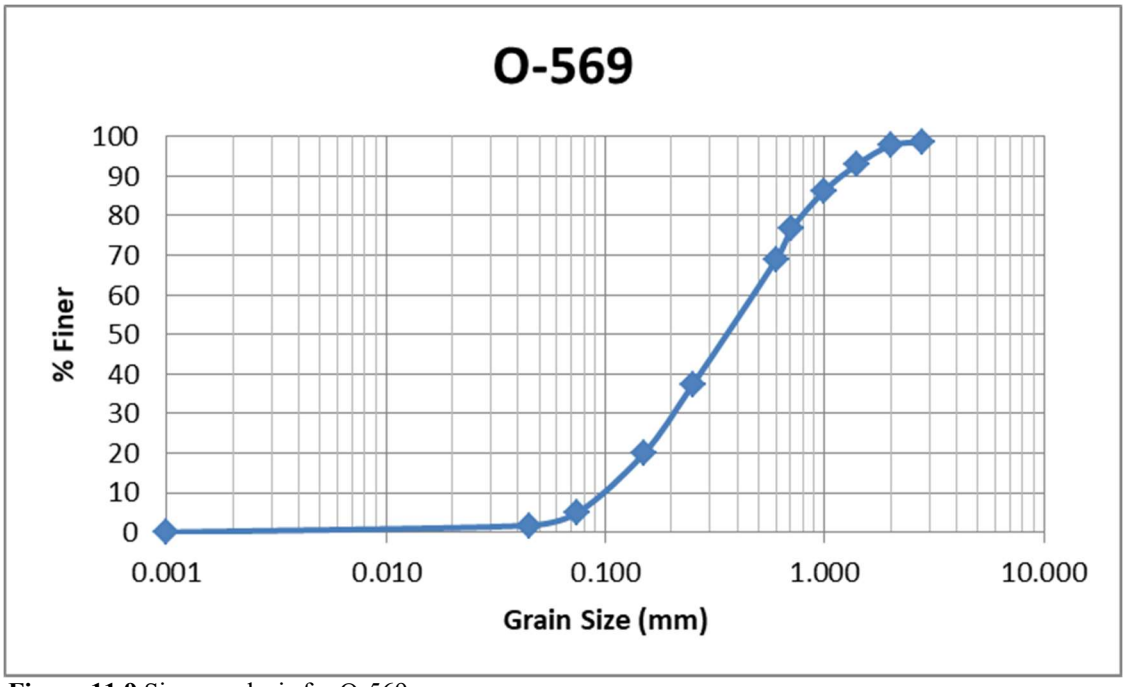

Figure 11.9 Sieve analysis for O-569.

1537

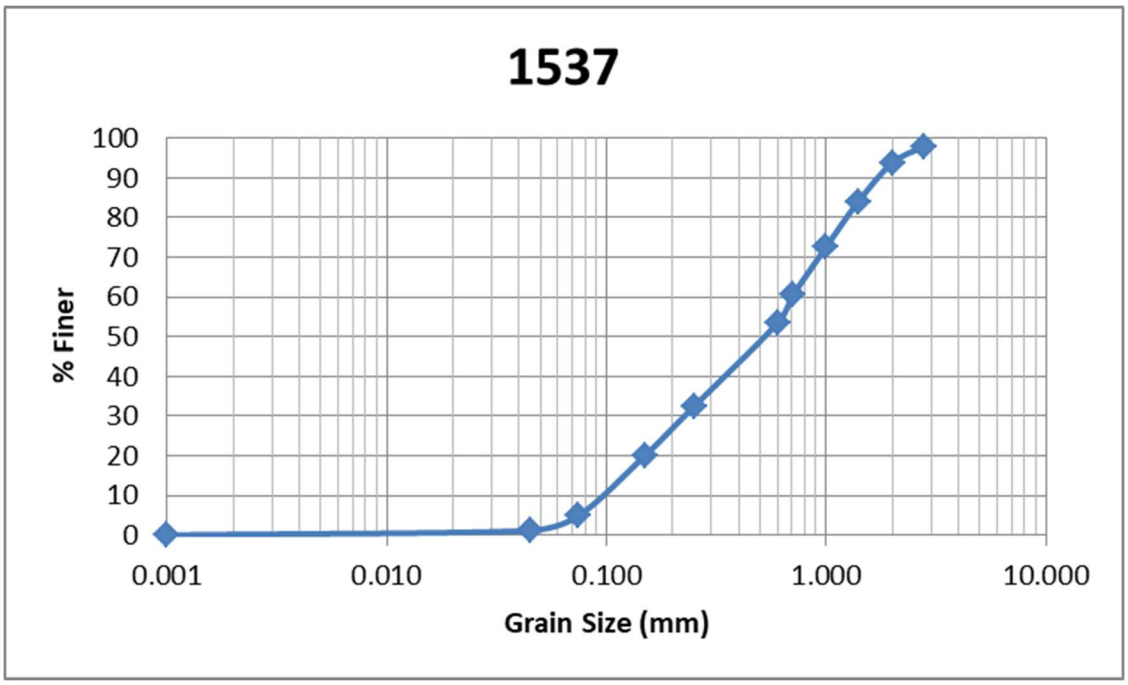

Figure 11.10 Sieve analysis for 1537.

2776

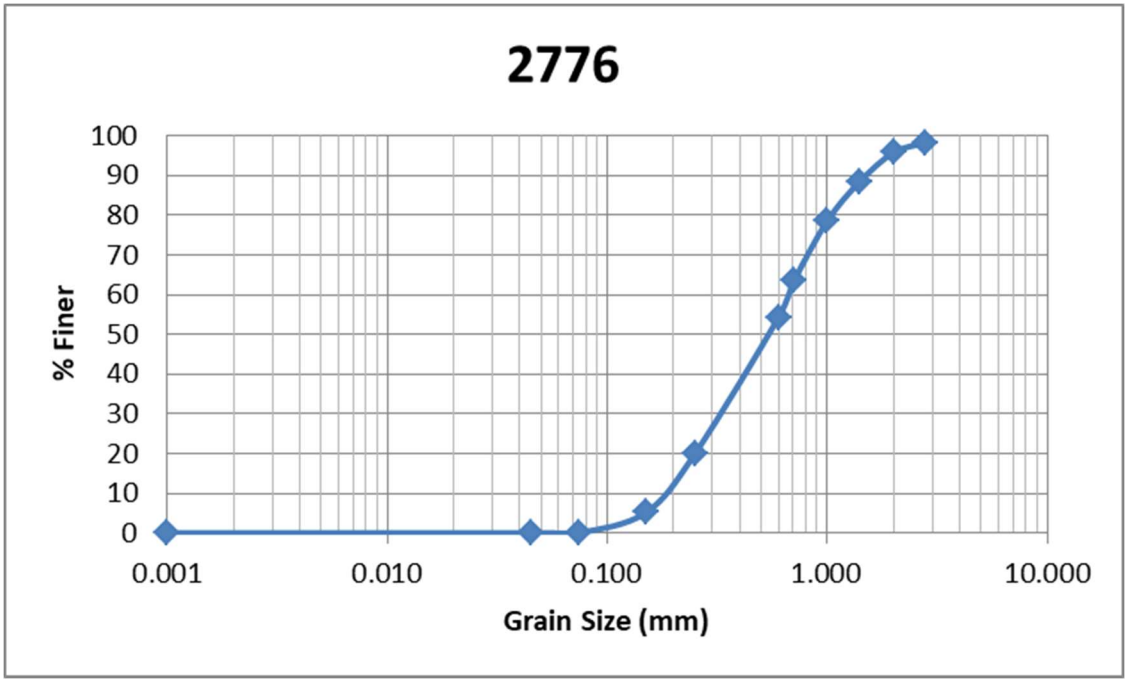

Figure 11.11 Sieve analysis for 2776.

DT-88a

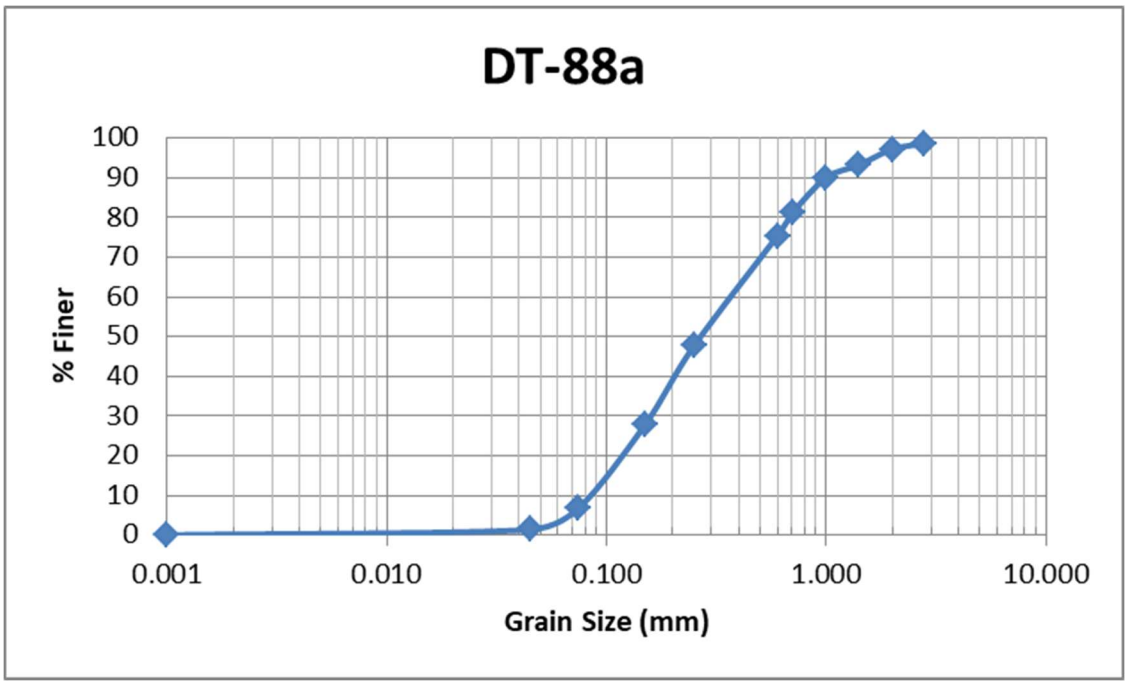

Figure 11.12 Sieve analysis for DT-88a.

Hel-3

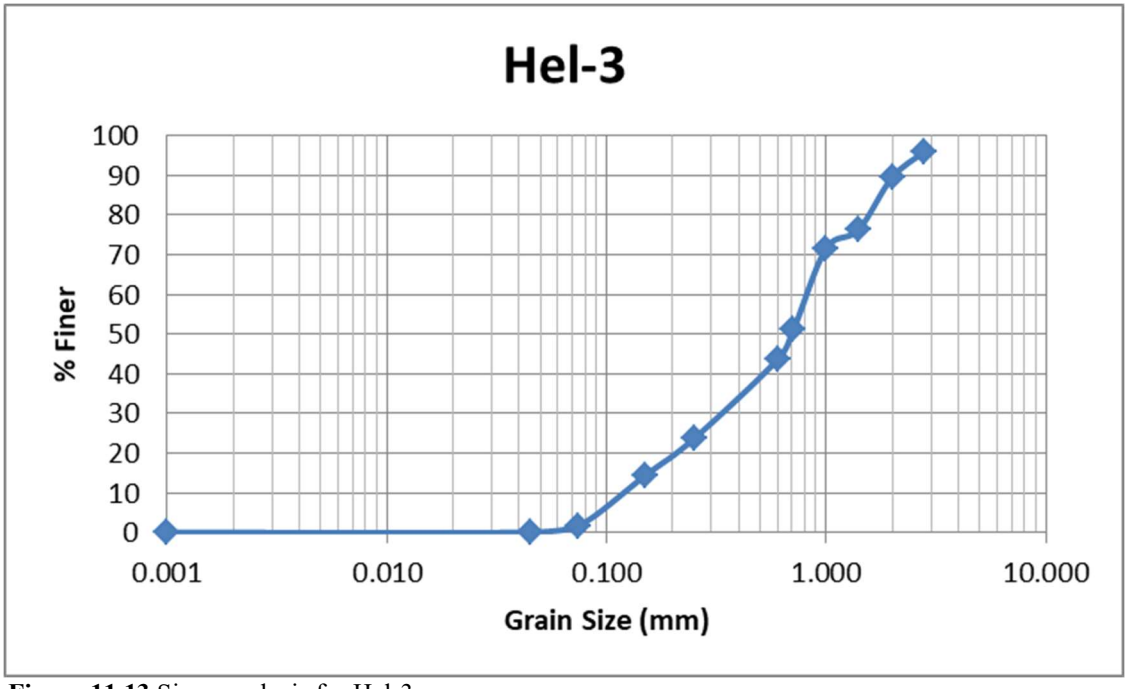

Figure 11.13 Sieve analysis for Hel-3.

SOU-IF

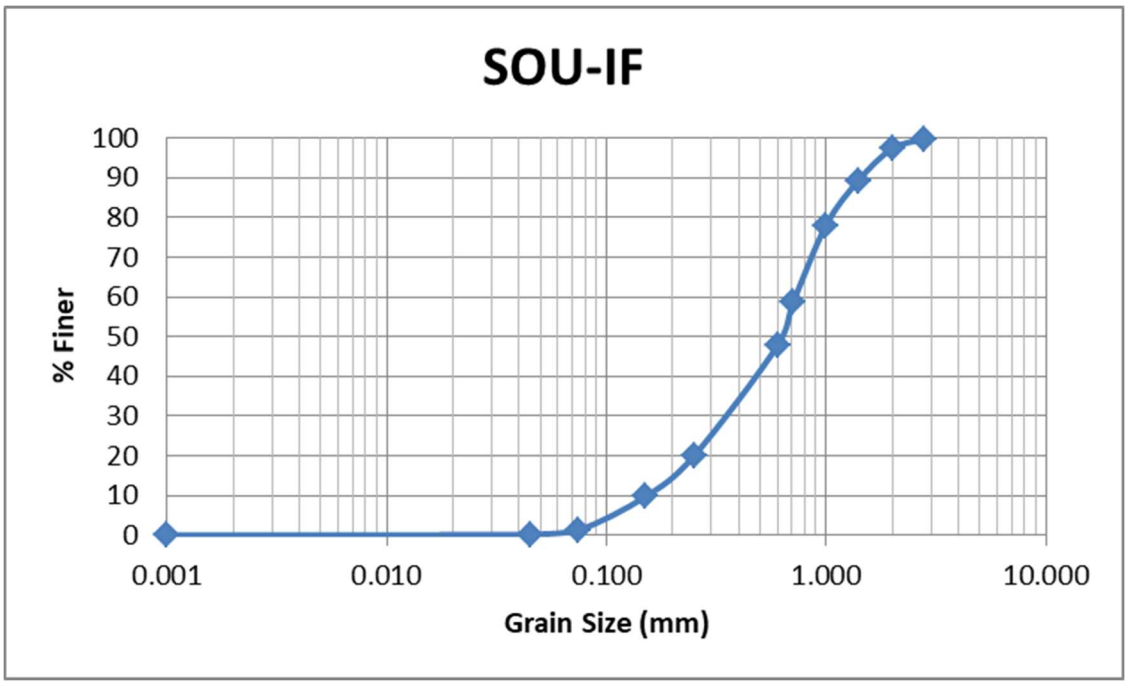

Figure 11.14 Sieve analysis for SOU-IF.

G-1

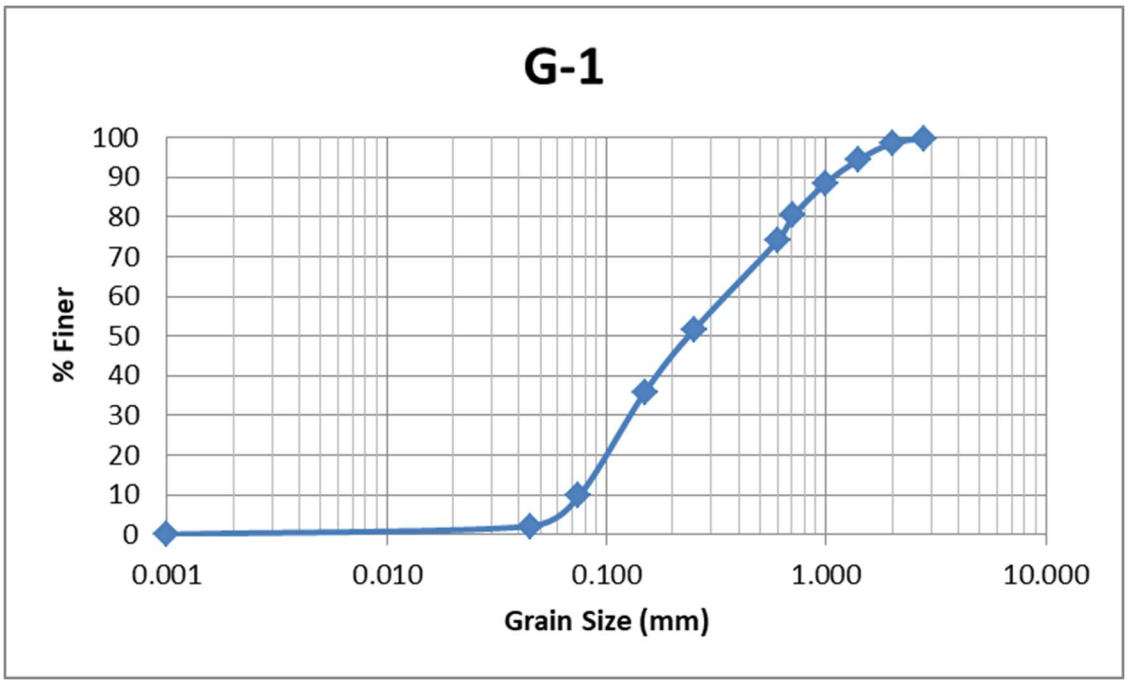

Figure 11.15 Sieve analysis for G-1.

G-2

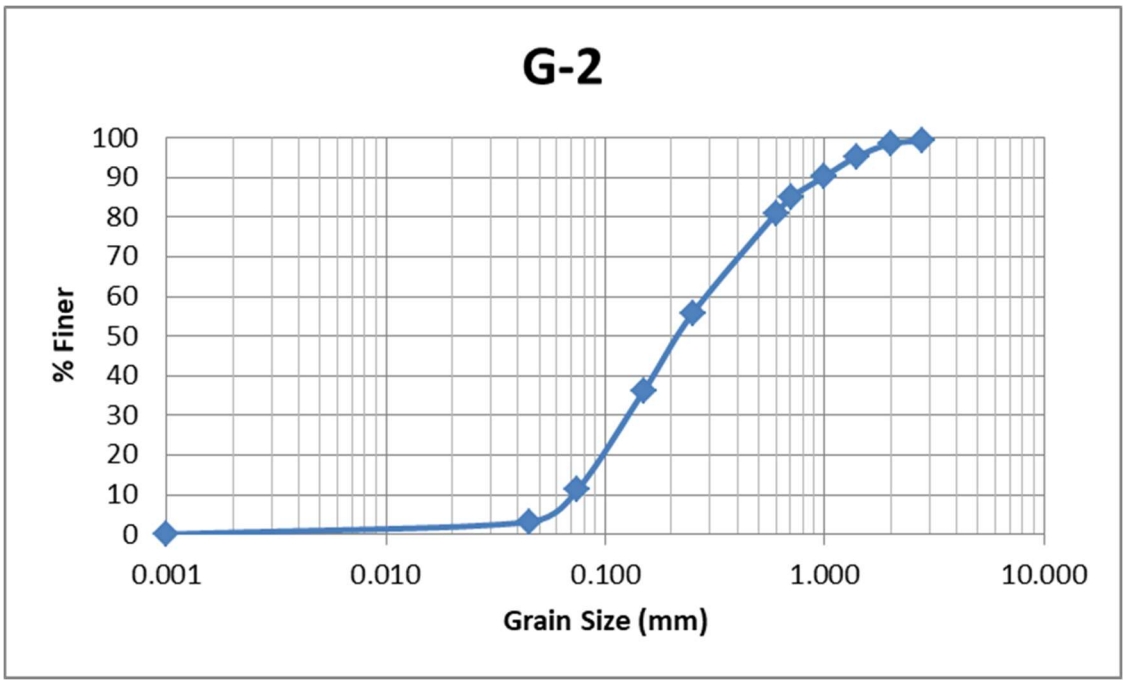

Figure 11.16 Sieve analysis for G-2.

M

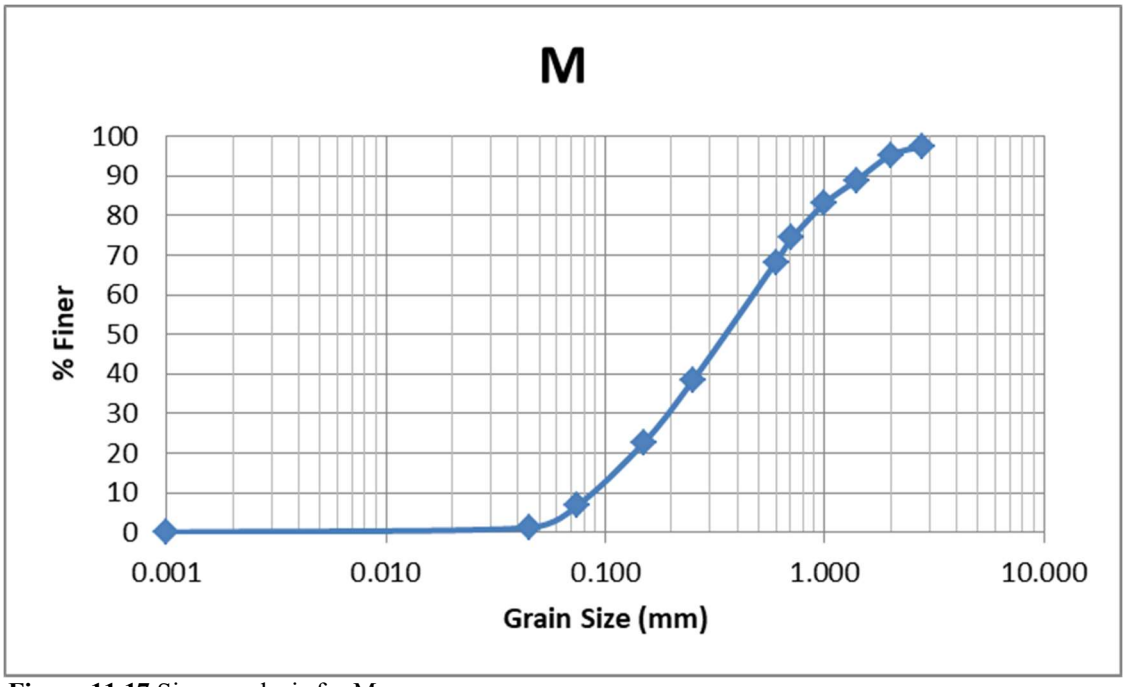

Figure 11.17 Sieve analysis for M.

QH-13

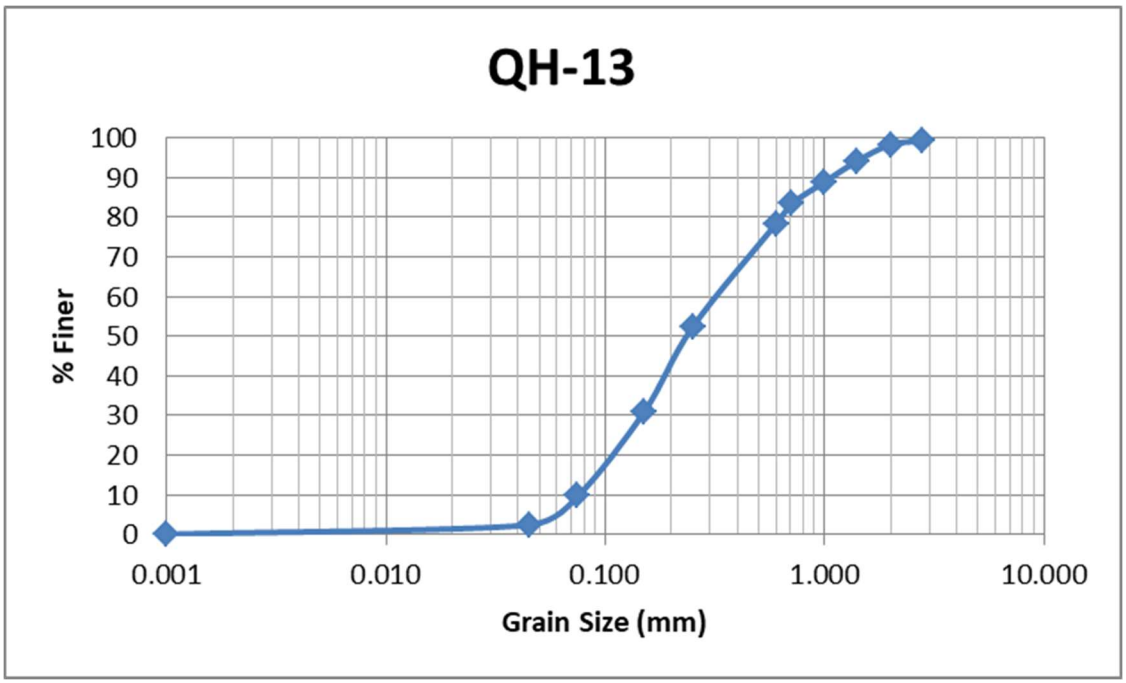

Figure 11.18 Sieve analysis for QH-13.

Z-552

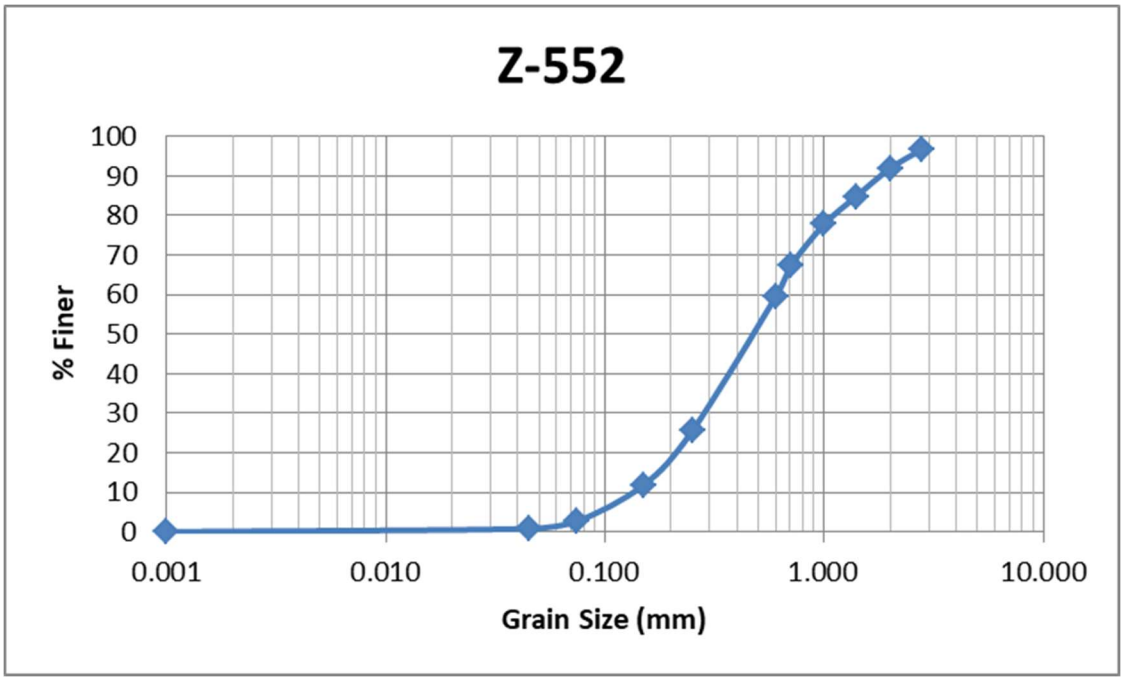

Figure 11.19 Sieve analysis for Z-552.

Mica Pegmatite

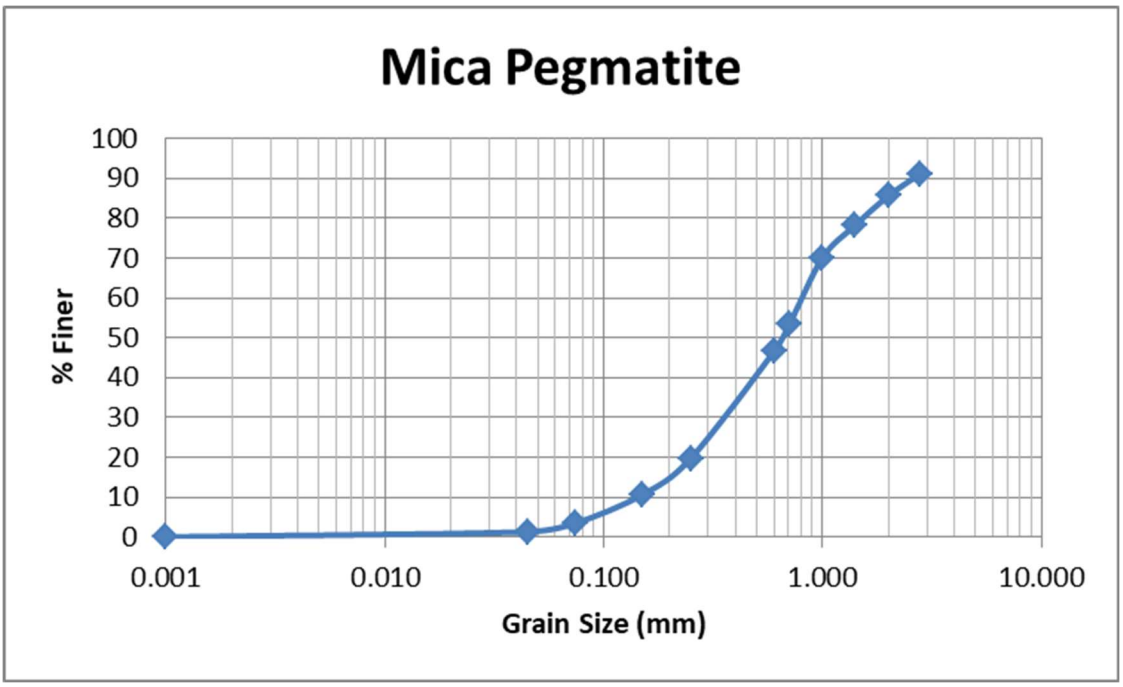

Figure 11.20 Sieve analysis for Mica Pegmatite.

Sericite Schist

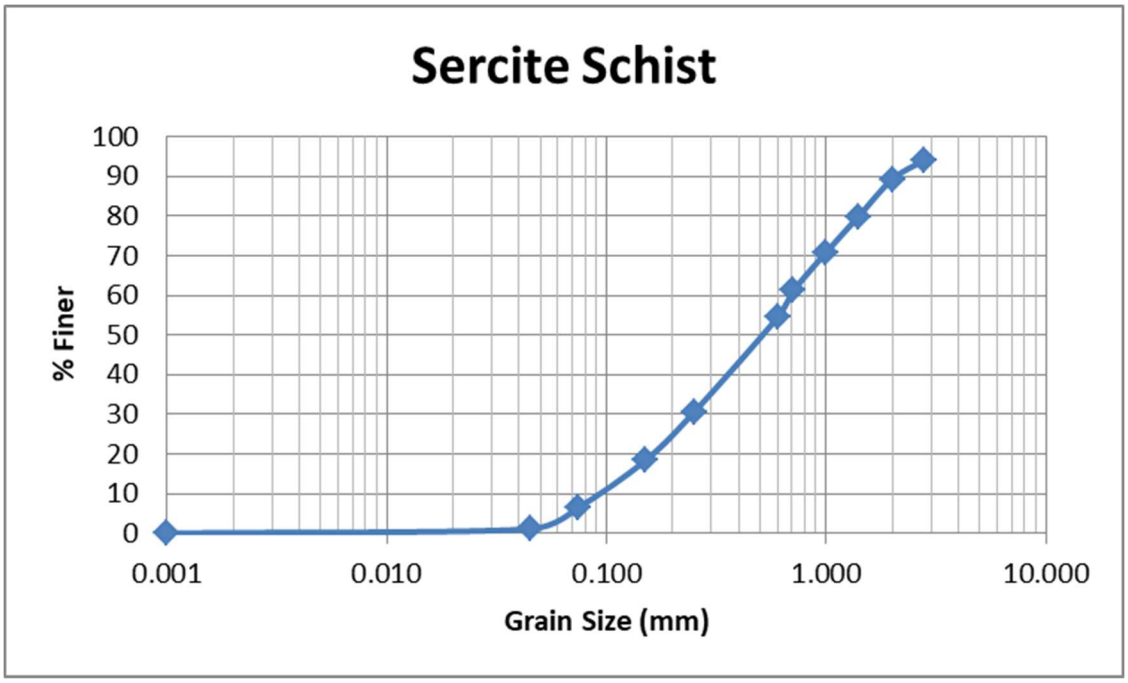

Figure 11.21 Sieve analysis for Sericite Schist.

Lake Ellen Kimberlite

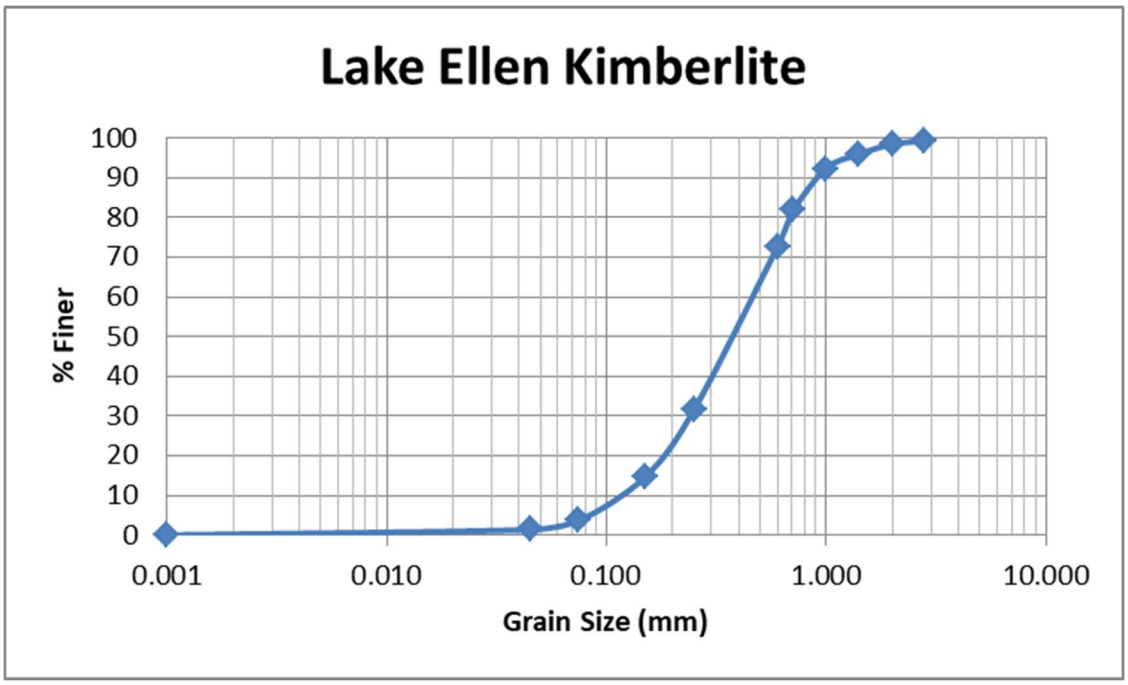

Figure 11.22 Sieve analysis for Lake Ellen Kimberlite.

Slag

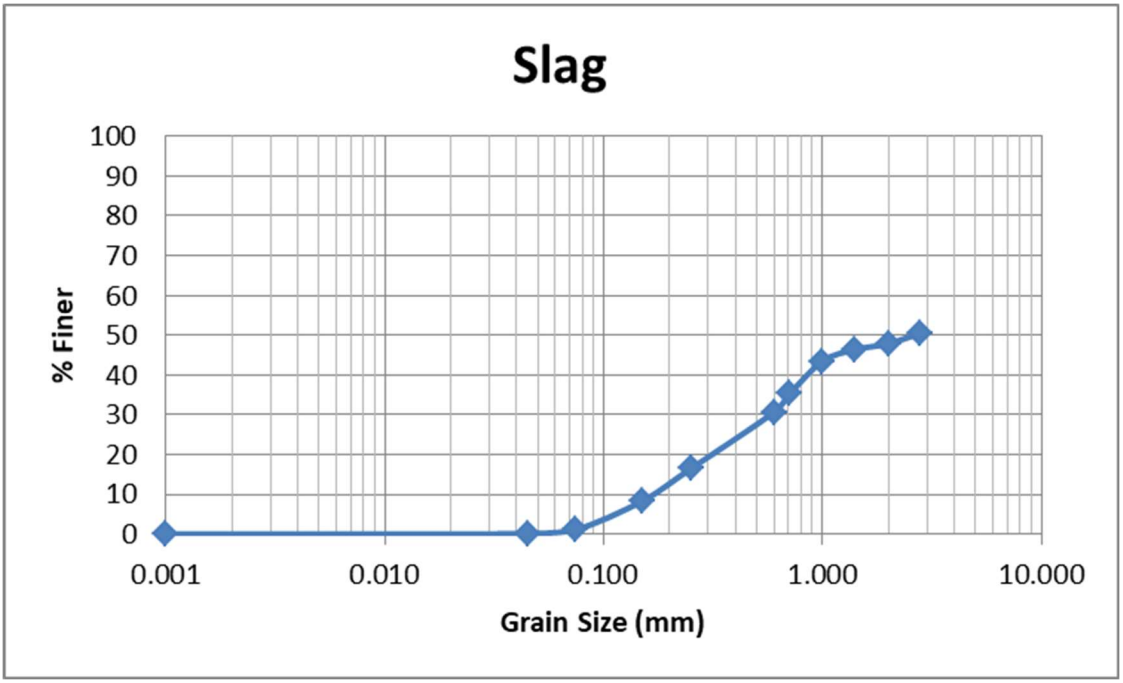

Figure 11.23 Sieve analysis for Slag.

12. Appendix 4 – XRCT

In sections 12.1 and 12.2 technical sheets that contain the various technical settings for each scan are presented. Section 12.3 contains additional photos of 3d reconstructions that were captured but not utilized in the main body of text.

12.1 Technique Sheets for XRCT Scans

Below are the technique sheets for each sample scanned in the XRCT. Information of interest contained within these sheets are the voltage, current, focal spot size, and filter used for each scan. These sheets also list the name of the detector installed in the XRCT and the distance that each sample was placed from the detector.

UMN XRCT
CT Acquisition
Technique Sheet
EG-181

Xray source: Feinfocus FXE
- voltage: 150 kV
- current: 225 µA
- focal spot size: 6 microns
- focal spot mode: n/a

Detector: Dexela 2923 [2237]
- pixel pitch: [75 x 75] microns
- mode: Sequence (Low gain)
- gain:
- binning: 1x1
- framerate: 2.3 fps (434.784 ms integration time)

- flip: horizontal
- rotation: none
- crop: none

- defect map: 89967 defective pixels (0.752805417032713%) (saved) (89967 defective pixels, 0.752805417032713%)
- offset map: 0.0971, dev 0.00556, 280 fravg, 2.3 fps (acquired 7/7/2016 10:22:53 AM)
- gain map 0: 0.741, dev 0.0535, 280 fravg, 2.3 fps (acquired 7/7/2016 10:25:55 AM)
- gain map 1: 0.398, dev 0.0282, 280 fravg, 2.3 fps (acquired 7/7/2016 10:28:13 AM)
- gain map 2: 0.0203, dev 0.00149, 280 fravg, 2.3 fps (acquired 7/7/2016 10:30:27 AM)

Distances:
- tube to detector: 800 [mm] (FDD)
- tube to part: 130 [mm] (FOD)
- calculated Ug: 0.03092 [mm](0.412 pixels)
- zoom factor: x6.15

Fixturing:
Filter: 200kv 30.0w 2.3 fps 1lr 1mm Al

CT Scan:
- project name: E:\EG-181\EG-181.nsipro
- type: step
- # projections: 1080
- # frames averaged: 3
- delay: 0 ms
- monitor xray down: max allowed image variation 5%
- start: 7/7/2016 11:26:57 AM
- end: 7/7/2016 12:10:23 PM
- duration: 43m26s

Notes:

Figure 12.1 Technique report for sample EG-181.

UMN XRCT
CT Acquisition
Technique Sheet
Eagle-1

Xray source: Feinfocus FXE
- voltage: 150 kV
- current: 225 µA
- focal spot size: 6 microns
- focal spot mode: n/a

Detector: Dexela 2923 [2237]
- pixel pitch: [75 x 75] microns
- mode: Sequence (Low gain)
- gain:
- binning: 1x1
- framerate: 2.3 fps (434.784 ms integration time)

- flip: horizontal
- rotation: none
- crop: none

- defect map: 89967 defective pixels (0.752805417032713%) (saved) (89967 defective pixels, 0.752805417032713%)
- offset map: 0.0971, dev 0.00556, 280 fravg, 2.3 fps (acquired 7/7/2016 10:22:53 AM)
- gain map 0: 0.741, dev 0.0535, 280 fravg, 2.3 fps (acquired 7/7/2016 10:25:55 AM)
- gain map 1: 0.398, dev 0.0282, 280 fravg, 2.3 fps (acquired 7/7/2016 10:28:13 AM)
- gain map 2: 0.0203, dev 0.00149, 280 fravg, 2.3 fps (acquired 7/7/2016 10:30:27 AM)

Distances:
- tube to detector: 800 [mm] (FDD)
- tube to part: 130 [mm] (FOD)
- calculated Ug: 0.03092 [mm](0.412 pixels)
- zoom factor: x6.15

Fixturing:
Filter: 200kv 30.0w 2.3 fps 1lr 1mm Al

CT Scan:
- project name: E:\Eagle-1\Eagle-1.nsipro
- type: step
- # projections: 1080
- # frames averaged: 3
- delay: 0 ms
- monitor xray down: max allowed image variation 5%
- start: 7/7/2016 10:33:39 AM
- end: 7/7/2016 11:17:32 AM
- duration: 43m53s

Notes:

Figure 12.2 Technique report for sample Eagle-1.

UMN XRCT
CT Acquisition
Technique Sheet
DC

Xray source: Feinfocus FXE
- voltage: 150 kV
- current: 225 µA
- focal spot size: 6 microns
- focal spot mode: n/a

Detector: Dexela 2923 [2237]
- pixel pitch: [75 x 75] microns
- mode: Sequence (Low gain)
- gain:
- binning: 1x1
- framerate: 2.3 fps (434.784 ms integration time)

- flip: horizontal
- rotation: none
- crop: none

- defect map: 89967 defective pixels (0.752805417032713%) (saved) (89967 defective pixels, 0.752805417032713%)
- offset map: 0.0951, dev 0.00553, 280 fravg, 2.3 fps (acquired 6/2/2016 11:17:35 AM)
- gain map 0: 0.73, dev 0.0428, 280 fravg, 2.3 fps (acquired 6/2/2016 11:21:06 AM)
- gain map 1: 0.44, dev 0.0258, 280 fravg, 2.3 fps (acquired 6/2/2016 11:23:26 AM)
- gain map 2: 0.0491, dev 0.00295, 280 fravg, 2.3 fps (acquired 6/2/2016 11:25:45 AM)

Distances:
- tube to detector: 775 [mm] (FDD)
- tube to part: 120 [mm] (FOD)
- calculated Ug: 0.03275 [mm](0.437 pixels)
- zoom factor: x6.46

Fixturing:
Filter: 200 kv 30 w 2.3 fps 1mm Al lr 1

CT Scan:
- project name: E:\DC\DC.nsipro
- type: step
- # projections: 1080
- # frames averaged: 3
- delay: 0 ms
- monitor xray down: max allowed image variation 5%
- start: 6/2/2016 11:28:38 AM
- end: 6/2/2016 12:16:46 PM
- duration: 48m08s

Notes:

Figure 12.3 Technique report for sample DC.

UMN XRCT
CT Acquisition
Technique Sheet
Bag-1

Xray source: Feinfocus FXE
- voltage: 150 kV
- current: 225 µA
- focal spot size: 6 microns
- focal spot mode: n/a

Detector: Dexela 2923 [2237]
- pixel pitch: [75 x 75] microns
- mode: Sequence (Low gain)
- gain:
- binning: 1x1
- framerate: 1.8 fps (555.554 ms integration time)

- flip: horizontal
- rotation: none
- crop: none

- defect map: 89967 defective pixels (0.752805417032713%) (saved) (89967 defective pixels, 0.752805417032713%)
- offset map: 0.0974, dev 0.00562, 200 fravg, 1.8 fps (acquired 6/1/2016 11:40:46 AM)
- gain map 0: 0.743, dev 0.0495, 200 fravg, 1.8 fps (acquired 6/1/2016 11:43:46 AM)
- gain map 1: 0.416, dev 0.0287, 200 fravg, 1.8 fps (acquired 6/1/2016 11:46:42 AM)
- gain map 2: 0.0654, dev 0.00445, 200 fravg, 1.8 fps (acquired 6/1/2016 11:48:49 AM)

Distances:
- tube to detector: 775 [mm] (FDD)
- tube to part: 120 [mm] (FOD)
- calculated Ug: 0.03275 [mm](0.437 pixels)
- zoom factor: x6.46

Fixturing:
Filter: 160 kv 24.5 w 1.8 fps 1mm Al lr 1

CT Scan:
- project name: E:\Bag-1\Bag-1.nsipro
- type: step
- # projections: 1080
- # frames averaged: 3
- delay: 0 ms
- monitor xray down: max allowed image variation 5%
- start: 6/1/2016 11:53:26 AM
- end: 6/1/2016 12:43:37 PM
- duration: 50m10s

Notes:

Figure 12.4 Technique report for sample Bag-1.

UMN XRCT
CT Acquisition
Technique Sheet
V-1

Xray source: Feinfocus FXE
- voltage: 150 kV
- current: 225 µA
- focal spot size: 6 microns
- focal spot mode: n/a

Detector: Dexela 2923 [2237]
- pixel pitch: [75 x 75] microns
- mode: Sequence (Low gain)
- gain:
- binning: 1x1
- framerate: 1.8 fps (555.554 ms integration time)

- flip: horizontal
- rotation: none
- crop: none

- defect map: 89967 defective pixels (0.752805417032713%) (saved) (89967 defective pixels, 0.752805417032713%)
- offset map: 0.0987, dev 0.00566, 210 fravg, 1.8 fps (acquired 7/7/2016 1:31:09 PM)
- gain map 0: 0.698, dev 0.0469, 210 fravg, 1.8 fps (acquired 7/7/2016 1:33:57 PM)
- gain map 1: 0.384, dev 0.0255, 210 fravg, 1.8 fps (acquired 7/7/2016 1:36:19 PM)
- gain map 2: 0.026, dev 0.00183, 210 fravg, 1.8 fps (acquired 7/7/2016 1:38:32 PM)

Distances:
- tube to detector: 800 [mm] (FDD)
- tube to part: 225 [mm] (FOD)
- calculated Ug: 0.01533 [mm](0.204 pixels)
- zoom factor: x3.56

Fixturing:
Filter: 200kv 24.5w 1.8 fps 1lr 1mm Al

CT Scan:
- project name: E:\V-1\V-1.nsipro
- type: step
- # projections: 1080
- # frames averaged: 3
- delay: 0 ms
- monitor xray down: max allowed image variation 5%
- start: 7/7/2016 1:41:24 PM
- end: 7/7/2016 2:32:13 PM
- duration: 50m48s

Notes:

Figure 12.5 Technique report for sample V-1.

UMN XRCT
CT Acquisition
Technique Sheet
O-219

Xray source: Feinfocus FXE
- voltage: 150 kV
- current: 225 µA
- focal spot size: 6 microns
- focal spot mode: n/a

Detector: Dexela 2923 [2237]
- pixel pitch: [75 x 75] microns
- mode: Sequence (Low gain)
- gain:
- binning: 1x1
- framerate: 1.8 fps (555.554 ms integration time)

- flip: horizontal
- rotation: none
- crop: none

- defect map: 89967 defective pixels (0.752805417032713%) (saved) (89967 defective pixels, 0.752805417032713%)
- offset map: 0.0974, dev 0.00562, 200 fravg, 1.8 fps (acquired 6/1/2016 11:40:46 AM)
- gain map 0: 0.743, dev 0.0495, 200 fravg, 1.8 fps (acquired 6/1/2016 11:43:46 AM)
- gain map 1: 0.416, dev 0.0287, 200 fravg, 1.8 fps (acquired 6/1/2016 11:46:42 AM)
- gain map 2: 0.0654, dev 0.00445, 200 fravg, 1.8 fps (acquired 6/1/2016 11:48:49 AM)

Distances:
- tube to detector: 775 [mm] (FDD)
- tube to part: 120 [mm] (FOD)
- calculated Ug: 0.03275 [mm](0.437 pixels)
- zoom factor: x6.46

Fixturing:
Filter: 160 kv 24.5 w 1.8 fps 1mm Al lr 1

CT Scan:
- project name: E:\0-219\0-219.nsipro
- type: step
- # projections: 1080
- # frames averaged: 3
- delay: 0 ms
- monitor xray down: max allowed image variation 5%
- start: 6/1/2016 2:04:44 PM
- end: 6/1/2016 2:55:29 PM
- duration: 50m45s

Notes:

Figure 12.6 Technique report for sample O-219.

UMN XRCT
CT Acquisition
Technique Sheet
SLC-55

Xray source: Feinfocus FXE
- voltage: 150 kV
- current: 225 µA
- focal spot size: 6 microns
- focal spot mode: n/a

Detector: Dexela 2923 [2237]
- pixel pitch: [75 x 75] microns
- mode: Sequence (Low gain)
- gain:
- binning: 1x1
- framerate: 2 fps (500.004 ms integration time)

- flip: horizontal
- rotation: none
- crop: none

- defect map: 89967 defective pixels (0.752805417032713%) (saved) (89967 defective pixels, 0.752805417032713%)
- offset map: 0.0964, dev 0.00559, 220 fravg, 2 fps (acquired 6/2/2016 2:03:19 PM)
- gain map 0: 0.715, dev 0.0427, 220 fravg, 2 fps (acquired 6/2/2016 2:06:20 PM)
- gain map 1: 0.375, dev 0.0224, 220 fravg, 2 fps (acquired 6/2/2016 2:08:44 PM)
- gain map 2: 0.0249, dev 0.00157, 220 fravg, 2 fps (acquired 6/2/2016 2:10:56 PM)

Distances:
- tube to detector: 775 [mm] (FDD)
- tube to part: 170 [mm] (FOD)
- calculated Ug: 0.02135 [mm](0.285 pixels)
- zoom factor: x4.56

Fixturing:
Filter: 200 kv 24.5 w 2.0 fps 1mm Al lr 0.5

CT Scan:
- project name: E:\SLC55\SLC55.nsipro
- type: step
- # projections: 1080
- # frames averaged: 3
- delay: 0 ms
- monitor xray down: max allowed image variation 5%
- start: 6/2/2016 2:13:45 PM
- end: 6/2/2016 3:01:55 PM
- duration: 48m09s

Notes:

Figure 12.7 Technique report for sample SLC-55.

UMN XRCT
CT Acquisition
Technique Sheet
SLC-2476

Xray source: Feinfocus FXE
- voltage: 150 kV
- current: 225 µA
- focal spot size: 6 microns
- focal spot mode: n/a

Detector: Dexela 2923 [2237]
- pixel pitch: [75 x 75] microns
- mode: Sequence (Low gain)
- gain:
- binning: 1x1
- framerate: 3.4 fps (294.114 ms integration time)

- flip: horizontal
- rotation: none
- crop: none

- defect map: 89967 defective pixels (0.752805417032713%) (saved) (89967 defective pixels, 0.752805417032713%)
- offset map: 0.0929, dev 0.00546, 400 fravg, 3.4 fps (acquired 6/2/2016 9:37:11 AM)
- gain map 0: 0.701, dev 0.0501, 400 fravg, 3.4 fps (acquired 6/2/2016 9:41:06 AM)
- gain map 1: 0.369, dev 0.0266, 400 fravg, 3.4 fps (acquired 6/2/2016 9:43:48 AM)
- gain map 2: 0.0408, dev 0.00287, 400 fravg, 3.4 fps (acquired 6/2/2016 9:46:03 AM)

Distances:
- tube to detector: 775 [mm] (FDD)
- tube to part: 120 [mm] (FOD)
- calculated Ug: 0.03275 [mm](0.437 pixels)
- zoom factor: x6.46

Fixturing:
Filter: 220 kv 40 w 3.4 fps 1mm Al lr 1

CT Scan:
- project name: E:\2476\2476.nsipro
- type: step
- # projections: 1080
- # frames averaged: 3
- delay: 0 ms
- monitor xray down: max allowed image variation 5%
- start: 6/2/2016 9:49:06 AM
- end: 6/2/2016 10:27:31 AM
- duration: 38m25s

Notes:

Figure 12.8 Technique report for sample SLC-2476.

UMN XRCT
CT Acquisition
Technique Sheet
MVT-1

Xray source: Feinfocus FXE
- voltage: 150 kV
- current: 225 µA
- focal spot size: 6 microns
- focal spot mode: n/a

Detector: Dexela 2923 [2237]
- pixel pitch: [75 x 75] microns
- mode: Sequence (Low gain)
- gain:
- binning: 1x1
- framerate: 2.3 fps (434.784 ms integration time)

- flip: horizontal
- rotation: none
- crop: none

- defect map: 89967 defective pixels (0.752805417032713%) (saved) (89967 defective pixels, 0.752805417032713%)
- offset map: 0.0971, dev 0.00556, 280 fravg, 2.3 fps (acquired 7/7/2016 10:22:53 AM)
- gain map 0: 0.724, dev 0.0527, 280 fravg, 2.3 fps (acquired 7/7/2016 12:27:31 PM)
- gain map 1: 0.398, dev 0.0282, 280 fravg, 2.3 fps (acquired 7/7/2016 10:28:13 AM)
- gain map 2: 0.0203, dev 0.00149, 280 fravg, 2.3 fps (acquired 7/7/2016 10:30:27 AM)

Distances:
- tube to detector: 800 [mm] (FDD)
- tube to part: 130 [mm] (FOD)
- calculated Ug: 0.03092 [mm](0.412 pixels)
- zoom factor: x6.15

Fixturing:
Filter: 200kv 30.0w 2.3 fps 1lr 1mm Al

CT Scan:
- project name: E:\Skarn\Skarn.nsipro
- type: step
- # projections: 1080
- # frames averaged: 3
- delay: 0 ms
- monitor xray down: max allowed image variation 5%
- start: 7/7/2016 12:30:18 PM
- end: 7/7/2016 1:13:31 PM
- duration: 43m12s

Notes:

Figure 12.9 Technique report for sample MVT-1.

UMN XRCT
CT Acquisition
Technique Sheet
1716

Xray source: Feinfocus FXE
- voltage: 150 kV
- current: 225 µA
- focal spot size: 6 microns
- focal spot mode: n/a

Detector: Dexela 2923 [2237]
- pixel pitch: [75 x 75] microns
- mode: Sequence (Low gain)
- gain:
- binning: 1x1
- framerate: 1.7 fps (588.234 ms integration time)

- flip: horizontal
- rotation: none
- crop: none

- defect map: 89967 defective pixels (0.752805417032713%) (saved) (89967 defective pixels, 0.752805417032713%)
- offset map: 0.0976, dev 0.00561, 200 fravg, 1.7 fps (acquired 6/1/2016 9:43:44 AM)
- gain map 0: 0.679, dev 0.0452, 200 fravg, 1.7 fps (acquired 6/1/2016 9:48:24 AM)
- gain map 1: 0.399, dev 0.0268, 200 fravg, 1.7 fps (acquired 6/1/2016 9:38:05 AM)
- gain map 2: 0.0603, dev 0.00396, 200 fravg, 1.7 fps (acquired 6/1/2016 9:40:33 AM)

Distances:
- tube to detector: 775 [mm] (FDD)
- tube to part: 120 [mm] (FOD)
- calculated Ug: 0.03275 [mm](0.437 pixels)
- zoom factor: x6.46

Fixturing:
Filter: 190 kv 24.5 w 1.7 fps 0.005" Cu lr 1

CT Scan:
- project name: E:\1716\1716.nsipro
- type: step
- # projections: 1080
- # frames averaged: 3
- delay: 0 ms
- monitor xray down: max allowed image variation 5%
- start: 6/1/2016 9:51:10 AM
- end: 6/1/2016 10:44:31 AM
- duration: 53m21s

Notes:

Figure 12.10 Technique report for sample 1716.

12.2 Calibration Reports for XRCT Scans

Below are the calibration reports for each sample scanned in the XRCT. Information of interest contained within these reports are the magnification and optimum voxel size.

EG-181
UMN XRCT
CT Calibration summary

Computation date: ..... 7/7/2016 12:21:55 PM

Tracking:: ..... 8 points used, over 60 views

Calibration tool: ..... Spacing [5]mm ([0.197] inches)

Detector pixel pitch: ..... 0.075x0.075 mm (0.00295x0.00295 inches)

Image modification: ..... H-flip

Xray-source / Detector distance: ..... 813.937 mm (32.045 inches)
Rotation axis / Detector distance: ..... 678.158 mm (26.699 inches)
Rotation axis / Xray-source distance: ..... 135.778 mm (5.346 inches)

Magnification: **x5.99**
Optimum voxel size: ..... 12.5 microns (0.0004926 inches)
Geometric unsharpness: x5
5 micron focal spot will be 24.97 micron wide (0.33 pixels)

Rotation: ..... Found Counter-Clockwise (CCW) rotation direction
Rotation axis: ..... -0.003872144864399860.9999925032189740
Rotation axis angle: ..... 179.778 degree

Image center: ..... (113.727, 144.935) mm / (4.477, 5.706) inches

Calibration images folder: ..... Calibration
Starting image used: ..... calib*.tif
60 images, 6 degree step

radiographs "Calibration\calib*.tif"
6 degree angle step (assuming a full 360 degree acquisition)

Figure 12.11 Calibration report for sample EG-181.

Eagle-1
UMN XRCT
CT Calibration summary

Computation date: ..... 7/7/2016 11:22:40 AM

Tracking:: ..... 8 points used, over 60 views

Calibration tool: ..... Spacing [5]mm ([0.197] inches)

Detector pixel pitch: ..... 0.075x0.075 mm (0.00295x0.00295 inches)

Image modification: ..... H-flip

Xray-source / Detector distance: ..... 809.606 mm (31.874 inches)
Rotation axis / Detector distance: ..... 674.564 mm (26.558 inches)
Rotation axis / Xray-source distance: ..... 135.042 mm (5.317 inches)

Magnification: **x6**
Optimum voxel size: ..... 12.5 microns (0.0004925 inches)
Geometric unsharpness: x5
5 micron focal spot will be 24.98 micron wide (0.33 pixels)

Rotation: ..... Found Counter-Clockwise (CCW) rotation direction
Rotation axis: ..... -0.00389984171817646 -0.9999923955883730
Rotation axis angle: ..... 179.777 degree

Image center: ..... (113.609, 144.772) mm / (4.473, 5.7) inches

Calibration images folder: ..... Calibration
Starting image used: ..... calib*.tif
60 images, 6 degree step

radiographs "Calibration\calib*.tif"
6 degree angle step (assuming a full 360 degree acquisition)

Figure 12.12 Calibration report for sample Eagle-1.

DC
UMN XRCT
CT Calibration summary

Computation date: ..... 6/2/2016 12:22:30 PM

Tracking:: ..... 8 points used, over 60 views

Calibration tool: ..... Spacing [5]mm ([0.197] inches)

Detector pixel pitch: ..... 0.075x0.075 mm (0.00295x0.00295 inches)

Image modification: ..... H-flip

Xray-source / Detector distance: ..... 782.09 mm (30.791 inches)
Rotation axis / Detector distance: ..... 658.018 mm (25.906 inches)
Rotation axis / Xray-source distance: ... 124.072 mm (4.885 inches)

Magnification: **x6.3**
Optimum voxel size: ..... 11.9 microns (0.0004684 inches)
Geometric unsharpness: x5.3
5 micron focal spot will be 26.52 micron wide (0.35 pixels)

Rotation: ..... Found Counter-Clockwise (CCW) rotation direction
Rotation axis: ..... -0.00397405634911515 -0.9999921034068890
Rotation axis angle: ..... 179.772 degree

Image center: ..... (114.146, 144.665) mm / (4.494, 5.695) inches

Calibration images folder: ..... Calibration
Starting image used: ..... calib*.tif
60 images, 6 degree step

radiographs "Calibration\calib*.tif"
6 degree angle step (assuming a full 360 degree acquisition)

Figure 12.13 Calibration report for sample DC.

Bag-1
UMN XRCT
CT Calibration summary

Computation date: ..... 6/1/2016 1:00:53 PM

Tracking:: ..... 8 points used, over 60 views

Calibration tool: ..... Spacing [5]mm ([0.197] inches)

Detector pixel pitch: ..... 0.075x0.075 mm (0.00295x0.00295 inches)

Image modification: ..... H-flip

Xray-source / Detector distance: ..... 786.726 mm (30.973 inches)
Rotation axis / Detector distance: ..... 661.776 mm (26.054 inches)
Rotation axis / Xray-source distance: ... 124.95 mm (4.919 inches)

Magnification: **x6.3**
Optimum voxel size: ..... 11.9 microns (0.000469 inches)
Geometric unsharpness: x5.3
5 micron focal spot will be 26.48 micron wide (0.35 pixels)

Rotation: ..... Found Counter-Clockwise (CCW) rotation direction
Rotation axis: ..... -0.0036386168853403 -0.99999338021167 0
Rotation axis angle: ..... 179.792 degree

Image center: ..... (114.465, 144.831) mm / (4.506, 5.702) inches

Calibration images folder: ..... Calibration
Starting image used: ..... calib*.tif
60 images, 6 degree step

radiographs "Calibration\calib*.tif"
6 degree angle step (assuming a full 360 degree acquisition)

Figure 12.14 Calibration report for sample Bag-1.

V-1
UMN XRCT
CT Calibration summary

Computation date: ..... 7/7/2016 2:40:07 PM

Tracking:: ..... 15 points used, over 60 views

Calibration tool: ..... Spacing [5]mm ([0.197] inches)

Detector pixel pitch: ..... 0.075x0.075 mm (0.00295x0.00295 inches)

Image modification: ..... H-flip

Xray-source / Detector distance: ..... 810.961 mm (31.928 inches)
Rotation axis / Detector distance: ..... 580.464 mm (22.853 inches)
Rotation axis / Xray-source distance: ..... 230.497 mm (9.075 inches)

Magnification: **x3.52**
Optimum voxel size: ..... 21.3 microns (0.0008393 inches)
Geometric unsharpness: x2.5
5 micron focal spot will be 12.59 micron wide (0.17 pixels)

Rotation: ..... Found Counter-Clockwise (CCW) rotation direction
Rotation axis: ..... -0.0038468999245842 -0.99999260065311 0
Rotation axis angle: ..... 179.78 degree

Image center: ..... (115.406, 144.758) mm / (4.544, 5.699) inches

Calibration images folder: ..... Calibration
Starting image used: ..... calib*.tif
60 images, 6 degree step

radiographs "Calibration\calib*.tif"
6 degree angle step (assuming a full 360 degree acquisition)

Figure 12.15 Calibration report for sample V-1.

O-219
UMN XRCT
CT Calibration summary

Computation date: ..... 6/1/2016 3:03:47 PM

Tracking:: ..... 7 points used, over 60 views

Calibration tool: ..... Spacing [5]mm ([0.197] inches)

Detector pixel pitch: ..... 0.075x0.075 mm (0.00295x0.00295 inches)

Image modification: ..... H-flip

Xray-source / Detector distance: ..... 786.398 mm (30.961 inches)
Rotation axis / Detector distance: ..... 661.521 mm (26.044 inches)
Rotation axis / Xray-source distance: ... 124.877 mm (4.916 inches)

Magnification: **x6.3**
Optimum voxel size: ..... 11.9 microns (0.0004689 inches)
Geometric unsharpness: x5.3
5 micron focal spot will be 26.49 micron wide (0.35 pixels)

Rotation: ..... Found Counter-Clockwise (CCW) rotation direction
Rotation axis: ..... -0.00385362725075878 -0.9999925747509390
Rotation axis angle: ..... 179.779 degree

Image center: ..... (114.488, 144.819) mm / (4.507, 5.702) inches

Calibration images folder: ..... Calibration
Starting image used: ..... calib*.tif
60 images, 6 degree step

radiographs "Calibration\calib*.tif"
6 degree angle step (assuming a full 360 degree acquisition)

Figure 12.16 Calibration report for sample O-219.

SLC-55
UMN XRCT
CT Calibration summary

Computation date: ..... 6/2/2016 3:11:21 PM

Tracking:: ..... 11 points used, over 60 views

Calibration tool: ..... Spacing [5]mm ([0.197] inches)

Detector pixel pitch: ..... 0.075x0.075 mm (0.00295x0.00295 inches)

Image modification: ..... H-flip

Xray-source / Detector distance: ..... 784.349 mm (30.88 inches)
Rotation axis / Detector distance: ..... 609.712 mm (24.004 inches)
Rotation axis / Xray-source distance: ..... 174.636 mm (6.875 inches)

Magnification: **x4.49**
Optimum voxel size: ..... 16.7 microns (0.0006574 inches)
Geometric unsharpness: x3.5
5 micron focal spot will be 17.46 micron wide (0.23 pixels)

Rotation: ..... Found Counter-Clockwise (CCW) rotation direction
Rotation axis: ..... -0.0035797589199084 3 -0.9999935926425110
Rotation axis angle: ..... 179.795 degree

Image center: ..... (113.271, 144.666) mm / (4.459, 5.696) inches

Calibration images folder: ..... Calibration
Starting image used: ..... calib*.tif
60 images, 6 degree step

radiographs "Calibration\calib*.tif"
6 degree angle step (assuming a full 360 degree acquisition)

Figure 12.17 Calibration report for sample SLC-55.

SLC-2476
UMN XRCT
CT Calibration summary

Computation date: ..... 6/2/2016 10:44:56 AM

Tracking:: ..... 8 points used, over 60 views

Calibration tool: ..... Spacing [5]mm ([0.197] inches)

Detector pixel pitch: ..... 0.075x0.075 mm (0.00295x0.00295 inches)

Image modification: ..... H-flip

Xray-source / Detector distance: ..... 785.164 mm (30.912 inches)
Rotation axis / Detector distance: ..... 660.54 mm (26.005 inches)
Rotation axis / Xray-source distance: ... 124.625 mm (4.906 inches)

Magnification: **x6.3**
Optimum voxel size: ..... 11.9 microns (0.0004687 inches)
Geometric unsharpness: x5.3
5 micron focal spot will be 26.5 micron wide (0.35 pixels)

Rotation: ..... Found Counter-Clockwise (CCW) rotation direction
Rotation axis: ..... -0.00384877837472553 -0.9999925934250830
Rotation axis angle: ..... 179.779 degree

Image center: ..... (114.966, 144.862) mm / (4.526, 5.703) inches

Calibration images folder: ..... Calibration
Starting image used: ..... calib*.tif
60 images, 6 degree step

radiographs "Calibration\calib*.tif"
6 degree angle step (assuming a full 360 degree acquisition)

Figure 12.18 Calibration report for sample SLC-2476.

MVT-1
UMN XRCT
CT Calibration summary

Computation date: ..... 7/7/2016 1:19:07 PM

Tracking:: ..... 8 points used, over 60 views

Calibration tool: ..... Spacing [5]mm ([0.197] inches)

Detector pixel pitch: ..... 0.075x0.075 mm (0.00295x0.00295 inches)

Image modification: ..... H-flip

Xray-source / Detector distance: ..... 811.643 mm (31.954 inches)
Rotation axis / Detector distance: ..... 676.286 mm (26.625 inches)
Rotation axis / Xray-source distance: ... 135.357 mm (5.329 inches)

Magnification: **x6**
Optimum voxel size: ..... 12.5 microns (0.0004924 inches)
Geometric unsharpness: x5
5 micron focal spot will be 24.98 micron wide (0.33 pixels)

Rotation: ..... Found Counter-Clockwise (CCW) rotation direction
Rotation axis: ..... -0.00387079655009755 -0.9999925084389720
Rotation axis angle: ..... 179.778 degree

Image center: ..... (113.612, 144.722) mm / (4.473, 5.698) inches

Calibration images folder: ..... Calibration
Starting image used: ..... calib*.tif
60 images, 6 degree step

radiographs "Calibration\calib*.tif"
6 degree angle step (assuming a full 360 degree acquisition)

Figure 12.19 Calibration report for sample MVT-1.

1716
UMN XRCT
CT Calibration summary

Computation date: ..... 6/1/2016 10:53:33 AM

Tracking:: ..... 8 points used, over 60 views

Calibration tool: ..... Spacing [5]mm ([0.197] inches)

Detector pixel pitch: ..... 0.075x0.075 mm (0.00295x0.00295 inches)

Image modification: ..... H-flip

Xray-source / Detector distance: ..... 784.593 mm (30.89 inches)
Rotation axis / Detector distance: ..... 659.843 mm (25.978 inches)
Rotation axis / Xray-source distance: ... 124.75 mm (4.911 inches)

Magnification: **x6.29**
Optimum voxel size: ..... 11.9 microns (0.0004695 inches)
Geometric unsharpness: x5.3
5 micron focal spot will be 26.45 micron wide (0.35 pixels)

Rotation: ..... Found Counter-Clockwise (CCW) rotation direction
Rotation axis: ..... -0.00381749566443868 -0.9999927133368780
Rotation axis angle: ..... 179.781 degree

Image center: ..... (115.902, 145.033) mm / (4.563, 5.71) inches

Calibration images folder: ..... Calibration
Starting image used: ..... calib*.tif
60 images, 6 degree step

radiographs "Calibration\calib*.tif"
6 degree angle step (assuming a full 360 degree acquisition)

Figure 12.20 Calibration report for sample 1716.

12.3 Additional Photos of 3d Sample Reconstructions

Below are additional photos of samples scanned using XRCT and reconstructed in 3d. These photos were not included in the main body of text as they did not add concrete value to the overall conversation.

EG-181

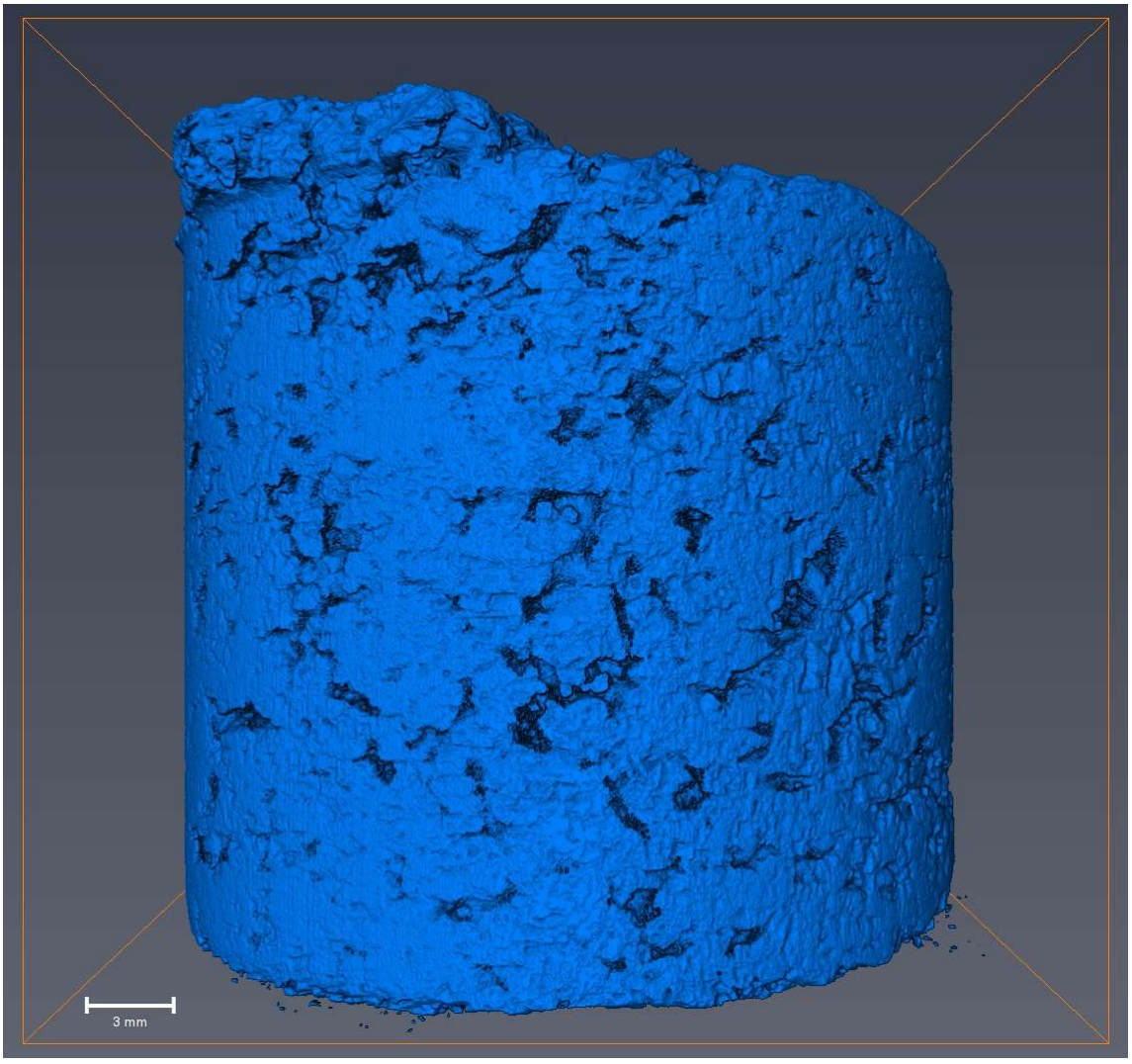

Figure 12.21 A full sample 3d reconstruction of EG-181 with an (X, Z) display orientation.

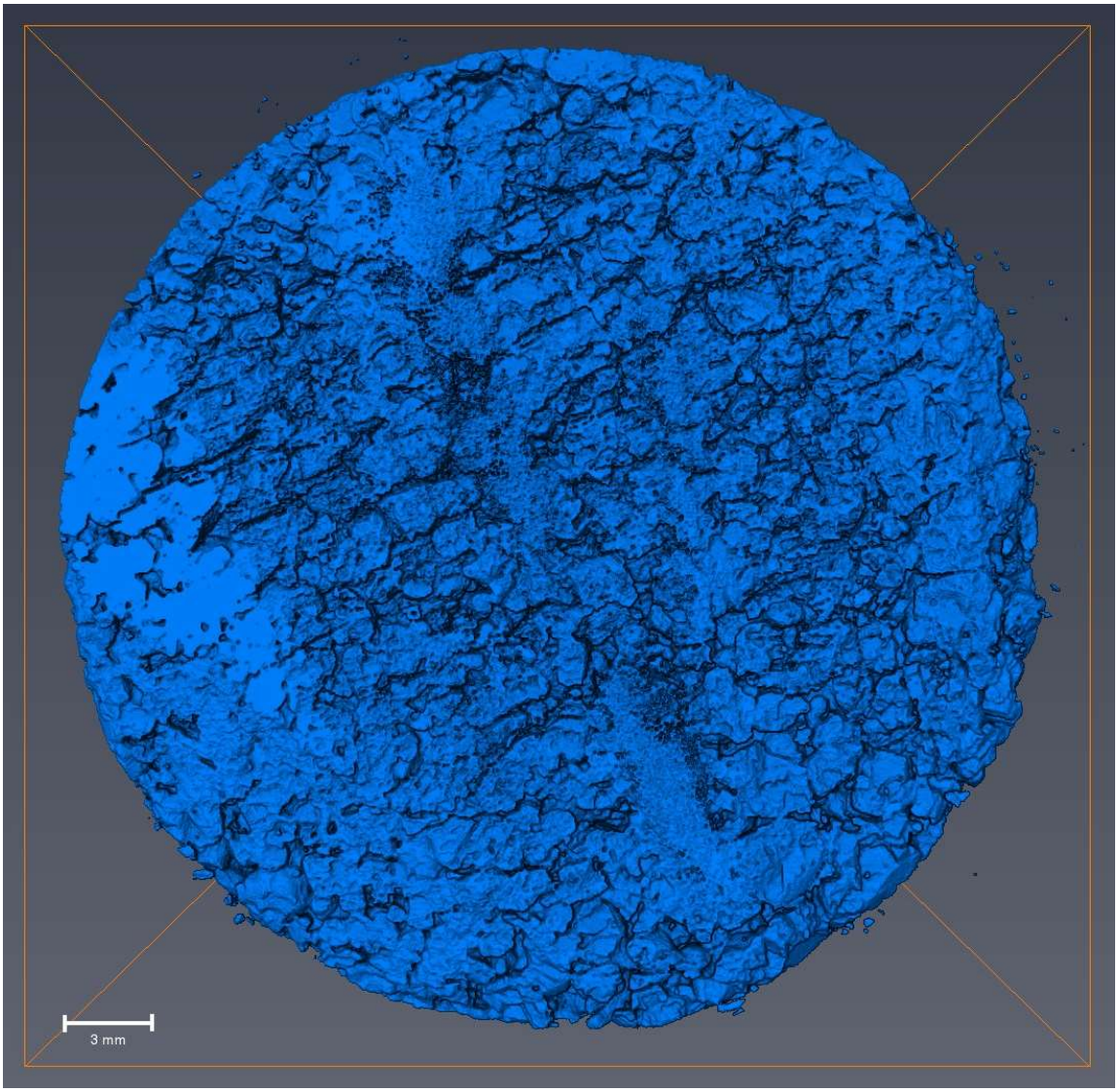

Figure 12.22 A full sample 3d reconstruction of EG-181 with an (X, Y) display orientation.

Eagle-1

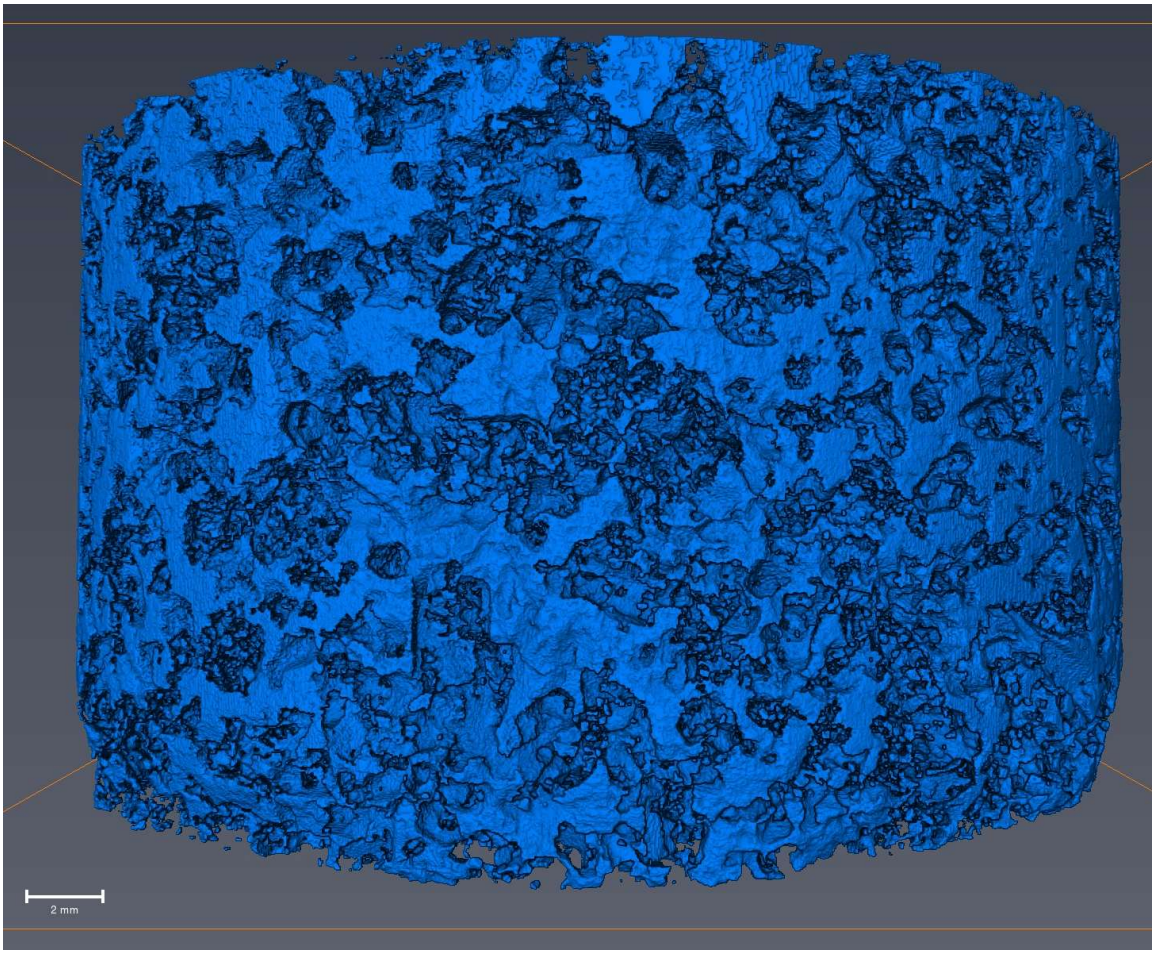

Figure 12.23 A half sample 3d reconstruction of Eagle-1 with an (X, Z) display orientation. This reconstruction utilizes slices 0 through 1182 out of a total 2363 slices.

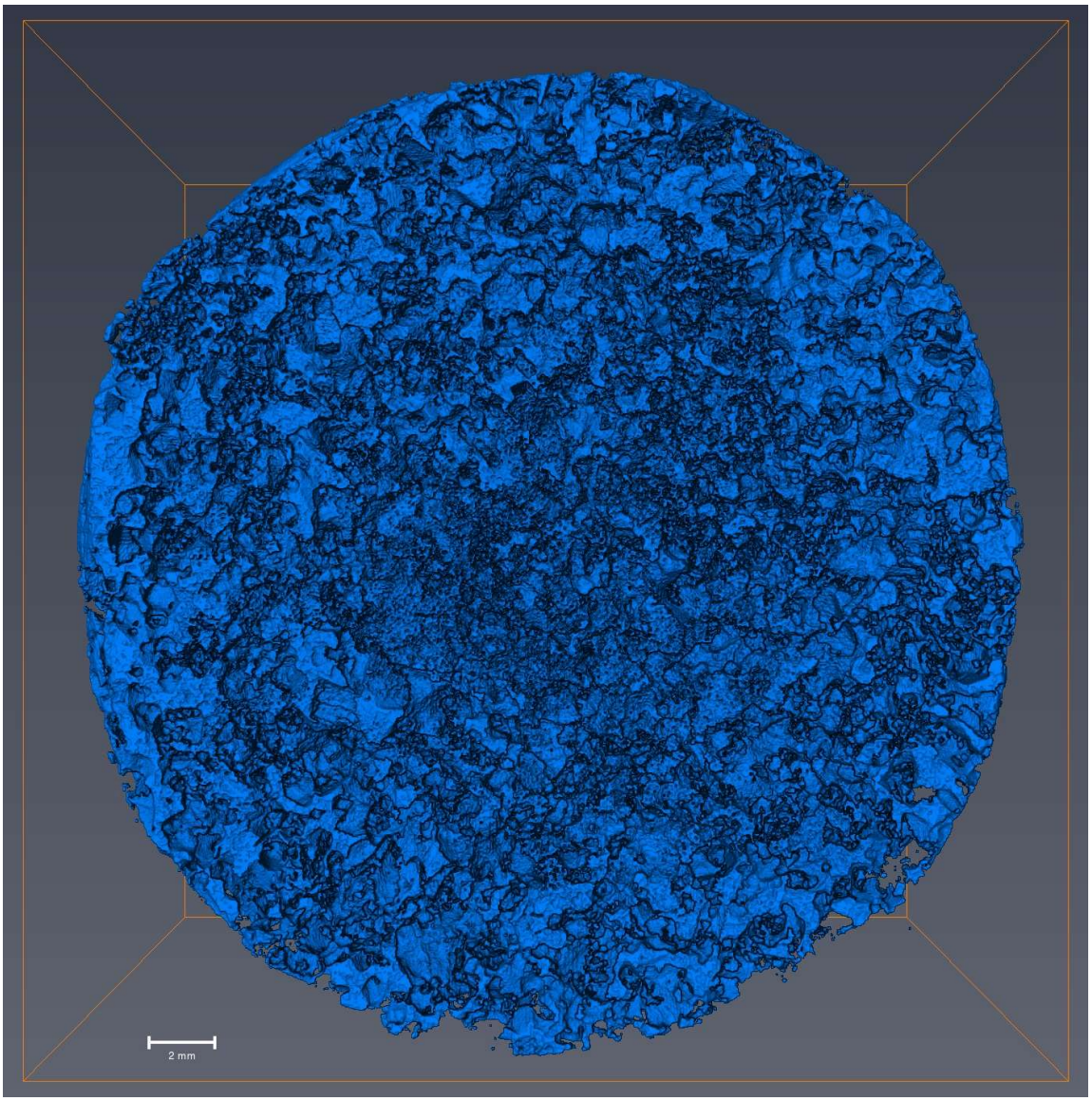

Figure 12.24 A half sample 3d reconstruction of Eagle-1 with an (X, Y) display orientation. This reconstruction utilizes slices 0 through 1182 out of a total 2363 slices.

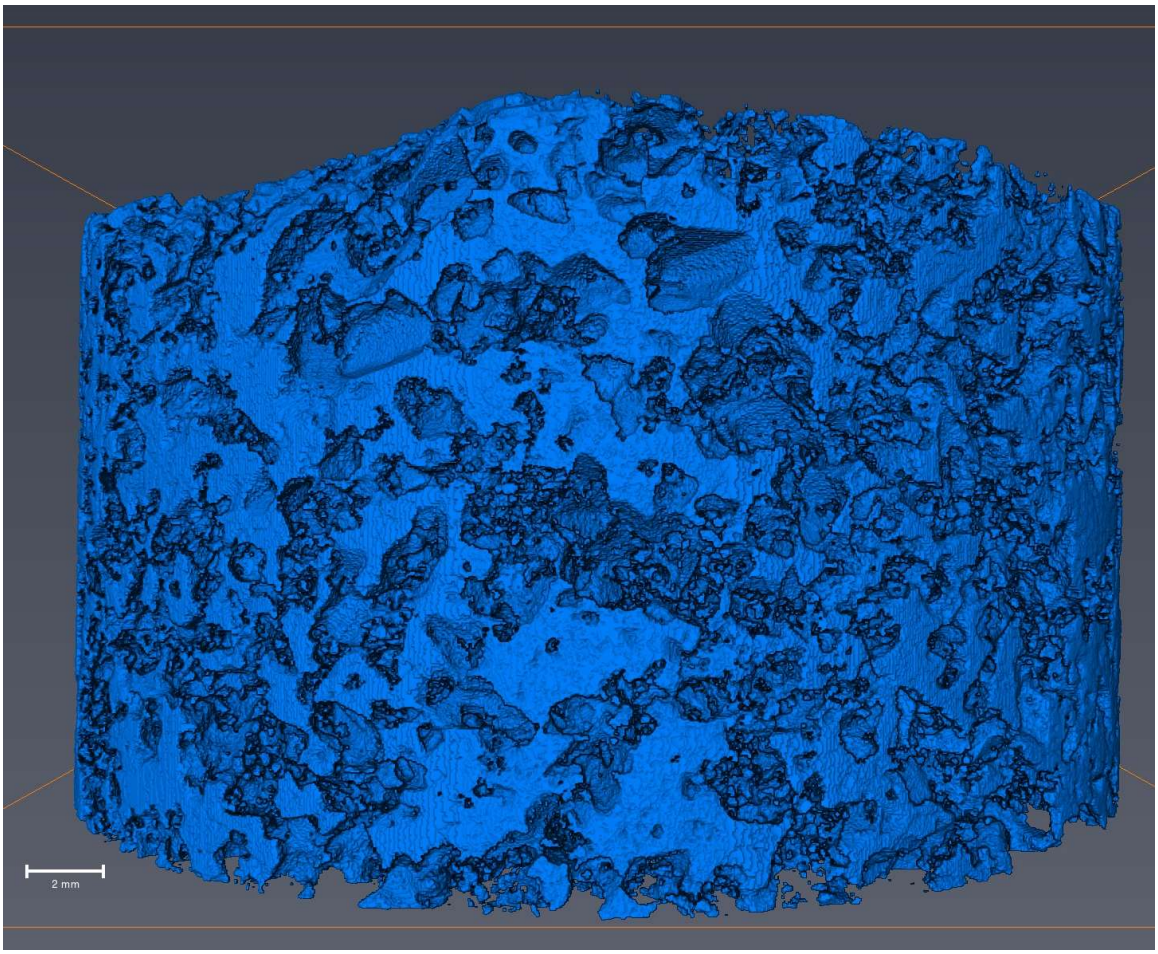

Figure 12.25 A half sample 3d reconstruction of Eagle-1 with an (Y, Z) display orientation. This reconstruction utilizes slices 1183 through 2362 out of a total 2363 slices.

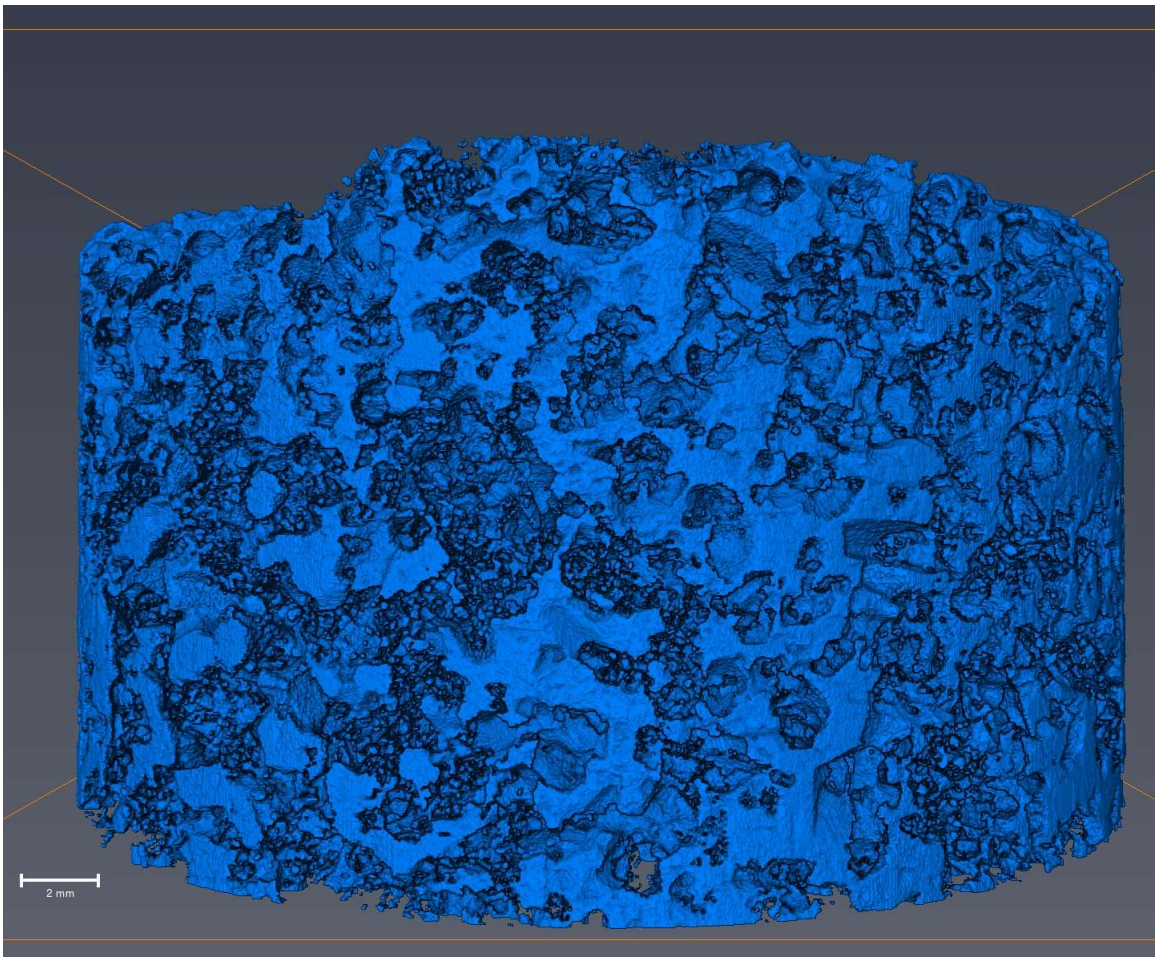

Figure 12.26 A half sample 3d reconstruction of Eagle-1 with an (X, Z) display orientation. This reconstruction utilizes slices 1183 through 2362 out of a total 2363 slices.

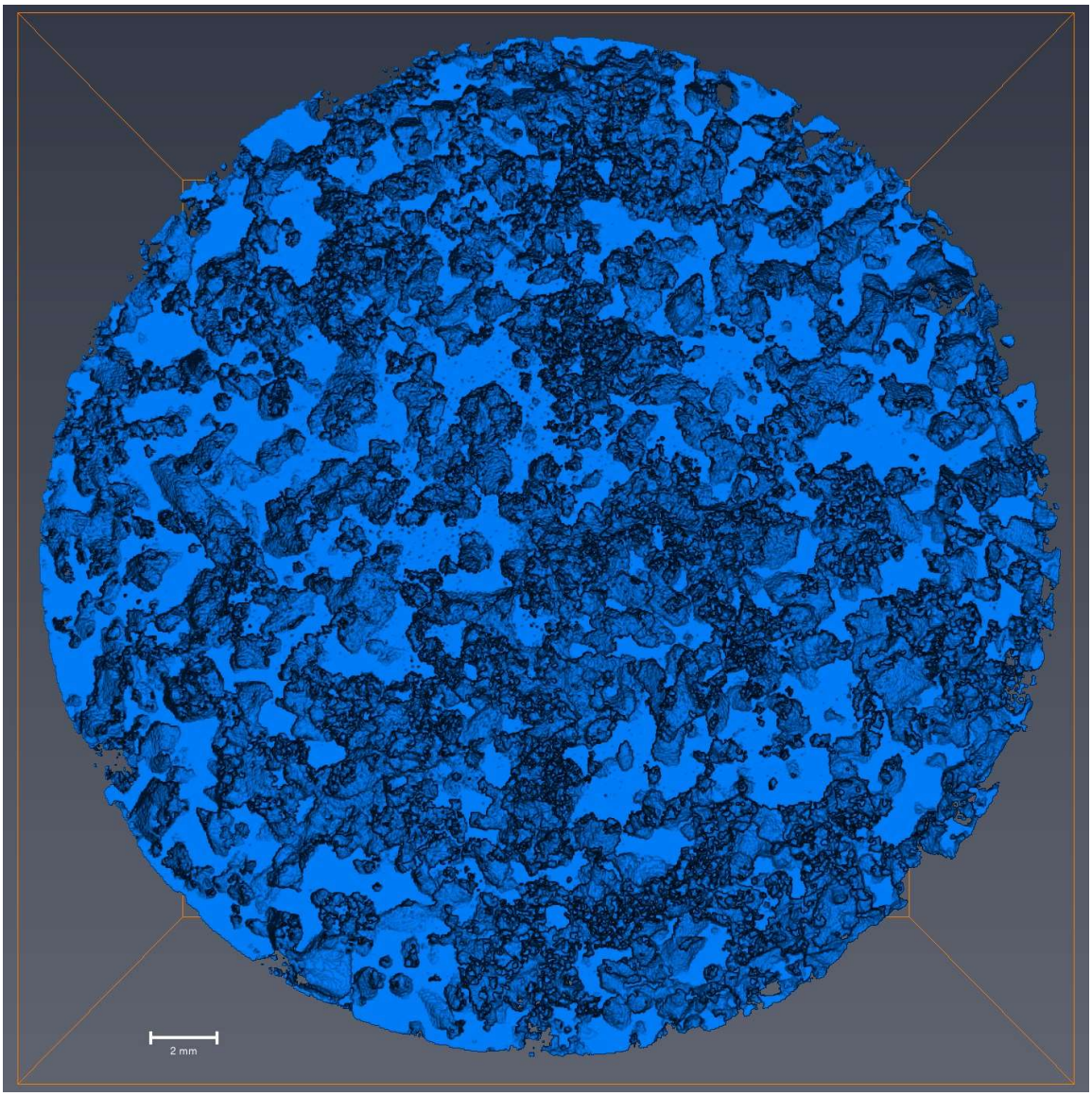

Figure 12.27 A half sample 3d reconstruction of Eagle-1 with an (X, Z) display orientation. This reconstruction utilizes slices 1183 through 2362 out of a total 2363 slices.

DC

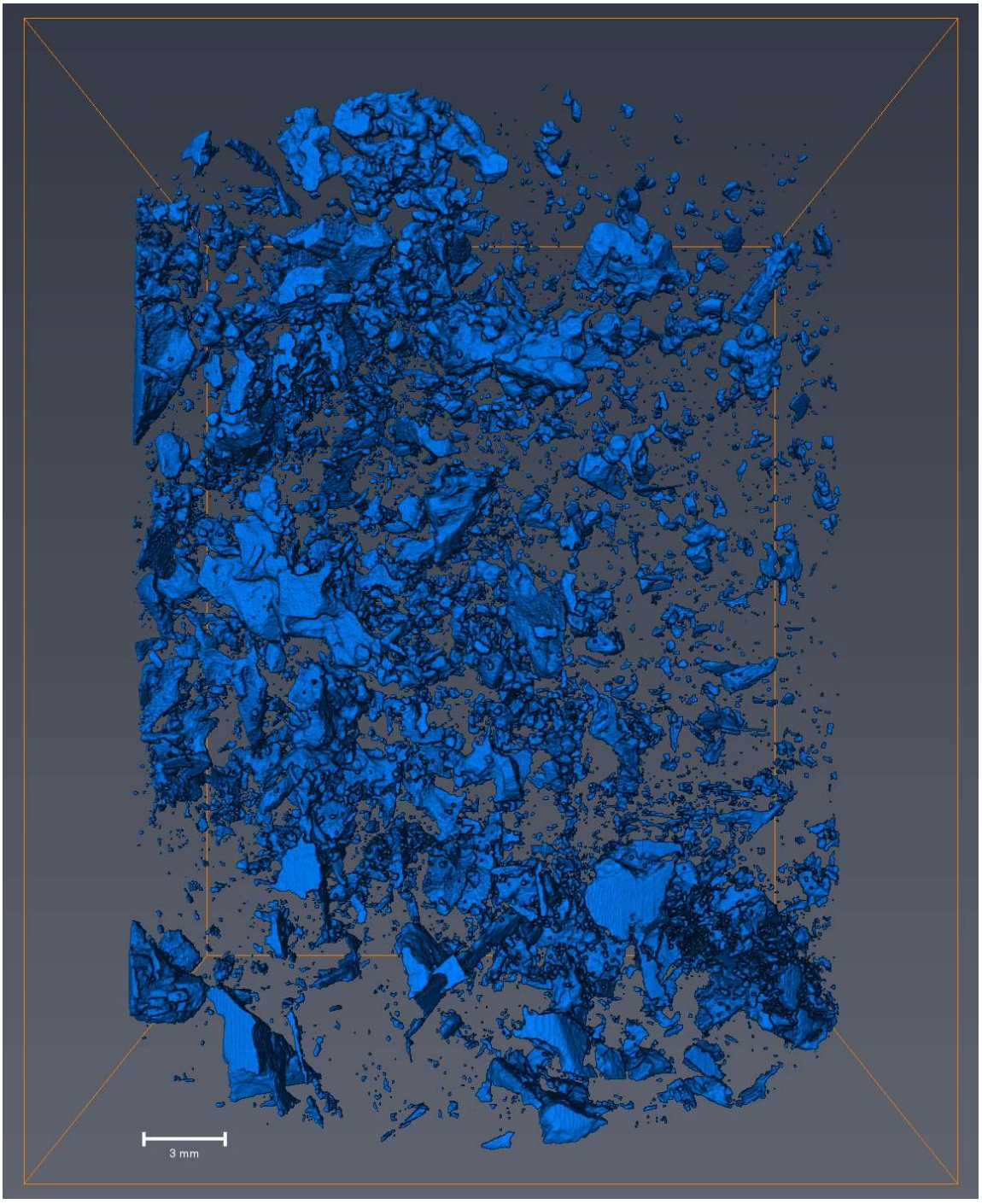

Figure 12.28 A full sample 3d reconstruction of DC with an (X, Z) display orientation.

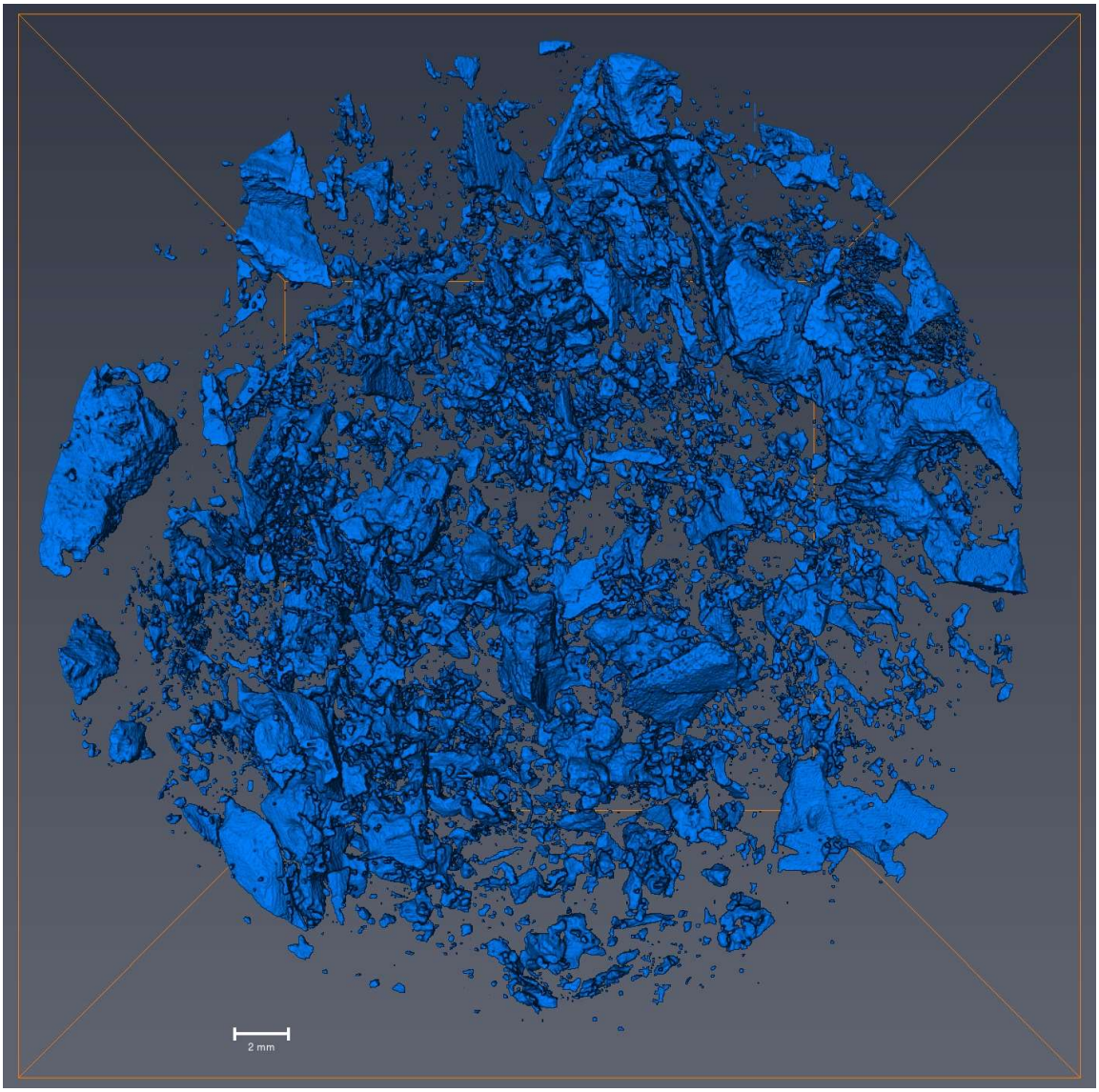

Figure 12.29 A full sample 3d reconstruction of DC with an (X, Y) display orientation.

Bag-1

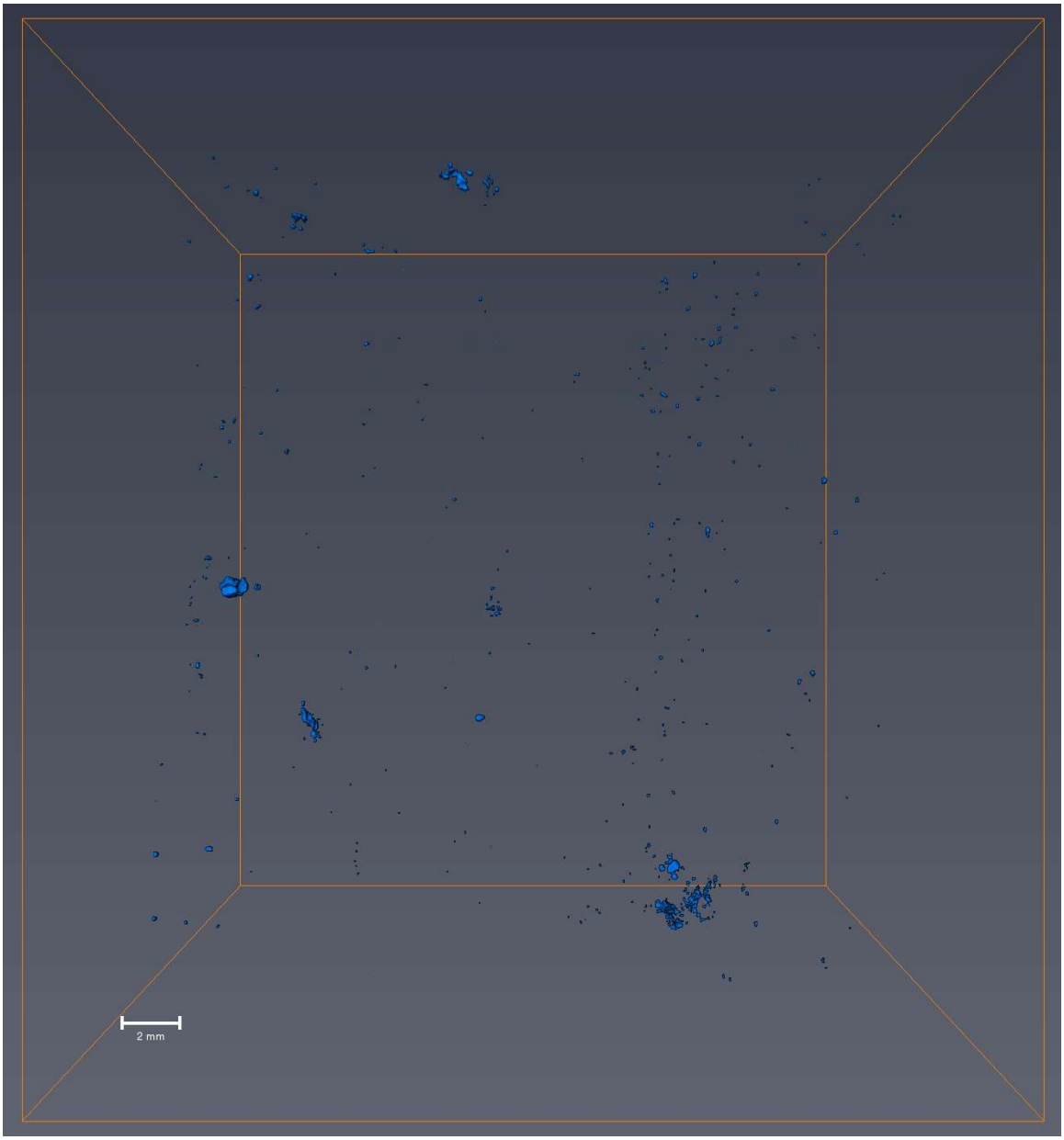

Figure 12.30 A full sample 3d reconstruction of Bag-1 with an (X, Z) display orientation.

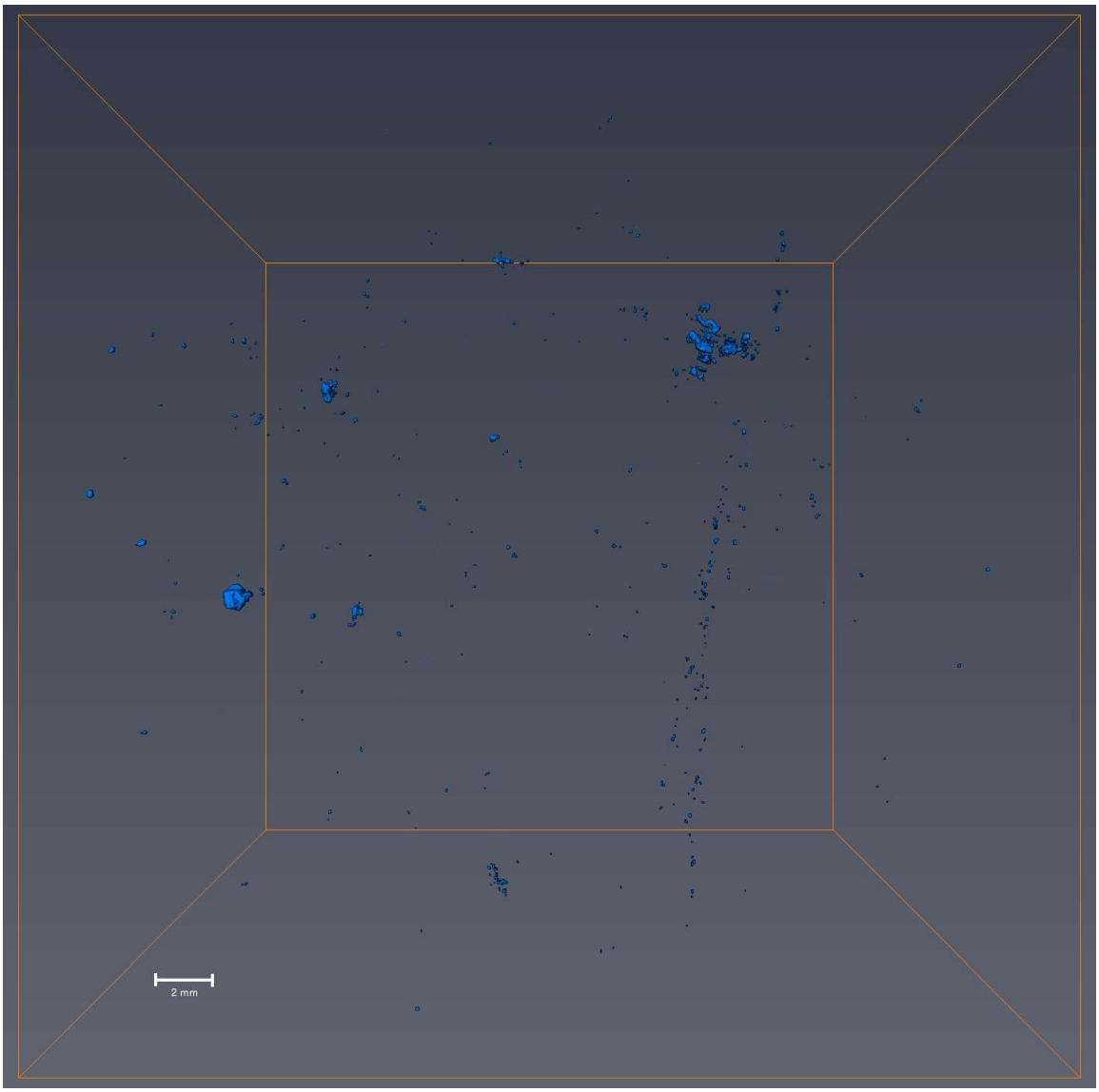

Figure 12.31 A full sample 3d reconstruction of Bag-1 with an (X, Y) display orientation.

V-1

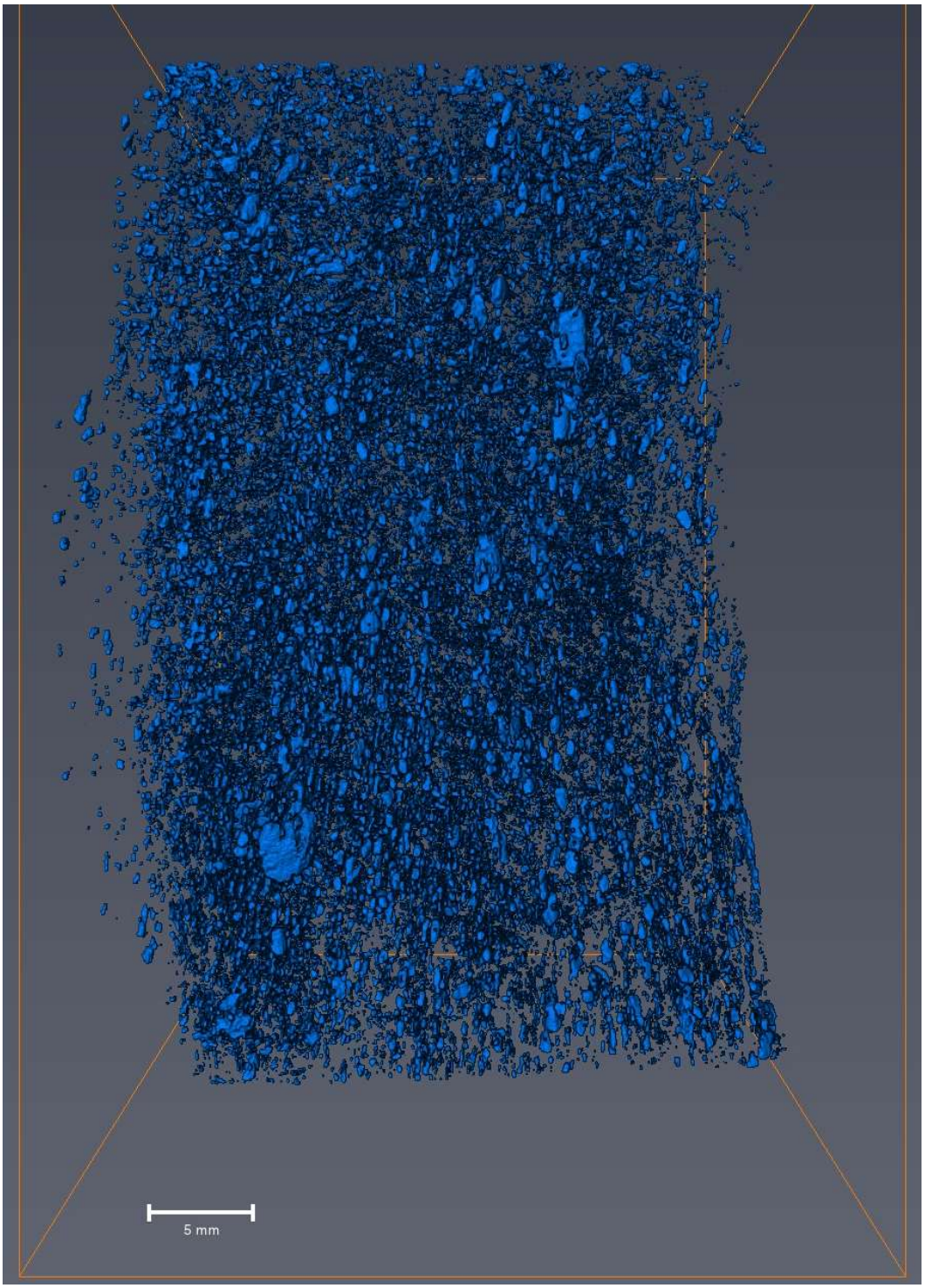

Figure 12.32 A full sample 3d reconstruction of V-1 with an (X, Z) display orientation.

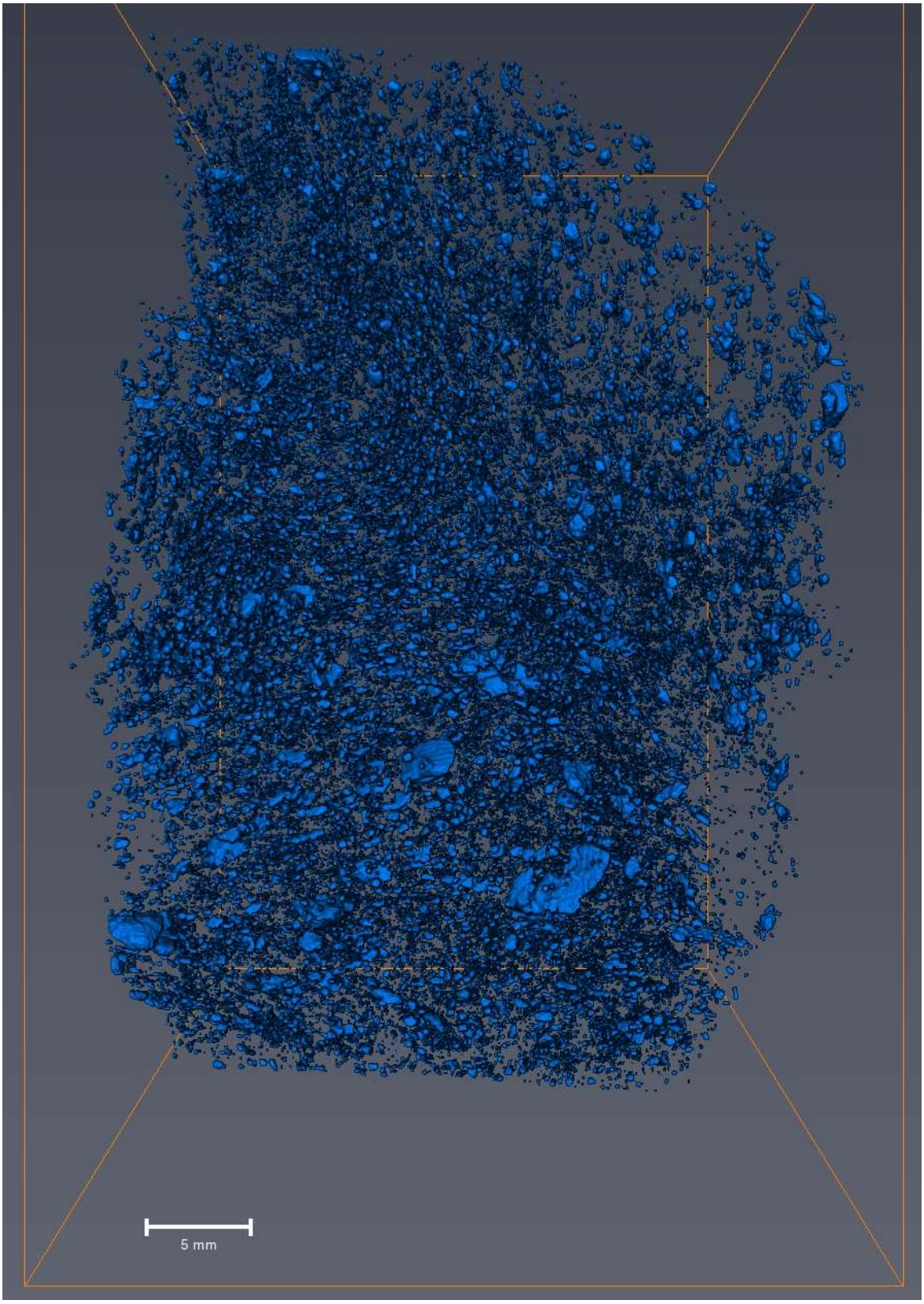

Figure 12.33 A full sample 3d reconstruction of V-1 with an (X, Y) display orientation.

O-219

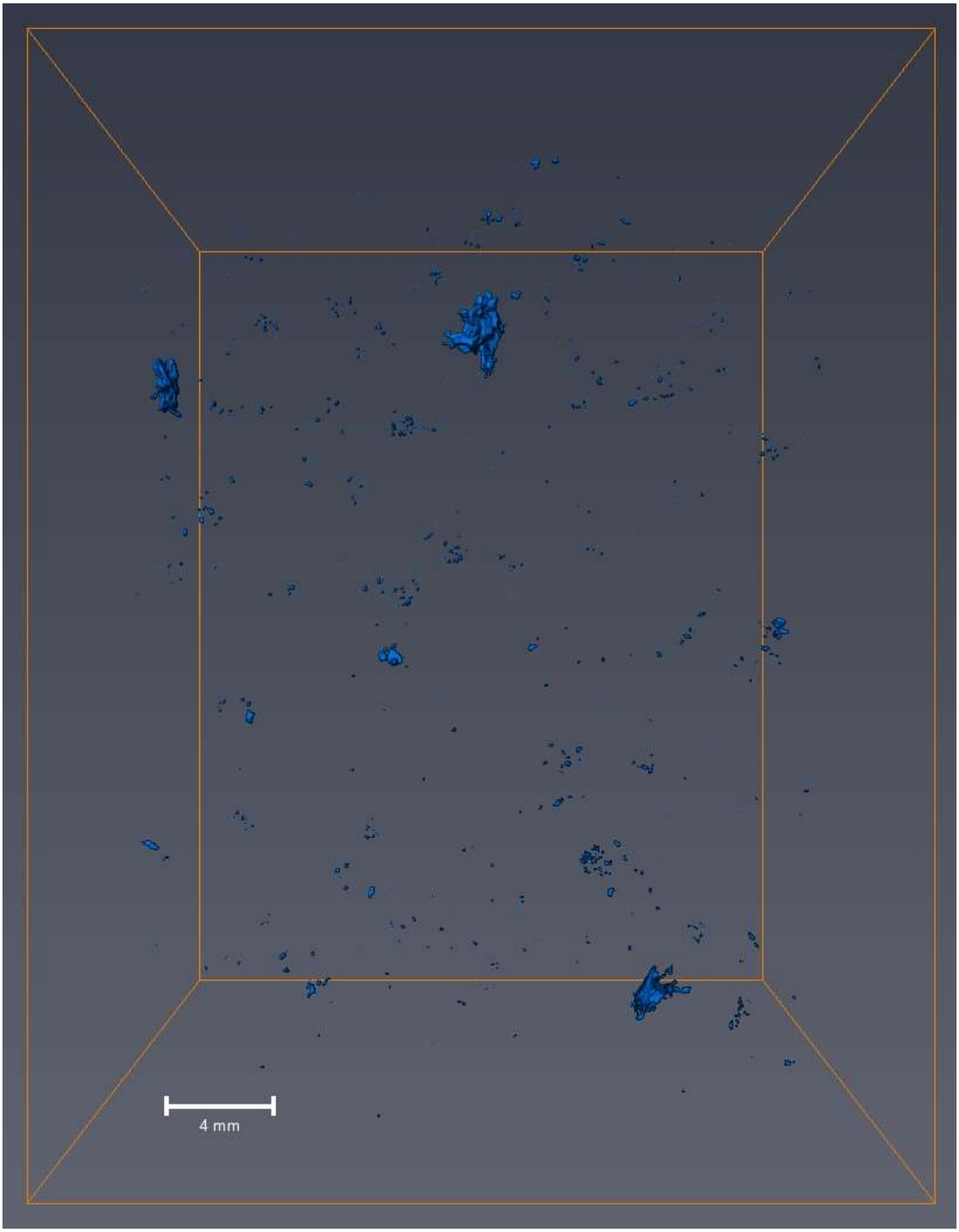

Figure 12.34 A full sample 3d reconstruction of O-219 with an (X, Z) display orientation.

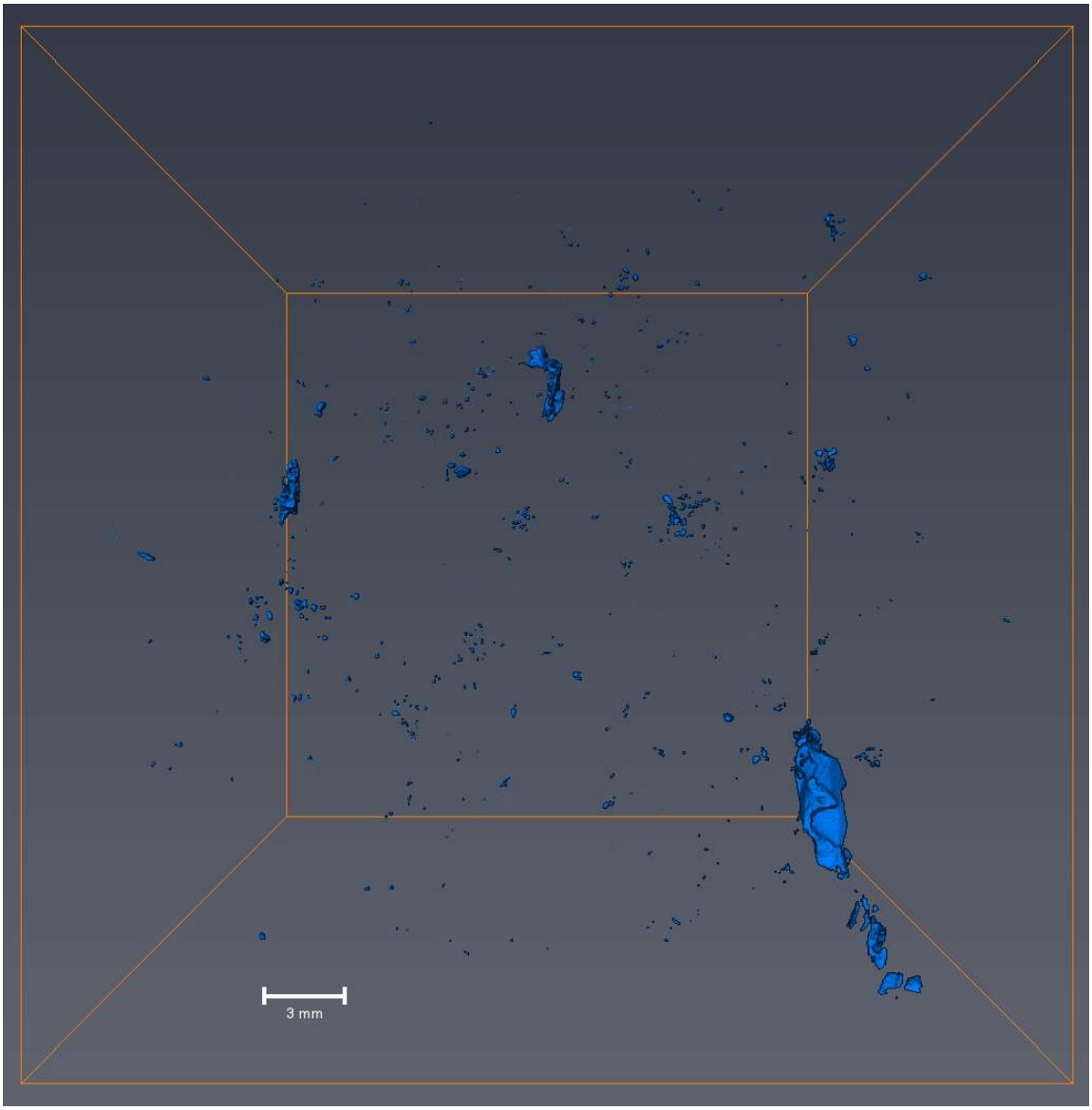

Figure 12.35 A full sample 3d reconstruction of O-219 with an (X, Y) display orientation.

SLC-55

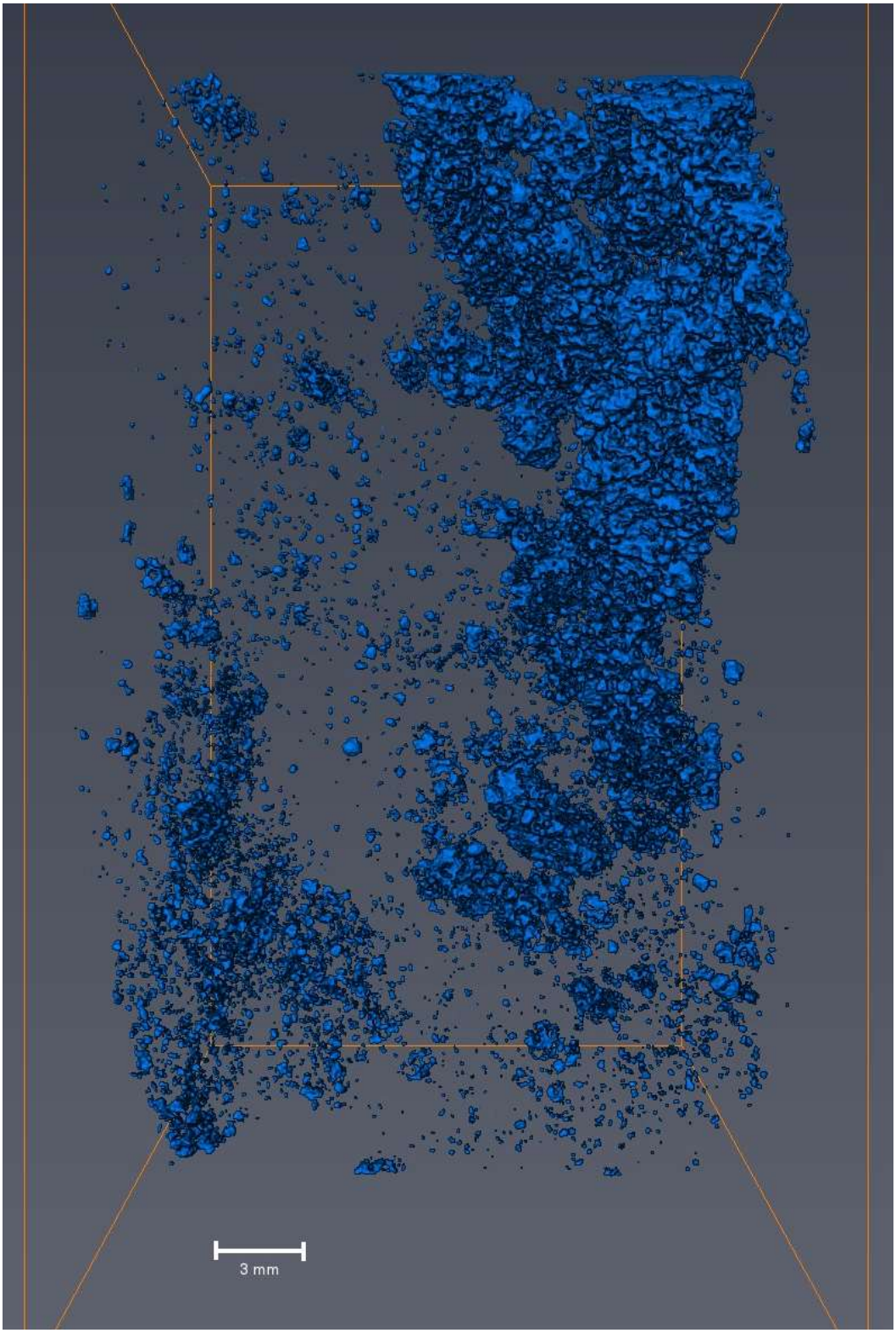

Figure 12.36 A full sample 3d reconstruction of SLC-55with an (X, Z) display orientation.

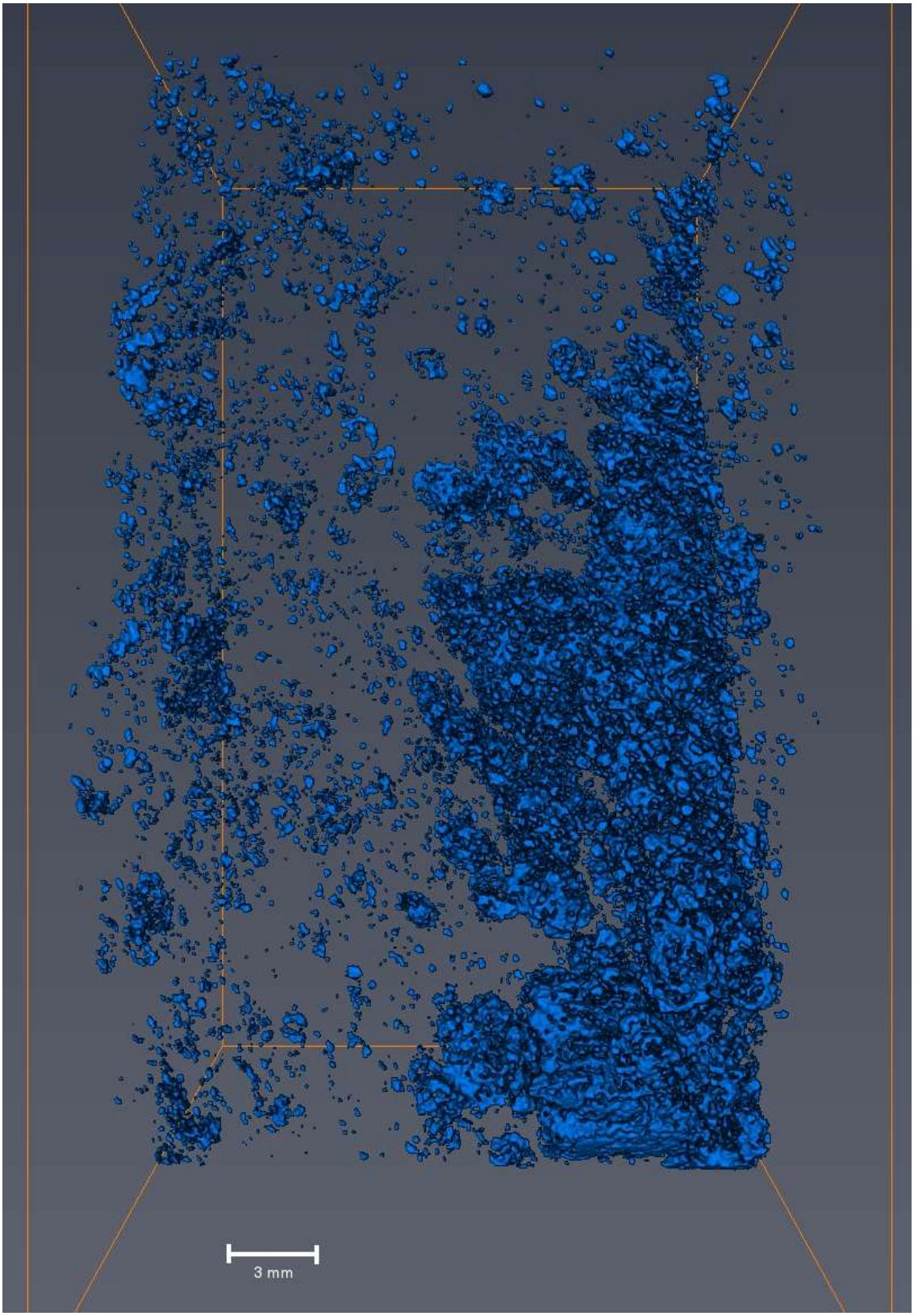

Figure 12.37 A full sample 3d reconstruction of SLC-55with an (X, Y) display orientation.

SLC-2476

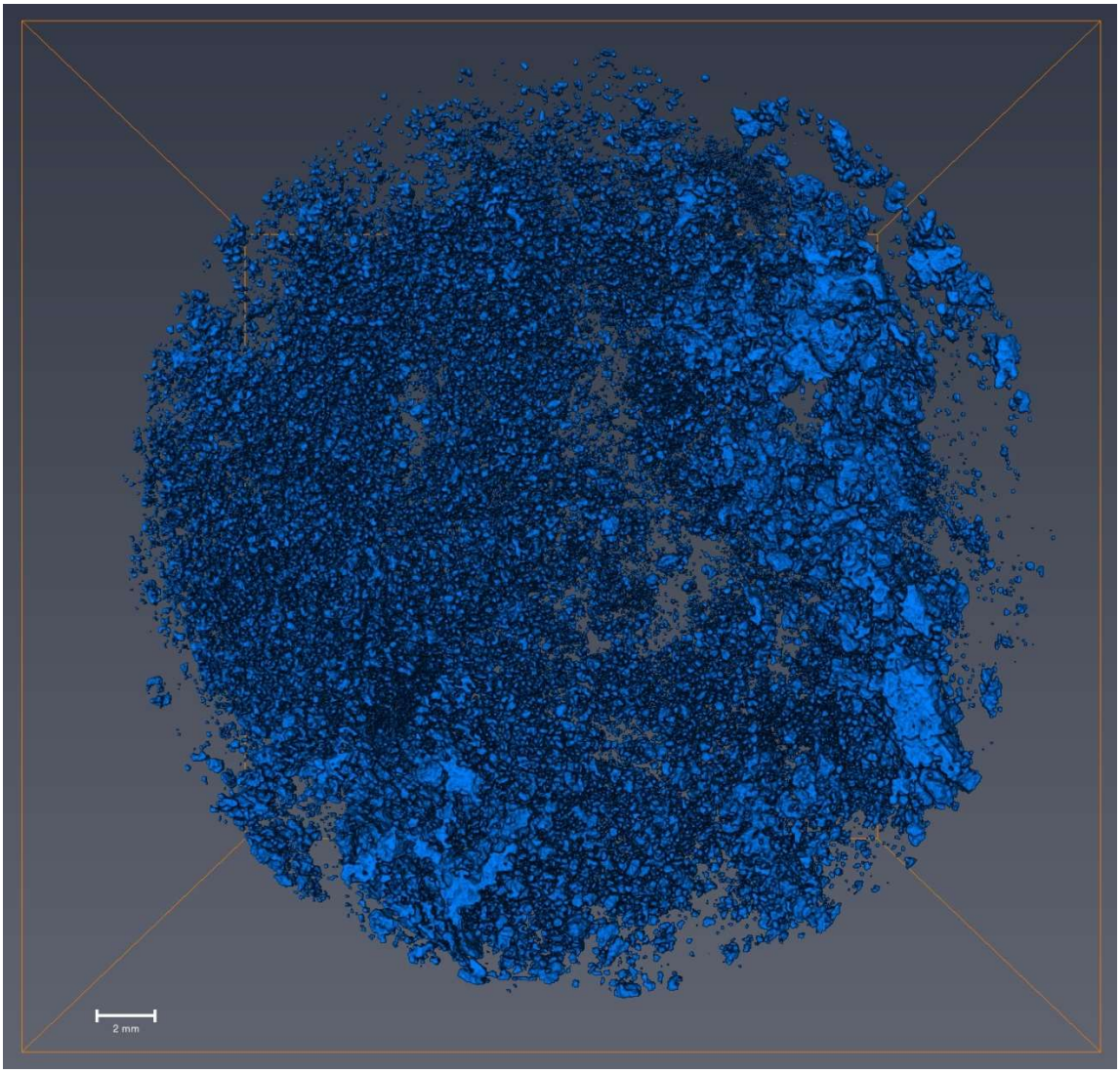

Figure 12.38 A full sample 3d reconstruction of SLC-2476with an (X, Y) display orientation.

MVT-1

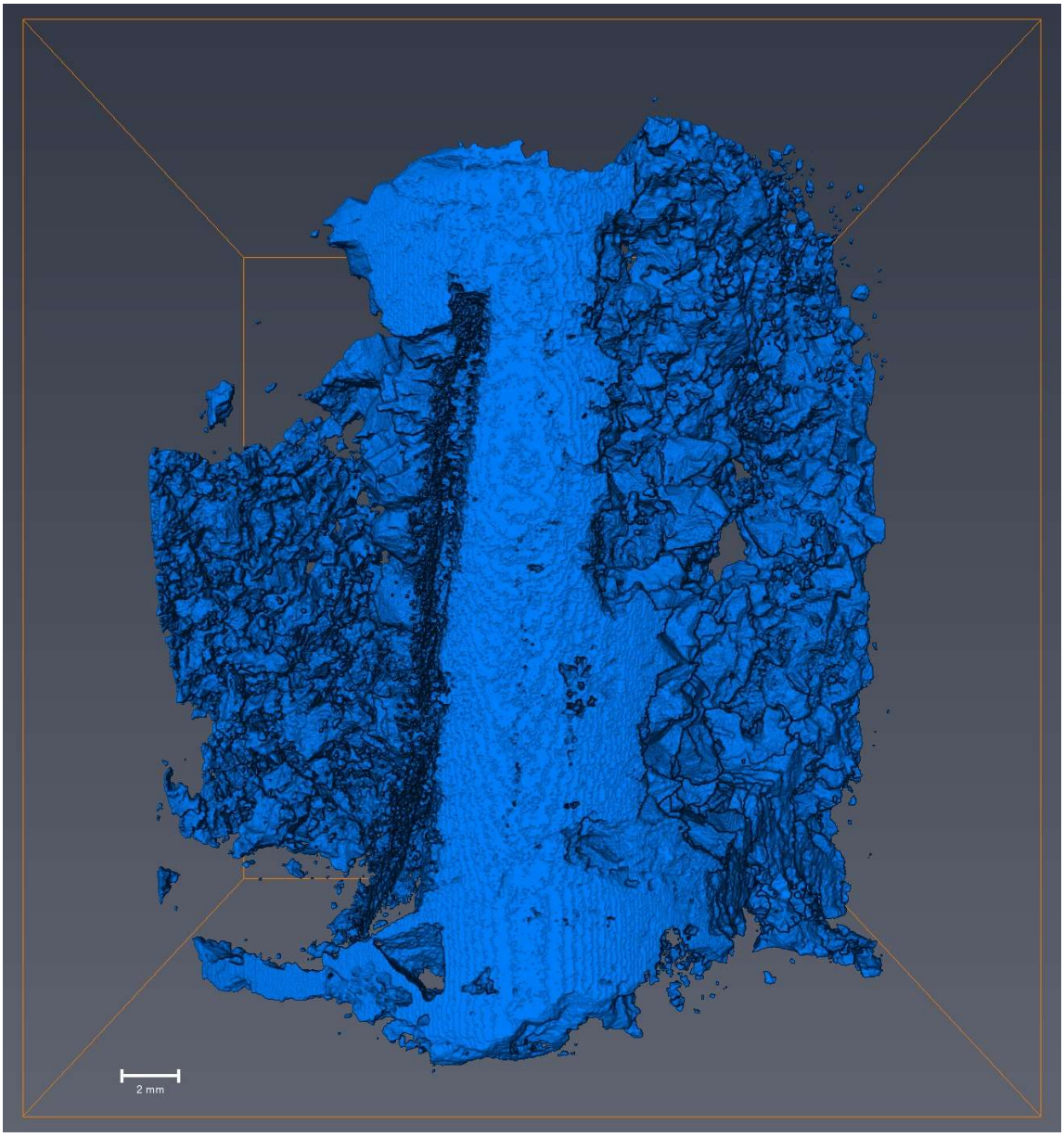

Figure 12.39 A full sample 3d reconstruction of MVT-1 with an (X, Z) display orientation.

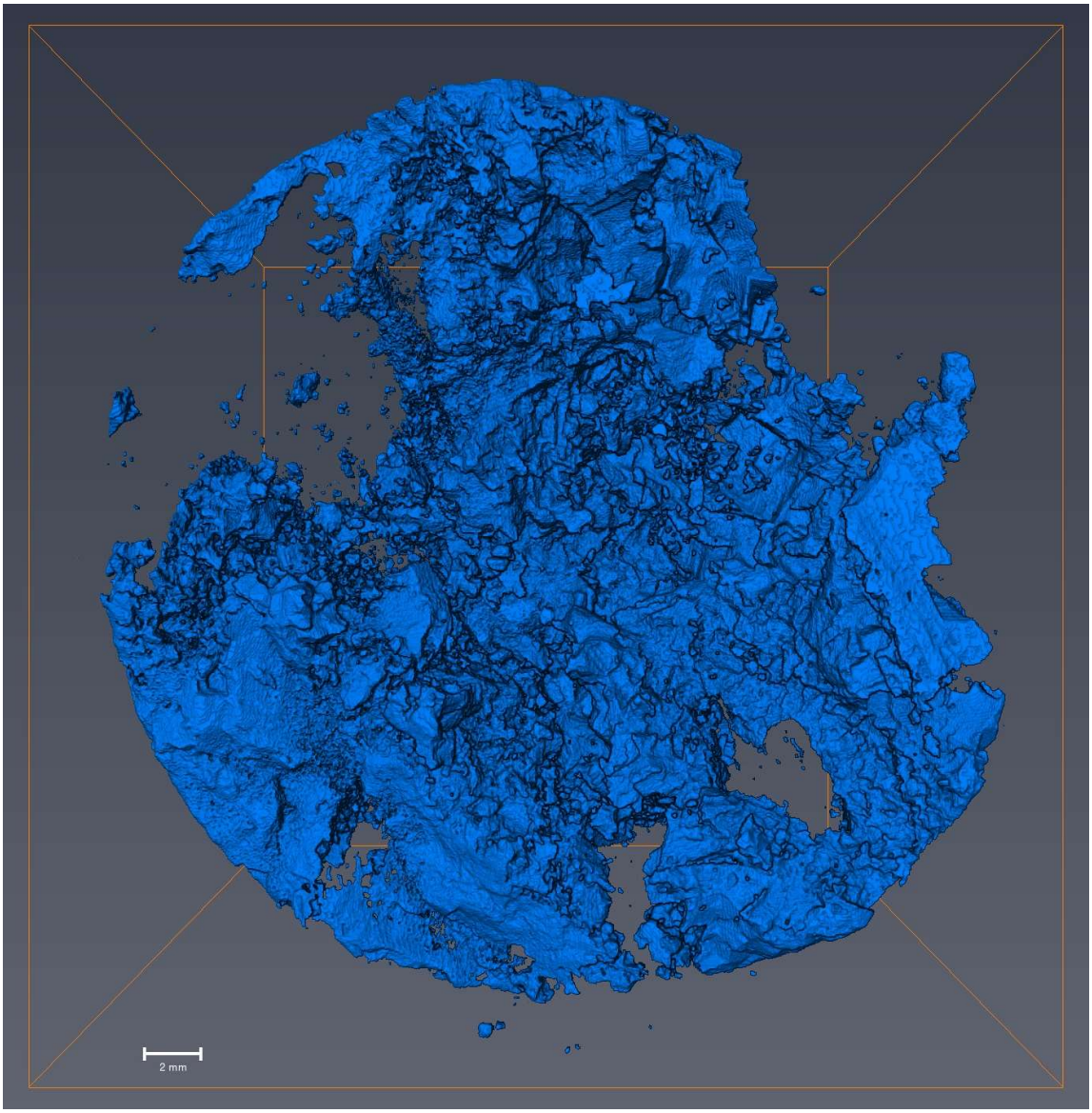

Figure 12.40 A full sample 3d reconstruction of MVT-1 with an (X, Y) display orientation.

1716

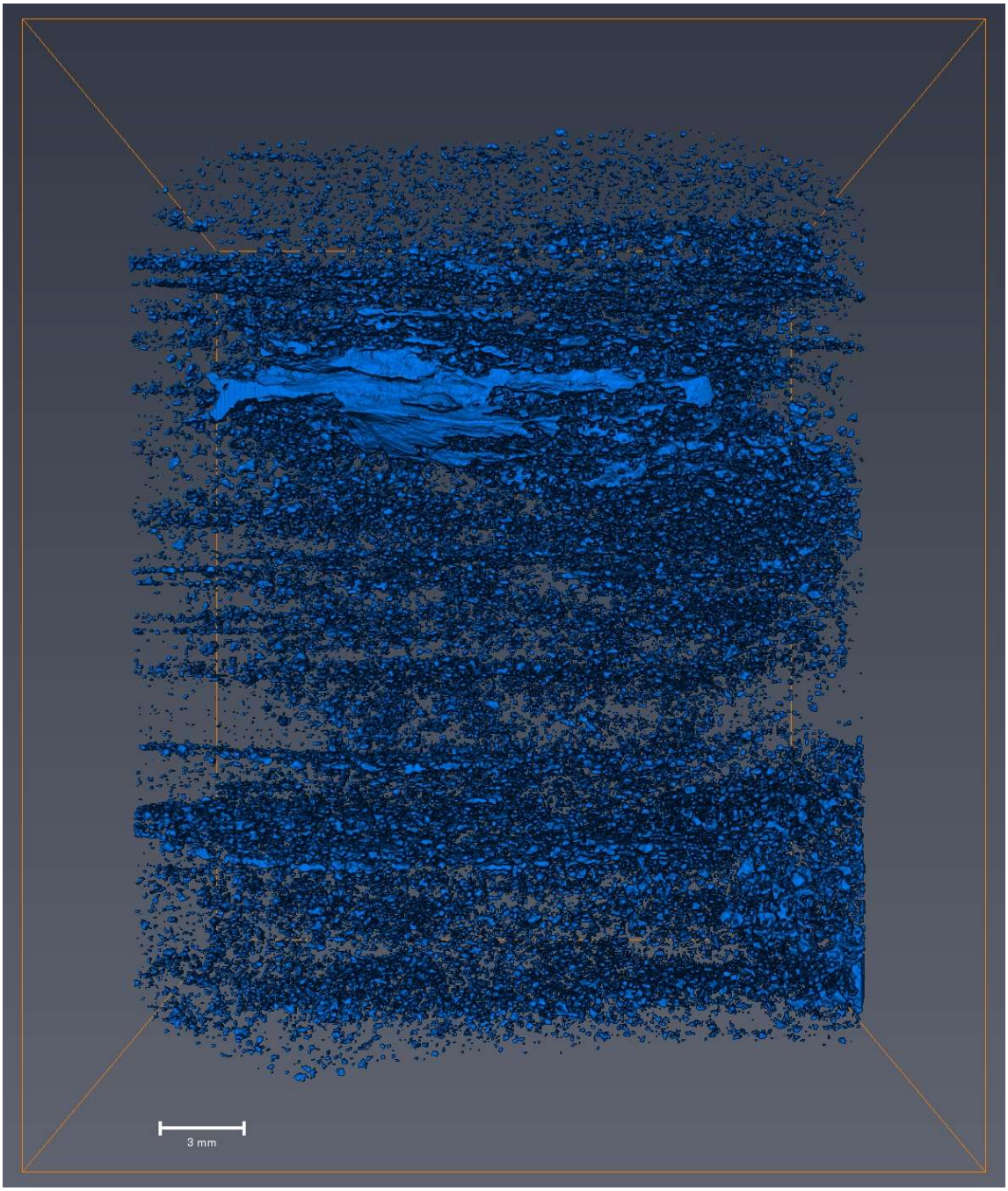

Figure 12.41 A full sample 3d reconstruction of 1716 with an (X, Z) display orientation.

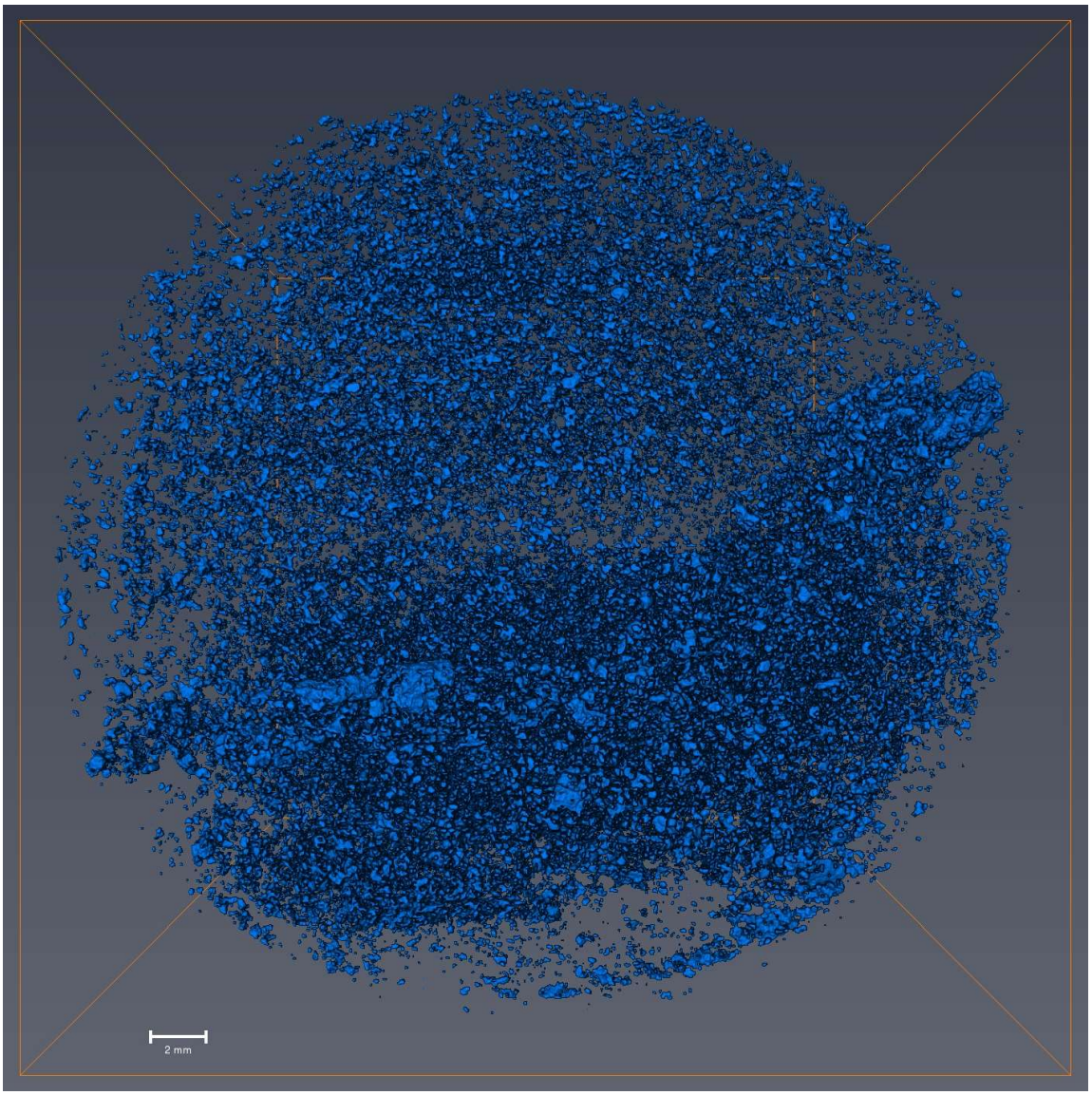

Figure 12.42 A full sample 3d reconstruction of 1716 with an (X, Y) display orientation.

13. Appendix 5 – Summary of ore deposit formation models

13.1 Liquid Magmatic Deposits

Liquid magmatic ore deposits form when metals, either already present within the magma or sourced from surrounding country rock assimilation, crystallize out of a cooling magma. There are two common models that will be discussed that each formed at least one of the samples utilized in this work. The first is the differentiation of a silicate melt that allows an ore mineral to crystallize out and the other method is when sulfide minerals become immiscible from the rest of the melt (Ridley, 2013).

13.1.1 Differentiation of a Silicate Melt

This type of deposit commonly hosts chromite ((Fe, Mg) Cr_2O_4) ores. Chromite deposits can form in two different environments; either by injection of a mantle-sourced magma into intracratonic crust, which results in a stratiform deposit. Or magmas can be injected into oceanic crust, which is recognized in the geologic record by being found in ophiolites, and results in a podiform deposit (Duke, 1983; Zhou and Robinson, 1997; González-Jiménez et al., 2014). Typically, these mantle-sourced magmas only contain a few percent chromium, the principle economic metal of chromite ore, and therefore must evolve under specific conditions that allows for significant concentrations of chromite to crystallize out.

There are three commonly proposed models to explain how chromite crystallizes out of the melt. Within the stratiform type of deposit, it is commonly hypothesized that silica saturation occurred and forced the melt composition off the olivine-chromite eutectic, triggering chromite fractionation until the melt composition returned to stability

on the olivine-chromite eutectic (Duke, 1983; Ridley, 2013). The two proposed models for silica saturation are either contamination by surrounding country rocks or by the mixing of magmas as fresh parental magma is injected into the existing melt that is more highly evolved (Zhou and Robinson, 1997; Spandler et al., 2005). The third model for chromite crystallization proposes oxygen fugacity changes within a melt; interaction of the melt with aqueous fluids can cause a change in oxygen fugacity and thereby force the crystallization of chromite. This model is currently used to explain the occurrence of podiform deposits (González-Jiménez et al., 2014).

13.1.2 Immiscible Sulfide Melt

Ore bodies formed from an immiscible sulfide melt are known to host the vast majority of world's supply of nickel, platinum-group elements (PGEs) and are also a significant source of copper (Ridley, 2013). These deposits form when a mafic to ultramafic melt is generated from the mantle that is enriched in chalcophile elements and PGEs as the mantle is partially melted (fig. 13.1; Naldrett, 2010).

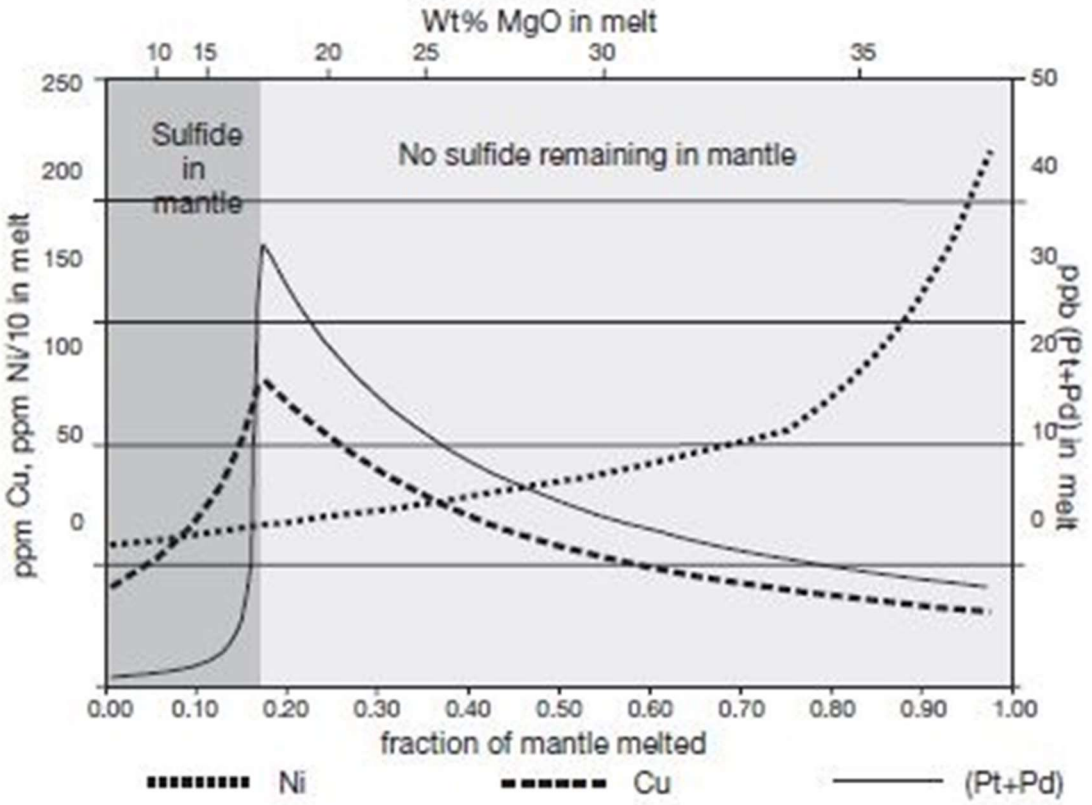

Figure 13.1 Variation in metal contents of partial melts that were derived from mantle melting at 20 kbar (Naldrett, 2010).

At some point during the magma's ascension or final emplacement sulfur saturation may occur. This causes the chalcophile metals of the melt, such as Cu or Ni, to form their own phases by combining with S to form sulfides. Since thermodynamics will not allow both sulfide and silicate phases to coexist in one melt, the sulfide-rich melt becomes immiscible from the silicon-rich melt, allowing sulfide minerals to form globules that eventually crystallize when they have cooled sufficiently (fig 13.2; Naldrett and Duke, 1980; Maier, 2005; Naldrett, 2010). Because of the higher density of a sulfide melt (~4.5 g/cm^3) compared to that of a silica magma (~2.8 g/cm^3), the sulfide globules tend to settle towards the bottom of a magma chamber or conduit and accumulate. It is because of this

process that layers of massive sulfide ores are created at the bottom of magma chambers, followed by silicates with sulfide blebs disseminated throughout; the amount of sulfide ore vs. silicate decreases as one moves stratigraphically higher in section (Ridley, 2013).

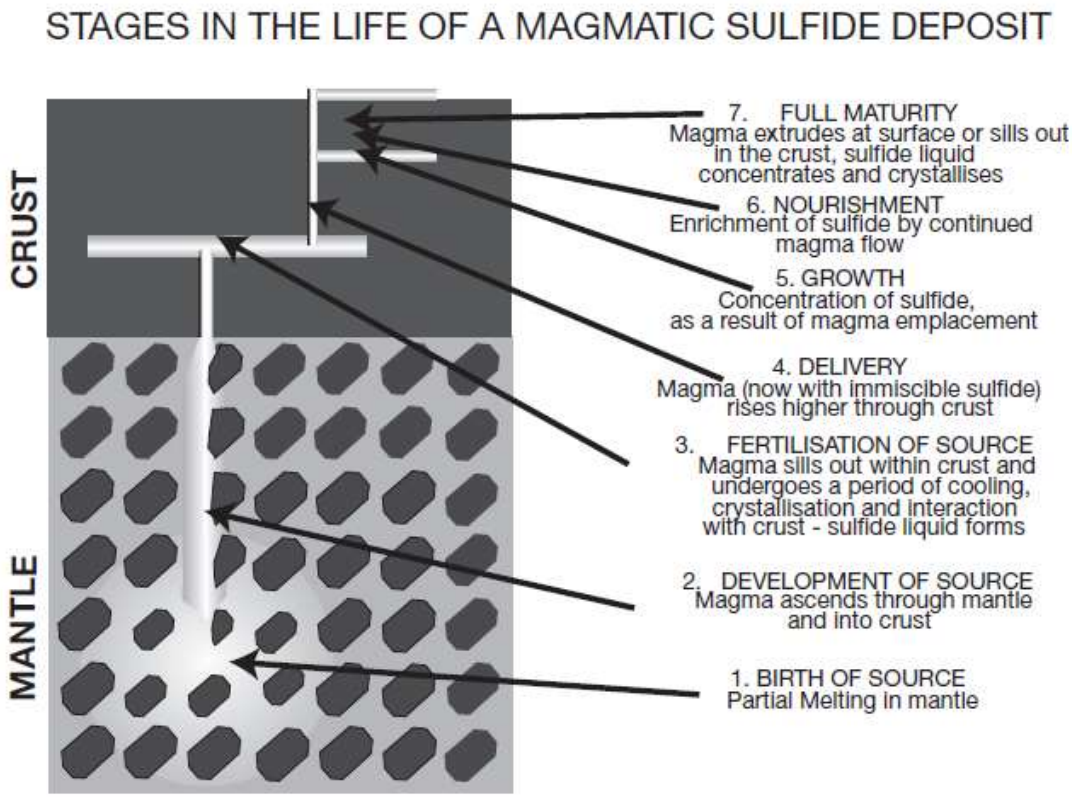

Figure 13.2 Stages from conception to development to delivery and growth of a magmatic sulfide deposit (Naldrett, 2010).

13.2 Hydrothermal Deposits

Hydrothermal ore deposits are deposits that form when ore minerals are precipitated from a hot, metal-rich aqueous fluid. Metals carried by these fluids are deposited either in void spaces present in the rocks or by the replacement of other pre-existing minerals when they precipitate from solution once their solubility is exceeded. This type of deposit can form in several different geological settings; from environments centered on magmatic rifting, orogenic activity, or in sedimentary basins. Samples

selected for this thesis represent both magmatic and sedimentary environments (Richards, 2011; Ridley, 2013).

13.2.1 Magmatic Environments

Hydrothermal deposits that form in magmatic environments do so around areas where there is an upward migration of magma. The deposits are not centered where the magma itself is emplaced but offset where hydrothermal fluids circulate because of temperature gradients and resulting hydrothermal convection. There are two types of fluids that circulate in these systems: magmatic-hydrothermal fluids and groundwater. Magmatic-hydrothermal fluids are solutions of water and volatiles that were originally part of the magma but exsolved as decompression occurred because of the rising magma. Groundwater is any water that is present in the rock that is being intruded by the magma; it can be meteoric, connate, or oceanic in origin depending on the environment the deposit is being formed. As the magma rises the groundwater is heated and begins to convect within the system; this process can scour metals from the country rock and precipitate ore minerals when metal solubility is exceeded (Sillitoe, 2010; Ridley, 2013).

13.2.1.1 Porphyry

Porphyry deposits are representative of hydrothermal fluids escaping from a magmatic intrusion into the crust. The most important commodities that these deposits are mined for are Cu, Mo, and Ag (Ridley, 2013). These deposits occur typically within continental or oceanic volcanic arcs (fig. 13.3; Sillitoe, 2010). They most commonly form either during subduction or just after subduction has ceased, but have also been known to

form because of post-collisional thermal rebound or extension and also delamination of the sub-continental lithospheric mantle (Richards, 2011).

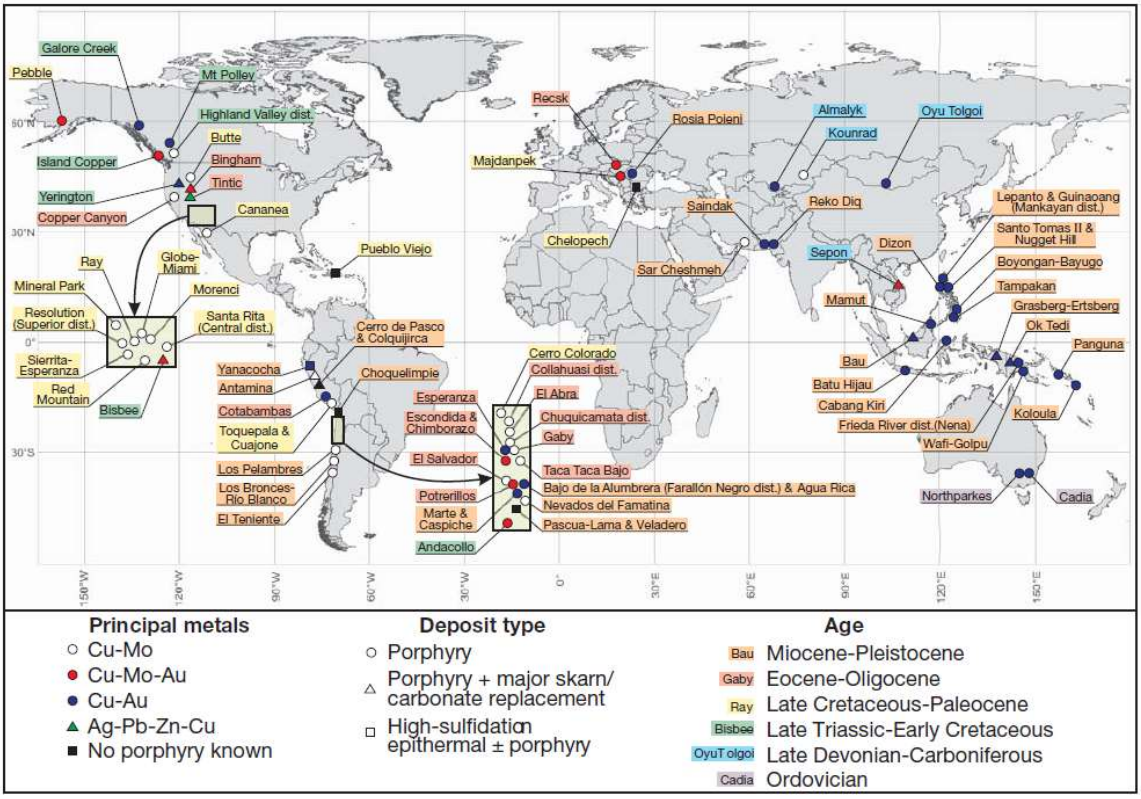

Figure 13.3 Worldwide locations of porphyry deposits that also illustrates the principle metals contained with, the deposit sub-types, and the age that the deposits formed (Sillitoe, 2010).

Porphyry deposits form when a pluton-sized body of magma that is crystallizing reaches a saturation point with respect to its fluid phase. The fluid begins exsolving from the melt, most likely as gas bubbles, which then move upwards towards the cupola where they begin to collect. Eventually as the fluids continue to collect, a critical fluid pressure is reached that exceeds the lithostatic pressure causing the rocks above the cupola to begin hydrofracturing, creating a network of stockwork veins or sometimes breccias. The over pressurized fluids move throughout the fracture rock and as they depressurize and

begin to cool specific mineral assemblages begin to precipitate out of the fluids within typical zones of alteration (fig. 13.4, 13.5; Sillitoe, 2010; Ridley, 2013).

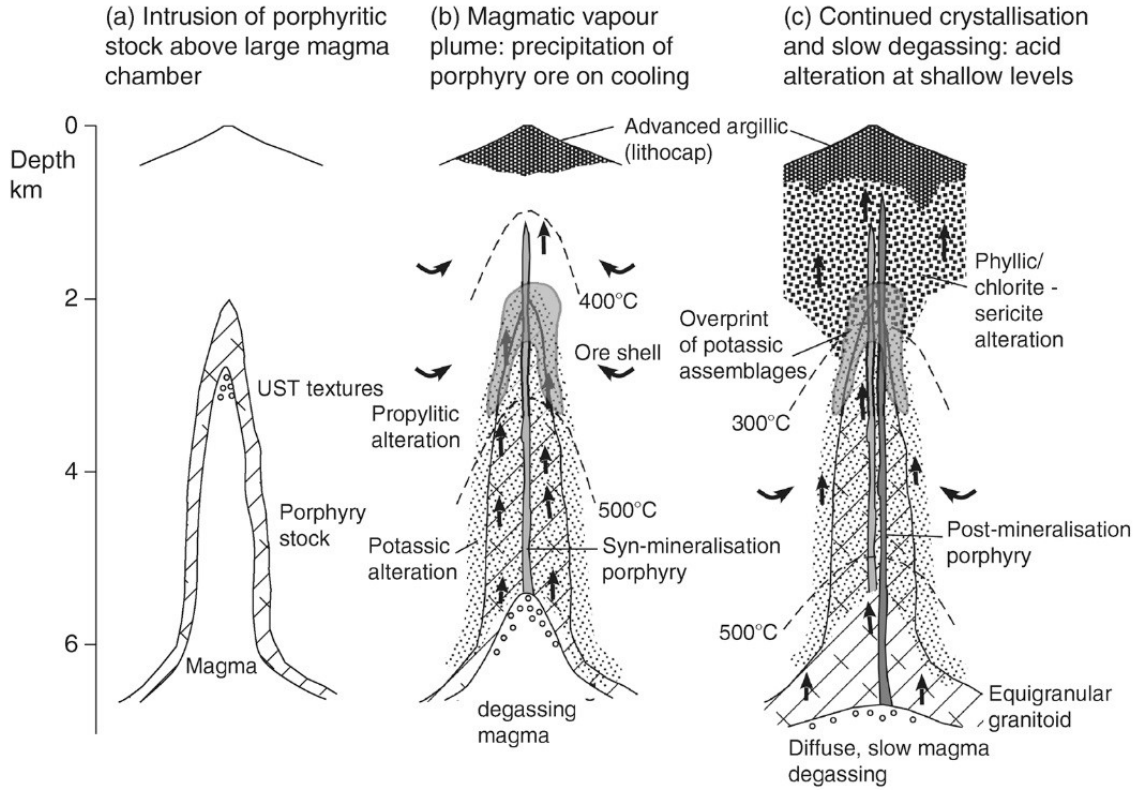

Figure 13.4 Schematic diagram illustrating the progressive development of a porphyry deposit (Ridley, 2013).

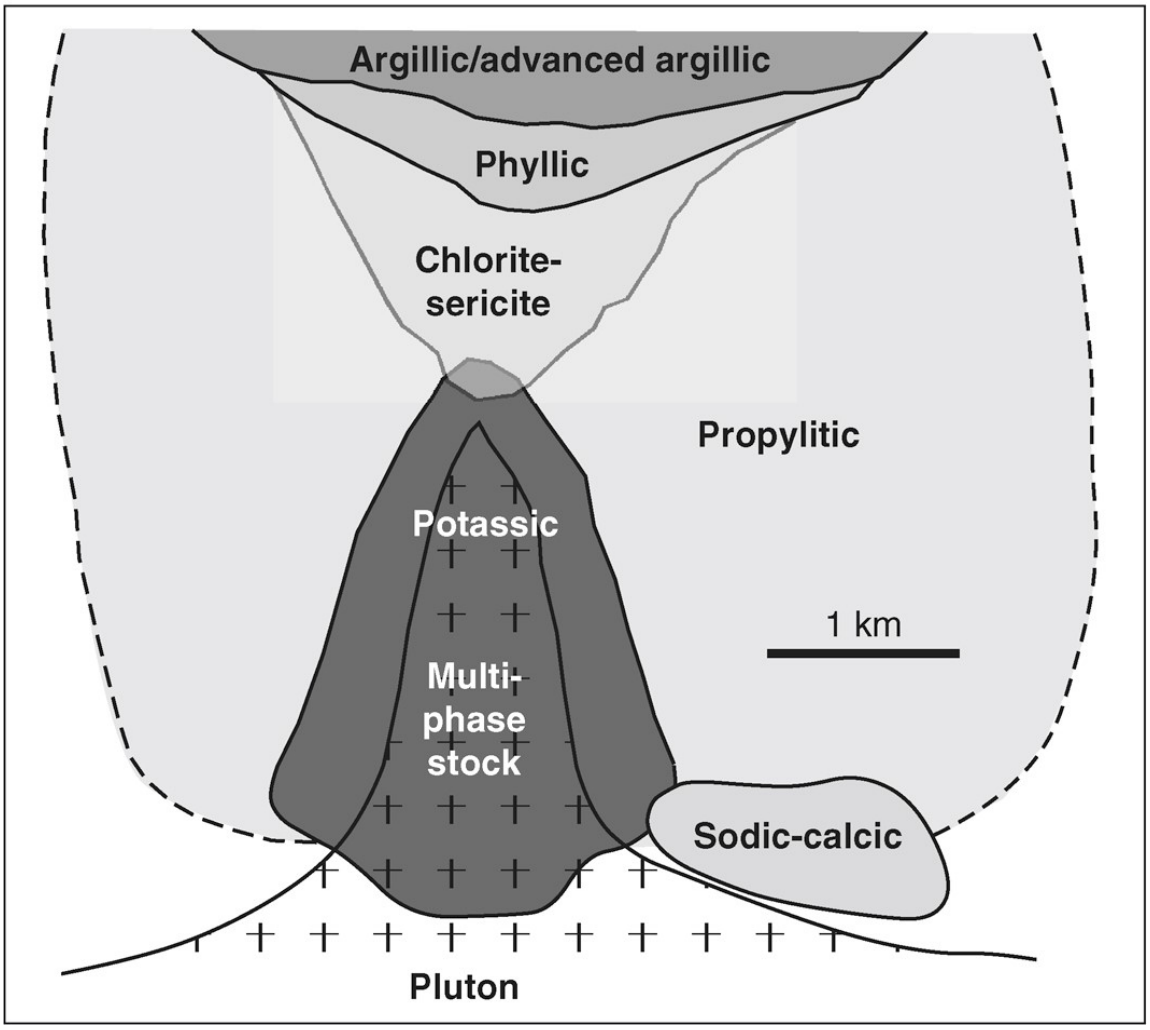

Figure 13.5 Schematic diagram illustrating where in a porphyry deposit the common zones of alteration occur (Ridley, 2013).

13.2.1.2 Volcanic-hosted Massive Sulfide (VHMS)

VHMS deposits are bodies of massive sulfide ore that form in relatively deep marine environments at or just below the seafloor surface. VHMS deposits are polymetallic deposits that represent important sources of Cu, Zn, Pb, Au and Ag, which can all be potentially found within a single deposit (Ridley, 2013). These deposits form by the circulation of hydrothermal fluids and heated seawater leaching metals from the surrounding rocks and depositing them as sulfides upon cooling and mixing. During their

formation, these deposits are situated near active magmatic spreading centers which provide both the heat and some metals that allow for the circulation of a metal-rich hydrothermal fluid. They form in any submarine region undergoing some sort of tectonic extension or rifting. However, the deposits that are typically mined form in back-arcs, rifted arcs, and oceanic and continental nascent-arcs because these are more likely to be preserved as they are not subject to subduction (fig 13.6; Galley et al., 2007; Ridley, 2013).

As these deposits develop, there is typically a progression of increasing temperatures within the hydrothermal system that results in the deposit forming in sequential stages represented by key ore mineral precipitation events (fig. 13.7). In addition to the temperature of the hydrothermal fluids, there are other variables that can affect the deposits formation (fig. 13.8). For example, if the deposits host rock is highly permeable the ore bearing fluids will disperse throughout, resulting in a highly disseminated distribution of ore and a much smaller deposit size (fig 13.8; Large, 1992).

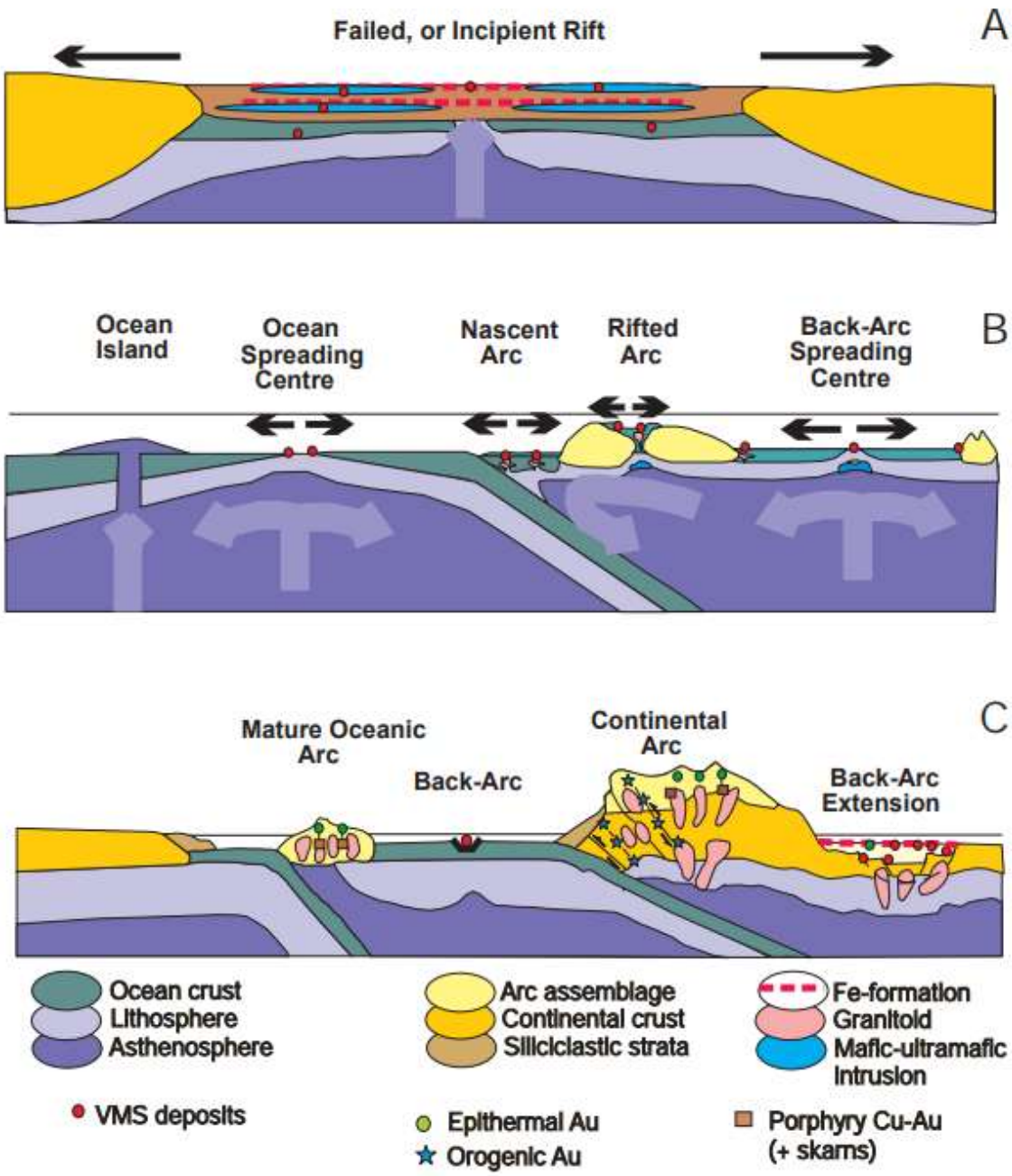

Figure 13.6 Schematic diagrams of three principle tectonic environments where VHMS deposits can form. Early environments were dominated by mantle plum rifting during the creation of the ocean crust. Typically found in primitive basalts or komatiite host rocks (top). Formation of ocean basins with the associated spreading centers. Typically found in bimodal-mafic, bimodal-felsic, and mafic-dominated host rocks (middle). A mature arc displaying ocean-continent subduction fronts. Typically found in felsic-dominated and bimodal-siliciclastic host rocks (bottom, Galley et al., 2007).

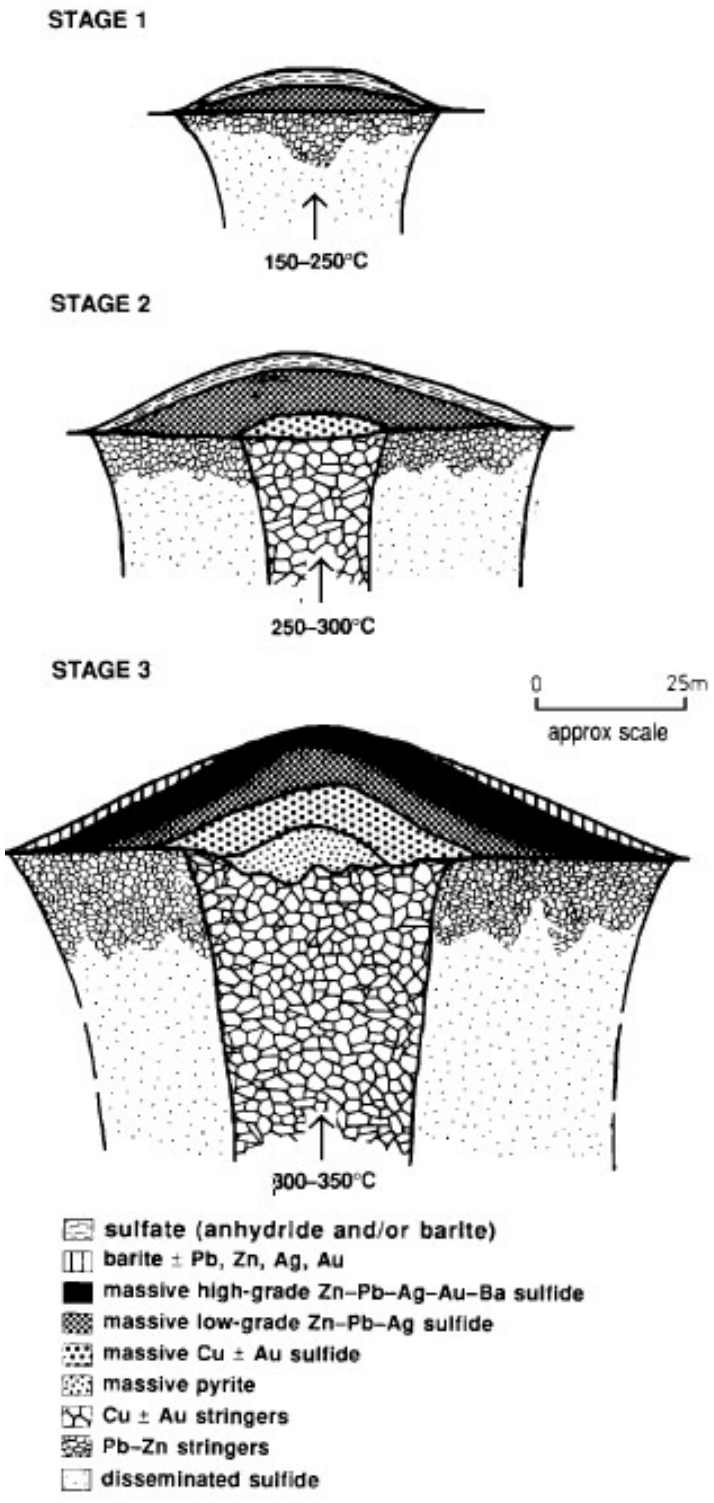

Figure 13.7 Schematic diagram illustrating the three main stages of a VHMS deposit formation. Stage 1: As the hydrothermal system begins to form low-temperature (150°-250°C) fluids are the first to circulate. Stage 2: the hydrothermal system continues to develop the fluid temperatures will rise through the range of 250°-300°C. Stage 3: Once the hydrothermal fluids reach the temperature range of 300°-350°C (Large, 1992).

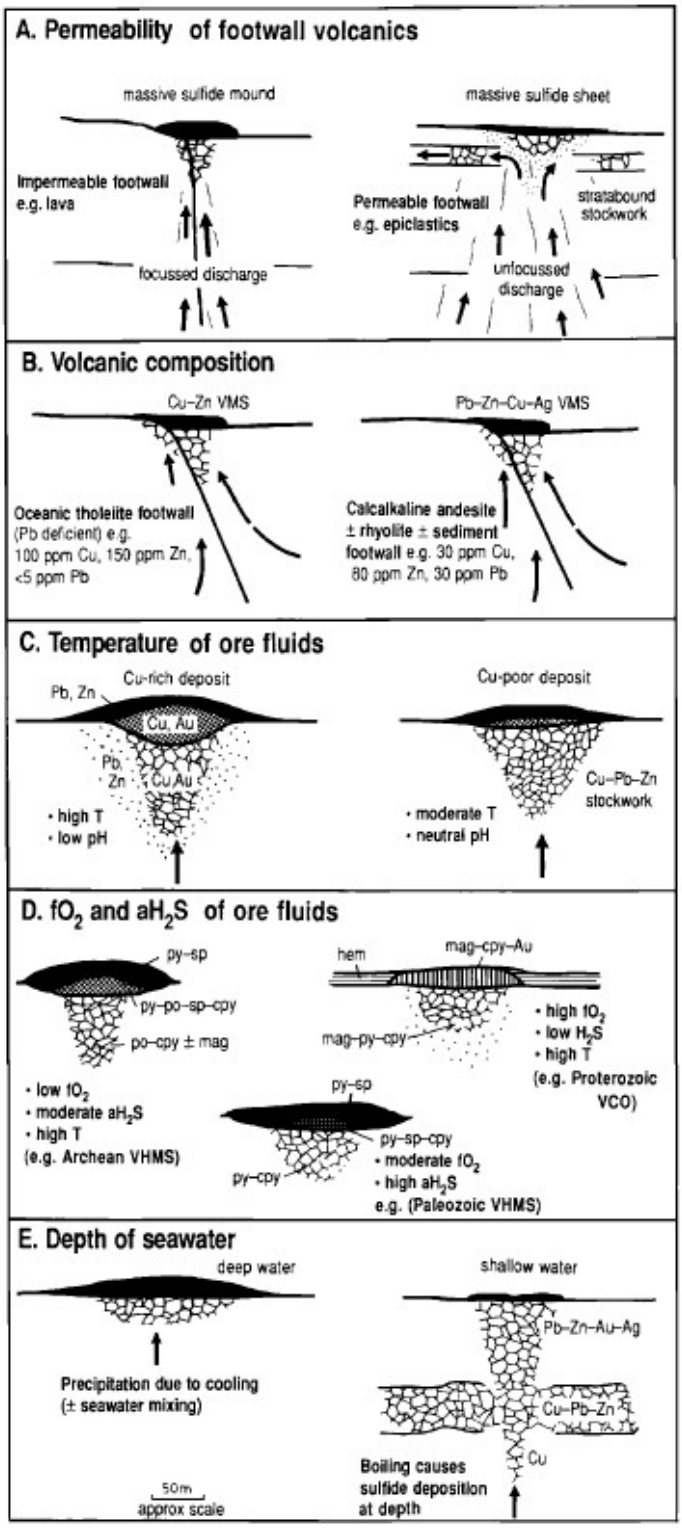

Figure 13.8 Schematic diagrams illustrating the effects that different variables can have on a VMHS deposit. Permeability of the country rock (A) Melt composition of the associated volcanic magma (B) Temperature and pH of ore bearing hydrothermal fluids (C) oxygen fugacity and aH_2S of ore fluids (D) and depth of the seawater (E, Large, 1992).

13.2.2 Sedimentary Environments

Hydrothermal deposits in sedimentary environments mostly form without heat or fluids derived from a magmatic source. This means that the temperature of fluids is much lower compared to hydrothermal deposits that form in a magmatic environment and results in a more limited ore mineralogy occurring within sedimentary deposits. These deposits are all found within sedimentary basins and ore mineralization is considered to either be syngenetic (ores mineralizing at the same time as sedimentation) or epigenetic (ores mineralizing at a later time; Ridley, 2013).

13.2.2.1 Mississippi Valley-type (MVT)

MVT deposits are Pb-Zn sulfide deposits that are found principally within limestones, dolostones, and occasionally sandstones. These deposits are epigenetic in that they typically replace carbonate material within the host rock and to a lesser extent fill void space (fig. 13.9; Leach et al., 2010). MVT deposits are found within sedimentary basins that represent former shallow marine environments. They occur in either intracrationic or broad rift basins that formed at passive continental margins or within the interior of continents (Ridley, 2013).

MVT deposits form when a saline-rich (10 to 30 wt% NaCl eq.) sedimentary fluid is expelled from a basin and intrudes into shallow carbonate rocks through either the existing porosity of the carbonate host rocks or by other transfer pathways such as faults or fractures. These brines are likely the source of S for these deposits, which can come from sulfur-bearing organic material, H_2S reservoir gas, or as reduced S from anoxic waters present within stratified basin waters. The brine temperatures range from 50 to

200°C and dissolve metals from the host rocks as they traverse rock packages. Ore precipitation mainly occurs because of fluid mixing but can also include changes in pH, temperature, or redox conditions (Leach et al., 2010; Ridley, 2013).

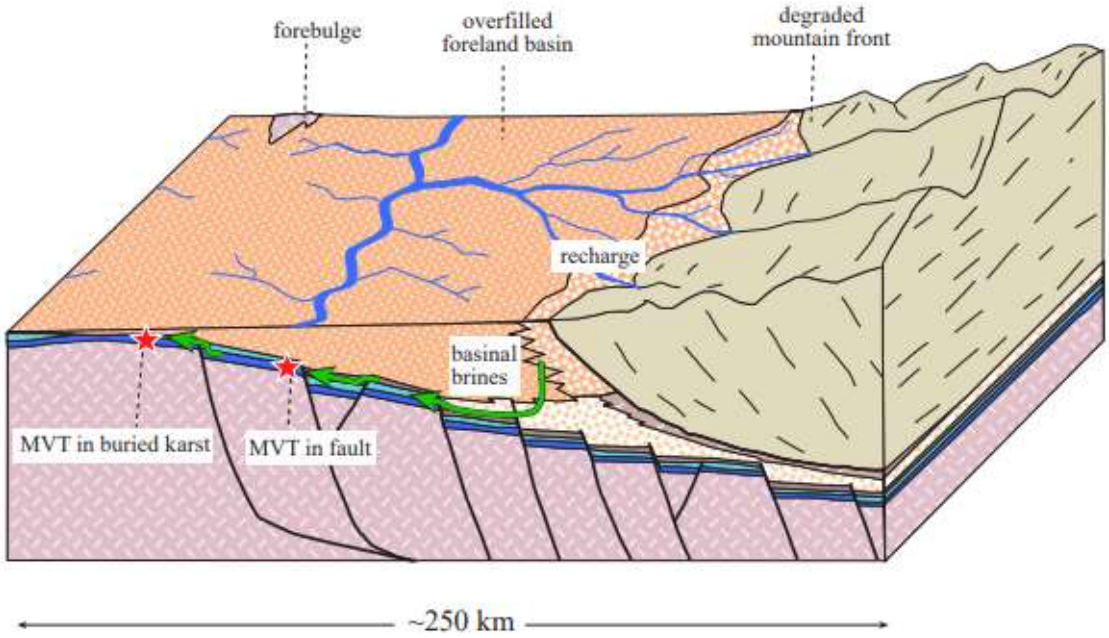

Figure 13.9 Schematic diagram illustrating gravity driven fluid flow in a sedimentary basin with locations of potential MVTs deposits indicated (Bradley and Leach, 2003).

13.2.2.2 SSC

Sediment-Hosted Stratabound Copper Deposit (SSC), sometimes called red-bed copper deposits, are strata bound, laterally extensive, and contain mainly Cu minerals. However, they can also host minor amounts of Ni, Ag, Zn, Pb, Co, and U-bearing ore minerals (Ridley, 2013). These deposits are hosted within carbonaceous shales, siltstones, and to a lesser extent, sandstones and they always occur “downstream” from a pre-existing red-bed within basins. SSC deposits are also commonly affiliated with rift

basins. The host rocks, typically referred to as grey beds, are usually rich in organics, represent a sedimentary environment that was anoxic, and are therefore rich in S.

For an SSC deposit to form there are several conditions that must be present within the basin. (1) A Cu containing red-bed acts as a source rock for the metal, (2) <100 °C chloride rich brine transports the metal to a grey-bed via fractures or porosity, (3) the destination grey-bed must be sulfur-rich, (4) structural deformation must have occurred that created traps which also have confining beds above them (fig. 13.10; (Brown, 1992; Hayes et al., 2015).

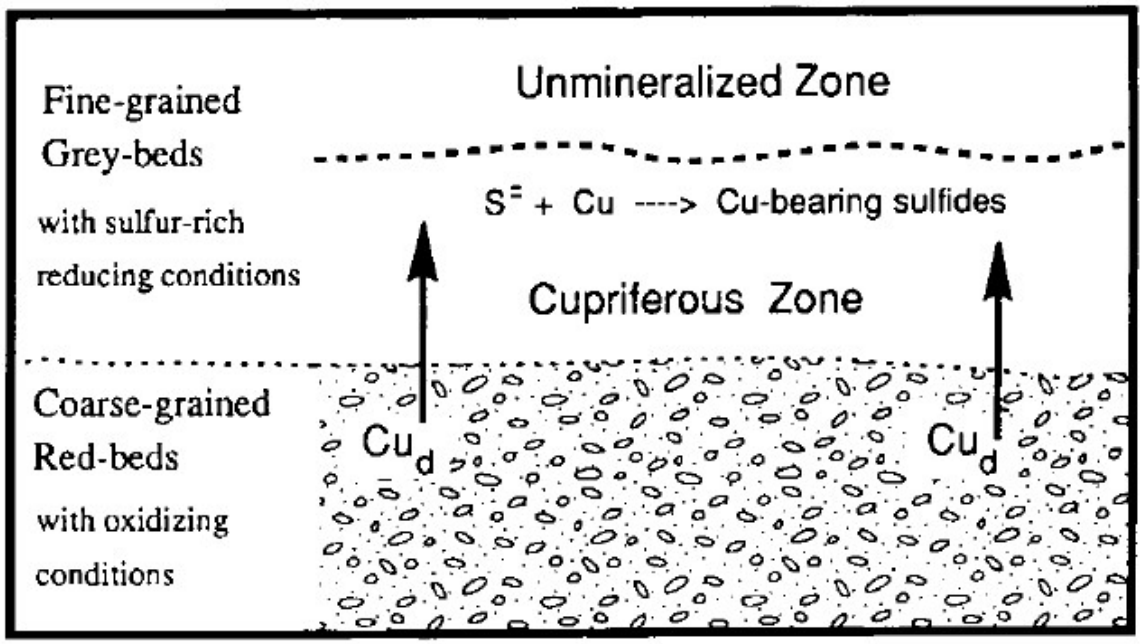

Figure 13.10 A schematic diagram providing a deposit scale model for SSC deposits. The thick dotted line represents the greatest extent that Cu mineralization appears within grey-beds (Brown, 1992).